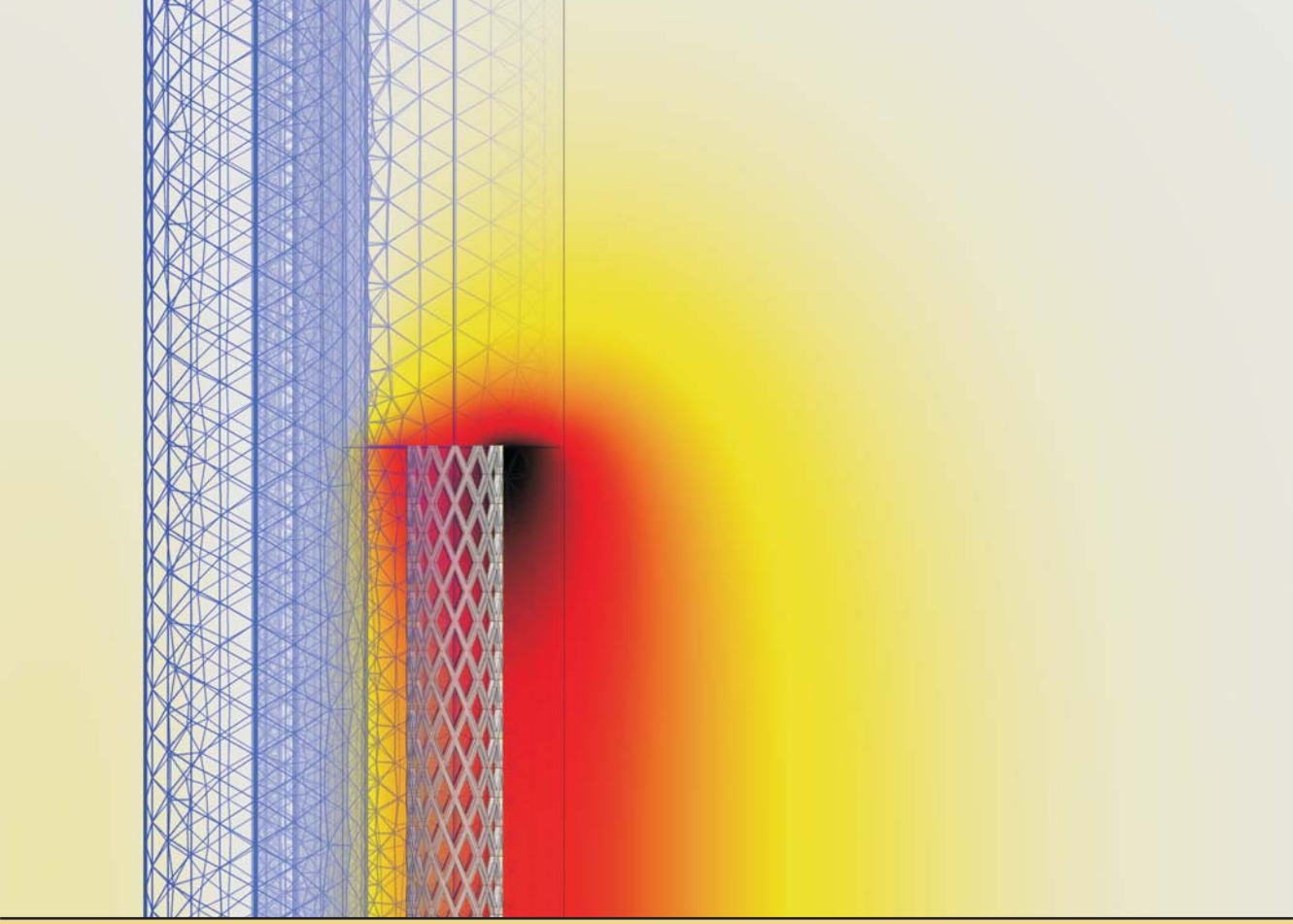

Tony Richard de Oliveira de Almeida

Development of a Stent-Based Electrode for Radio Frequency Thermal Ablation Procedure

2012

· U C ·

Universidade de Coimbra

Universidade de Coimbra
Faculdade de Ciências e Tecnologia
Departamento de Engenharia Eletrotécnica e de Computadores

Development of a Stent-Based Electrode for Radio Frequency Thermal Ablation Procedure

Tony Richard de Oliveira de Almeida

Coimbra - Portugal
2012

Universidade de Coimbra
Faculdade de Ciências e Tecnologia
Departamento de Engenharia Eletrotécnica e de Computadores

Development of a Stent-Based Electrode for Radio Frequency Thermal Ablation Procedure

Dissertação submetida para a obtenção do grau de
Doutor em Engenharia Eletrotécnica, na especialidade de
Materiais e Campos Eletromagnéticos

Tony Richard de Oliveira de Almeida

Coimbra - Portugal
2012

Tese realizada sob orientação do
Professor Doutor Carlos Fernando Ramos Lemos Antunes
Professor Catedrático do
Departamento de Engenharia Eletrotécnica e de Computadores
Faculdade de Ciências e Tecnologia
Universidade de Coimbra

Aos meus filhos Cármen e Elói,
à minha esposa Márcia e
à memória do meu pai

Agradecimentos

Apesar do corpo da tese estar escrito em inglês, não posso deixar de expressar, na minha língua materna, os meus mais sinceros agradecimentos a todos aqueles que, de uma forma ou de outra, foram parte importante deste trabalho.

Em primeiro lugar, quero agradecer ao meu orientador, o Professor Doutor Carlos Lemos Antunes, toda a sua disponibilidade e orientação científica com que me apoiou no decurso dos trabalhos que conduziram à apresentação desta dissertação. A sua motivação e empenho foram fundamentais para, se me é permitido expressar desta forma, levar este barco a bom porto.

À Nélia Raposeiro, agradeço todo o apoio prestado durante o trabalho de simulação, assim como a ajuda na revisão final do texto.

Ao Nuno Gonçalves, agradeço por me ter "convertido" ao LaTeX, assim como todo o apoio prestado na produção deste documento.

Ao Pedro Faia, agradeço a disponibilidade do Laboratório de Tecnologia dos Materiais Eletrónicos e Ultrassons do DEEC/FCTUC, o que permitiu fazer a caracterização elétrica do fórceps.

Ao Departamento de Engenharia Eletrotécnica e de Computadores da Faculdade de Ciências e Tecnologia da Universidade de Coimbra e à Fundação para a Ciência e a Tecnologia pelo apoio institucional à realização do meu doutoramento.

Ao Dr. Nuno Pinto, diretor do Matadouro da Beira Litoral (Aveiro), agradeço a disponibilidade na obtenção das várias amostras de tecido biológico necessárias para a realização da parte experimental deste trabalho.

À Covidien Portugal, agradeço a disponibilidade do equipamento que foi imprescindível para a realização dos testes de ablação térmica por radiofrequência.

Quero também agradecer profundamente aos meus amigos, à minha família, e muito especialmente à minha mulher e aos meus filhos pelas infindáveis horas que lhes roubei e que sei nunca, de forma alguma, poderei compensar. Márcia, obrigado pela tua grande compreensão, apoio e incentivo durante todo este tempo.

E muito especialmente ao meu pai, a quem devo muito do que sou hoje e a quem acho que nunca pude agradecer o suficiente tudo o que fez por mim. Onde quer que estejas, muito obrigado.

Contents

Resumo **xix**

Abstract **xxi**

1 Introduction **1**

1.1 Motivation and Objectives 1

1.2 Organization of the Thesis 4

1.3 Contribution 5

2 Properties of Tissue **9**

2.1 Electrical Properties of Biological Tissues 10

2.1.1 Dielectric and Electrical Conductivity in Biological Tissues . 10

2.1.2 Complex Permittivity 11

2.1.3 Relaxation 14

2.1.4 Dispersion in Biological Tissues 17

2.1.5 Available Data 19

2.1.6 Parametric Model for Describing the Dielectric Properties of Biological Tissues 21

2.1.7 Temperature Dependence of the Electrical Properties 23

2.1.8 *In Vivo* and *Ex Vivo* Properties 25

2.1.9 Tumorous Tissues 26

2.2 Magnetic Properties of Biological Tissues 27

2.3 Thermal Properties of Biological Tissues 28
2.3.1 Thermal Conductivity and Heat Diffusion 28
2.3.2 Bioheat Equation 29
2.3.3 Available Data on Thermal Properties of Biological Tissues . 30
2.3.4 Factors Affecting Thermal Conductivity 31

3 Radio Frequency Ablation 35
3.1 Historical Introduction 35
3.2 Radio Frequency Ablation 44
3.2.1 Mechanism of Radio Frequency Ablation 44
3.2.2 Thermal Necrosis 46
3.3 RF Ablation Electrodes 48
3.3.1 Monopolar Electrodes 48
3.3.2 Bipolar Electrodes 55
3.3.3 Combination of Electrode Designs 57
3.3.4 Multiple Electrode Systems 59
3.3.5 Saline-Enhanced RF Ablation 60
3.3.6 Size and Geometry of RF Lesions 61
3.4 Commercial RF Ablation Systems 64
3.4.1 Covidien – Cool-tip^{TM} RF Ablation System 66
3.4.2 AngioDynamics – StarBurst Radiofrequency Ablation System 67
3.4.3 Boston Scientific – RF 3000 Radiofrequency Ablation System 68
3.4.4 Olympus – CelonPOWER System 69

4 Preliminary Experimental Tests 73
4.1 Introduction 73
4.2 Preliminary Set-up 74
4.2.1 Description 74
4.2.2 Results 76
4.3 Numerical Simulation 82
4.3.1 Theoretical Model 82
4.3.2 Description of the Model 83
4.3.3 Physical Properties and Boundary Conditions 84
4.3.4 Numerical Results 85
4.4 Connecting the Electrode to the RF Generator Through a Forceps . . . 88
4.5 Conclusions 92

5 Characterization of the Induced Lesion **95**
5.1 Objectives . . . 95
5.2 *Ex Vivo* Experimentation . . . 96
5.2.1 Experimental Set-up . . . 96
5.2.2 Measurement of the Electrical Conductivity . . . 97
5.2.3 Methodology . . . 102
5.2.4 Results . . . 102
5.3 Numerical Simulation . . . 109
5.3.1 Description of the Model . . . 109
5.3.2 Physical Properties and Boundary Conditions . . . 110
5.3.3 Determination of the Lesion Volume from the Numerical Solutions . . . 111
5.3.4 Numerical Results . . . 112
5.4 Conclusions . . . 114

6 Effects of the Geometry of the Electrode on the Temperature Distribution **115**
6.1 Objective . . . 115
6.2 Numerical Model . . . 116
6.2.1 Theoretical Model . . . 116
6.2.2 Description of the Model . . . 116
6.2.3 Physical Properties and Boundary Conditions . . . 117
6.3 Determination of the Lesion Size . . . 118
6.4 Results and Discussion . . . 118
6.5 Conclusions . . . 126

7 RF Ablation of a Cholangiocarcinoma: Numerical Simulation **129**
7.1 Introduction . . . 129
7.2 RF Ablation Without Saline Solution . . . 130
7.2.1 Theoretical Model . . . 130
7.2.2 Description of the Model . . . 131
7.2.3 Determination of the Volume Size . . . 134
7.2.4 Results . . . 134
7.3 Saline-Enhanced RF Ablation: First Approach . . . 138
7.3.1 Modelling the Saline Solution in the Tissue . . . 138
7.3.2 Results and Discussion . . . 139
7.4 Saline-Enhanced RF Ablation: Second Approach . . . 148

7.4.1 Conductivity of the Tumorous Tissue 148
7.4.2 Results and Discussion 150
7.5 Conclusions 155

8 Conclusion **161**
8.1 Summary of the Research 161
8.2 Future Work 163

Bibliography **165**

Errata **195**

List of Tables

2.1 Mechanisms present in the dielectric response of different biological systems. 19
2.2 Parameters of Equation (2.26) for predicting the dielectric properties of liver tissue (from [GLG96b]). 22

3.1 Technical specifications of commercial RF ablation generators 65

4.1 Material properties used in the numerical simulation of the preliminary stent-based electrode (from [HST+01]). 84

5.1 Material properties (from [HST+01], except electrical conductivity of liver tissue). 110

7.1 Blood vessels properties used in the numerical simulation of the cholangiocarcinoma RF ablation. 133
7.2 Material properties used in the numerical simulation of the cholangiocarcinoma RF ablation. 133

List of Figures

2.1 Equivalent circuit of a parallel plate capacitor filled with a non-ideal dielectric 12
2.2 Example of the polarization decay after removing an applied electric field. 12
2.3 Step electric field applied to a dielectric medium and its relaxed response 15
2.4 Conductivity, normalized permittivity $(\varepsilon' - \varepsilon_\infty)/(\varepsilon_s - \varepsilon_\infty)$, and loss factor $\omega\varepsilon_0\varepsilon''/(\varepsilon_s - \varepsilon_\infty)$ vs. frequency for a single constant case. . . . 16
2.5 Relative permittivity of a biological tissue as function of frequency . . 17
2.6 Debye dispersion considering a multi-term dispersion model. Change of the relative permittivity for the n-term. 21
2.7 Frequency dependence of the dielectric permittivity and the electrical conductivity of liver tissue obtained from Equation (2.26) 23
2.8 Electrical conductivity of tumour and normal liver tissue 26
2.9 Magnetotactic bacterium cell with magnetosomes 27

3.1 Illustration of Guericke's sulphur globe 36
3.2 Replica of Hauskbee's generator and Gray's experiment 37
3.3 Illustration of the Gray's *The electrical boy* 38
3.4 Plate from Galvani's *De viribus electricitatis in motu musculari commentarius* presenting his laboratory 40
3.5 Representation of a voltaic pile used in Aldini's electroshock therapy . 41

3.6 d'Arsonval adjusting the spark gap of his improved high-frequency generator . . . 42
3.7 The first medical diathermy machine used in the United Kingdom . . 43
3.8 Representation of a hepatic RF ablation set-up . . . 44
3.9 Placement of four ground electrodes equally spaced from the RF electrode . . . 45
3.10 Catheter-based electrodes commonly used for cardiac RF ablation . . 48
3.11 Original needle-based electrode . . . 49
3.12 Correlation of tip exposure to lesion length . . . 50
3.13 Four different electrode designs . . . 51
3.14 Longitudinal section of a cooled electrode . . . 52
3.15 Screw-tip cannulated electrode . . . 53
3.16 Electric field intensity obtained with a expandable umbrella-like electrode . . . 54
3.17 Expandable coiled electrode Invatec MIRAS RC . . . 54
3.18 Bipolar RF ablation. Electrical field intensity on a longitudinal plane to the bipolar-expandable electrodes . . . 55
3.19 Necrosis coagulation obtained in an *ex vivo* bovine liver with bipolar RF ablation for different power settings . . . 56
3.20 Bipolar 18 gauge needle-based electrode for RF ablation of osteoid osteoma (detail) . . . 57
3.21 Five basic designs of RF ablation electrodes . . . 58
3.22 Combinations designs for single-shaft electrodes . . . 58
3.23 Example of multiple electrode designs . . . 60
3.24 Type of distortions of the induced lesion volume . . . 62
3.25 Development of the induced lesion during a RF ablation with a bipolar electrode . . . 63
3.26 Cool-tip™ RF ablation system – power generator and perfusion unit . 66
3.27 StarBurst© Radiofrequency Ablation System . . . 67
3.28 RF 3000© Radiofrequency Power Generator . . . 68
3.29 CelonPOWER System . . . 69
3.30 Multi-polar mode with CelonPOWER System: possible electrode couples and path of electric current between the electrodes . . . 70

4.1 Preliminary stent-based electrode . . . 74
4.2 Location of the RTDs . . . 75

4.3 Set-up for the preliminary experimentation work 75
4.4 Tissue dehydration during RF ablation procedure 76
4.5 Temperature readings using a copper tube electrode for an applied voltage of 40 V 77
4.6 Longitudinal section of the lesion induced with a tubular copper electrode 77
4.7 Temperature readings using the stent-based electrode for a step-like voltage varying from 26 to 55 V (at $t = 210$s) 78
4.8 Temperature readings using the stent-based electrode for an applied voltage of 50 V. 79
4.9 Temperature readings using the stent-based electrode for an applied voltage of 75 V. 79
4.10 Longitudinal section of the lesion induced with the stent-based for an applied voltage of 50 V 80
4.11 Longitudinal section of the lesion induced with the stent-based for an applied voltage of 75 V 80
4.12 Current intensity, impedance and power delivered to the tissue during a RF ablation at an applied voltage of 75 V 81
4.13 Stent-based electrode condition after the set of experimental tests . . . 81
4.14 Proposed model for simulation of the preliminary experimental set-up 85
4.15 Temperatures values obtained after simulation of the step-like applied voltage described in Equation (4.1). 86
4.16 Temperatures values obtained after simulation an applied voltage of 50 V 86
4.17 Temperatures values obtained after simulation an applied voltage of 75 V 87
4.18 Longitudinal section of an induced thermal lesion obtained for an applied voltage of 50 V after 395 s. A 50°C isothermal curve obtained after numerical simulation is overlapped (red curve). 87
4.19 Longitudinal section of an induced thermal lesion obtained for an applied voltage of 75 V after 220 s. A 50°C isothermal curve obtained after numerical simulation is overlapped (red curve). 88
4.20 (a) BI-PAL endoscopic biopsy forceps; (b) Detail of the electrical connection through the forceps's shaft. 90
4.21 Attaching the biopsy forceps to the stent 90

4.22 Impedance and current values for an applied voltage of 100 V in a set-up using a biopsy forceps for electrical connection between the electrode and the RF power generator 90
4.23 Electrical characterization of the biopsy forceps. Impedance values, magnitude and phase, obtained from 40 Hz to 110 MHz. 91

5.1 Wallflex biliary self-expandable metallic stent from Boston Scientific. 96
5.2 Experimental set-up used for characterize the size of the volume lesion obtained with the stent-based electrode 97
5.3 Equipotential and current lines due to an electrode placed on the surface of a homogeneous medium of electrical resistivity ρ 98
5.4 Generalized configuration of four electrodes located on the surface of a homogeneous medium of electrical resistivity ρ 98
5.5 Wenner electrode configuration 99
5.6 Wenner electrode configuration 101
5.7 Schematic of the circuit used for conditioning the voltage and the current obtained from the measuring probe 101
5.8 Current intensity delivered by the power generator measured during a RF ablation procedure of 15 minutes for an applied voltage of 25 V and 100 V. 102
5.9 Induced thermal lesions in bovine liver after a RF ablation procedure of 15 minutes at an applied voltage of (a) 25 V, (b) 50 V, (c) 75 V, and (d) 100 V. 104
5.10 Longitudinal section of the induced lesion obtained for an applied voltage of 50 V after, 5, 10 and 15 minutes. 105
5.11 Longitudinal section of the induced lesion obtained for an applied voltage of 75 V after, 5, 10 and 15 minutes. 105
5.12 Longitudinal section of the induced lesion obtained for an applied voltage of 100 V after, 5, 10 and 15 minutes. 105
5.13 Average temperature readings measured at 1 and 2 cm from the electrode for an applied voltage of 25, 50, 75 and 100 V. 106
5.14 Average temperatures after (a) 5 minutes; (b) 10 minutes; and (c) 15 minutes. 107
5.15 Cylindrical volume approximation of the lesions induced in the tissue by RF ablation. 108

5.16 Model considered for numerical characterization of the induced lesion. Only a quarter of the model was considered taking into account the symmetry of the problem. 109
5.17 Temperature distribution on a longitudinal section of the model for an applied voltage of 25 V after 15 minutes 112
5.18 Lesion volume assessed from an isothermal surface of 50°C considering an applied voltage of 50 V after (a) 5 minutes; (b) 15 minutes . . 113
5.19 Lesion volume assessed from an isothermal surface of 50°C considering an applied voltage of 100 V after (a) 5 minutes; (b) 15 minutes . 113
5.20 Cylindrical volume approximation of the lesions induced in the tissue by RF ablation. Numerical and experimental results. 113

6.1 Different stent geometries obtained after varying the number of interlaced helices. 117
6.2 Maximum temperature obtained for an applied voltage of 25 V after 15 minutes versus the number of wires used to build the stent-based electrode 119
6.3 Isothermal surfaces of 50 and 60°C obtained after 5 minutes at 50 V with a stent-based electrode using 4 interlaced helices. 120
6.4 Isothermal surfaces of 50 and 60°C obtained after 5 minutes at 50 V with a stent-based electrode using 12 interlaced helices. 120
6.5 Isothermal surfaces of 50 and 60°C obtained after 5 minutes at 50 V with a stent-based electrode using 24 interlaced helices. 120
6.6 Isothermal surfaces of 50 and 60°C obtained after 5 minutes at 50 V, 75 V, and 100 V. 121
6.7 Isothermal surfaces of 50 and 60°C obtained considering an applied voltage of 50 V after 5 minutes, 10 minutes, and 15 minutes 121
6.8 Volume delimited by the isothermal surface of 50°C considering an applied voltage of 50 V. 123
6.9 Volume delimited by the isothermal surface of 50°C considering an applied voltage of 75 V. 123
6.10 Volume delimited by the isothermal surface of 50°C considering an applied voltage of 100 V. 124
6.11 Volume delimited by an isothermal surface of 50°C versus the numbers of helices of the electrode. Results after 5, 10 and 15 minutes . . 124

6.12 Temperature distribution obtained after using a stent-based electrode of 4 helices for an applied voltage of 50 V during 40 seconds. Maximum temperature: 69.4°C. 125
6.13 Temperature distribution obtained after using a stent-based electrode of 24 helices for an applied voltage of 50 V during 40 seconds. Maximum temperature: 46.3°C. 125
6.14 Volume delimited by the isothermal surface of 60°C considering an applied voltage of 75 V 126

7.1 Cross sectional representation of the location of portal vein, hepatic artery, and bile duct in the considered model 132
7.2 Simplified model of the portal hepatis. 132
7.3 Volumes obtained considering an isothermal surface of 50°C for applied voltages from 20 to 35 V. 135
7.4 Volumes obtained considering an isothermal surface of 60°C for applied voltages from 20 to 35 V. 135
7.5 Electrical current delivered by the electrode for applied voltages from 20 to 35 V 136
7.6 Volume obtained considering an isothermal surface of 50°C for an applied voltage of 20 V. 137
7.7 Volume obtained considering an isothermal surface of 50°C for an applied voltage of 35 V. 137
7.8 Detail of the porta hepatis model showing the tumour divided in three sections 138
7.9 Volume of lesion obtained for an applied voltage of 20 V considering an isothermal surface of 50°C. 141
7.10 Volume of lesion obtained for an applied voltage of 20 V considering an isothermal surface of 60°C. 141
7.11 Volume of lesion obtained for an applied voltage of 28 V considering an isothermal surface of 50°C. 142
7.12 Volume of lesion obtained for an applied voltage of 28 V considering an isothermal surface of 60°C. 142
7.13 Volume of lesion obtained for an applied voltage of 35 V considering an isothermal surface of 50°C. 143
7.14 Volume of lesion obtained for an applied voltage of 35 V considering an isothermal surface of 60°C. 143

7.15 Current density (norm) obtained for an applied voltage of 35 V with $ks = 2$. 144
7.16 Volume of lesion obtained for several voltage values considering isothermal surfaces of 50°C, with $ks = 2$ 145
7.17 Volume of lesion obtained for several voltage values considering isothermal surfaces of 50°C, with $ks = 5$ 145
7.18 Volume of lesion considering an isothermal surface of 50°C at 22 V without saline solution ($ks = 1$) 146
7.19 Volume of lesion considering an isothermal surface of 50°C at 22 V for $ks = 2$ 146
7.20 Volume of lesion considering an isothermal surface of 50°C at 22 V for $ks = 5$ 147
7.21 Volume of lesion obtained for different applied voltages considering an isothermal surface of 50°C and $ks = 3$ 147
7.22 Representation of the electrical conductivity of the tumour enhanced with saline solution 149
7.23 Volumes obtained for $s = 5 \cdot 10^{-3}$ considering an isothermal surface of 50°C for an applied voltage of 20 V 151
7.24 Volumes obtained for $s = 5 \cdot 10^{-3}$ considering an isothermal surface of 50°C for an applied voltage of 30 V 151
7.25 Volumes obtained for $s = 5 \cdot 10^{-3}$ considering an isothermal surface of 60°C for an applied voltage of 20 V 152
7.26 Volumes obtained for $s = 5 \cdot 10^{-3}$ considering an isothermal surface of 60°C for an applied voltage of 30 V 152
7.27 Volumes obtained considering an isothermal surface of 50°C at 20 V for $ks = 2$ 153
7.28 Volumes obtained considering an isothermal surface of 50°C at 20 V for $ks = 5$ 153
7.29 Volumes obtained considering an isothermal surface of 50°C at 30 V for $ks = 2$ 154
7.30 Volumes obtained considering an isothermal surface of 50°C at 30 V for $ks = 5$ 154
7.31 Volumes obtained considering an isothermal surface of 50°C with $ks = 3$ and $s = 1.7 \cdot 10^{-3}$ after 300 seconds 156

7.32 Volumes obtained considering an isothermal surface of 50°C with $ks = 3$ and $s = 6.75 \cdot 10^{-3}$ after 300 seconds 156
7.33 Volumes enclosed by an isothermal surface of 50°C at 20 V after 300 seconds with $ks = 2$ 157
7.34 Volumes enclosed by an isothermal surface of 50°C at 20 V after 300 seconds with $ks = 5$ 157

Resumo

Os *stents* metálicos auto-expansíveis são endopróteses normalmente utilizadas no tratamento paliativo dos sintomas provocados pelo crescimento de tumores cancerígenos no interior de órgãos tubulares, como sejam o cólon, o esófago ou o ducto biliar. A função deste dispositivo é a desobstrução do órgão por ação mecânica, exercendo uma força radial sobre as paredes do ducto, após ter sido posicionado. O nitinol, uma liga de níquel e titânio que, para além de possuir propriedades mecânicas únicas de elasticidade e de memória de forma, apresenta uma excelente biocompatibilidade, é um material que tem sido usado largamente na construção destas endopróteses.

Por outro lado, a ablação térmica por radiofrequência é um procedimento clínico que se tem revelado bastante eficaz no tratamento de tumores localizados em órgãos de tecidos moles. O tratamento de hepatocarcinomas com recurso a esta metodologia é talvez um dos mais documentados na literatura.

Nesta dissertação de doutoramento é proposto um elétrodo tubular que tem por base a utilização de um *stent* metálico auto-expansível. Pretende-se com este elétrodo possibilitar o tratamento de tumores localizados em órgãos tubulares através da ablação térmica por radiofrequência. É proposta uma metodologia que consiste na colocação do elétrodo segundo procedimentos convencionais no local a tratar, e.g., por laparoscopia, sendo posteriormente ligado a um gerador de radiofrequência através de um fórceps adaptado eletricamente para o efeito. Neste trabalho, é apresentada uma análise numérica e experimental da utilização deste elétrodo, de forma a avaliar e caracterizar o tipo de lesão térmica que é possível induzir.

Os dados obtidos a partir do trabalho experimental revelaram resultados promissores quando a aplicação deste tipo de elétrodo. Verificou-se que é possível induzir necrose térmica no tecido adjacente ao elétrodo, obtendo-se um volume regular e bem

definido. Dos dados experimentais, ainda foi possível definir e aferir um modelo numérico que permitiu simular a distribuição da temperatura no tecido biológico e prever o volume da lesão que pode ser induzida.

A partir da simulação numérica foi possível estudar o efeito da geometria do *stent* na distribuição da temperatura no tecido e determinar o tamanho e a forma do volume da lesão que é possível obter. Sendo que muitos dos *stents* disponíveis comercialmente são, em estrutura, muito semelhantes ao modelo estudado neste trabalho, é possível concluir que estes podem ser considerados potenciais elétrodos para ablação por radiofrequência, sem que para isso seja necessária qualquer alteração.

Foi ainda simulada a ablação térmica por radiofrequência de um tumor localizado no ducto biliar, de forma a estudar o efeito da transferência de calor por convecção devida ao fluxo de sangue em vasos sanguíneos localizados próximo do elétrodo. Para minimizar este efeito, foi ainda considerada uma ablação por radiofrequência coadjuvada pela injeção de uma solução salina no tecido tumoral, permitindo deste modo alterar a deposição de energia no tumor. Os resultados indicam que é possível melhorar a forma do volume da lesão induzida atendendo a um compromisso entre a tensão aplicada e a solução salina utilizada, se bem que o fenómeno de convecção térmica é ainda assim significativo na distribuição da temperatura no tumor.

Finalmente, as principais conclusões deste trabalho evidenciam que o procedimento proposto de ablação térmica por radiofrequência utilizando um *stent* metálico auto-expansível como elétrodo ativo é viável. Sugere-se ainda que os *stents* atualmente disponíveis no mercado possam ser vistos como potenciais elétrodos, os quais, depois de colocados, podem ser ligados ao gerador de radiofrequência através do fórceps modificado aqui proposto.

Palavras–chave: ablação por radiofrequência, tumor, cancro, colangiocarcinoma, elementos finitos, elétrodo, condutividade elétrica, simulação numérica, terapia por hipertermia, stent, endoprótese, análise experimental.

Abstract

Self-expandable metallic stents are endo-prosthesis commonly used for the palliative treatment of the symptoms caused by the growth of cancerous tumours inside tubular organs, like the colon, oesophagus or bile duct. After placing and deploying the stent, this device relieves the stricture problems by mechanical action, applying a radially outward force on the walls of the duct. Nitinol is an alloy of nickel and titanium that presents unique properties of elasticity and shape memory, besides excellent biocompatibility characteristics. For this, it has been widely used for producing this type of endo-prosthesis.

Additionally, radio frequency thermal ablation is a medical procedure that has been considered as an effective therapy for the treatment of tumours located in soft-tissue organs. The hepatic radio frequency ablation for the treatment of hepatocarcinomas might be one of the most well-documented in the literature.

In this Ph.D dissertation, it is proposed a tubular electrode based on a self-expandable stent. It is intended, with this electrode, to perform radio frequency thermal ablation therapy of tumours located in tubular organs. It is also proposed a methodology that consists of placing and deploying the electrode according common procedures, e.g., through laparoscopy. Next, the electrode is connected to the radio frequency power generator through an electrically modified forceps. In this work, it is presented a numerical and experimental analysis for characterization of the thermal induced lesion that is possible to achieve using the proposed electrode.

Experimental data revealed promising results about the application of the proposed electrode. It was verified that it is possible to induce thermal necrosis in the tissue adjacent to the electrode, obtaining a regular, well-defined volume. Also, from the experimental results, it was possible to define and validate a numerical model that

allows to simulate the temperature distribution in the biological tissue and anticipate the volume of the induced lesion.

From the numerical simulation, it was studied the effect of the geometry of the stent on the temperature distribution in the tissue, and it was assessed the size and the shape of the volume. Taking into account that many of the currently available stents in the market are very similar to the structure of the model considered, it is possible to conclude that these stents can be regarded as potential radio frequency ablation electrodes without any particular modification.

It was also simulated a radio frequency thermal ablation of a tumour located in a bile duct. It was intended to study the effect of the convective heat transfer caused by the blood flood in the blood vessels that are near the electrode. Additionally, it was considered a saline-enhanced radio frequency ablation, which consists of the injection of a saline solution into the tumorous tissue in order to modify the energy deposition in the tumour. The results show that, considering a compromise between the applied tension and the amount of saline solution used, it might be possible to improve the shape of the volume of induced lesion. However, the convective heat transfer still has a significant effect on the temperature distribution in the tumour.

Finally, the main conclusions of this work evince that the proposed radio frequency thermal ablation procedure using a self-expandable metallic stent as an active electrode can be regarded as a feasible solution. It is also suggested that the current stent solutions commercially available can be considered as potential electrodes that can be connected to the radio frequency power generator, after placed and deployed, through the modified forceps proposed in this work.

Keywords: radio frequency ablation, tumour, cancer, cholangiocarcinoma, finite elements, electrical conductivity, numerical simulation, endo-prosthesis, stent, hyperthermia therapy, experimental analysis.

CHAPTER 1

Introduction

While there are several chronic diseases more
destructive to life than cancer, none is more feared.
Charles Horace Mayo
in Carcinoma of the Right Segment of the Colon
Annals of Surgery, Vol. 83, March 1926

1.1 Motivation and Objectives

Cancer is the world's second biggest killer after cardiovascular disease, responsible for 7.6 million deaths in 2008 (around 13% of all deaths). Also, the International Agency for Research on Cancer (IARC) estimated there were 12.4 million new cancer cases and 28 million of people alive with cancer within five years from primary diagnosis. By 2030, it is expected 26.4 million incident cases of cancer and 17 million cancer deaths per year [Wor08].

Colorectal cancer accounts for 8% of all cancer deaths, making it the fourth most common cause of death from cancer. About 20% of colorectal cancers are diagnosed as a disseminated disease, and the majority of metastatic patients has unresectable cancer. In these cases, as well as for patients with colonic obstruction and incurable

metastases, surgery is palliative and the use of self-expanding metallic stents seems to be a reasonable option [SJV+10].

Oesophageal cancer is the eighth most common cancer worldwide and, with its very poor survival rate, it is the sixth most common cause of death from cancer. More than 50% of patients with oesophageal carcinoma are found to be incurable at the time of diagnosis. For these cases, palliative cares are the choice and self expandable metallic stents are an effective option for relieving symptoms and improving the quality of life [BKP+09].

Liver cancer has a very poor prognosis, being the number of deaths almost the same as the number of new cases. It is, therefore, the third most common cause of death from cancer [PBFP05]. Cholangiocarcinoma, or bile duct cancer, comprises 10% to 25% of liver cancers in men in Europe and North America, and a much larger proportion in women. It is often diagnosed at an advanced stage and it is already considered as an incurable disease at the time of presentation. For these cases, palliative treatment is necessary. Biliary obstruction for unresectable cholagiocarcinoma cases can be managed by placing percutaneously a self expandable stent [PPH+09].

In recent years, radio frequency (RF) ablation has been used as a promising minimally invasive treatment method for primary and metastatic liver tumours, and its application has been extended with some success for the treatment of small renal carcinomas, lung, breast and bone tumours. It has been also studied its application on other areas of hyperthermia treatment.

In these medical procedures, the targeted tissue is a mass located in a soft-tissue organ, and so the electrodes commonly used in these cases are needle-based. On the other hand, this kind of electrodes are hard to apply in tumours that are located in hollow organs, like the oesophagus, colon or bile duct.

A stent is a hollow metal expandable endo-prosthesis, usually made from nitinol (an alloy of nickel and titanium), steel or even chrome and cobalt alloys. Nitinol stents, however, present some good mechanical and biocompatibility characteristics turning this kind of stents into a popular endo-prosthesis [SSA+04, SPD04, TMB+02]. The necessity and presence of a metallic stent, used for the palliative treatment of the symptoms due to the stricture of the tubular organ, can be, therefore, regarded as an electrode to apply radiofrequency (RF) energy for a hyperthermia treatment of the tumour. This idea was the trigger for the research presented in this work.

The global objective of this study is to verify the capability of using a stent-based electrode for heating a biological tissue in order to induce thermal necrosis, which

is the main purpose of a RF ablation procedure. This work unfolds in the following goals:

- To verify the feasibility of a self-expandable metallic stent as an electrode for RF thermal ablation of tumours located in tubular organs.

- To provide a solution for deploying the electrode easily in place, and connect it to the RF power generator. One of the great advantages of the RF ablation treatment is the fact that it consists of a minimally invasive therapy that can be performed with percutaneous or laparoscopic approaches. Also, the insertion of the stent is usually performed percutaneously. Thus, providing an electrical connection between the stent-based electrode and the RF power generator that preserves these characteristics is considered valuable.

- To characterize the lesion profile that is attainable, using a stent-based electrode. It is important to assess the dimension and the shape of the thermal lesion that it can be induced using this electrode. Also, it is necessary to understand how some parameters, like voltage and time, affect the volume of the lesion.

- To obtain a numerical model that reproduces the RF ablation procedure with a stent-based electrode. This can provide a valuable tool to predict the temperature distribution and assess the volume of damage. Finite element analysis is considered in this work.

- To analyse the effect of the geometry of the stent on the volume size and shape of induced lesion.

- To study the effect of convective heat transfer due to the presence of major blood vessels near the location of the stent-based electrode. The convective heat transfer due to the blood flow represents an important disturbance that can affect the temperature distribution significantly, thus obtaining an unexpected volume lesion that might compromise the tubular organ where the stent-based electrode is inserted.

The present study is, therefore, articulated in experimental and numerical studies. It was intended to verify the feasibility of the proposed electrode experimentally and, at the same time, to gather experimental data to validate a numerical model to be used to predict the temperature distribution in more complex scenarios.

1.2 Organization of the Thesis

This thesis is composed of eight chapters, including this introductory chapter. In chapter 2, it is presented a review on the electrical and thermal properties of the biological tissues. This chapter gives an insight on the properties of the tissue that were considered on the numerical model proposed. Since this subject is rather complex, it was considered to cover the fundamental issues that were considered more relevant for the present work, and pointing out the most relevant references in the literature for further reading.

Chapter 3 contains a short historical introduction on electricity and medicine. A section is devoted to introducing the mechanisms underlying the radio frequency ablation, and it is also explained how thermal necrosis is induced in the biological tissue. It follows a section that presents an overview on the RF electrodes design, from plain electrodes to hybrid designs, some of them available in the market. The last section of this chapter introduces the commercial RF power generators solutions that are currently available.

Chapter 4 consists of the description of the preliminary experimental work. In this chapter, it is presented the experimental tests performed to verify the feasibility of the proposed electrode. A commercial self expandable metallic stent is used as a RF electrode. The temperature of the tissue is measured to verify if it is heated to the point of inducing thermal necrosis. Also, it is presented the numerical modelling of the experimental set-up. It is observed that the numerical results are in strong agreement with the experimental results. Finally, it is proposed an electrical connector device to connect the stent-based electrode to the RF power generator. It is a solution that allows to place and deploy the electrode in the pretended location using conventional percutaneous procedures, and connect it to power generator in a functional way.

Chapter 5 presents the experimental and numerical work to characterize the induced lesions obtained with this electrode. It is studied how the size of the volume varies with time and applied voltage. The tests are performed on bovine liver samples collected a couple of hours after abating the animals and the assessment of the induced lesions is performed by visual observation. In order to approximate the numerical model to the experimental set-up, it was measured the electrical conductivity of the liver samples. It is described the measurement system that was used as well as the measurement probe, which is based in the four-electrode method. Again, the numerical and experimental results show good agreement, confirming the numerical model as an excellent tool for estimating the temperature distribution in more complex problems.

Chapter 6 consists of a study of the effect of the geometry of the stent on the temperature distribution. It is concerned with the mesh density of the stent and how it affects the size and shape of the volume of damaged tissue. The main conclusion of this chapter is that commercial stent solutions can be regarded as a RF electrode without any modification, considering the solution previously presented in chapter 4.

Chapter 7 describes the numerical simulation of a RF ablation procedure on a cholangiocarcinoma, a cancerous tumour in the bile duct. The presence of the hepatic artery and the porta vein are responsible for a strong convective heat transfer that significantly affects the temperature distribution around the electrode. In order to minimize this effect, and to obtain a regular lesion volume, a saline-enhanced RF ablation is considered. The obtained results show that a compromise between the saline solution and applied voltage has to be considered, so a regular lesion can be obtained. Still, the convective heat transfer has an evident influence on the final outcome.

The final chapter concludes by summarizing the work presented in this thesis, and suggests further steps for future works.

1.3 Contribution

In this work, it is presented a valid contribution for the hyperthermia treatment of tumours located in tubular organs like the oesophagus, colon or bile duct. In contrast to all previous works, which are centred in the RF ablation of tumours in soft-tissue organs, this study presents a solution based on a mechanical device that has been commonly used in palliative treatments for minimizing stricture problems associated to the growth of the tumour inside hollow organs.

The main contributions of this work are:

1. Proposal of a novel stent-based electrode for the treatment of tumours located in tubular hollow organs by RF thermal ablation. The proposed solution consists of a conventional self expandable metallic stent that can be placed and deployed by conventional percutaneous procedures in the location to be treated. The electrical connection of the electrode is achieved through a modified biopsy forceps which allows, this way, a simplified procedure to apply the stent-based electrode on the target tumour.

2. Realization of experimental work to assess and characterize the size and shape of the volume of induced lesion obtained applying the proposed stent-based electrode.

3. Conception of a numerical model, based in the finite element method, that can be used to predict the temperature distribution during a RF ablation procedure involving the proposed electrode. This model considers the non-linear temperature-dependence of the electrical conductivity of the biological tissue. Experimental data are obtained for validating the proposed model.

4. Analysis of the geometry of a self expandable metallic stent on the voltage and temperature distribution in a biological medium, and their effect on the obtained volume of damaged tissue. It is suggested that commercial available metallic stents can be used as RF active electrodes.

5. Analysis of the temperature distribution during a RF ablation procedure of a cholangiocarcinoma. RF ablation and enhanced-saline RF ablation were considered. Some recommendations are presented concerning the applied voltage and the concentration of the saline solution for obtaining a regular lesion volume.

Finally, from the results obtained along this work, there were presented the following papers and communications (ordered chronologically):

- C. F. L. Antunes, T. R. O. Almeida, N. Raposeiro, B. Gonçalves, and P. Almeida, "Effects of the geometry of a tubular electrode on the temperature distribution in biological tissue," in *14th Biennial IEEE Conference on Electromagnetic Field Computation*, Chicago, USA, 2010. [AAR$^+$10c]

- C. F. L. Antunes, T. R. O. Almeida, N. Raposeiro, B. Gonçalves, and P. Almeida, "Thermal ablation in biological tissue using tubular electrode," in *14th Biennial IEEE Conference on Electromagnetic Field Computation*, Chicago, USA, 2010. [AAR$^+$10b]

- C. F. L. Antunes, T. R. O. Almeida, N. Raposeiro, B. Gonçalves, and P. Almeida, "A tubular electrode for radiofrequency ablation therapy," in *ICBET 2010 - International Conference on Biomedical Engineering and Technology*, Paris, France, 2010. [AAR$^+$10a]

- C. F. R. L. Antunes, T. R. Almeida, N. Raposeiro, B. Gonçalves, P. Almeida, and A. Antunes, "A tubular electrode for radiofrequency ablation therapy," *World Academy of Science, Engineering and Technology*, no. 70, pp. 517–523, 2010. [AAR$^+$10d]

- C. F. L. Antunes, T. R. Almeida, and N. Raposeiro, "Finite element modeling of cholangiocarcinoma radiofrequency ablation," in *10th International Conference of the European Bioelectromagnetic Association*, Rome, Italy, 2011. [AAR11c]

- C. F. L. Antunes, T. R. Almeida, and N. Raposeiro, "Inducing thermal lesion on a cholangiocarcinoma considering a saline-enhanced radiofrequency ablation," in *EHE2011 – 4th International Conference on Electromagnetic Fields, Health and Environment*, Coimbra, Portugal, 2011. [AAR$^+$11b]

- C. F. L. Antunes, T. R. Almeida, N. Raposeiro, B. Gonçalves, and P. Almeida, "Determination of lesion volume induced in biological tissue using a tubular electrode for radiofrequency ablation - numerical and experimental analysis," in *EHE2011 – 4th International Conference on Electromagnetic Fields, Health and Environment*, Coimbra, Portugal, 2011. [AAR11a]

- C. F. L. Antunes, T. R. Almeida, and N. Raposeiro, "Producing a regular volume for thermal lesion on a cholangiocarcinoma considering a saline-enhanced radiofrequency ablation," in *XV International Symposium on Electromagnetic Fields in Mechatronics, Electrical and Electronic Engineering. ISEF 2011.*, Funchal, Madeira Island (Portugal), 2011. [AAR11d]

- C. F. R. L. Antunes, T. R. Almeida, and N. Raposeiro, "Saline–enhanced RF ablation on a cholangiocarcinoma: a numerical simulation," *COMPEL – The International Journal for Computation and Mathematics in Electrical and Electronic Engineering*, vol. 31, no. 4, pp. 1055–1066, 2012. [AAR12a]

- C. F. R. L. Antunes, T. R. O. Almeida, N. Raposeiro, B. Gonçalves, and P. Almeida, "Intraductal RF/stent ablation," in *CIRSE 2012 – Cardiovascular and Interventional Radiological Society of Europe*, Lisbon, Portugal, 2012. [AAR$^+$12b]

- C. F. R. L. Antunes, T. R. O. Almeida, and N. Raposeiro, "Producing a regular volume for thermal lesion on a cholangiocarcinoma considering a saline–enhanced radiofrequency ablation (accepted for publication)," *Electrical Review*, 2012. [AAR12c]

- C. F. R. L. Antunes, T. R. O. Almeida, and N. Raposeiro, "Using a tubular electrode for radiofrequency ablation: numerical and experimental analysis (accep-

ted for publication)," *COMPEL – The International Journal for Computation and Mathematics in Electrical and Electronic Engineering*, 2012. [AAR12d]

CHAPTER 2

Properties of Tissue

It would be possible to describe everything scientifically, but it would make no sense; it would be without meaning, as if you described a Beethoven symphony as a variation of wave pressure.

Albert Einstein

As part of the presented work, numerical simulations of radio frequency ablation were performed in order to foresee the volume and the shape of damaged tissue that might be obtained using the proposed electrode. In order to define a proper numerical model, physical characteristics of the biological tissue have to be properly set so that the obtained results are as reliable as possible. Mass density, specific heat, thermal conductivity and electrical conductivity are characteristics, among others, that play a significant role in the behaviour of the biological tissue when submitted to a radio frequency electrical current.

This chapter will review some fundamental issues about the electrical and thermal conductivity in biological tissues that were taken into account during the developed work.

2.1 Electrical Properties of Biological Tissues

The electric properties of matter are of practical interest in physical sciences and engineering. As electrical technology improved during the nineteenth century, the importance on the electrical properties of the materials grew among the scientific community. After the controversy between Luigi Galvani and Alessandro Volta (summarized in section 3.1), particular attention was given to the study of properties of electrical conductivity of biological tissues in order to understand some biological phenomena such as nerve excitation and frequency dependence of the excitation threshold. Later, when diathermy awoke some attention as a medical valid procedure, it became necessary to understand the way the tissue is heated to improve the technique. An interesting short review on the history of the study of the electrical properties of biological tissue can be found in Foster and Shawn [FS89]. Also, Foster [Fos02] presented a detailed and enthralling biography on Herman P. Schwan, an important contributor to the field of biomedical engineering, particularly on the study of the dielectric properties of biological materials and interaction of electromagnetic fields with biological systems.

This section presents an overview on electrical properties of biological materials. For a detailed review on the subject concerning the electrical properties, as well as the polarization mechanisms in biological material, Pethig and Kell [Pet84], Foster and Schwan [FS89], Grimnes and Martinsen [GM00] (chapters 3 and 4), and Gabriel [Gab07] are good references. Complementary information about data concerning values for dielectric permittivity and electrical conductivity are available in Stuchly and Stuchly [SS90], Stoy *et al.* [SFS82], Duck [Duc90], and Gabriel *et al.* [GGC96, GLG96a, GLG96b].

2.1.1 Dielectric and Electrical Conductivity in Biological Tissues

A biological medium consists of a heterogeneous material containing water, dissolved organic molecules, macromolecules, ions and indissoluble matter. Its constituents are strongly organized in cellular and sub-cellular structures, forming macroscopic elements and soft and hard tissues. To analyse the response of such complex structure to an applied electric field it becomes necessary to describe the material on a macroscopic level.

In practice, the biological tissue has free and bound charges, so when an electric field is applied to this kind of medium, charges will migrate and displace. Biolo-

gical tissue can be considered as being both electrical insulator and conductor, so the material can be characterized as having dielectric permittivity, ε, and electrical conductivity, σ. The electrical conductivity arises mainly from ionic conductivity although other mechanisms can be also presented, particularly for aqueous biological materials [PK87].

As an insulator, in response to an applied electric field, the bound charges presented in the biological tissue are submitted to a displacement, producing dipoles that align with the imposed electric field, polarizing the medium. The resulting electric displacement, **D**, due to an applied electric field, **E**, is described by:

$$\mathbf{D} = \varepsilon \mathbf{E} \tag{2.1}$$

The dielectric permittivity can be expressed as:

$$\varepsilon = \varepsilon_0 \varepsilon_r \tag{2.2}$$

where ε_0 is the dielectric permittivity of free space, and it has the value $8.854 \cdot 10^{-12}$ $\mathrm{F\,m^{-1}}$, whilst ε_r is the relative permittivity of the matter. It can be seen that the dielectric permittivity is a measure of the response of the matter to an applied electric field. The bulk properties of the considered medium can then be exemplified considering a parallel-plate capacitor of plate area A and separation d. Between the plates is placed the biological medium under consideration (Figure 2.1). The capacitance, C, of this set-up is expressed by:

$$C = \varepsilon_0 \varepsilon_r \frac{A}{d} \tag{2.3}$$

The equivalent circuit also includes a conductance, G, in parallel with the capacitance:

$$G = \sigma \frac{A}{d} \tag{2.4}$$

2.1.2 Complex Permittivity

As stated before, the response of a material to a constant electric field involves the displacement of electric charges. This displacement establishes a polarization, **P**, inside the material. For a linear, isotropic material, **P** can be written as:

$$\mathbf{P} = (\varepsilon_r - 1)\varepsilon_0 \mathbf{E} \tag{2.5}$$

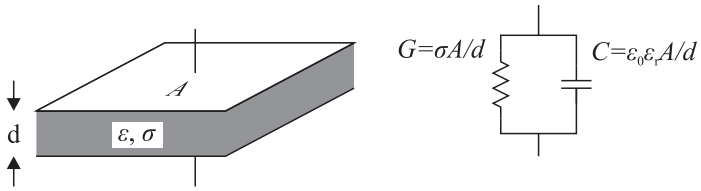

Figure 2.1: Equivalent circuit of a parallel plate capacitor filled with a non-ideal dielectric. The material has a relative permittivity ε_r and a conductivity σ.

If the field **E** is suddenly removed, it could be possible to notice that **P** does not decay instantly, but it will decay gradually towards zero (Figure 2.2). The displaced charges take a finite time to *relax* to their natural random position and orientation. Thus, the time scale and shape of the decay of **P** are related to the structure of the material and the mechanism causing the polarization.

In the same way, as charges take some time to return to their natural positions, they also require time to align with the electric field. However, if the changes in the electric field occur slowly as compared with the displacement of the charges, there is sufficient time to develop a time-dependent polarization that is in equilibrium with the electric field at each instant of time. Considering this *quasi-static* polarization, Equation (2.5) can be expressed as:

$$\mathbf{P}(t) = (\varepsilon_r - 1)\varepsilon_0 \mathbf{E}(t) \tag{2.6}$$

For an increasing frequency of an applied sinusoidal electric field, there will be a point at which polarization will not be able to follow the variation of the electric field, and it will lag behind the value of $\mathbf{E}(t)$. Under such condition, Equation (2.6) still can describe the ongoing polarization on the material, provided that ε_r is expressed as a complex value:

$$\hat{\varepsilon} = \varepsilon' - j\varepsilon'' \tag{2.7}$$

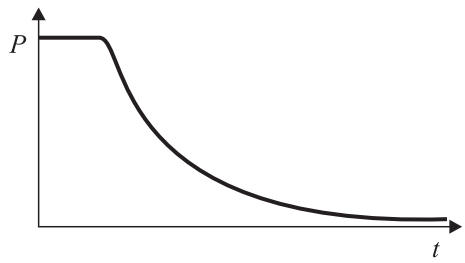

Figure 2.2: Example of the polarization decay after removing an applied electric field.

where $j^2 = -1$, ε' is the real part, and ε'' is the imaginary part of the complex dielectric permittivity $\hat{\varepsilon}$.

To show that Equation (2.7) reflects the mentioned lagging, consider an applied sinusoidal electrical field given by:

$$\mathbf{E}(t) = \mathbf{E}\sin(\omega t) = \mathbf{E}\cos(\omega t - \pi/2) \tag{2.8}$$

The phasor representation of Equation (2.8) is:

$$\tilde{\mathbf{E}} = \mathbf{E}\, \mathrm{e}^{-j\frac{\pi}{2}} \tag{2.9}$$

From (2.7) and (2.9), Equation (2.1) becomes:

$$\tilde{\mathbf{D}} = \varepsilon_0 \sqrt{\varepsilon'^2 + \varepsilon''^2}\, \mathbf{E}\, \mathrm{e}^{j(-\delta - \frac{\pi}{2})} \tag{2.10}$$

where $\tan\delta = \varepsilon''/\varepsilon'$. Expressing Equation (2.10) in time-domain:

$$\mathbf{D}(t) = \varepsilon_0 \Re\left(\sqrt{\varepsilon'^2 + \varepsilon''^2}\, \mathbf{E}\, \mathrm{e}^{j(\omega t - \delta - \frac{\pi}{2})}\right) \tag{2.11}$$

where $\Re$ is the function that obtains the real part of its operand, and ω is the radian frequency [rad/s]. Equation (2.11) makes clear that $\mathbf{D}(t)$ lags behind of $\mathbf{E}$(t) with a phase angle of δ.

The phase delay δ implies an energy absorption by the medium. If $\varepsilon'' = 0$ then $\hat{\varepsilon} = \varepsilon'$ is real and there is no energy absorption: the energy to build up the electric field during one half of the cycle is totally recuperated on the next half of the cycle. When $\varepsilon'' > 0$, i.e., there is a phase lag between $\mathbf{D}$ and $\mathbf{E}$, the medium will consume energy from the applied field. Considering again the bulk properties of the tissue, using the example of Figure 2.1, after applying a sinusoidal voltage $V(t)$, the current across the capacitor is:

$$I(t) = j\omega\varepsilon_0(\varepsilon' - j\varepsilon'')V(t)\frac{A}{d} \tag{2.12}$$

Because the electric field, $\mathbf{E}(t)$, between the plates is given by $V(t)/d$ [V/m], the current density is $I(t)/A$ [A/m], and disregarding the fringe effect, thus:

$$J(t) = j\omega\varepsilon_0\varepsilon' E(t) + \omega\varepsilon_0\varepsilon'' E(t) \tag{2.13}$$

By definition, electrical conductivity (which may be complex) is the ratio J/E.

Therefore, from Equation (2.13):

$$\frac{J(t)}{E(t)} = j\omega\varepsilon_0\varepsilon' + \omega\varepsilon_0\varepsilon'' \tag{2.14}$$

The imaginary part of (2.14) is associated to the capacitance of the dielectric, so ε' corresponds to the relative permittivity. Hence, the dielectric conductivity is defined as the real part of Equation (2.14):

$$\sigma = \omega\varepsilon_0\varepsilon'' \tag{2.15}$$

The presence of a finite value ε'' has the effect of producing an electrical conductivity of magnitude $\omega\varepsilon_0\varepsilon''$. It represents a power loss associated to all the loss mechanisms in the material. For that reason, ε'' is commonly known as *loss factor*. Also, the phase angle δ is known as *loss angle*. $\tan\delta$ is called *loss tangent* or *dissipation factor* and represents the energy lost per cycle divided by energy stored per cycle.

2.1.3 Relaxation

From the previous discussion, it is clear that the dielectric flux density, $\mathbf{D}$, resulting from an applied alternating electric field, $\mathbf{E}$, will lag the electric field by a phase of δ. As the frequency increases, polar molecules and cellular components have less time to rotate and so polarization and permittivity decrease: ε' and ε'' are frequency dependent.

This time-dependent behaviour is called *relaxation*. However, instead of an alternating function, the concept of relaxation is connected to an excitation step function: first, the medium is submitted to a step disturbance, and then it is allowed to relax to the new equilibrium state.

In the simplest case, considering the following step function:

$$\mathbf{E}(t) = \begin{cases} 0 & t \leqslant 0 \\ E & t > 0 \end{cases} \tag{2.16}$$

the polarization of a medium will relax toward the steady state as a first-order process characterize by a relaxation time τ [Sch57]:

$$\mathbf{D}(t) = \varepsilon_\infty \mathbf{E}(t) + (\varepsilon_s - \varepsilon_\infty)(1 - \mathrm{e}^{-t/\tau})\,\mathbf{E}(t) \tag{2.17}$$

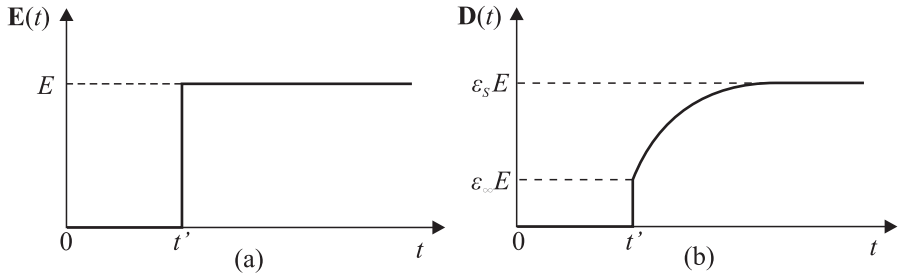

Figure 2.3: (a) Step electric field applied to a dielectric medium; (b) time-dependent polarization after the step disturbance.

where ε_∞ is the value of permittivity at high-frequency, and ε_s is the value of permittivity at low-frequency. These values are also often referred as infinite and static permittivity, respectively[1].

The term $\varepsilon_\infty E$ corresponds to the almost instantaneous response of the dielectric to the applied step electric field. On the other hand, $\varepsilon_s E$ is the response long after applying the step disturbance (Figure 2.3). The time constant τ is the *relaxation time*, characteristic of the dielectric, and it depends on the physical process involved. It can vary from a small value in the order of picoseconds, if molecular dipole reorientation is involved, to seconds, when counterion polar effect arises.

Assuming the sum of different polarization contributions in response to different electric field step functions, it can be shown that [BB78]:

$$\hat{\varepsilon} = \varepsilon_\infty + \frac{\varepsilon_s - \varepsilon_\infty}{1 + j\omega\tau} \tag{2.18}$$

The relationship expressed in (2.18) is known as the *Debye model* or *Debye relaxation*. This model was introduced and named after Peter Debye (1884 – 1966).

Comparing Equations (2.7) and (2.18), one can easily verify that:

$$\varepsilon' = \varepsilon_\infty + \frac{\varepsilon_s - \varepsilon_\infty}{1 + (\omega\tau)^2} \tag{2.19a}$$

$$\varepsilon'' = \frac{(\varepsilon_s - \varepsilon_\infty)\omega\tau}{1 + (\omega\tau)^2} \tag{2.19b}$$

However, Equation (2.18) does not include the conduction currents at infinite time that might arise, for example, from the drift of free ions in static field. In that case,

[1]The static permittivity is also represented by ε_0 in some references, but the notation presented in this text is preferred to avoid confusion with permittivity in free space, ε_0.

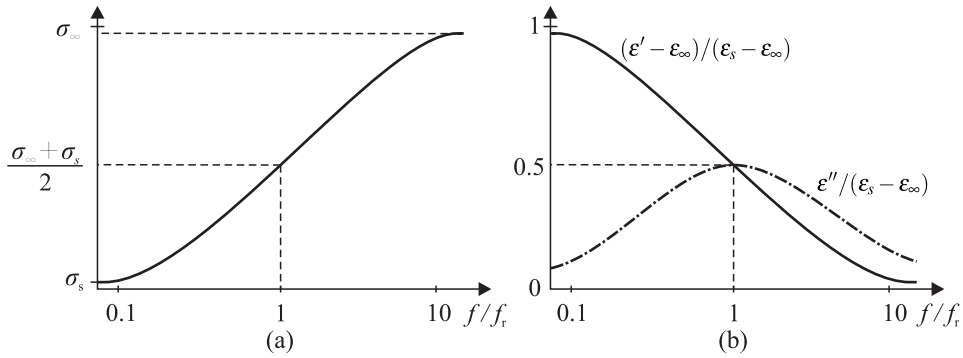

Figure 2.4: (a) Electrical conductivity vs. frequency; (b) normalized dielectric permittivity $(\varepsilon'-\varepsilon_\infty)/(\varepsilon_s-\varepsilon_\infty)$ and loss factor $\omega\varepsilon_0\varepsilon''/(\varepsilon_s-\varepsilon_\infty)$ vs. frequency. As frequency increases the permittivity of the medium decreases while the conductivity increases. For a single constant case, the relaxation frequency is the same in (a) and (b) with a maximum value of losses.

Debye model can be expanded to include the static conductivity σ_s:

$$\hat{\varepsilon} = \varepsilon_\infty + \frac{\varepsilon_s - \varepsilon_\infty}{1 + j\omega\tau} - j\frac{\sigma_s}{\omega\varepsilon_0} \tag{2.20}$$

and Equation (2.19) becomes:

$$\varepsilon' = \varepsilon_\infty + \frac{\varepsilon_s - \varepsilon_\infty}{1 + (\omega\tau)^2} \tag{2.21a}$$

$$\varepsilon'' = \frac{\sigma_s}{\omega\varepsilon_0} + \frac{(\varepsilon_s - \varepsilon_\infty)\omega\tau}{1 + (\omega\tau)^2} \tag{2.21b}$$

The total electrical conductivity, σ, can be expressed as:

$$\sigma = \sigma_s + \frac{(\sigma_\infty - \sigma_s)(\omega\tau)^2}{1 + (\omega\tau)^2} \tag{2.22}$$

where σ_∞ stands for high-frequency conductivity. Note that Equations (2.18) to (2.22) are function of the angular frequency, ω.

It is possible to conclude from these equations that, as frequency increases, permittivity of the medium decreases. On the other hand, conductivity increases with frequency through a maximum value (Figure 2.4).

The real and imaginary parts of the permittivity cannot vary independently with frequency and, accordingly, the frequency dependence of ε' determines that of σ and conversely. Any decrease with frequency in ε' must be accompanied by an increase in σ. The Kramers-Kronig relations provide a necessary connection between the con-

ductivity and the permittivity. A special case of the more general Kramers-Kronig relations is given by [GM00]:

$$\varepsilon_s - \varepsilon_\infty = \frac{(\sigma_\infty - \sigma_s)\tau}{\varepsilon_0} \tag{2.23}$$

This expression is valid only if there is no static conductivity. σ_∞ and σ_s only refer to the ac lossy part of the dielectric.

Figure 2.4 illustrates the variation in the permittivity and conductivity with frequency for a single time constant relaxation. Conductivity (Figure 2.4a), normalized permittivity $(\varepsilon' - \varepsilon_\infty)/(\varepsilon_s - \varepsilon_\infty)$, and loss factor $\omega\varepsilon_0\varepsilon''/(\varepsilon_s - \varepsilon_\infty)$ (Figure 2.4b) are depicted. f_r refers to the *relaxation frequency* or *characteristic frequency* at which $\omega\tau = 1$, so that $f_r = 1/(2\pi\tau)$. At the relaxation frequency, the permittivity is halfway between its two limiting values, while the loss factor reaches its highest value. In this particular case, where a single time constant is considered, the conductivity is halfway between its limiting values at the same relaxation frequency.

2.1.4 Dispersion in Biological Tissues

As it was previously referred, relaxation is related to the time dependence of a dielectric medium to react to an applied electric field. This is a time domain concept. *Dispersion*, on the other hand, corresponds to frequency domain concept of this dependency. In the previous section, it was shown that permittivity and conductivity are functions of frequency. Also, it was only considered the case of a *single dispersion*. For this case, it was shown that permittivity presents two different frequency-independent values, ε_s and ε_∞, with a transition value which is verified at the relaxation frequency.

However, due to its complex nature, biological tissues can exhibit 3 or 4 more or

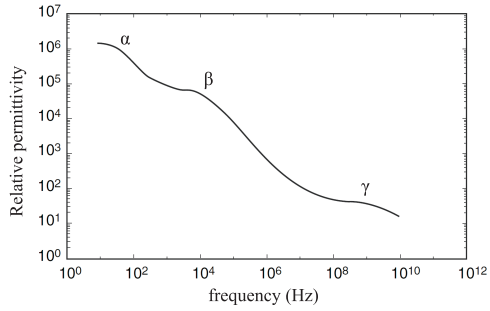

Figure 2.5: Relative permittivity of a biological tissue as function of frequency evidencing the three main dispersion regions.

less distinct dispersion regions (Figure 2.5). The three principal dispersion regions, α, β and γ dispersions, were initially pointed out by Schwan [Sch57].

The α *dispersion* occurs at extremely low frequencies (usually less than 1 kHz) and is the least well understood of the three dispersion mechanisms [GSS78, GM10]. This dispersion region is characterized by a huge increase of permittivity with a corresponding small decrement in conductivity. About this dispersion, Schwan mentioned [Sch94]: *"The discovery of the α dispersion came as a great surprise"*. This dispersion could be due to the relaxation of counterions surrounding the charged cell membranes (the *counterion atmosphere*). Other mechanisms relating to interactions in the vicinity of the cells membranes are also pointed out (charging of intracellular membrane-bound organelles and a frequency dependency in the impedance of the cell membrane itself).

The β *dispersion* is verified at frequencies from 0.1 MHz to 100 MHz. This dispersion is mainly due to the inhomogeneity of the material that causes charges to accumulate at boundaries separating tissue regions of different dielectric properties after an electric field is applied. Finite periods of time are required before boundaries can reach charge neutrality, giving rise to the relaxation phenomenon (interfacial polarization).

The γ *dispersion* is due to the relaxation of the water, so its parametrization is close to the values used to characterize the dispersion of pure water. Although this effect would not be expect for frequencies below 20 GHz (frequency at which pure water relaxes), macromolecule-bound water appears to be responsible for this. Such water appears to exhibit a broad spread spectrum of dispersion extending from about 100 MHz up to 100 GHz [Sch94, GM00].

Although it is not depicted in Figure 2.5, it might also appear a weaker subsidiary dispersion region identified in some protein solutions between the β and γ regions, typically referred as δ dispersion. This dispersion is thought to be partially caused by relaxation of water molecules bound to the surface of macromolecules, relaxation of smaller dipolar segments or side chains of biological molecules, and counterion diffusion along small regions of the charged surface. Taking into account the several variables involved trying to characterize this dispersion, the δ dispersion is usually treated as the tail end of the β dispersion or a widening of the γ dispersion.

Table 2.1 summaries the several mechanisms that are involved in the dielectric response of different biological components, from simple water and electrolytes to complex structures [Sch94]. Electrolytes display only the γ dispersion characteristic

Table 2.1: Mechanisms present in the dielectric response of different biological systems.

Water and electrolytes	γ
Biological Macromolecules:	
Amino acids	$\delta+\gamma$
Proteins	$\beta+\delta+\gamma$
Nucleic acids	$\alpha+\beta+\delta+\gamma$
Vesicles, no charge surface	$\beta+\gamma$
Vesicles, with charge surface	$\alpha+\beta+\gamma$
Cells with membranes:	
+ fluids free of protein	$\beta+\gamma$
+ protein	$\beta+\delta+\gamma$
+ surface charge	$\alpha+\beta+\gamma$
+ membrane relaxation	$\alpha+\beta+\gamma$
+ organelles	$\beta+\delta+\gamma$
+ tubular system	$\alpha+\beta+\gamma$
Cells with membranes, surface charges organelles, proteins	$\alpha+\beta+\delta+\gamma$

of water. The presence of macromolecules as amino acids adds a δ dispersion that is caused by bound water and rotation of the molecule. For proteins, rotating side groups are involved instead. Proteins and nucleic acids also add α and β dispersions. For vesicles[2], β dispersion arises from interfacial polarization. In the presence of a charge surface, α dispersion also appears due to the counterion atmosphere. Finally cell suspensions free of proteins exhibit β and γ dispersions due to interfacial polarization and water relaxation, respectively. In the presence of proteins, a δ dispersion also appears, and the presence of surface charges or membrane relaxation adds a α dispersion.

2.1.5 Available Data

According to Gabriel *et al.* [GGC96], dielectric data obtained prior 1950 for electrically characterize biological tissue has only historical value. Published work in the 1950's and 1960's is predominantly from Herman P. Schwan (1915 – 2005) and his co-workers, which was comprehensively reviewed by Durney *et al.* [DMl86]. In this work, Durney presented a tabulated summary of the measured values of the dielectric

[2]Vesicle – a supramolecular assembly made up of many different molecules

properties of biological matter as a function of frequency and temperature. Later, there were important data reviews from Stuchly e Stuchly [SS80], Francis Duck [Duc90], and Foster e Schwan [FS89, FS96].

More recently, Gabriel *et al.* [GGC96, GLG96a, GLG96b] presented a trilogy of papers which consists on a well-documented and vast review of the data published in the second half of the past century [GGC96], followed by a large acquisition of dielectric measurements performed by the authors [GLG96a]. The experimental data was obtained using automatic swept-frequency network and impedance analysers in the frequency range of 10 Hz to 20 GHz, and they were compared with the data available in the literature so far. Finally, all this information was used to proposed a parametric model which describes the variation of the dielectric properties of biological tissues as a function of frequency [GLG96b].

All the data gathered in the work of Gabriel and her co-workers are presented in graphical format. However, Gabriel and Gabriel [GG96] placed on-line a large tabulated database of dielectric and conductivity values for several types of biological tissues, as well as parametric data for modelling the frequency dependence of the dielectric properties of 45 types of tissue.

About this database, the authors pointed out the following limitations:

- Most measurements were carried out on excised tissue.

- Taking into account the data available on literature for most tissues, the values obtained from the parametric model can be used with confidence for frequencies above 1 MHz.

- At lower frequencies, i.e., frequencies below 100 Hz, the parametric model has to be used with caution. In this frequency range, there is a large lack of data and the data available have larger than average uncertainties. This is due to limitations caused by electrode polarization that arises when measuring at low frequencies, inducing systematic errors: the formation of a ion layer in the vicinity of the electrode modifies the electric field distribution around it, obtaining this way a higher value of the measured capacity [GSS78].

- The anisotropy of the dielectric properties was not accounted for. According to Gabriel *et al.*, the geometry of the sampling probe did not allow to orient the electric field along and across the structure of the tissue so the anisotropy was not demonstrated in their database.

More recently, Peyman *et al.* [PHG05] presented a review involving measurements in the range of 100 to 10^4 MHz of 40 types of tissues (*in vivo* and *in vitro*) which enlarges the knowledge base on the frequency dependence of the biological tissues in the microwave range. In general, these results are in reasonably good agreement with those of Gabriel *et al.* [GG96].

2.1.6 Parametric Model for Describing the Dielectric Properties of Biological Tissues

As mentioned in section 2.1.4, the dielectric spectrum of a biological tissue may present 3 or 4 dispersion regions. Each one of these dispersion regions is characterized by single relaxation time, τ, and it can be approximately described by a first-order process response according to Equation (2.18) (Debye model).

Hurt [Hur85] estimated the terms for a multiple-term Debye model to describe the permittivity of muscle tissue as function of frequency:

$$\hat{\varepsilon} = \varepsilon_\infty - j\frac{\sigma_s}{\omega\varepsilon_0} + \sum_{i=1}^{n} \frac{\Delta\varepsilon_n}{1 + j\omega\tau_n} \tag{2.24}$$

where each term of the sum represents one of the dispersion regions characterized by a relaxation time, τ_n, and with a change in the relative permittivity of $\Delta\varepsilon_n = \varepsilon_{sn} - \varepsilon_{\infty n}$ (Figure 2.6).

However, it is very common that relaxation times are not well separated such that $\tau_1 \ll \tau_2 \ll \ldots$. Instead, the material will show a broad dispersion which encloses all the relaxation times. There are many empirical models to describe this behaviour (Gabriel [Gab07] presents a brief review on this subject). One of the most used is the

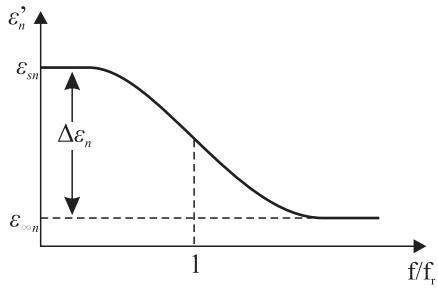

Figure 2.6: Debye dispersion considering a multi-term dispersion model. Change of the relative permittivity for the n-term.

Table 2.2: Parameters of Equation (2.26) for predicting the dielectric properties of liver tissue (from [GLG96b]).

$\Delta\varepsilon_1 =$	39.0	$\alpha_1 =$	0.10	$\tau_1 =$	8.84 ps
$\Delta\varepsilon_2 =$	6000	$\alpha_2 =$	0.20	$\tau_2 =$	530.52 ms
$\Delta\varepsilon_3 =$	5.0×10^4	$\alpha_3 =$	0.20	$\tau_3 =$	22.74 μs
$\Delta\varepsilon_4 =$	3.0×10^7	$\alpha_4 =$	0.05	$\tau_4 =$	15.915 ms

ε_∞=	4.0
$\sigma_s =$	0.02

Cole-Cole model:

$$\hat{\varepsilon} = \varepsilon_\infty + \frac{\varepsilon_s - \varepsilon_\infty}{1 + (j\omega\tau)^{(1-\alpha)}} \tag{2.25}$$

where α represents a distribution parameter such as $0 \leqslant \alpha < 1$. For $\alpha = 0$ the Cole-Cole model represents Debye dispersion.

Taking into account the Cole-Cole model instead of Debye model in the multi-term dispersion model considered in (2.24), the complex permittivity can be expressed as:

$$\hat{\varepsilon} = \varepsilon_\infty - j\frac{\sigma_s}{\omega\varepsilon_0} + \sum_{i=1}^{n} \frac{\Delta\varepsilon_n}{1 + (j\omega\tau_n)^{(1-\alpha_n)}} \tag{2.26}$$

Instead of using a model with three major dispersion regions, Gabriel *et al.* [GLG96b] considered a model with four dispersion regions, providing this way more flexibility to achieve a better fit to the data available. After some tuning work for adjusting the parameters (it was referred by Gabriel that the fitting process was visual and using Microsoft Excel spreadsheet), Equation (2.26) can be used to predict the dielectric behaviour over the desired frequency range.

In Figure 2.7, it is shown the frequency dependence of the dielectric permittivity and the electrical conductivity of liver tissue, according to Equation (2.26) and using the data presented in Table 2.2 [GLG96b]. Also, it is shown the values obtained from literature superimposed on the curves obtained from the parametric model of Equation (2.26). For dielectric permittivity, the values estimated by Equation (2.26) are very close to those obtained from experimental measurement, particularly above 100 kHz. On the other hand, values of estimated conductivity are similar to experimental data above 10-100 MHz. In more general, Gabriel *et al.* [GLG96b] stated that this model can be used with confidence for frequencies above 1 MHz, and some caution should be taken at low frequencies.

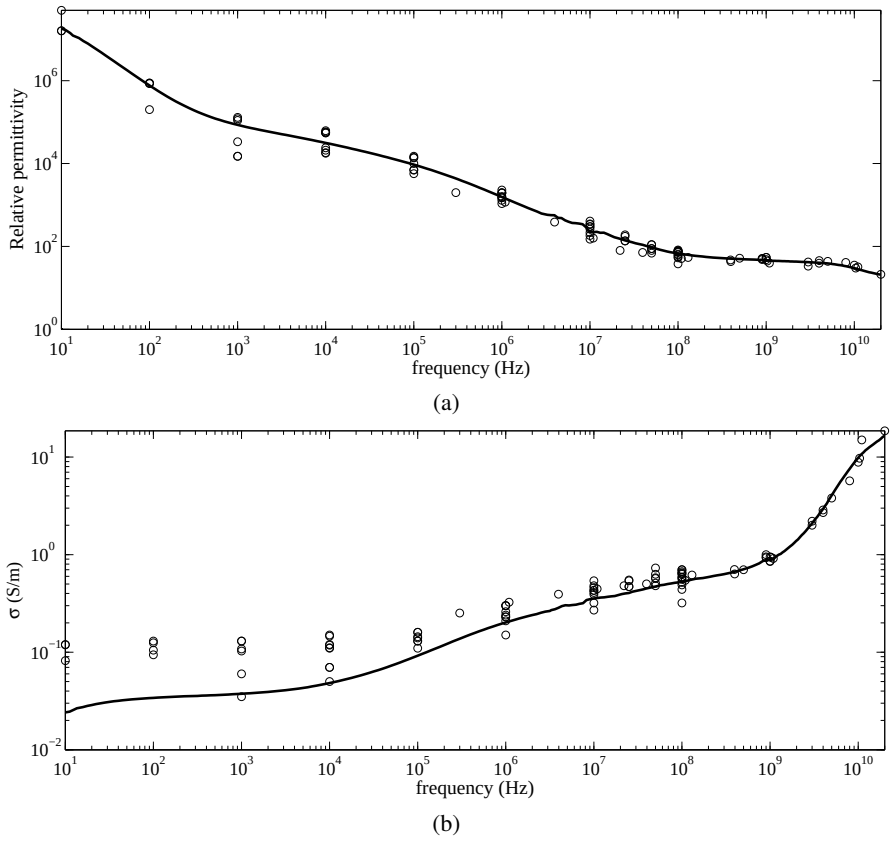

Figure 2.7: Frequency dependence of (a) the dielectric permittivity and (b) the electrical conductivity of liver tissue obtained from Equation (2.26).

2.1.7 Temperature Dependence of the Electrical Properties

As expected, the electrical properties of the biological tissues are also temperature-dependent. The displacement of charges, whether to amass at tissues interfaces or to realign through rotation, is retarded by collisions with other particles in the surrounding medium. Since the movement of charges is temperature-dependent, temperature plays this way an important role on the values of permittivity and conductivity. Also, this dependency might represent either reversible changes in the electric properties of the tissue due to, e.g, changes in ionic conductivity, or irreversible changes due to tissue damage.

Schwan and Foster [SF80b] have shown that the temperature dependence of the conductivity is much more pronounced than that of the dielectric permittivity. Near to the relaxation frequency, assuming a single time constant medium, it can be con-

sidered the relationship:

$$\frac{d\varepsilon}{\varepsilon} = \frac{d\sigma}{\sigma}\frac{\varepsilon_s - \varepsilon_\infty}{\varepsilon_s + \varepsilon_\infty} \tag{2.27}$$

where $d\varepsilon/\varepsilon$ is the relative change in dielectric permittivity due to the relative change in conductivity $d\sigma/\sigma$. Since ε_s and ε_∞ are fairly independent of temperature, and ε_s is much larger than ε_∞, the change of the dielectric permittivity with temperature must be smaller than that of the conductivity.

The temperature coefficients that quantify the influence of temperature on the permittivity and the conductivity are frequency-dependent. Foster and Schwan [FS96] point out differences on the frequency dependence of the temperature coefficients at low and high frequencies.

At low frequencies (from 44 kHz to 1 MHz), for small increments of temperature, the conductivity of tissues varies in a reversible way, showing a temperature coefficient of about 2% per °C. This rise of conductivity can be easily be associated to an increment of thermally induced charges. However, for large temperature increases, approximately above 44.5°C, the dielectric properties show abrupt and irreversible changes. These changes are due to thermal damages inflicted on the tissue, and they depend on the tissue type, duration of heating, as well as other factors. For example, in excised tissue maintained at 44°C, the low-frequency conductivity decreased initially by approximately 10% during the first hour, then gradually increased by approximately 50% during the next 8 h. Also, it was reported tenfold changes in the permittivity value over similar periods of time [FS96]. From these results, it can be concluded that there are a lot of uncertainty on the monitoring of temperature.

At high frequencies, particularly at microwave frequencies, the temperature coefficient of conductivity reflect two different effects, sometimes contradictory. As temperature increases, the ionic conductivity and the relaxation frequency, which is also temperature dependent [SF80b], increase. At frequencies below the relaxation frequency, this will result in a decrease in the loss and, hence, in a decrease in the dipolar contribution to the conductivity. At low frequencies, this contribution varies inversely as the relaxation frequency, and consequently it presents a temperature coefficient of about $-2\%/°\text{C}$. In tissues, the contributions of dipolar loss and ionic conduction to the total conductivity are comparable at about 2 GHz. Thus, the temperature coefficient of the conductivity should change sign close to this frequency. Foster and Schwan [FS96] confirmed that the electrical conductivity of muscle and brain tissues has the same temperature coefficient as that of simple electrolytes, about $2\%/°\text{C}$, while

there is a sign change in the temperature coefficient near 2 GHz, to about $-2\%/^{\circ}$C above this frequency. At microwave frequencies the permittivity of tissues reflects that of water, the static permittivity of which varies little with temperature.

At radio frequency range, interfacial polarization associated with the charging of cell membranes is predominant. The low-frequency permittivity increment depends on the cell size and the membrane capacitance, factors that are practically insensitive to temperature. On the other hand, the relaxation frequency scales as the conductivity of tissue electrolyte, exhibiting temperature coefficients of about $2\%/^{\circ}$C. This way, it is expected temperature coefficients of the order of 0 to $2\%/^{\circ}$C, depending on the frequency.

2.1.8 *In Vivo* and *Ex Vivo* Properties

The electrical properties of tissue modify after excising or following death, and these changes are particularly noticeable at low frequencies [FS96]. There are several works on this subject reported by Foster and Schwan [FS96], Stuchly and Stuchly [SS90], and Grimmes and Martinsen [GM00].

After death or excision, the biological tissue is no longer supported. With the interruption of the blood flow, metabolism continues, but in an anaerobic way [GM00]. Osmosis will cause cell swelling and tissue damage. As a consequence, the extracellular pathways narrow, normally leading to a decrease in the low-frequency conductivity. The reduction of the blood volume also accounts for variations in the electrical conductivity because blood is a good conductor [SK56, SF80b]. As cell destruction develops, the electrical conductivity increases with time.

Schwan and Kay [SK56] and Geddes and Baker [GB67] studied the variation of the electrical conductivity after tissue excision and its degradation by cell death. More recently, Haemmerich *et al.* [HOT^{+}02] performed a similar study, where it was also analysed the changes in the electrical conductivity *in vivo* after occlusion and *post-mortem*. It was found a slight decrease of the electrical conductivity in the first 30-60 minutes, depending on the type of tissue. However, in the long term, the electrical conductivity increases. These variations are more evident at low frequency measurements. High frequency measurements are related to the water and protein content of the tissues, so a slower and less pronounced deterioration is expected [SF80b].

After these results, it becomes clear that accurate results require *in vivo* measurements. In case this is not possible, *ex vivo* and *in vitro* measurements must be taken cautiously.

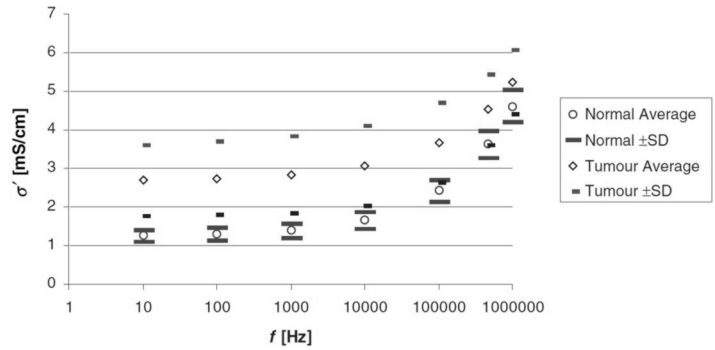

Figure 2.8: Electrical conductivity of tumour and normal liver tissue (from [HST+03]).

2.1.9 Tumorous Tissues

It has been reported [Pet84] that permittivity and conductivity of cancerous tissues are greater than in healthy tissue.These differences may have origin in the following aspects [FS89]:

- *Differences in water content* – Cancerous tissues have considerably higher water content than healthy tissues, so it is expected a somewhat larger permittivity and conductivity values for higher frequencies. Schepps and Foster [SF80a] observed this correspondence comparing excised tumorous and healthy tissues. The measurements were made considering dielectric measurements between 10 MHz to 17 GHz in canine tumorous tissues at body temperature;

- *Presence of necrosis within the tumour* – In the inner regions of the tumours there are relative few blood vessels, so the cells within these regions are deprived of nutrients. Necrosis in the tumour leads to breakdown of cell membranes, increasing the conductivity at low frequencies (audio and radio frequency ranges). Smith *et al.* [SFW86] reported that the conductivity of the tumour tissue was 6 to 7.5 times higher and its permittivity was 2 to 5 times lower than that of the normal tissue. Measurements were performed on a frequency range between 1 kHz to 13 MHz, on implanted carcinomas in rabbit livers. Haemmerich *et al.* [HST+03] studied the association between necrosis of the tumorous tissue and the changes in the electrical conductivity, reporting a strong correlation between them. Largest differences were observed at measurements below 1 kHz (Figure 2.8), so it is suggested this frequency range for tumour diagnosis by electrical impedance tomography (EIT).

Taking into account the differences between the electrical properties of tumorous and healthy tissues, there has been ongoing work on the development of diagnostic techniques of breast cancer [SWS02], prostate cancer [HSH+09a, HSH+09b], hepatic cancer [LIR+10] and lung cancer [KMU+94].

2.2 Magnetic Properties of Biological Tissues

For the most part of biological tissues, magnetic permeability is very close to that of the free space (i.e, diamagnetic) which implies that there is no direct interaction with the magnetic component of electromagnetic fields at low field strengths. Although all living organisms are essentially made of diamagnetic organic compounds, there are some paramagnetic molecules (e.g., O_2) and ferromagnetic microstructures (haemoglobin core, magnetite) also present [Hab08].

These magnetic materials are compounds of iron, particularly iron oxides, which are involved in the reduction-oxidation biochemical reactions of the living beings. In organisms, iron is stored as the mineral *ferrihydrite* ($5Fe_2O_3 \cdot 9H_2O$) within the iron storage protein ferritin. The ferrihydrite is a superparamagnetic antiferromagnet at body temperature, and as such, its magnetic properties are potentially important for understanding the environmental consequences of electromagnetic field exposure, including exposure to strong fields within magnetic resonance imaging scanners [Dob07].

Moreover, biological magnetites (Fe_3O_4) are usually found in single domain units. Although the magnetite is more commonly associated with sedimentary rocks, it is also found in living organisms, with the magnetotactic bacteria as the best well-known example. Such bacteria use chains of single domain biological magnetites that are arranged in order to sense the geomagnetic field and use it for navigation (Figure 2.9).

Although still on some controversy, it has been reported [DG96] the presence of magnetite in human nervous tissue. This suggests that magnetite may provide a

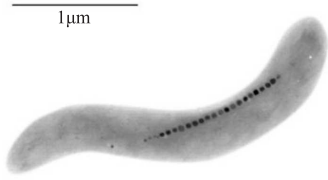

Figure 2.9: Magnetotactic bacterium cell with magnetosomes [Fra].

mechanism for direct interaction of external magnetic fields with the human central nervous system [Dob07]. It has been reported that extreme low frequency (ELF) fields might create biological effects by acting on such particles, although such effects occur only under strong magnetic fields (at least 2-5 μT) [Hab08].

2.3 Thermal Properties of Biological Tissues

As in any material, heat transport in biological tissues may occur by conductive, convective or radiative processes. Knowledge of tissue thermal transport properties is imperative for any therapeutic medical tool which employs the localized application of heat to perfused biological tissue. In this present work, only thermal conduction through tissue and convective heat transport due to tissue perfusion and blood flux are taken into account.

In this section, a brief summary on thermal properties is presented. Good reviews on this subject can be obtained from Bowman [BCW75], Chato [Cha87], and Diller [DVP00].

2.3.1 Thermal Conductivity and Heat Diffusion

Biological tissue is capable of heat transfer-energy transport by virtue of a temperature gradient. Among the three basic mechanisms of heat transfer, i.e., conduction, convection, and radiation, conduction is usually most important in determining the heat transfer within the biological tissue. The capability of a material to transport energy by conduction is best characterized in the steady state by its *thermal conductivity*, k.

The thermal conductivity is defined as the quantity of heat, Q, transmitted due to a unit temperature gradient, in a direction normal to a surface of unit area in unit time under steady-state conditions and where heat transfer is dependent only on the temperature gradient:

$$\frac{Q}{A} = -k\frac{\partial T}{\partial x} \tag{2.28}$$

where $\partial T/\partial x$ is the temperature gradient in the direction of the heat flow, and A is the cross-sectional area. The relationship expressed in Equation (2.28) is known as *Fourier's Law*. The negative sign is a consequence of the fact that the heat is transferred in the direction of the decreasing temperature. The ratio Q/A is designated by *heat flux*, expressed in units of watt per square metre [W/m^2] and the thermal conductivity, k, is expressed in watt per metre kelvin [W/m·K].

The ratio of thermal conductivity to the heat capacity is an important property termed the *thermal diffusivity*, α:

$$\alpha = \frac{k}{\rho\, c_p} \tag{2.29}$$

where c_p is the heat capacity, and ρ is the mass density. Thermal diffusivity is used where steady state conditions are not relevant, and it measures the ability of a material to conduct thermal energy relative to its ability to store thermal energy. Materials with a large value of α will respond quickly to changes in their thermal environment, whilst those with small values of α will take longer to reach a new equilibrium condition. α is related to the spatial and temporal variation of temperature in the material by:

$$\alpha \frac{\partial^2 T}{\partial x^2} = \frac{\partial T}{\partial t} \tag{2.30}$$

Equation (2.30), known as the *heat diffusion equation* or simply *heat equation*, provides the temperature distribution over the material as a function of time.

2.3.2 Bioheat Equation

Due to the complex morphology of the biological tissues, the mathematical description of heat transfer, and consequent temperature distribution in the tissue, is more complex than described in Equation (2.30). Living tissue is perfused by blood which affects the heat transfer process within the tissue. Also, metabolic processes represent a heat source that should be taken into account. Such conditions were considered in Pennes' pioneering work [Pen48] in the expression:

$$\rho c_p \frac{\partial T}{\partial t} = \nabla \cdot k \nabla T - \omega_b c_b (T - T_b) + Q_m \tag{2.31}$$

where ω_b represents the blood perfusion [kg/m^3·s], c_b the blood's specific heat [J/kg·K], T_b the blood's temperature, and Q_m is the heat generated from tissue metabolism. ∇ corresponds to the vector differential operator *del* and is equal to:

$$\nabla = \hat{\mathbf{x}} \frac{\partial}{\partial x} + \hat{\mathbf{y}} \frac{\partial}{\partial y} + \hat{\mathbf{z}} \frac{\partial}{\partial z} \tag{2.32}$$

where $\hat{\mathbf{x}}$, $\hat{\mathbf{y}}$ and $\hat{\mathbf{z}}$ are unit vectors in the three dimensional Cartesian coordinate system.

The mathematical description expressed in Equation (2.31) is the effort's result in trying to quantify convective heat transfer due to blood perfusion. Its main purpose is to describe the transversal temperature in the human forearm, and it corresponds to a mathematical model that handles blood perfusion in a simple way. This equation has become well known as *bioheat transfer equation* or simply *bioheat equation*.

The bioheat equation assumes that thermal equilibrium is attained between capillary blood and surrounding tissue. Capillaries are blood vessels with 5 to 15 μm, where blood velocity is very low. In other words, convective heat due to flowing blood was considered as a non-directional heat source that is only proportional to the volumetric blood flow and the difference between the tissue and blood temperatures, expressed in the term $-\omega_b c_b(T - T_b)$ of Equation (2.31). The directional convective mechanism is neglected.

Attending to this simplification of the bioheat equation, several authors attempted to quantify in a more precise manner the thermal interaction between large blood vessels and the surrounding tissue. Several models are actually proposed in literature. Good reviews on this subject are presented by Arkin *et al.* [AXH94] and Diller *et al.* [DVP00]. Essentially, all models proposed assume that the major process of thermal equilibrium occurs in pre- and/or post-capillaries vessels, so directional convective heat transfer mechanism should be considered.

Although the contributions introduced by these models provided a better mathematical understanding on the complex heat transfer process within the tissue, several limitations still arise. Also, the models presented cannot be generally applied for all type of tissues. Arkin *et al.* [AXH94] concludes that, due to the simplicity of Pennes' equation, it can still be considered the most practical for fast predictions of transient temperature profiles such as those expected in certain hyperthermia conditions.

2.3.3 Available Data on Thermal Properties of Biological Tissues

Unlike to what it is verified with the electrical properties, the reported data on thermal properties of biological tissue is more scattered. Duck [Duc90] gathered the results of several research works on measurement and determination of the thermal properties of the biological tissues (among other properties) between 1920 and 1989, and published them in tabular form in 1990. Presently, this work is largely used as reference in the field of hyperthermia [Cha03, EHD$^+$06, BK07, IWJR$^+$08, LKC$^+$10].

Additional information is also provided by Diller *et al.* [DVP00]. Besides presenting tabulated information on the thermal conductivity for a set of different types of

tissues, it also provides a large set of values for blood perfusion, although the most part of it is for mammalian species than human.

2.3.4 Factors Affecting Thermal Conductivity

Temperature

It is necessary to consider the temperature dependence of the thermal properties of the biological tissues when modelling heat transfer processes where the temperature change exceeds 10°C [DVP00]. Valvano *et al.* [VCD85] studied the effect of temperature variation on the thermal conductivity and the thermal diffusivity of biomaterials. This study was performed on a wide variety of tissue samples considering a temperature range between 3 to 45°C. This temperature range was chosen so that the results could be applied on hypothermia as well as on hyperthermia.

The biological tissue samples were obtained from dogs, pigs and rabbits freshly abated. The samples of human tissue were obtained at autopsy. Finally, the samples of human cancer tissue were excised and used within 24 hours. There were performed 3780 measurements on 65 samples, all larger than 1 cm^3. Linear regression was used to fit the measurements of each type of tissue to the following linear equations:

$$k(T) = k_0 + k_1 T \tag{2.33}$$

$$\alpha(T) = \alpha_0 + \alpha_1 T \tag{2.34}$$

The results show that the thermal conductivity of tissue is lower that of the water, while the temperature dependence approximates that of water. On the other hand, thermal diffusivity of tissue matched the thermal diffusivity of water for both magnitude and the temperature coefficient. From the data obtained, Equation (2.33) and Equation (2.34) can be written as:

$$k(T) = 0.4882 + 0.001265\,T \tag{2.35}$$

$$\alpha(T) = 0.1304 + 0.000519\,T \tag{2.36}$$

Nevertheless, the authors pointed out some limitations on this work. Blood perfusion was not taken into account. Also, there was some undetermined degree of degradation of the tissues when compared with their state *in vivo*. This was particularly significant with the samples of human tissue because they were kept in saline and refrigerated.

Bhattacharya and Mahajan [BM03] studied the effect of temperature variation on the thermal conductivity of collagen and bovine liver. They also identified that thermal conductivity is a linear function of temperature. Moreover, these changes in the thermal conductivity are reversible as long as temperature is within a certain temperature range. For the collagen, changes in the thermal conductivity became irreversible when the tissue is heated beyond 55°C. In the case of bovine liver, irreversible changes occurred over about 90°C.

Blood Perfusion

It was also verified that thermal conductivity is higher for living tissues. This fact arises from the dominant role played by blood perfusion that enhances the net heat transfer within living tissues. The *effective thermal conductivity*, k_{eff}, is the value that expresses the total ability of perfused tissue to transfer heat in steady state, and it is extremely sensitive to perfusion [Val11]. There are several models that attempt to express the effect of blood perfusion on the thermal conductivity. Among them, the bioheat transfer equation, Equation (2.31), is the first approach to this problem. Reviews on these mathematical models are presented in Arkin *et al.* [AXH94] and Diller *et al.* [DVP00].

Despite the evident dependence between thermal conductivity and blood perfusion, it is very common, in the literature concerning the numerical simulation of hyperthermia procedures, to characterize the heat transfer process within the tissue using the bioheat equation. It is usually considered the thermal conductivity independent of the blood perfusion [SS94, HST$^+$01, BPB01, LAW$^+$06, CN04, BGB07, OHC08], or even ignored [BAS05]. Baldwin *et al.* [BPB01], and Chang and Nguyen [CN04] considered a constant blood perfusion value while the surrounding tissue is not damaged. When the tissue is heated up significantly, damaged is induced, and perfusion stops due to blood coagulation.

The damage was quantified using a single parameter, $\Omega(x,t)$, which is calculated from an Arrhenius integral:

$$\Omega(x,t) = \int_0^t A \exp\left(\frac{\Delta E}{RT(x,\tau)}\right) d\tau \tag{2.37}$$

where A is a frequency factor [s^{-1}], ΔE is the activation energy barrier [J/mol], $T(x,\tau)$ is the temperature of the tissue [K], which is dependent of the position and time,

and R is the universal gas constant [8.314 J/mol·K]. This nomenclature comes from the fact that the Arrhenius equation was primarily used to describe the temperature dependence of the rate of a chemical reaction. Later, Moritz and Henriques [HM47, MH47, Mor47, Hen47], suggested Equation (2.37) as an expression for quantifying the damage induced in the tissue caused by temperature.

The parameters A and ΔE are dependent on the type of tissue. The parameter Ω is commonly referred as the *accumulated damage*. An accumulated damage of $\Omega = 1$ corresponds to a 63% probability of cell death at a specific point. This value has been reported [CN04] as the point at which tissue coagulation first occurs.

Tissue Composition

As expected, tissue composition, plays an important part on the thermal properties. Spells [Spe60] verified a linear relationship between water content and thermal conductivity that can be expressed by:

$$k = 0.054 + 0.573 m_{water} \quad \text{for } m_{water} > 0.2 \tag{2.38}$$

where m_{water} is the percentage of water in the tissue. Spells points out that results from Equation (2.38) are better suited for a water content above 50%.

Cooper and Trezek, cited in Diller *et al.* [DVP00], obtained an empirical relationship that relates thermal conductivity with the percentage of fat, protein and water in the tissue composition:

$$k = \rho(0.628 m_{water} + 0.117 m_{protein} + 0.231 m_{fat}) \tag{2.39}$$

where $m_{protein}$ and m_{fat}) are the mass fraction of protein and fat, respectively, and ρ is the mass density of tissue.

CHAPTER 3

Radio Frequency Ablation

Since electricity must have usefulness, and it cannot be looked for either in theology or law, there is obviously nothing left but medicine.

Johann Gottlob Krüger

3.1 Historical Introduction

Over centuries, electricity and its relationship with living beings has been a matter of profound interest and has, therefore, naturally been considered for medical purposes. Prior to the discovery of electricity, Egyptians knew about certain types of fishes that could deliver substantial electric shock to an organism in their aqueous environment. The first pictorial representations of electric catfishes are dated from 3100 BC, and they are located on the slate palette of the pre-dynastic Egyptian ruler Na'rmer [How85], although there are references to earlier representations [FF09]. The electric catfish of the Nile (*Malapterurus electricus*) has a strong electrogenic capability, and it can produce an electric discharge up to 350 V [Ng00]. It is not exactly clear how the Egyptians used this fish, but there are stories that say the catfish was

used for treating some nervous diseases as well as for relieving some pain conditions, probably by *"electrically stimulating the tissues to stimulate* [the] *touch and pressure fibres"* [Kom05].

In the classic era, there are many clear references to another electric fish among ancient Greeks and Romans: the dark electric ray or Atlantic torpedo (*Torpedo nobiliana*). It was commonly referred as *nerka* by Greeks, and by Romans as *torpedo* because of its ability to produce an electric shock up to 220 V, capable of benumbing or paralysing the fish or the persons coming in contact with them [Pic07]. Greek and Roman physicians used the electric ray in the treatment of gout, headaches as well as other ailments [TCG82]. They observed that the therapeutic effect was due to the torpor and the narcotic effect produced by the electric shock of the fish. Scribonius Largus, the court physician of the Roman emperor Claudius (10 BD – 54 AD), included this procedure in its work *De Medicamentis Empiricis, Physicis, et Rationabilibus*, a list of 271 prescriptions produced after a request of Gaius Julius Callistus, the emperor's freedman.

Despite the benefits and improvements in health achieved by the use of electric fishes, there was not an understanding of the nature of the electrical phenomenon itself. The first steps on the fields of electricity and magnetism were taken almost two thousand years later after the work of William Gilbert (1540 – 1603), Charles du Fay (1698 – 1739) and Benjamin Franklin (1706 – 1790) who identified repulsive and attractive forces as well as an electric "fluid" [Whi10]. By the end of the eighteenth century, there was a qualitative knowledge on electrostatics: electric charges could be identified, but it was not established any mathematical model or experimental procedure for measuring the relationship between charges. In 1785, Charles Augustin Coulomb (1736 – 1806) developed some experimentation work that led him to determine

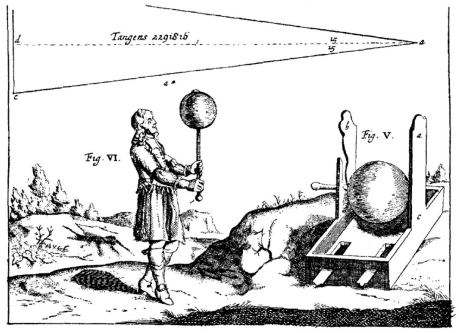

Figure 3.1: Illustration of Guericke's sulphur globe (from [dVH50]).

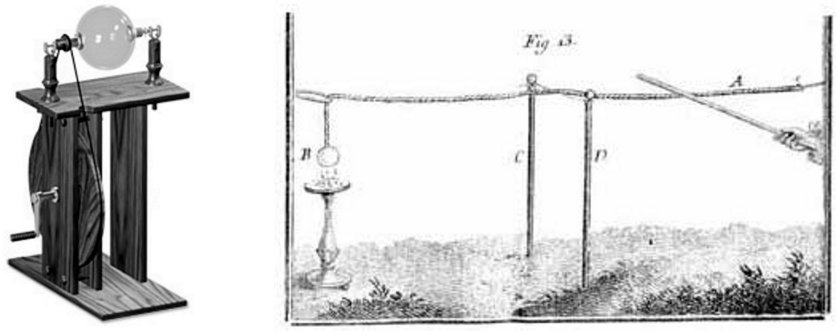

(a) (b)

Figure 3.2: (a) Replica of Hauskbee's generator (from [Nat]); (b) Illustration of Gray's experiment: an ivory ball attached to a twine attracks small brass leaves after a rubbed glass rod touches the twine which is supported by silk threads (from [Ass10]).

the magnitude of the force between two charged particles and established his well-known inverse-square law for the force of attraction or repulsion between charged objects. Finally, electrostatic theory would advance to a mature state of development by the theoretical work of Siméon-Denis Poisson (1781 – 1840).

With the progress of electrification, it started the modern history of medical electricity. In 1663, Otto von Guericke (1602 – 1685) developed what many consider now as the first electrical machine (Figure 3.1): a rotating frictional machine based on a sulphur globe that could be rubbed by hand to produce static electricity [End11, Kuh95a]. There are, however, some doubts on Guericke's main intents concerning the true nature of this device [dVH50]. In fact, he used the word "electricity" only once when describing his work on his text *Experimenta Nova Magdeburgica*. Rather, it is believed he was exploring about the nature of the Universe.

In 1706, after the observations of Jean-Felix Picard (1620 – 1682) on the phosphorescence of mercury, Francis Hauksbee the Elder (1660 – 1713) designed a machine to study this phenomenon. He built a machine consisting on a mercury filled glass globe from which most of the air has been removed (Figure 3.2a). When this globe was spun, whilst a woollen cloth was rubbed against it, it *"quickly produced a beautiful phenomenon,* viz*., a fine* purple *light, and* vivid *to that degree, that all the included* Apparatus *was easily and distinctly discernible by the help of it"* [Com08].

After this initial experience, he continued his experiments and decided to try other substances in addition to mercury. Finally, he focused his attention on the properties of glass after verifying that small pieces of leaf brass could be moved in the presence of the rubbed glass [Hom67]. He documented this work as well as presented a detailed

description of his device in *Physico-Mechanical Experiments on Various Subjects*, published in 1709. This text became the basis for the development of even better electrostatic generators which led to an increased practicality of electric study and demonstration.

The most immediate consequence from Hauksbee's work was the discovery of electrical conduction [Bri80]. In 1729, Stephen Gray (1666 – 1736) announced that electrification – the electricity obtained from friction – could flow hundreds of feet through twine that was suspended by silk threads (Figure 3.2b). However, replacing the silk threads by metal wires, it was observed that charges quickly dissipated [End11]. From this finding, Gray classified materials into two categories: *conductors* and *insulators*. One year later, on his studies to determine which material could conduct electricity, Stephen Gray became the first person to apply electricity to the human body. In order to demonstrate that the human body is a conductor, he suspended a young boy by silk cords so he could stay insulated from the ground, and charged him with a friction generator by his feet. With this arrangement, the boy's hands could attract pieces of brass leaves [Ben98]. This experiment became known as "the electrical boy" or "the flying boy" and it grew into a widespread demonstration like the one represented in Figure 3.3.

Johann Gottlob Krüger (1715 – 1759), Professor of Medicine at the University of Halle, is often referred as the first person to suggest the use of electricity in medicine [LF07]. According to Kuhfeld [Kuh95a], Krüger stated in 1743 that the subtle electrical effluvium, passing through the human body, might cause changes in the most deep-seated parts to restore. He even hypothesized that *"the best effect would*

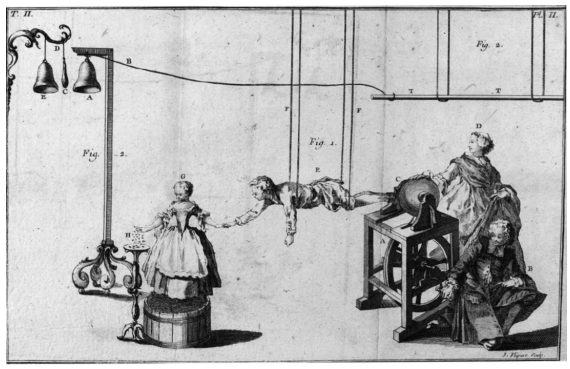

Figure 3.3: *The electrical boy*. The boy is electrically charged and transmits a shock to the girl also insulated from ground using a tar-covered barrel. Her other hand eventually is attracting feathers or small pieces of paper (from [Wat48]).

be found in paralysed limbs" [LF07]. This deduction came after observing involuntary muscular motion in people who submitted themselves repeatedly to electrification [Ber07]. He stated his conviction on this matter by writing that *"Since electricity must have usefulness, and it cannot be looked for either in theology or law, there is obviously nothing left but medicine"* [Pic03].

Short time later, Benjamin Franklin arrived to similar idea. However, he concluded that electricity was not the cure he expected it to be. The trigger that led Benjamin Franklin to study the electricity phenomenon was the demonstration of the "electrical boy" that meanwhile arrived to the English New World colonies. During his work, he also considered the use of electricity as a therapeutic procedure and tested electric shocks as a cure for paralysis. According to his words *"I sent the united shock (...) through the affected limb or limbs (...) the next morning the patients usually related (...) a prickling sensation (...). The limbs (...) seemed to receive strength (...). I do not remember that I ever saw any amendment after the fifth day (...)* [the patients] *became discouraged, went home, and in a short time relapsed"* [Mou91].

The debate on the therapeutic properties of electricity continued during the eighteen century. As the methods of producing electricity were improved, performers with most up-to-date "medical" electric equipment administrated electrical shocks for muscular stimulation and pain relieving. However, despite the large number of discoveries made until then, at the time there was no source that could deliver continuous flow of electricity, but that was about to change. By the end of the century, a controversy rose, introducing the analysis of direct currents in biological tissue and, ultimately, resulted in the creation of two separated and distinct disciplines: electrophysiology and electrical engineering.

In 1786, Luigi Galvani (1737 – 1798) observed that, while a freshly prepared frog leg, in contact with a grounded object, was being probed by a scalpel, the leg seized convulsively whenever a nearby frictional electrical machine gave off sparks [End11]. Later, he observed that these contractions could be obtained touching the nerve of the leg with a zinc rod, and the muscle with a copper rod, then bringing the two metals into contact. He even observed these contractions when no metal was involved. Facing these results, he ascribed these effects to *"animal electricity"*, a kind of electricity that was produced by living creatures. In 1791, he presented these results in his paper *De viribus electricitatis in motu musculari commentarius* (from which the plate in Figure 3.4 is obtained), which attracted the attention of Volta.

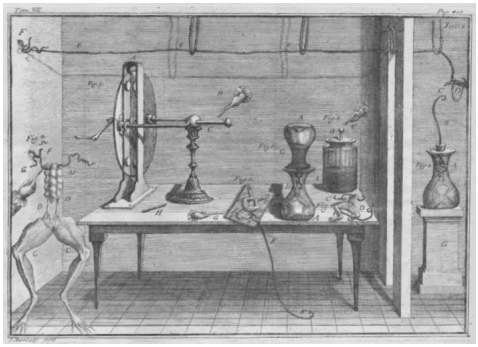

Figure 3.4: Plate from Galvani's *De viribus electricitatis in motu musculari commentarius* presenting his laboratory with the dissected frog legs, an electrostatic machine (on left) and a Leyden jar (on right) [Col04].

Alessandro Volta (1745 – 1827), professor of experimental physics at the University of Padua, repeated Galvani's experiments after reading his paper. Initially, he confirmed Galvani's conclusions. However, as he continued to study the true cause of the observed muscle activity, Volta later decided that Galvani results were obtained due to the presence of the dissimilar metals used in his experiments. Volta claimed that what Galvani had discovery was, in fact, *"bimetallic electricity"*.

Both interpretations from Galvani and Volta developed on a rivalry with supporters and detractors on both sides. Although both interpretations were not totally accurate, in light of what we know today, the controversy led to great contributions to science: Galvani's work introduced the study of bioelectricity and Volta's work started the study of electrochemistry.

At the dawn of the nineteenth century, Volta's invention – the *electric pile* – gained an important role in electroshock therapies after Galvani's nephew, Gionanni Aldini (1762 – 1834), finding out that the voltaic pile could stimulate sensory organs as well as muscles. An example of Aldini's therapies is presented in Figure 3.5: a voltaic pile is used for applying electric shock to treat depression [Kuh95b]. Although the pain from galvanic shocks were hard to tolerate, the parietal region was the best place to undergo the therapy. However, the most important finding by Aldini was that pulsed galvanic stimuli were more effective.

Howbeit, direct currents, or *galvanic currents* as they were known then, were also found to be dangerous. The electrochemical process that occur in the voltaic cell is likewise reproduced in the biological tissue and its effect is more pronounced the longer the current flows continually. This is an electrophoretic process[1]. According

[1]Electrophoresis – an electrokinetic phenomenon where charged colloidal particles or molecules migrate under the influence of an applied electric field.

to Paul Niemeyer,[2] a direct current produces *"a strong erythema and an increase in volume of subcutaneous areas, but in addition, especially at the negative pole, weals and patches of rash develop, the surface of which is covered with slough"* (quoted from [Mac93]). In the second half of the nineteenth century, these necrotic effects due to the electrolytic process of the applied galvanic current were already in use to destroy tumours.

In the pursuit of finding out how to produce electricity from magnetism, Joseph Henry (1797 – 1878) and Michael Faraday concluded independently, in 1831, that it is necessary a varying magnetic field to produce electricity [SK58]. Influenced by Faraday's work, Nicholas Callan (1799 – 1864) invented, in 1836, the induction coil, a device that would reveal to be ideal for therapeutic electrical shocks (although, there is some controversy about the name of the inventor [Cav06]). The electromedicine initiated its faradic era.

Along the nineteenth century, electrotechnology grew significantly. Electricity and magnetism found their way among medical therapies. Major advances were obtained after work by Guillaume Duchenne (1806 - 1875), who undertook experiments in electrotherapy. Duchenne stated that electric stimulation of muscles for treating palsy was ineffective in that it solely alleviated a symptom of the disease and left causative nervous disorder unaffected [Ham69]. However, electrical stimulation of muscles could be used for differential diagnosis of palsy as well as for muscular exercise during periods of natural recovery from paralysis, such as that normally following a stroke. Also, he used electrical stimulation for mapping out the nerves and muscles. Additionally, significant contributions arrived after work by Emil Heinrich du Bois-

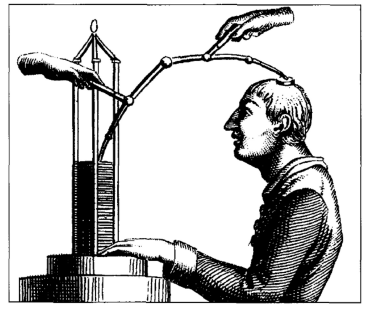

Figure 3.5: Representation of a voltaic pile used in Aldini's electroshock therapy for the treatment of depression [Kuh95b].

[2]Paul Niemeyer (1832 – 1890). German physician , Doctor in Medicine. He published a variety of popular medical writings, among them the title *Über die elektrische Behandlung (Faradisation).*, 1859, from which the quotation is original

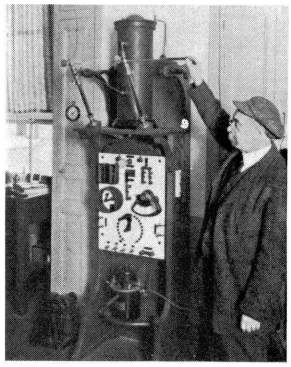

Figure 3.6: d'Arsonval adjusting the spark gap of his improved high-frequency generator [Guy84].

Reymond (1818 – 1896) and Hermann von Helmholtz (1821 – 1894) on nerve polarization, threshold stimulation, and speed of transmission of nerve impulses. These and other investigators laid the basis for the modern science of electrophysiology.

The introduction of the induction coil led to the development of electric circuits with resonant output that were the basis of the experiments of Heinrich Hertz (1857 – 1894) on the existence of electromagnetic waves. The connection of a Leyden jar, the forerunner of the capacitor, across the secondary winding of an induction coil provided the resonant circuit for producing *"Hertzian waves"* of a certain frequency. In a short time, generators of higher frequencies were created.

In 1891, Jaques-Arsène d'Arsonval (1851 – 1940) considered this alternate current for stimulating skeletal muscles. d'Arsonval became aware of the experiments of Hertz, and he made a spark-gap oscillator which was able to generate alternating current up to the low megahertz frequency (Figure 3.6) [Süs79, Ged99, Guy84]. He found out that, above the threshold of 10 kHz, neither pain due to electrical shock nor muscular contraction occurred. On the other hand, oxygen absorption, carbon dioxide elimination, and body temperature increased when such current flowed through the body [OB96]. d'Arsonval studied these effects and examined their variation with the frequency of the applied stimulus.

Similar results were obtained by Nikola Tesla (1856 – 1943), a Serbian-born inventor who was living in the United States of America. At the time, Tesla was performing similar experiments to those of d'Arsonval, and he found that alternate currents above 20 kHz could not be perceived by the human body. However, he noticed that metal objects became heated under the influence of a high frequency fields [Süs79]. In 1891, Tesla reported that a person connected to a source of high-frequency currents experienced heating.

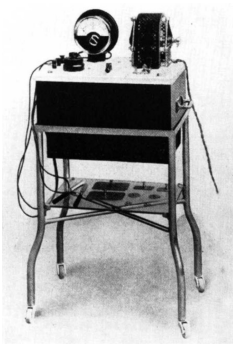

Figure 3.7: The first medical diathermy machine used in the United Kingdom (from [Ham69]).

The mechanisms behind the heating effect in the biological matter due to the high-frequency currents was not perfectly understood. d'Arsonval believed that this was the result of some sort of chemical activity [Süs79]. In 1899, it was recognized that these effects might be simply due to ohmic losses. However, it would take some years before Karl Franz Nagelschmidt (1875 – 1952) presented his theory on molecular oscillation induced by the high-frequency currents. He introduced the term *diathermy* and presented it in his textbook *"Lehrbuch der Diathermie"*, published in 1913.

Diathermy became established as a new surgical procedure, conferring physicians new surgical tools. Basically, it consisted on a pointed electrode inserted into the tumorous tissue to be treated. This electrode was connected to a radio frequency generator, producing a local current density, which would increase the temperature of the tissue, leading to its thermal destruction. In 1910, Lewis Jones, a medical doctor from St. Bartholomew's Hospital and friend of Nagelschmidt, convinced him to demonstrate his medical diathermy equipment in the United Kingdom (Figure 3.7). At the time, Jones and Nagelschmidt treated successfully three cases: a nevus of the tongue, a post-nasal tumour, and a case of enlarged tonsils [Cum22]. Since then, medical diathermy gained the support of several medical practitioners.

During the 1920s, the neurosurgeon Harvey Cushing (1869 – 1939), considered the founder of modern neurosurgery, introduced an innovative electrosurgical equipment developed by the eccentric inventor and doctorate in plant physiology, William T. Bovie (1882 – 1958). This machine produces a radio frequency current that flows into the body in such way that the electric current can cut, coagulate or dissect the tissue. On October 1, 1926, Cushing used for the first time Bovie's electrosurgical equipment for removing a meningioma[3] from a patient's head. The *"Bovie knife"*, as

[3]Meningioma – term introduced by Harvey Cushing to describe a tumour originating from the meninges.

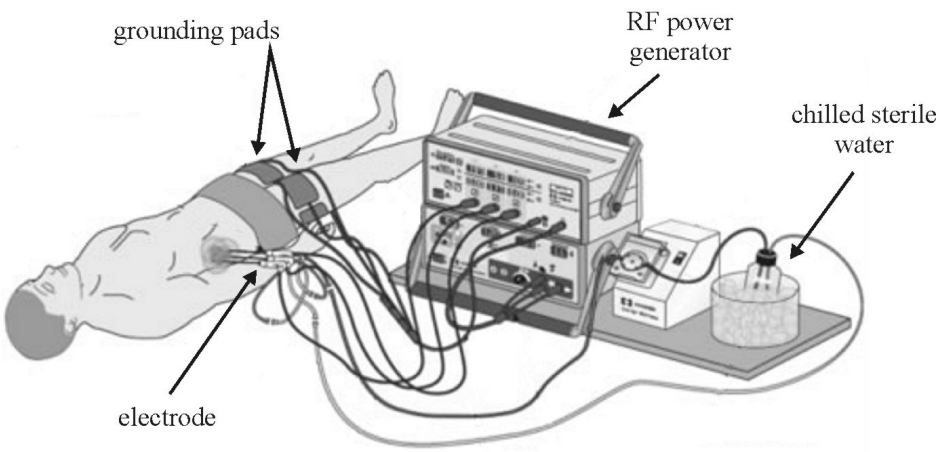

Figure 3.8: Representation of a hepatic RF ablation set-up. The electrode is inserted percutaneously into the patient for a tumour liver thermal ablation. The electrical circuit is closed through grounding pads applied to the patient's thighs. Chilled sterile water is used for cool down the electrode tip in order to achieve a larger volume of damaged tissue. (adapted from [Cov]).

it became later well known, permitted surgery with minimal blood loss, low infection rate, and little tissue damage [OB96]. Almost 100 years after the début of Bovie's device, the basic principles have not changed significantly.

These last developments in high-frequency electrical current applications paved the way for the subsequent use of radio frequency and microwave energy in medical therapies.

3.2 Radio Frequency Ablation

3.2.1 Mechanism of Radio Frequency Ablation

Radio frequency (RF) ablation is a minimally invasive medical procedure considered as an alternative to standard surgical resection. It has become very successful and widely accepted as a catheter-based treatment in many types of cardiac arrhythmias [NE06]. Its application extended with significant results as a medical treatment procedure for primary and metastatic liver tumours [AHLM07, AMM$^+$10] and has been explored for the treatment of unresectable solid tumours located in kidneys [MNL10, HJK$^+$10, SRDL10], lungs [CL10, SDD$^+$07], breasts [KITS11, MNE$^+$10], and bones [VSR09, VHC09]. More recently, it has been studied its application in the treatment of prostate [ZDM$^+$98], brain [MNY$^+$02], and pancreas tumours [TPM$^+$10], as well as

uterine fibroid [JOT12]. The range of publications is so large that only a short sample is presented. Concerning the hepatic RF ablation, some researches have questioned some of the results obtained with this methodology [SFT+09, GHS+08]. However, the Interventional Oncology Task Force and the Standards Division of the Society of Interventional Radiology stated that "*percutaneous RF ablation of hepatic tumors is a safe and effective treatment for selected patients with HCC*[4] *and colorectal carcinoma metastases*" [GGB+09].

The intent of the RF ablation is to induce thermal necrosis of the tumorous tissue by raising its temperature above 50°C. During RF ablation procedure, radio frequency current is driven into the volume of tissue to be treated placing an electrode with a small surface area. A large dispersive pad (grounding electrode) is typically applied to the patient's back or thigh to close the electrical circuit through the RF power generator (Figure 3.8). This grounding pad presents a large area in order to disperse the current at the skin, minimizing the risk of skin burns. Goldberg *et al.* [GSHG00] verified that an inappropriate choice and placement of grounding pads can heat significantly the skin, producing effects that can go from a slight redness to third-degree burns. Even the orientation of the rectangular grounding pads in relation to the RF ablation electrode may influence the temperature distribution on the skin surface. To minimize the risk of skin burn, it is recommended to use multiple large surface area pads, orienting the longest surface edge, so they face the RF electrode (Figure 3.9). More recently, Schutt *et al.* [SSH+07] studied the possibility of using additional grounding pads that were activated simultaneously or sequentially. The activation timing was adjusted to equilibrate skin temperature below each pad. Results showed advantages of the addi-

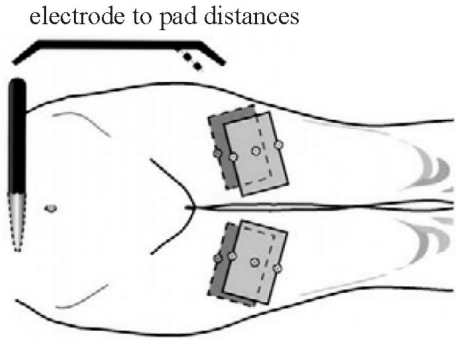

Figure 3.9: Placement of four ground electrodes (gray rectangles) equally spaced from the RF electrode (from [GSHG00], with permissions).

[4]HCC – Hepatocellular carcinoma.

tional pad area, particularly for the sequential activation solution, with considerable reduction of skin heating.

During the RF ablation, a sinusoidal, non modulated, alternating current in the range of 450–550 kHz is delivered to the tissue. Within the tissue, the electric current flow is carried by ions, mostly Na+, K+ and Cl– ions, which follow the natural paths in the interstices toward the dispersive electrode. The ions in the tissue try to follow the changes of the alternating current, which results in ionic agitation that generates frictional heat of the tissue. Thus, the energy is transferred into the tissue primarily by Joule heating, or resistive heating, associated to the ionic current.

Joule heating is proportional to the square of the current density, and the latter is inversely proportional to the square of the distance from the ablation electrode. Thus, resistive heating decreases with the distance from the electrode to the fourth power [NH95]. Significant heating of the tissue will take place only within a narrow rim of tissue in direct contact with the ablation electrode, which means that deeper tissue heating will take place as a result of passive heat conduction from this slim volume of tissue involving the electrode heated by Joule effect.

At the electrode–tissue interface, where the current density is highest, the rate of tissue heating is fast, and steady state temperatures are attained within a few seconds. On the other hand, temperature increases at a much slower rate in tissue sites away from the ablation electrode. This is due to the time required for heat conduction from the electrode–tissue interface. Hence, the rate of lesion growth will depend on these two processes: Joule heating and heat conduction. During the first seconds of the RF ablation procedure, the lesion will grow apace, as the tissue next to the electrode is heated up, then the volume of the thermal necrosis expands much slower, as the heat is conducted from the interface electrode–tissue to deeper tissue. [NH95].

3.2.2 Thermal Necrosis

Biologically, the effects of heat related therapies, such as RF ablation, involve multiple and complex mechanisms. Obviously, these effects will also depend on the temperature and duration of exposition to heat, as well as other local factors, like organ blood perfusion, tissue density, and electrolyte concentration.

As the temperature of the tissue increases, the biological tissue goes through different cellular damage stages [Gol01, HRT84, MH47, NMM+05]. For a slight temper-

ature increment, up to approximately 40°C, cellular homoeostasis[5] can be maintained. Depending on the type of tissue, increasing the temperature above 42 to 45°C can induce thermal injury in the tissue. This is a common range of temperature used in hyperthermia, at which cells become more sensitive to damage by other external agents as chemotherapy and radiation [HRT84, Iss08]. Keeping the temperature within this range for 3 to 50 hours, a progressive cellular degeneration similar to programmed cellular death occurs in steps of conformational change[6] of macromolecules, damage to membranes, chromosomes and cytoskeletons[7], retardation of energy metabolism, nuclear pyknosis[8], and inhibition of DNA, RNA, and protein synthesis [NMM+05]. However, even a long exposure to these temperatures will not kill all cells within a giving volume. It can be observed continued cellular function and tumour growth following relative prolonged heating. Increasing the temperature up to 45°C or above, irreversible cellular damage can be induced in approximately one hour [LBC96, MH47]. The time of exposition to achieve thermal necrosis is significantly shortened as the temperature reaches 50 to 52°C, taking just 4 to 6 minutes to produce irreversible thermal cytotoxicity [GGH+96, Gol01, MH47], e.g., it has been reported that an exposition of just two minutes at 50.8°C is lethal for myocardial cells [NMM+05]. Above 60°C, proteins undergo almost instantaneous coagulation. As proteins are the basic constituents of cytosolic and mitochondrial enzymes and nucleic acid-histone complexes, this implies nearly instantaneous cellular death. Finally, temperatures higher than 100°C produces tissue boiling and vaporization, followed by carbonization of the tissue. At this point, electrical conductivity decreases significantly, and electrical isolation of the electrode occurs, interrupting the RF ablation procedure. Therefore, it is necessary to heat and maintain the target tissue within the temperature range of 50 to 100°C. This way, convenient temperature for thermal necrosis is achieved without producing tissue carbonization and insulation of the electrode [Gol01].

Besides direct damage induced by heat in the tumorous tissue, temperature has also an important influence on the perfusion of the tumour [NMM+05]. RF ablation causes microvascular occlusion within the ablated zone [GHF+00], which may con-

[5] Cellular homoeostasis – ability or tendency of the cell to maintain internal equilibrium by adjusting its physiological processes.

[6] Conformational change – alteration in the shape usually the tertiary structure of a protein as a result of alteration in the environment (pH, temperature, ionic strength).

[7] Cytoskeleton – The lattice or internal framework of a cell composed of protein filaments and microtubules in the cytoplasm, and has a role in controlling cell shape, maintaining intracellular organization, and in cell movement.

[8] Nuclear pyknosis – a degenerative condition of a cell nucleus.

tinue even after RF ablation [MNM+00, MNB+01]. The progression of this marginal vascular damage may lead to ongoing tissue necrosis.

3.3 RF Ablation Electrodes

In the last 20 years, there has been a significant development of electrode solutions for RF ablation of soft tissues, e.g., liver and kidney. Several designs were suggested in the literature, from simple needle electrodes to complex, combined designs, and some of them turned into available commercial solutions. Every design proposed intends to induce a regular, well-defined volume of damaged tissue, large enough to destroy the tumour adequately, plus a surgical safety margin of 1 to 2 cm on all sides of the tumour, for potentially eradicate it [CJS+98, DSK+00].

In this section, it is intended to present a brief overview on the designs that have been proposed, observing the terminology suggested by Mulier *et al.* [MDP+05].

3.3.1 Monopolar Electrodes

Plain Electrodes

RF ablation was introduced in the middle 1980s as a minimally invasive technique for the treatment of cardiac arrhythmias. This pathology corresponds to loss of synchronization and departure of the normal pace of the heart. One of the anomalies that can cause this cardiac problem is an *ectopic focus*, which consists of a group of cells that develops spontaneous rhythmic activity and, at some point, imposes its pace to the rest of the heart. There are cases when pharmaceutical treatment cannot control the arrhythmia, so the abnormal tissue must be ablated.

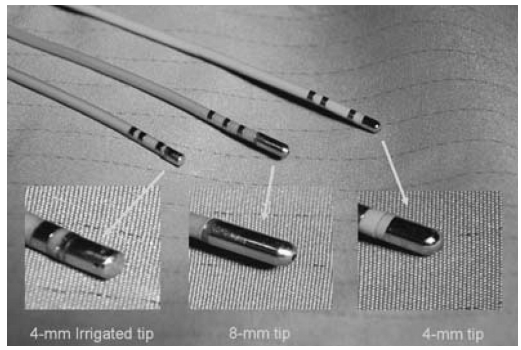

Figure 3.10: Catheter-based electrodes commonly used for cardiac radio frequency ablation (from [NE06]).

The ablation can be performed during open-heart surgery or using catheter procedures. In the latter, the RF current is delivered to the region of the heart to be treated through a catheter-based electrode (Figure 3.10) with a catheter tip between 4 to 10 mm. The catheter is inserted in a peripheral vessel and advanced into the heart chambers [Lab92, Lab94a, NE06]. These electrodes provide a small but precise volume of damaged tissue that is perfectly appropriated for this specific medical intervention.

First reports on RF ablation experiments on soft-tissue organs date from 1990 [MBBT90, RFPB90]. In these studies, it was used an adapted RF electrosurgical unit, similar to that of the Bovie knife, and a simple, plain electrode obtained from a modified standard stock needle, which was completely insulated, except for the distal tip (Figure 3.11). The region of coagulative necrosis obtained was well-defined, presenting an ellipsoid shape. The transverse induced lesion obtained was no larger than 14 mm, with 18 mm length.

The limited growth of the lesion volume is due to progressive insulation of the electrode during the RF ablation procedure. There are two mechanisms involved in the insulation of the electrode:

- *Boiling and evaporation of tissue fluids*. This leads to the formation of an insulating gas between the electrode and the immediately adjacent tissue;

- *Carbonization of the tissue*. The tissue next to the electrode, where the temperature is higher, gets dehydrated, and it starts to char, insulating the electrode.

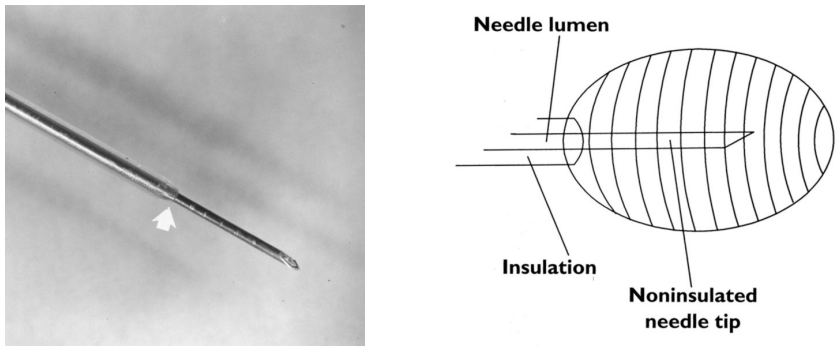

(a) (b)

Figure 3.11: Original needle-based electrode (from [MD01], with permissions). (a) Image of the needle modified into an RF ablation electrode. The needle is completely insulated, except for the distal tip (pointed out by the arrow); (b) Theoretical volume of injured tissue that would be induced by the electrode.

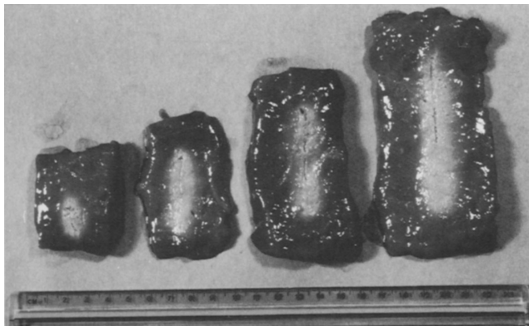

Figure 3.12: Correlation of tip exposure to lesion length. Lesions were created with 1, 3, 5, and 7 cm tip exposure (left to right) in calf liver at 90°C, using an 18-gauge probe during 6 minutes. Samples were cut lengthwise to show the lesion in cross-section. The light-coloured regions represent areas of coagulation necrosis. The thin depression in the centre of the lesion is the probe tract. Note that lesion length correlates well with tip exposure (from [GGD$^+$95], with permissions).

Goldberg *et al.* [GGD$^+$95] studied the effect of the dimensions of the electrode (length of exposed tip and diameter of the electrode), duration of the procedure and the volume of lesion obtained, considering a monopolar electrode. Varying the length of the electrode did not improve the lesion diameter. Lesions with mean diameters larger than 16 mm could not be produced. On the other hand, the lesion length correlated with the tip exposure (Figure 3.12). The rapid fall of temperature at increasing distances from the electrode and the dimensions of the electrode itself prevent the growth of the ablation volume. One should add that tissue conductivity and heat convection due to blood perfusion are also important factors that can affect the ablation volume significantly.

It became evident that this type of electrode was limited for RF ablation procedures. The ellipsoidal shape of the induced necrosis does not match the spheric geometry of most tumours [Gol01]. Also, the volume of necrosis obtained is critical because tumours can largely exceed 20 mm diameter [TK11]. If the volume of ablation is smaller than the volume of the tumour, it can result in recurrence [KO02, SGE$^+$00]. The treatment of large tumours could be achieved by producing multiple, overlapping lesions in order to thermally ablate the whole tumour. However, from studies already made on this matter, the lesion induced by the electrode should be a perfect sphere. Also, this strategy requires a perfect placement of the electrode on the tumour, which is clinically idealistic [CYY$^+$04, DFA$^+$01, SGE$^+$00].

The promising results from the initial experiments with plain electrodes lead to the development of new designs to overcome the limitations of this precursor electrode. Three major concepts were developed: extension of the electric field within the tis-

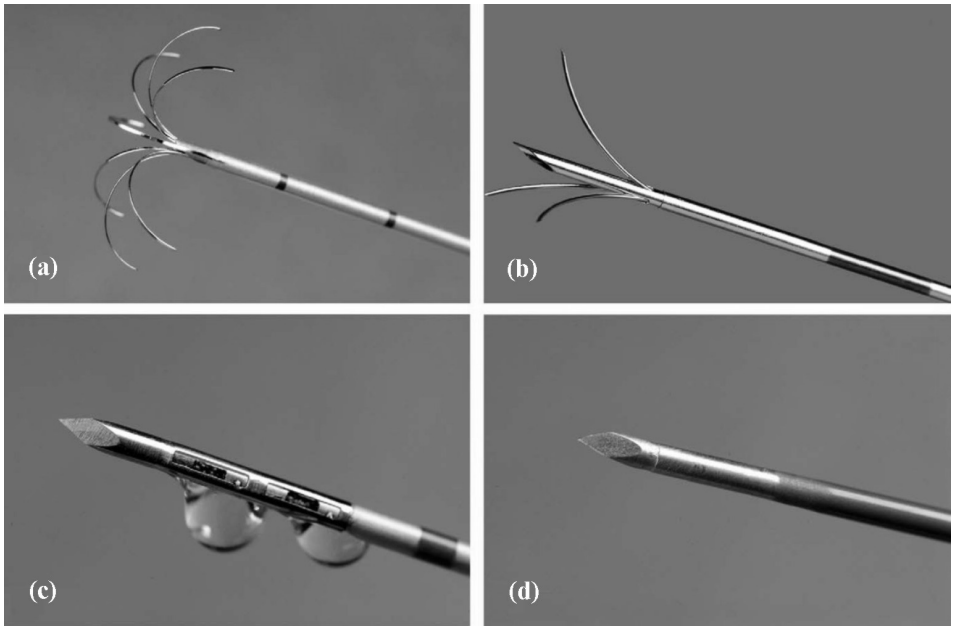

Figure 3.13: Four different electrode designs (a) Expandable 8-tine monopolar dry electrode; (b) Expandable 3-tine monopolar dry electrode; (c) Single monopolar wet electrode; and (d) Single monopolar dry, internally cooled electrode(from [ASC+05], with permissions).

sue (*expandable electrodes*, Figure 3.13a-b), saline perfusion from the electrode into the tissue (*wet electrodes*, Figure 3.13c), and internally cooling the electrode (*cooled electrodes*, Figure 3.13d).

Cooled Electrodes

The cooled electrode is a hollow electrode that contains an inner cannula, which divides the space inside the electrode into concentric outer and inner lumen [GGS+96, Lor96, MDP+05]. The inner lumen delivers a chilled perfusate that returns by the outer lumen without leaving the electrode (Figure 3.14). This continuous flux of a chilled fluid produces a heat sink effect that cools the electrode–tissue interface, minimizing the risk of tissue charring, which avoids the electrical insulation of the electrode: it is possible to deliver more power into the tissue, thus producing a larger lesion than using a plain electrode.

Haemmerich *et al.* [HCW+03] studied the effect of the coolant temperature on the size of the induced lesion. It was verified that, for a coolant temperature between 5 and 25°C there was no significant effect on the dimension of the lesion. *Ex vivo* experiments demonstrated that is possible to obtain a lesion with a cross sectional dimension of 30 mm, approximately, for coolant temperatures of 5, 15 and 25°C.

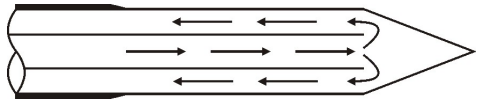

Figure 3.14: Longitudinal section of a cooled electrode. The inner lumen delivers chilled fluid to the tip of the electrode, cooling the interface electrode–tissue without leaving the electrode. The fluid is then returned by the outer lumen.

There is, however, a theoretical drawback that should be considered when using this type of electrode: because the tumorous tissue next to the electrode is being cooled during the ablation, it might not be sufficiently heated to induce coagulation necrosis. Nonetheless, it is suggested that the energy deposited during RF ablation continues to dissipate by conductive heat transfer from the peripheral to the central part of the thermal lesion, where the electrode is located. Thus, it is very likely that this region heats up above 50°C, the threshold to induce coagulation necrosis [GGS+96].

Wet Electrodes

The wet electrode consists of a hollow electrode with one or more holes located at the uninsulated tip through which an isotonic or hypertonic saline solution, e.g., 5–36%, is infused into the tissue, which allows to achieve larger lesion volumes than using a plain electrode [HNW+04, HMS95, LGM+97, MNM+97, MNM+00, MTD+02, PHL+99].

There have been proposed several explanations to justify the effect of the saline solution on the increased volume of damaged tissue. Some of them relies on changing of the electric properties of the medium, others on the hydration of the tissue, or both.

The perfused saline solution changes the inherent conductivity of the tissue, increasing it, which allows better dispersion of the current from the active electrode to the surrounding tissue [GAG+01, MNM+97, MNM+00, MTD+02]. Also, the electrical conductivity of the electrode–tissue interface is improved. The saline solution fills the gap between the electrode and the adjacent tissue with conductive ions. At the same time, prevents excessive heating next to the electrode, avoiding charring and impedance rise [MNM+00]. On the other hand, the injection of saline fluid during the RF ablation procedure improves the thermal conductivity of the tissue by convective heat transfer. This causes a flattening of the heat distribution, which permits greater energy delivery to a larger volume with less tissue boiling and carbonization next to the electrode [GAG+01, ALW+02]. It was also observed that larger lesions were in-

duced at lower temperatures than those obtained with no saline perfusion. This fact may evince that resistive heating is more significant than conductive heating during RF ablation [NYP+95, MNM+97].

Some of the early investigations [HMS95, MNM+97, MNM+00] studied the induced lesions obtained with a screw-tip wet electrode. Figure 3.15 shows an electrode used by Miao *et al.* [MNM+97] which consisted of a 5 Fr hollow catheter[9] (diameter of 1.67 mm) and a screw-like tip. The diameter of circular helix that describes the screw-tip was 10 mm, and there were four holes with 0.12 mm diameter in the tip for injecting the saline solution into the tissue. Averaged lesions sizes of 4 cm were obtained with RF ablation procedures of 12 minutes. However, this design was dropped later in favour of needle-based design electrodes.

Some precautions should be considered on the perfusion of the saline solution. Gillams and Lees [GL05] reported that saline can extravasate beyond the tumour when using high infusion rates (0.5 to 1.1 ml/min, according to these authors). In some cases, it can lead to the damage of areas outside the target volume.

Unproven concerns about saline solution injection are also pointed out in the literature, so that cautionary measures should be taken. A serious and possible drawback of saline infusion into the tumour is that it might rise the pressure inside the tumour, which may increase the possibility of local and remote migration of viable tumour cells and cause metastasis [MNM+97]. Also, there is a risk of peritoneal or track seeding of tumour cells with leaking saline [GAG+01].

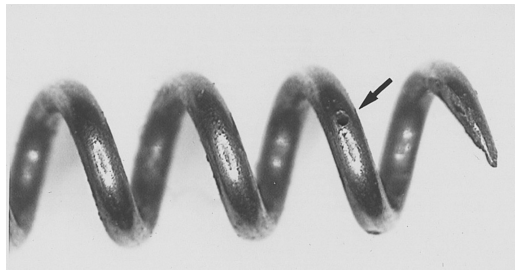

Figure 3.15: Screw-tip cannulated electrode. It consisted of a hollow screw catheter with 1.67 mm diameter (5 Fr) with one end hole and four side holes (0.12 mm in diameter) at its tip. The screw diameter was 10 mm. The arrow shows one of the four side holes (from [MNM+97], with permissions).

[9] French gauge or French scale – a standard set of diameters commonly used for round needles, catheters, and rubber tubing. It is often abbreviated as Fr or F. The French scale ranges from 3 Fr (1 mm) to 34 Fr (11.3 mm). 1 Fr = 0.33 mm.

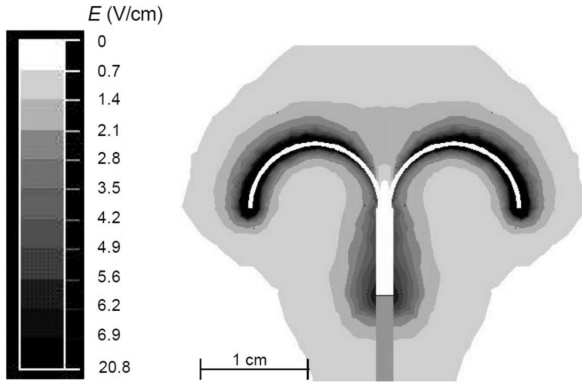

Figure 3.16: Electric field intensity obtained with a expandable umbrella-like electrode. It is possible to observe how the electric field follows the configuration of the electrode, allowing the deposition of the energy along a larger area (from [Hae01]).

Expandable Electrodes

The expandable electrode is a straight, insulated, hollow needle that is inserted into the tissue and placed in the desired position for RF ablation. Once the needle is set in place, the active electrode is deployed from the hollow shaft of the probe.

These electrodes, also known as *multi-tined electrodes*, comprise an array of 4 to 14 curved electrode tines (prongs) that are deployed from the hollow needle tip. After deployment, the electrode may present two of the most common configurations: umbrella-like (Figure 3.13(a)) or Christmas tree-like configuration (Figure 3.13(b)). The electric field follows the configuration of the deployed electrode (Figure 3.16), enlarging the contact surface between the electrode and the adjacent tissue. This reduces the circuit impedance and allows a larger energy deposition into the tissue. Also, the current density decreases next to the electrode, which reduces the risk of carbonization of the tissue. During RF ablation, tissue coagulation begins at the extremities of the prongs, resembling a clover or flower pattern (Figure 3.24 (b)). As

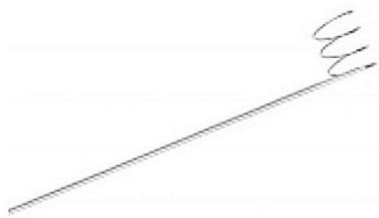

Figure 3.17: Expandable coiled electrode Invatec MIRAS RC. No longer commercially available (from [MDP+05], with permissions).

time elapses, these lesion areas expand and coalesce to form a coarse spheric necrotic volume [CLK+01, PSO+98, SRHG97].

In the literature, there are also some references to another type of expandable electrode named *coiled electrode* [MNM+03, MDP+05, NMM+05]. It consists of a spring-like active electrode that is deployed from the hollow probe, perpendicular to the shaft (Figure 3.17). This electrode was commercially produced by INVATEC SPA (Italy), but it is not currently available in the market.

3.3.2 Bipolar Electrodes

Bipolar RF ablation consists of replacing the grounding pad by a second parallel electrode in order to achieve a larger and more regular volume of damaged tissue than using a plain monopolar electrode [BGB+99, CDF+97, MGB+96].

As stated before in section 3.2.1, the electrical heating of the tissue decreases with the distance from the electrode to the fourth power when a monopolar electrode is considered. Also, the tissue adjacent to the electrode is rapidly heated by Joule effect, which arises problems of insulating gas formation, subsequent carbonization of the tissue, and electrical insulation of the electrode. Using a bipolar configuration, where the grounding pad is no longer necessary, the electrodes are placed close to each other so that the electric field gradient is almost constant in the region between the electrodes (Figure 3.18). The electric current is mainly confined to this area, so the tissue between the electrodes is preferentially heated [HTS+02, Hae01].

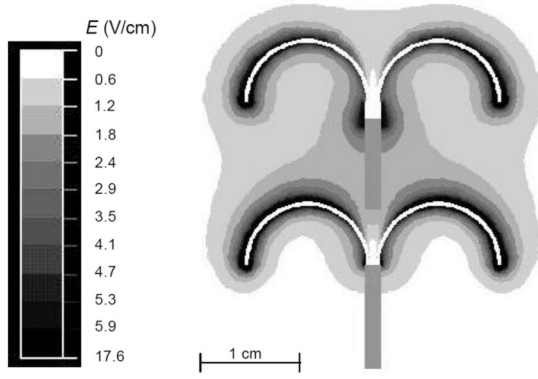

Figure 3.18: Bipolar RF ablation. Electrical field intensity on a longitudinal plane to the bipolar-expandable electrodes. It is shown that the electric field is almost constant in the area between the electrodes. (from [Hae01]).

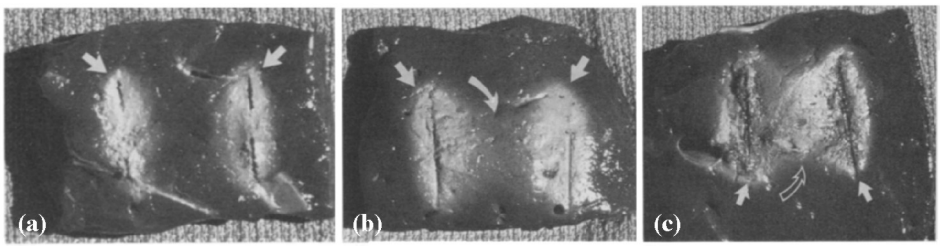

Figure 3.19: Necrosis coagulation obtained in an *ex vivo* bovine liver with bipolar RF ablation for different power settings. The lesions were obtained using two electrodes separated by 35 mm distance, with exposed distal tips of 30 mm length. Results were obtained after 15 minutes at (a) 10 W; (b) 15 W; and (c) 20 W. It is visible larger area of tissue necrosis between the needle tracks as the power increases (from [MDP+05], with permissions).

Another interesting benefit of using bipolar electrodes is the lack of a grounding pad. As already mentioned, one of the complications that can arise from monopolar RF ablation is grounding pad skin burns, which in some cases may cause third degree burns [CMB+04, MMN+02, WRC+00]. Clearly, removing the grounding pad, it eliminates the risk of skin burns.

McGahan *et al.* [MGB+96] verified that the distance between needles, the electric power applied, duration of the procedure, and temperature are all decisive factors in producing coagulation necrosis. In case the applied power or the temperature are too high, charring of the tissue next to the electrode occurs, which limits considerably the size of the destroyed tissue. Low power or short time might not increase significantly the temperature within the tissue. In Figure 3.19, it is shown the effect of power on the lesion induced in the tissue considering two electrodes with an uninsulated tip of 30 mm, both separated by 35 mm distance, for a constant application time of 15 minutes. As applied power is increased (from Figure 3.19a to Figure 3.19c), the lesion becomes larger and well-defined in the area between the electrodes. Complete coagulation necrosis between both electrodes is achieved at 20 W.

More recently, Cosman *et al.* [CG11] presented an extensive research on the effect of the distance between electrodes, electrode positioning, uninsulated tip length, electrode diameter, tip temperature and duration of the procedure on the geometry of induced lesions. Experimental tests were performed *ex vivo* on different types of biological tissues. Also, *in vivo* experimentation was performed in a clinical environment for the treatment of sacroiliac joint pain. For this latter, it was only performed temperature measurement. *In vivo* temperature readings corroborate those obtained *ex vivo*. Also, conclusions on the effect of the distance between electrodes agreed with McGahan *et al.* [MGB+96].

Despite these results, bipolar RF ablation using two electrodes was almost totally dropped by the end of the 1990s, particularly in the area of RF ablation of soft tissues. The requirement of placing the electrodes in correct parallel position, as well as the lack of a more extensive knowledge on the geometry of the induced lesion, made this methodology less frequently used [CG11, NMM+05].

Single-Shaft Bipolar Electrode

An alternative solution to the use of two electrodes for performing bipolar RF ablation consists of incorporating both electrodes in a single shaft, placed proximally and distally on the same insulated probe. In Figure 3.20, it is presented a bipolar 18 gauge needle-based electrode[10]. The tip of the probe is 9 mm long and contains both electrodes (labelled as E1 and E2) axially separated by an insulator material, which is displayed in a lighter shade.

Although promising results have been reported, still additional research experiments are claimed in order to confirm the suitability of this kind of electrode for complete and reliable ablation of tumorous tissue [BGB+03, HVW+06a, MTWG06].

3.3.3 Combination of Electrode Designs

In the attempt of obtaining larger, regular, predictable lesions, complex electrode designs emerged from the combination of the basic designs so far referred in this text: cooled, wet, bipolar and expandable electrodes [MDP+05]. In Figure 3.21, it is illustrated how these designs can be associated to obtain six new combined designs: cooled-wet, expandable-wet, bipolar-wet, bipolar-cooled, bipolar-expandable and bi-

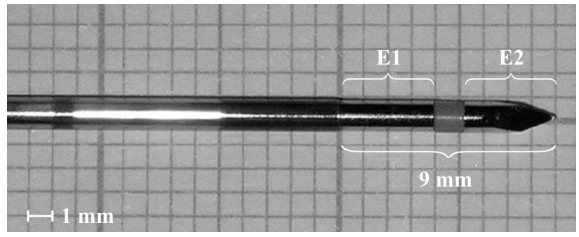

Figure 3.20: Bipolar 18 gauge needle-based electrode for RF ablation of osteoid osteoma (detail). The 9 mm tip is formed by two electrodes – E1 nd E2 –, separated by a small piece of insulator material (from [MTWG06], with permissions).

[10] Needle gauge – a common measure for the diameter of hypodermic needles. Smaller gauge numbers refer larger outer diameter. 18 gauge = 1.3 mm.

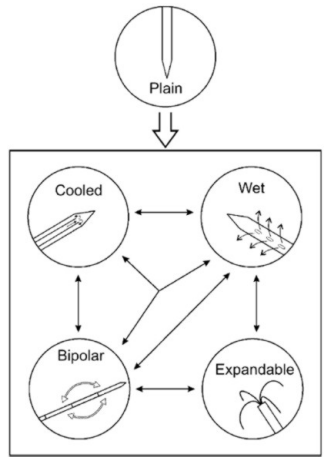

Figure 3.21: Five basic designs of RF ablation electrodes (plain, cooled, wet, expandable and bipolar) have led to the development of six combination designs: cooled-wet, expandable-wet, bipolar-wet, bipolar-cooled, bipolar-expandable and bipolar-cooled-wet (from [MDP+05], with permissions).

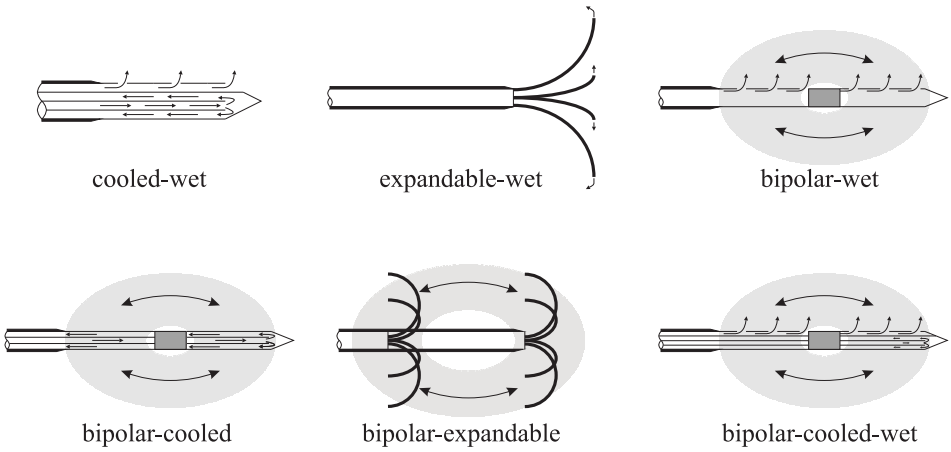

Figure 3.22: Combinations designs for single-shaft electrodes. Small curved single-head arrows indicate saline solution perfusion into the tissue. Curved double-head arrows indicate current path in the bipolar configurations.

polar-cooled-wet. A brief description is presented. Detailed information can be obtained from Mulier *et al.* [MDP+05].

- *Cooled-wet electrode* – It allows continuous injection of saline solution into the tissue adjacent to the cooled electrode. It can achieve larger ablation volumes than both the wet and the cooled electrode separately.

- *Expandable-wet electrode* – Usually the distal end of the tines are open, which allows the perfusion of the saline solution. It has been reported that this electrode achieves larger lesions than the original electrodes separated.

- *Bipolar-wet electrode* – The bipolar part of the electrode refers to a single shafted probe. The saline solution flows into the tissue from each electrode.

- *Bipolar-cooled electrode* – It consists on a bipolar single-shafted electrode which is internally cooled.

- *Bipolar-expandable electrode* – It consists of two expandable electrodes that are arranged in parallel into one shaft, connected in a bipolar fashion and separated by an insulator material.

- *Bipolar-cooled-wet electrode* – A triple combination design that consists of two cooled-wet electrodes incorporated into one shaft, separated by an insulated portion and connected in a bipolar fashion.

A simplified representation of combined single-shaft electrode designs is depicted in Figure 3.22. The small single-head arrows indicate saline solution perfusion into the tissue. For the designs that combine bipolar configuration, the electric current path is represented by the curved double-head arrows and the grey light shaded oval.

3.3.4 Multiple Electrode Systems

RF ablation can be carried out with more than one electrode applied into the tissue to be treated (excluding the grounding pad, of course). In this case, it is said that a *multiple electrode system* is being used. The bipolar RF ablation presented in section 3.3.2 is an example of this type of electrode configuration.

As reported by Mulier *et al.* [MDP+05], the use of multiple electrode systems can be described according to:

- *Number of electrodes used* – A multiple electrode system can comprise two, three or more electrodes.

- *Electric mode* – In the *monopolar mode* the current flows from all electrodes of the system to a grounding pad. In the *bipolar mode* the current flows from two parallel inserted electrodes or group of electrodes.

- *Activation mode* – The electrodes can be activated *consecutively*, i.e, the next electrode is activated after finalizing the RF ablation procedure with the presently active electrode. They can also be activated *simultaneously*, or in a rapid *switching* mode. For this last activation mode, additional hardware is required to control the switching pattern.

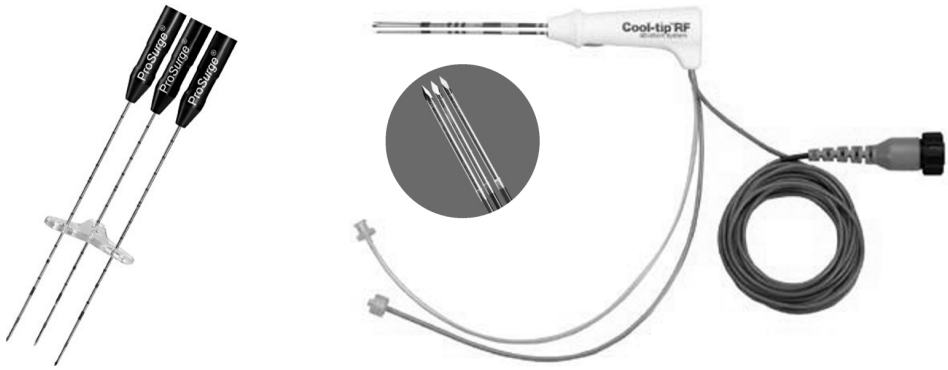

(a) (b)

Figure 3.23: Example of multiple electrode designs. (a) Multiple bipolar-cooled electrode CelonPro*Surge* from Celon [Cel05a]; (b) Multiple cooled electrode Cool-Tip^{TM} from Covidien [Cov09]

- *Location of the inserted electrode* – It describes the part of the organ to be treated. If the electrodes are inserted in the same part of the organ, it is said a *mono-focal* RF ablation. On the other hand, if the electrodes are inserted in different parts of the organ, in order to treat different locations simultaneously, it is called a *multi-focal* RF ablation, e.g., bifocal RF ablation. For this case, additional hardware is required for distributing the current in an alternating mode to the different locations.

Considering these variables, the number of possible combinations is unlimited. Figure 3.23 depicts two examples of multiple electrode systems available in the market. The CelonProSurge probe (Figure 3.23a) is a multiple, bipolar-cooled electrode for mono-focal insertion from Celon. The RF generator performs the control of the activation of the electrodes. In Figure 3.23b, it is shown the Cool-Tip^{TM} electrode from Covidien. It is a multiple, cooled electrode for mono-focal insertion. It can be used in simultaneous or switching mode.

3.3.5 Saline-Enhanced RF Ablation

Saline-enhanced RF ablation refers to the procedure where the saline solution is directly injected into the tissue be treated with a needle than the RF ablation electrode [ALW^{+}02]. The infusion of the saline solution is not, therefore, through the electrode but through a separate needle, in contrast to wet electrodes. However,

some authors refer RF ablations with wet electrodes as saline-enhanced procedures [KLK06, LAU+10, TSN+09].

Saline-enhanced ablation consists of an injection of the saline as a bolus prior the RF ablation, and it may also be instilled during the RF ablation [LHK+04, LKL+03]. This way, the advantages of using saline solution can be combined with any kind of RF ablation electrode.

3.3.6 Size and Geometry of RF Lesions

As expected, size and geometry of the lesion that can be induced during a RF ablation procedure are relevant factors. It is intended to destroy the whole tumour, including a surgical margin of 1 to 2 cm, in order to avoid recurrence and without affecting, at least significantly, healthy tissue. The geometry of the induced lesion is clearly determined by the geometry of the electrode, location of the tumour, tumour consistency, and cooling effect by perfusion due to convective heat transfer. It should also be considered the effect by saline solution distribution when wet electrodes are being used [PTS+04].

During RF ablation procedure, the electrodes are commonly inserted percutaneously into the tissue to be treated under ultrasound, computed tomography, or computer resonance guidance [GD01]. Given its low cost, widespread availability, and real-time capabilities, ultrasound monitoring is the preferred mechanism for guiding electrode insertion at many institutions [FNH+08]. During RF ablation, hyperechoic areas due to gas formation rise in the region under treatment. However, these foci are not well correlated with the dimensions of the induced lesion and, therefore, they should be viewed only as a rough approximation [CLG+00, LDH+02, RLV+00]. This fact turns into an important issue the characterization of size and geometry of the lesions produce by RF ablation electrodes.

There is a myriad of reports characterizing the lesions obtained in diverse types of tissues, considering different types of electrodes and RF ablation methodologies. Mulier *et al.* [MNM+03] performed an extensive literature search on the size and geometry of hepatic lesions using available commercial devices between 1990 and 2003. Also, commercial suppliers were contacted and asked to provide data on this subject. Although actual electrodes and RF generators radio frequency have evolved since its publication (and some other just disappeared from market), this report is still very significant about the results presented. A brief highlight over this document follows.

According to the authors, the data available on basic performance of commercial electrodes is sparse. In most of the studies, only the calculated volume is reported, not clarifying about the shape of the lesion, an important parameter in a clinical environment. Information on diameter or radius is meagre. It is usually reported the maximum diameter, which is oncologically irrelevant. In order to ensure that the whole tumour is heated up significantly, minimal diameter would be essential.

Induced lesions are seldom perfectly spherical. Rather, they usually approximate to ellipses or flattened spheres. Mulier *et al.* classify this distortion in two types (Figure 3.24a):

- *Type 1 distortion* – it refers to a lesion asymmetrically smaller than expected. It can be verified in the perfused liver, when RF ablation is performed close to blood vessels, where convective heat transfer may influence the final result.

- *Type 2 distortion* – it refers to a distortion much larger than expected, and it is normally connected to RF ablation with wet electrodes. Saline solution may spread to an area larger than intended, inducing non-regular necrosis volumes, and causing unwanted lesions [GL05].

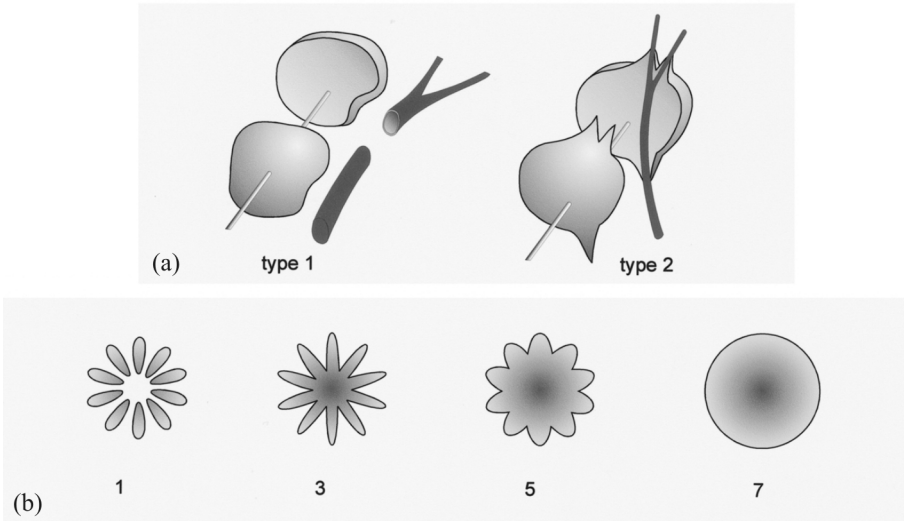

Figure 3.24: Type of distortions of the induced lesion volume. (a) Distortion type 1 – lesion asymmetrically smaller than expected, e.g., by cooling effect of nearby blood vessel; distortion type 2 – lesion asymmetrically larger than expected, e.g, by preferential diffusion of saline solution along vessels. (b) Lesion on the transverse plane when using an expandable electrode. It refers to the grow of the necrosis area as it coalesces into a circular shape (from [MNM+03], with permissions).

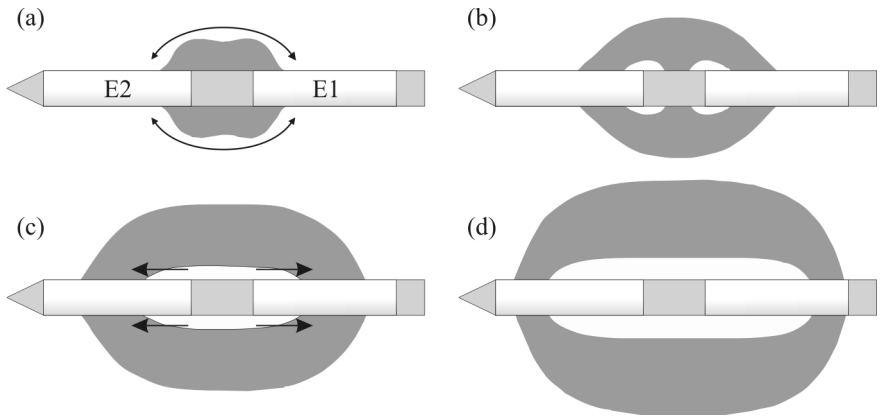

Figure 3.25: Development of the induced lesion during a RF ablation with a bipolar electrode. (a) When RF ablation starts, electric current (curve arrows) flows along the shortest path between the two electrodes E1 and E2, first coagulating the tissue next to the electrodes; (b) As time elapses, the ablation region enlarges, and the tissue begins to dehydrate next to the electrodes (white areas); (c)-(d) Dehydrated volume increases and extends along the probe (arrows).

Also, incomplete fusion of RF ablation lesions between prongs is noted in most expandable commercial electrodes. Considering a plane transverse to the prongs of an expandable electrode, RF ablation lesions may present the following pattern of growth (Figure 3.24b): lesions first appear as discontinuous areas centred around each prong. As the zone of the necrosis grows, it coalesces into a roughly circular shape [CLK$^+$01, PSO$^+$98, SRHG97].

In the perfused liver tissue, the dimensions of the induced lesions are usually smaller and more variable than the length of the electrode tip or the diameter of the expanded prongs suggest, e.g., a 3 cm electrode does not assure a 3 cm minimal coagulation. Complete blood interruption by Pringle manoeuvre[11] or hepatic vein occlusion produces a larger, less elliptic, less distorted and more completely coalesced lesion than in perfused liver. This may partially explain lower tendency of local recurrence – 4 to 9% – in series using Pringle manoeuvre then using a percutaneous approach – 30 to 60%.

Pereira *et al.* [PTS$^+$04] studied the shape and reproducibility of *in vivo* necrosis obtained with four commercial RF ablation systems. They verified that umbrella-like electrodes (Figure 3.13a) achieved more spherical volumes, while Christmas tree-like expandable electrodes (Figure 3.13b) produced thermal lesions similar to an inverted

[11] Pringle manoeuvre – Temporary occlusion of the portal vein and hepatic artery by clamping the hepatic pedicle [Nic11].

cone. Multiple triple cooled electrode for mono-focal application, like the one depicted in Figure 3.23b, led to larger lesions that approximated to an ellipsoid shape according to a longitudinal plane to the electrode. The largest lesions were achieved with wet electrodes. However, the diffusion of saline led to marked distortions in the necrotic volume, which matches the information reported by Mulier *et al.* [MNM+03]. It should be noted that the wet electrodes used in Pereira's work are not longer commercially available.

With respect to bipolar electrodes, these were not considered by Mulier *et al.* [MNM+03] and Pereira *et al.* [PTS+04] because commercial solutions were made only available after 2003. Häcker *et al.* [HVW+06a, HVW+06b] studied the induced lesions using cooled bipolar electrodes, and reported that regular, elliptical lesions were obtained using these electrodes. During ablation, the induced necrosis grows from the volume between and extends peripherally and along the probe (Figure 3.25).

3.4 Commercial RF Ablation Systems

Currently, there are four major manufactures of RF ablation systems that globally provide their commercial solutions:

- *Covidien (Mansfield, Massachusetts, USA)* – Formerly known as Tyco Healthcare, owner of the industrial brand Valleylab. Valleylab acquired the whole line of radio frequency applications to Radionics, actual Integra LifeSciences. At the time, the RF ablation system was known as *CC-1 Cosman Coagulator*.

- *AngioDynamics (Latham, New York, USA)* – AngioDynamics bought, in January 2007, RITA Medical Systems in order to expand its core business to the area of oncological thermoelectric therapies.

- *Boston Scientific Corporation (Natick, Massachusetts, USA)* – Boston Scientific expanded to the RF ablation equipment market in 2001 after acquiring RadioTherapeutics.

- *Olympus Medical System (Hamburg, Germany)* - In April 2004, Olympus held a majority stake in Celon AG Medical Instrument. Celon is still the commercial brand for RF ablation equipment from Olympus.

Besides these equipments, in the literature there are also references to *Integra Elektrom HiTT 106*, a RF ablation system based on wet-electrodes, and *Invatec MIRAS*

Table 3.1: Technical specifications of commercial RF ablation generators

	Covidien	**AngioDynamics**	**Boston Scientific**	**Celon**
Commercial Designation	Cool-tip RF System	RITA 1500X	RF 3000	CelonPOWER System
Maximum Output Power (W)	200	250	200	250
Frequency (kHz)	480	460	460	470
Operating mode	Pulsated	Continuous	Continuous	Continuous
Power monitoring	Yes	Yes	Yes	Yes
Current monitoring	Yes	Grounding electrodes (alarm)	Grounding electrodes (alarm)	not available
Impedance monitoring	Yes	Yes	Yes	Yes (impedance & resistance)
Temperature monitoring	Yes	Yes	No	Yes
Power control	Automatic (based in the impedance)	Manual or automatic (based in temperature)	Manual	Power control (based in resistance)
Algorithm	Power delivered during fix time periods	Gradually increase of power until reaching defined temperature (Temperature control mode)	Generally, power is increased by steps. Generator is switched to stand-by if output power decreases abruptly	Power is delivered continuously but decremented significantly for a short time when resistance increases rapidly
Electrode type	Simple and multiple cooled electrode	Wet or wet-expandable electrode	Plain or expandable electrode	Simple or multiple bipolar electrode

system, which was based on cooled-expandable electrodes with coiled-shape tines. However, these systems are no commercially longer available.

In Table 3.1, it is presented a summary of the technical specifications of the current commercial solutions. A brief description on these RF ablations systems will now be introduced.

3.4.1 Covidien – Cool-tip^{TM} RF Ablation System

The *Cool-tip^{TM} RF ablation system* from *Covidien* (Figure 3.26) consists of a RF power generator and a peristaltic perfusion pump unit. It operates with simple or multiple cooled electrodes (Figure 3.13d and Figure 3.23b), using chilled water as coolant fluid.

The RF power generator provides a maximum current of 2 A, for maximum output power of 200 W, at 480 kHz [Cov09, Cov12]. During RF ablation, the RF generator monitors the electrical impedance of the tissue. The output power is adjusted to avoid insulation of the electrode due to a steep increment of the impedance. It is usual to set the output power to its maximum value during a predetermined period (usually no more than 15 minutes). As soon as the impedance grows abruptly, the generator turns off for a short period to facilitate tissue cooling and rehydration, as well as, to allow the dissipation of gas formed between the electrode and the adjacent tissue. This way, when the RF generator switches back on, it can deliver more power into the tissue, minimizing the treatment duration and producing larger lesions [ABLG11, GSG^{+}99, NMM^{+}05]. In case the electrical impedance exceeds 999 Ω, the RF generator turns off and emits an error message.

Figure 3.26: Cool-tip^{TM} RF ablation system – power generator and perfusion unit

The internally monopolar cooled electrodes present a small calibre: they are based on a 17 gauge trocar[12] which allows an easy percutaneous insertion. As already mentioned, there are available single-shafted electrodes, with exposed tips varying from 0.7 to 3 cm length, and multiple electrode systems with 3 electrodes for mono-focal applications, with exposed tips of 3 or 4 cm length. The electrodes have a thermocouple planted in the tip that is used to monitor the temperature during the RF ablation.

There is also available a switching controller unit that allows to operate up to three electrodes in switching mode, which can be used for mono-focal or multi-focal RF procedures.

3.4.2 AngioDynamics – StarBurst Radiofrequency Ablation System

The *StarBurst*© *Radiofrequency Ablation System* consists of the RF generator 1500X (Figure 3.27a), formerly known as RITA 1500X, that operates with the expandable electrode family StarBurst© (Figure 3.13b) [Ang, Ang12]. Besides the RF generator, there is also available a peristaltic infusion pump unit for using with wet-expandable electrodes.

The RF generator provides a maximum output power of 250 W, at 460 kHz, within an impedance range of 40–60 Ω, decrementing with impedance for values above this range (Figure 3.27b). The RF generator switches off when the impedance reaches

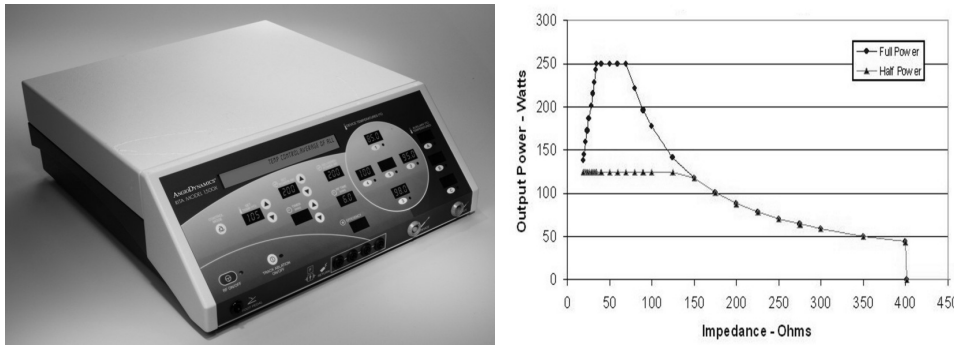

(a) (b)

Figure 3.27: StarBurst© Radiofrequency Ablation System. (a) Model 1500X RF generator; (b) Output power vs. load impedance. It is shown how the output voltage drops outside the impedance range of 40–60Ω (from [Ang]).

[12]Trocar – surgical instrument with a three-sided sharply pointed end, that is used enclosed in a tube. Commonly used for withdrawing fluids from a body cavity or to introduce ports in the abdomen, e.g., during laparoscopic surgery.

Figure 3.28: RF 3000© Radiofrequency Power Generator

200 Ω. In the *automatic temperature control mode*, the power delivery is automatically controlled based on the average of the temperature readings from the electrode, which has a temperature sensor placed in each prong [MNM+03]. This operating mode rises and maintains the tissue temperature according to a target value previously set by the operator [Ang]. This operating mode works effectively with the expandable electrode used in this system because of the dispersion in current density and large electrode surface area [ALW+02].

The StarBurst© electrode family is an extensive set of monopolar electrode models which includes expandable and wet-expandable electrodes on a 14 gauge trocar, with 4 or 9 prongs. When fully deployed, these electrodes resemble the configuration of a Christmas tree with a diameter up to 5 cm. These electrodes allow to produce scalable ablations, i.e., the electrode prongs are expanded progressively during the RF ablation procedure in order to achieve a more regular induced lesions [Ang10a, Ang10b, Ang10c, Ang10d, PTS+04].

Finally, there is also available a plain electrode on a 17 gauge cannula, with a scalable exposed tip from 1 to 2.5 cm [Ang10e].

3.4.3 Boston Scientific – RF 3000 Radiofrequency Ablation System

The *RF 3000© Radiofrequency Ablation System* from *Boston Scientific* is based on the RF 3000 power generator (Figure 3.28) that operates with the LeVeen electrode family (Figure 3.13a). The power output of the RF generator is defined manually by the user up to a maximum value of 200 W at an operating frequency of 461 kHz. Maximum output power is achieved if the tissue impedance measured by the RF generator is between 25 and 100 Ω. Outside this impedance range, the maximum output decreases with impedance. The RF generator switches off if the tissue impedance goes higher

than 400 Ω. Same thing occurs if the impedance drops below 15 Ω. Besides these maximum output power restrictions, neither impedance or temperature are taken into account for controlling the power delivered to the tissue [Bos, Bos12].

During operation, initial power is increased in small steps to a maximum value, and the treatment goes during a pre-set time defined by the operator, unless there is an abrupt decrement of the power output due to insulation of the RF electrode. In this case, the generator switches to a stand-by mode. RF ablation will only resume by external action of the operator [Bos, MNM+03].

The LeVee electrode family is a set of monopolar expandable electrodes with 10 to 14 prongs. Once the electrode is fully deployed, it resembles an umbrella with a diameter that can vary from 2 to 5 cm, depending on the model [Bos06a, Bos06b]. Unlike the expandable electrodes from AngioDynamics, LeVee electrodes are fully expanded before performing RF ablation.

3.4.4 Olympus – CelonPOWER System

The *CelonPOWER System* from *Olympus* is perhaps the less referred RF ablation commercial system in literature, but it is also the only one that proposes a solution based on bipolar electrodes. It comprises a RF power generator and a peristaltic pump unit used for injecting a chilled saline solution into the internal cooling circuit of the electrodes (Figure 3.29).

The power generator is able to supply a maximum output power of 250 W at 470 kHz. Contrary to other RF generators, the power output is automatically feedback-controlled by measuring the electrical resistance of the tissue instead of the im-

Figure 3.29: CelonPOWER System

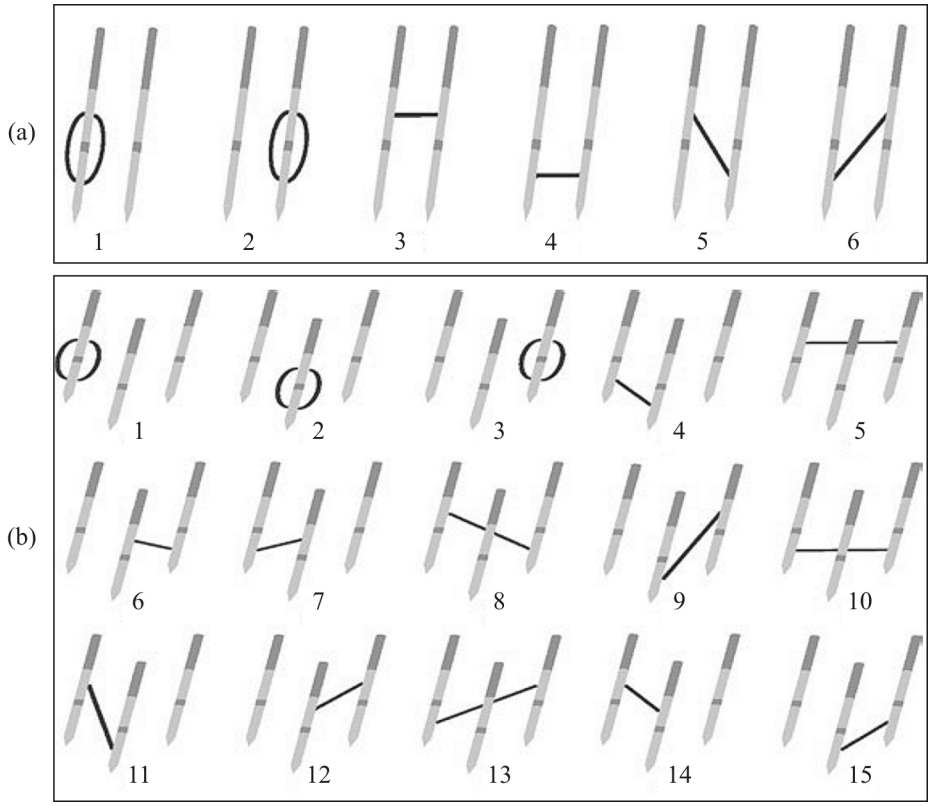

Figure 3.30: Multi-polar mode with CelonPOWER System: possible electrode couples and path of electric current between the electrodes. Possible combinations considering (a) two bipolar electrodes; (b) three bipolar electrodes (from [HVW$^+$06b], with permissions)

pedance, according to a protocol designated *Resistance Controlled Automatic Power* [Cel, Cel05a, HVW$^+$06a, HVW$^+$06b]. The advantage of measuring the electric resistance is that the length of the cables and type of electrode have no impact on the measurement value [HVW$^+$06a]. When activated, the RF generator delivers an output power according to a pre-set value defined by the operator. During the RF ablation procedure, the generator is continuously measuring the resistance of the tissue and, if it increases rapidly, the generator decrements automatic and significantly the output power. As soon as the resistance drops to normal values, the output power is restored to its pre-set value [HVW$^+$06b].

The RF generator allows the connection up to 3 bipolar electrodes that are detected automatically. The operation mode of the RF generator will depend on the number of probes that are attached to it. When only one probe is connected, the RF generator operates in bipolar mode: the current flows between the two electrodes of the

probe. When there are two or three probes connected, in this case the RF generator operates in multi-polar mode. In this case, the RF generator switches among every possible electrode pair, one after another, activating each pair during 2 seconds. This way, the current flows through the tissue between each pair of probes, as depicted in Figure 3.30. When 2 probes are connected, there are 6 combinations of electrodes (Figure 3.30a). The number of combinations goes up to 15 combinations when using 3 probes (Figure 3.30b) [HVW$^+$06a, HVW$^+$06b].

In multi-polar mode, the RF output is somewhat similar to the previous description. The electric resistance is measured between each pair of active electrodes. When the electric resistance increases significantly, output power is reduced and maintained until switching to the next pair of electrodes. The new pair is once again operated at the pre-set output power until an intervention by the power control algorithm due to an increase in resistance, or the system switched to the next pair of electrodes.

Finally, the CelonProSurge is an extensive family of bipolar electrodes. These electrodes are presented with three different diameters 18 gauge (1.3 mm), 15 gauge (1.8 mm) and 3.3 mm (non-standard gauge dimension). The 18 gauge electrode is commonly used for small volume RF ablations, e.g., for the treatment of osteoid osteomas or facet articulation pain. Larger volume lesions are obtained with the 15 gauge electrode. The 3.3 mm probe is recommended for open surgery procedures. Olympus claims that its larger active surface reduces the time of application on 25% when compared with the 15 gauge probe [Cel05b]. However, there is no reference to this fact in the scientific literature. The length of the active tip of these electrode varies from 9 to 40 mm (sum of the lenghts of the electrodes, insulator and tip).

CHAPTER 4

Preliminary Experimental Tests

...experiment is nothing else than a mode of cooking the facts for the sake of exemplifying the law.
Alfred Whitehead

4.1 Introduction

In this chapter, it is described and discussed the preliminary experimental work performed during the present work. From the obtained results, it was intended:

- To verify whether it is possible to use a commercial self-expandable metallic stent as a potential electrode for RF ablation of tumours located in tubular organs, such as colon or bile duct;
- To test a practical procedure for deploying the stent in place for RF ablation and connecting it to the RF power generator;
- To validate the numerical model to be used in subsequent simulations of the present investigation.

From the numerical and experimental results obtained, it can be observed that it is possible to achieve regular volume lesions using a stent-based electrode. Also, numerical results are in strong agreement with those obtained by experimentation, thus providing a useful tool for the study of the methodology proposed in this work. Finally, the electrical connector proposed for linking the electrode to the RF power generator revealed a good performance, indicating the this is also a solution to be considered in future work.

4.2 Preliminary Set-up

4.2.1 Description

Preliminary work was performed to verify if it was possible to heat biological tissue with a tubular electrode. There were used samples of porcine liver and bovine liver that were acquired from a local butcher. For each liver sample, a hole was made in which the electrode was placed.

Two different electrodes were used: a simple copper tube with a diameter of 12 mm and a length of 30 mm, and a nitinol self-expandable stent with the same dimensions of the copper tube. These electrodes were connected to a RF power generator from Covidien [Val04] through a wire obtained after dismounting one of the cooled electrodes commonly used with the RF generator. The wired was welded at a single point of the electrode (Figure 4.1). For each trial, the electrode was placed in the hole made in the each liver, and the liver sample was placed on a grounding pad.

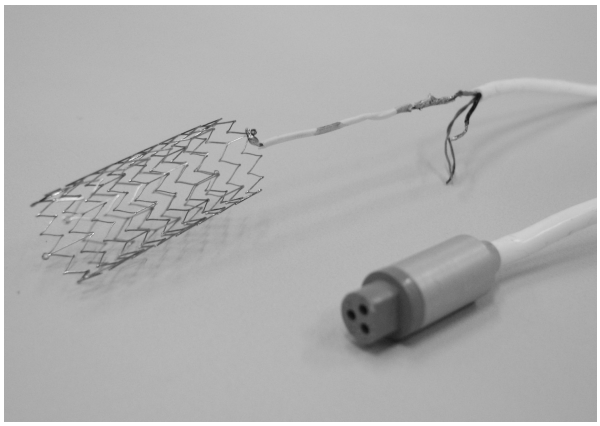

Figure 4.1: Preliminary stent-based electrode. A vascular stent from *Cook* with 12 mm diameter and 30 mm long. The electrode is welded in a single point to a connector obtained from a original cooled electrode commonly used with the RF generator.

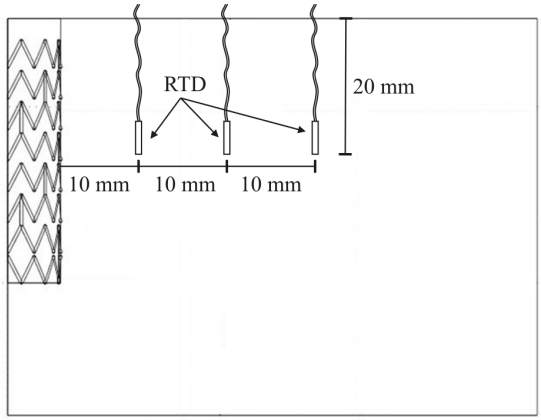

Figure 4.2: Location of the RTDs. The temperature probes were placed 1 cm away from each other, along a line that is perpendicular at the midpoint of the stent axis. The first electrode was placed 1 cm away from the stent.

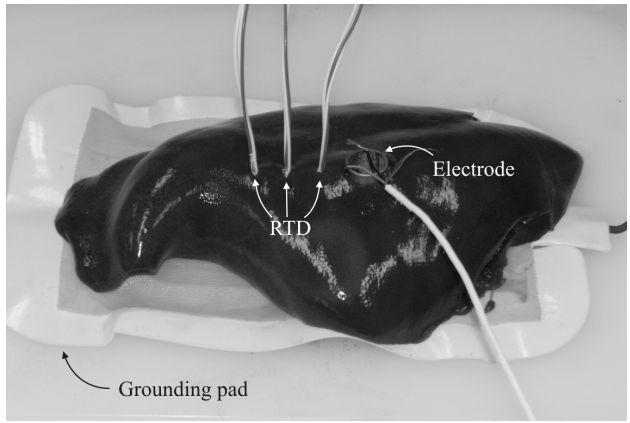

Figure 4.3: Set-up for the preliminary experimentation work. One of the first set-ups implemented to study the possibility of using a stent as an RF ablation electrode. A porcine liver placed on a grounding pad with a tubular copper electrode placed in the thicker part of the liver as well as three RTDs for temperature reading.

Three resistance temperature detectors (RTD) were used as temperature sensors. They were placed along a line that is perpendicular at the midpoint of the stent axis, and each sensor distances 1 cm from each other. The first temperature sensor was placed 1 cm away from the stent (Figure 4.2). Next, the RTDs were connected to a National Instruments NI-USB-9219 acquisition board. Data was recorded and saved on a laptop using LabVIEW Signal Express software. Also, values of voltage, current intensity, power and impedance measured by the RF generator were recorded. In

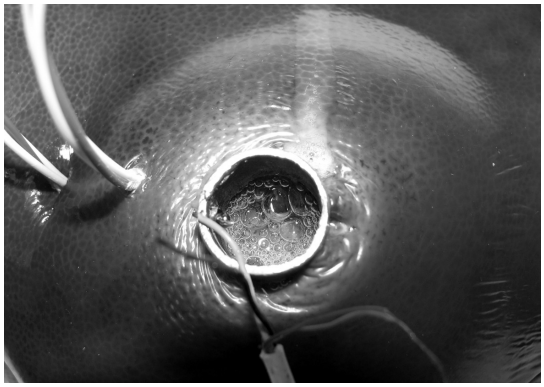

Figure 4.4: Tissue dehydration during RF ablation procedure. The tissue around the electrode swells while is being heat, releasing water content that fills the hollow space of the electrode.

Figure 4.3, it is presented one of the typical set-ups used along the experimental tests performed. Particularly in this figure, it is presented one of the first set-ups used with the copper tubular electrode. The test was performed on a porcine liver that was placed on a grounding pad. On top of the liver, there were made 4 incisions, three small ones to place the RTDs, and a larger one to place the electrode. The electrode was placed on thicker part of the liver.

4.2.2 Results

Copper Tube Electrode

The first trials were performed using a simple copper tube that was used as an electrode (Figure 4.3). The generator was set for a RF ablation period of 10 minutes with an output voltage of 40 V (1 A). As the tissue was being heated, it could be observed tissue swelling in the volume around the electrode, while the hollow space where the electrode was placed was being filled with water from the destroyed cells adjacent to the electrode (Figure 4.4).

After almost 7 minutes, temperature reaches approximately 60°C at 1 cm from the electrode, which corresponds to a value at which immediate cellular death can result. In Figure 4.5, it is presented the temperature reading at each RTD sensor during the experiment. As expected, the closer to the electrode, the higher the temperature reading. At 1 cm from the electrode, the temperature rises considerably much faster than at 2 cm or 3 cm. After the generator turned off, $t = 600$ s, it can be observed that the temperature obtained at 1 cm decreases almost immediately. On the other

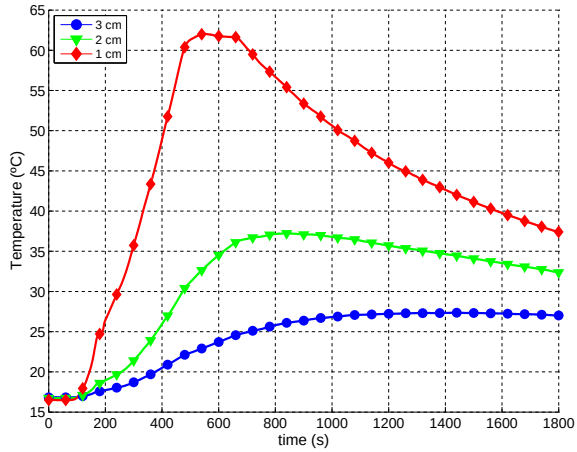

Figure 4.5: Temperature readings using a copper tube electrode for an applied voltage of 40 V. The RF power generator switches off after 10 minutes. Temperatures at 2 and 3 cm still increase after it due to conductive heating.

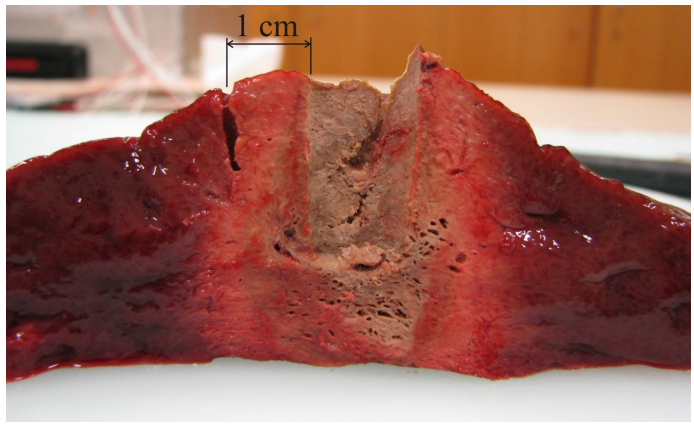

Figure 4.6: Longitudinal section of the lesion induced with a tubular copper electrode. It can be observed that the tissue is totally destroyed within 1 cm from the electrode.

hand, temperatures at 2 and 3 cm from the electrode still increase for a while due to conductive heating from the centre to the peripheral tissue.

It is shown in Figure 4.6 a longitudinal section of the liver along the axis of the electrode. By visual analysis, it is possible to observe that all tissue within 1 cm away from the electrode was destroyed. Farther from the electrode, between 1 to 2 cm away from it, it can be observed some denaturation of the tissue (the tissue is slightly lighter). At 2 cm, the temperature does not reach 40°C, so from this point it cannot be induced any lesion to the tissue. Also, it can be noticed from Figure 4.6 that the

tissue below the active electrode is destroyed. This is because the liver was placed on the grounding pad, so the active and grounding electrodes were close to each other, which explains this particular geometry of the induced lesion.

Stent-Based Electrode

In the experiments involving the stent-based electrode, it was considered two different conditions concerning the applied RF voltage: a varying step-like voltage and a constant voltage.

It is shown in Figure 4.7 the temperature readings obtained during a RF ablation for an applied voltage given by:

$$V(t) = \begin{cases} 26 & \text{for } t \in [0, 210[\\ 55 & \text{for } t \in [210, 655] \end{cases} \quad [\text{V}] \tag{4.1}$$

where time, t, is expressed in seconds.

When the applied voltage increases from 26 to 55 V, it can be observed that temperature grows much faster at 1 cm from the RF ablation electrode than at longer distances, which evinces that tissue heating at 2 and 3 cm from the electrode is mainly by conductive heating than Joule heating.

Additionally, in Figures 4.8 and 4.9 are presented the results for an applied constant voltage of 50 and 75 V, respectively. In the first case, the RF ablation procedure took about 6.5 minutes (400 seconds), and about 3.5 minutes (220s) at 75 V. In the

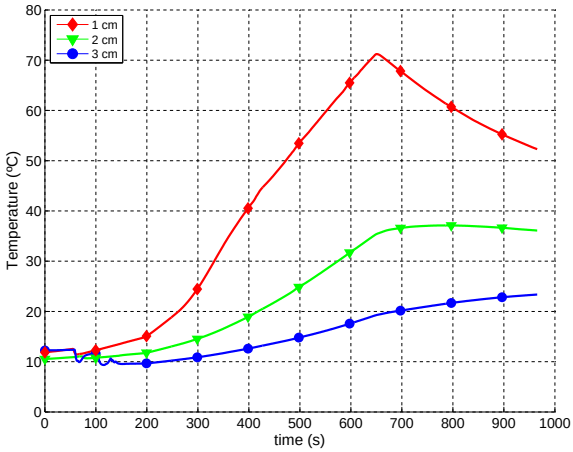

Figure 4.7: Temperature readings using the stent-based electrode for a step-like voltage varying from 26 to 55 V (at $t = 210$s). The RF power generator switches off at $t = 655$s.

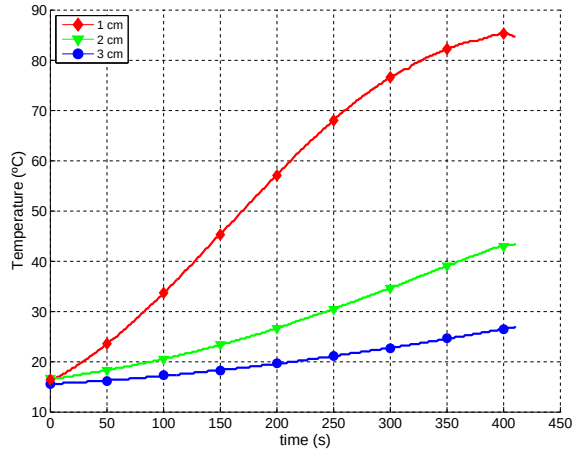

Figure 4.8: Temperature readings using the stent-based electrode for an applied voltage of 50 V.

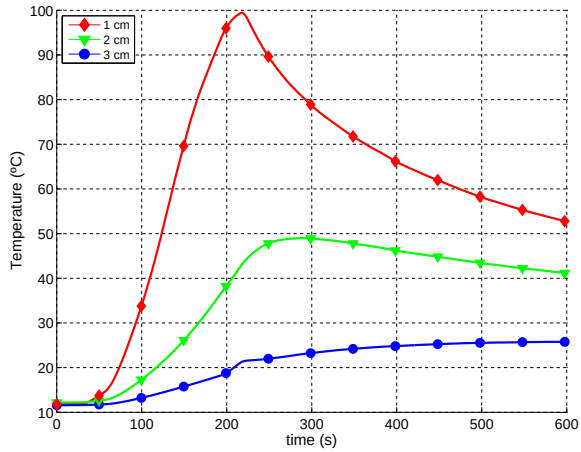

Figure 4.9: Temperature readings using the stent-based electrode for an applied voltage of 75 V.

latter case, the RF power generator was shut off when the temperature measured at 1 cm from the stent reached 100°C.

In all the experiments performed, the tissue involving the stent-based electrode is heated properly in order to induce thermal necrosis. The temperature profile is very similar to the one obtained using the copper electrode, i.e., the temperature at 1 cm from the electrode is high enough to induced thermal necrosis. At farther distances, this is only achieved if the applied voltage is high enough. At 75 V, it is possible to achieve in a short time a temperature value to induced thermal necrosis at 2 cm from

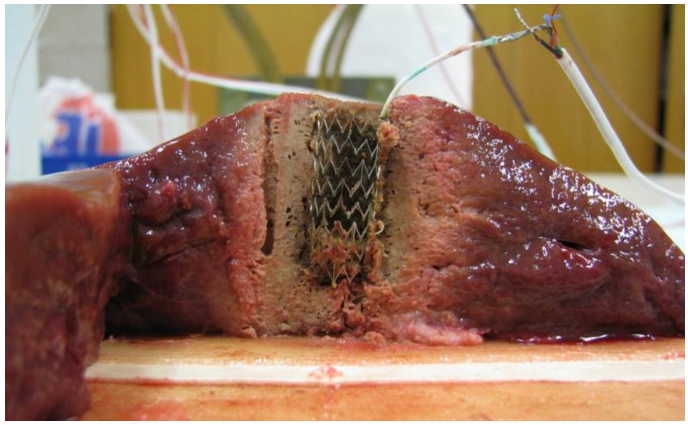

Figure 4.10: Longitudinal section of the lesion induced with the stent-based for an applied voltage of 50 V. It can be observed that the lesion induced is similar to the one obtained using the tubular copper electrode.

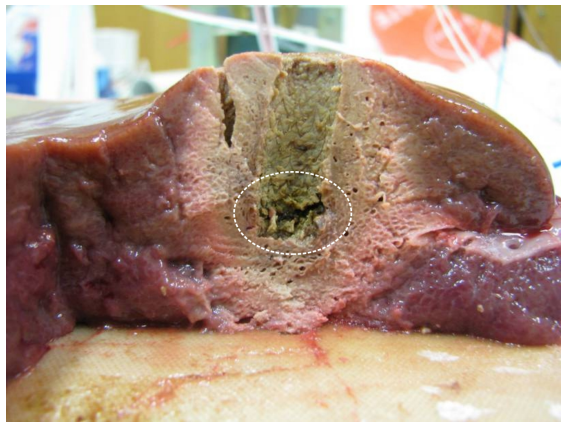

Figure 4.11: Longitudinal section of the lesion induced with the stent-based for an applied voltage of 75 V. The tissue adjacent to the bottom side of the electrode shows signs of some carbonization (dashed line).

the electrode. However, the tissue adjacent to the electrode is heated excessively thus insulating the electrode due to charring and gas formation.

In Figures 4.10 and 4.11, it is presented the longitudinal section of the induced lesion at 50 and 75 V, respectively. It can be observed that the obtained lesions resemble the one obtained with the tubular copper electrode. At 75 V (Figure 4.11), it can be noticed that the adjacent tissue at the bottom side of the electrode presents some signs of carbonization (delimited with the dashed line). In this case, the current driven by the RF generator reached its maximum value (2 A), delivering 100 W during the whole procedure (Figure 4.12c). From Figure 4.12a, it can be observed that

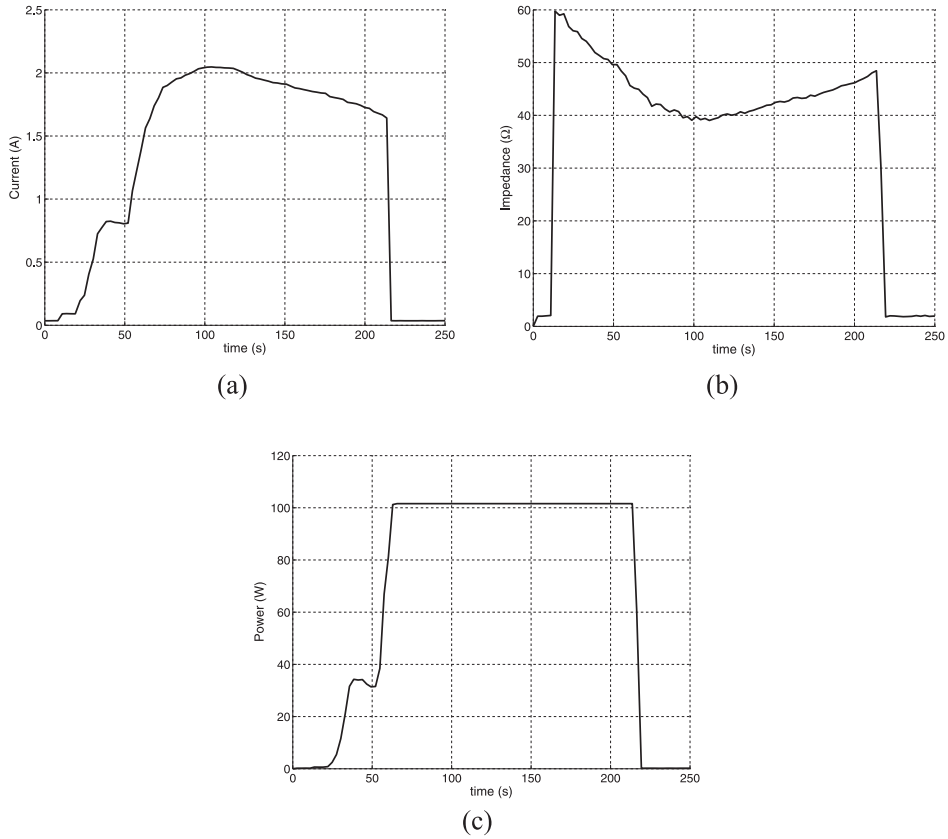

Figure 4.12: (a) Current intensity, (b) impedance and (c) power delivered to the tissue during a RF ablation at an applied voltage of 75 V. Power and current intensity increase up to the maximum values allowed by the RF power generator. Later, the current intensity decreases as the impedance at the electrode rises.

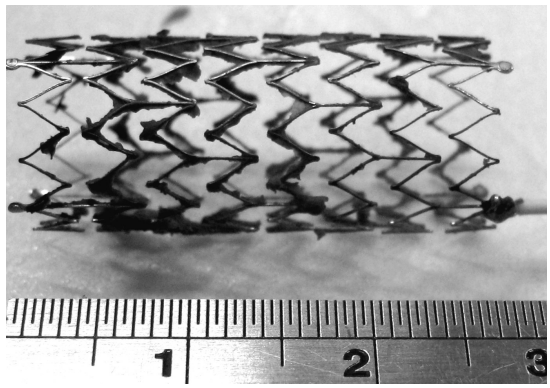

Figure 4.13: Stent-based electrode condition after the set of experimental tests. It did not present any detectable change or mechanical deformation.

the electric current decreases almost linearly after 100 s: the tissue adjacent to the electrode starts to dehydrate, as well as some gas formation occurs, which increases the tissue impedance (Figure 4.12b).

Finally, Figure 4.13 presents the stent-based electrode after being used in the experiments performed. At the end, it did not show any change or mechanical deformation, at least visible at bare eye. In fact, the stent was used repeatedly without any problem. The only significant issue verified was that removing the stent at the end of the RF ablation proved to be difficult. The biological tissue models to the stent mesh and, during the RF ablation procedure, it adheres to the electrode, which makes difficult to remove it after from the tissue.

4.3 Numerical Simulation

4.3.1 Theoretical Model

The numerical analysis of the experimental procedure so far performed consists of a coupled thermal electrical analysis. The temperature at each point of the tissue can be expressed by the bioheat equation presented in section 2.3.2. Nevertheless, Equation (2.31) must also take into account the energy deposition delivered by the electrode. Considering this, the temperature at the tissue is given by:

$$\rho c_p \frac{\partial T}{\partial t} = \nabla \cdot k \nabla T - \omega_b c_b (T - T_b) + Q_m + q \tag{4.2}$$

The term Q_m can be neglected because the heat generated by the tissue metabolism is very small compared with the term q, which corresponds to the energy deposition delivered by the RF ablation electrode [CN04, HCW+03, Lab94b]. In fact, because the experiments were carried out in *ex vivo* samples, the term Q_m is equal to zero. For the same reason, the term associated to convective heat transfer due to blood perfusion, $\omega_b c_b (T - T_b)$, is also considered equal to zero.

At the frequency of 470 kHz, the operating frequency of the RF power generator used during the experimental tests, and over the distance at which the energy is deposited around the electrode, the tissue can be considered totally resistive. The RF ablation electrode dissipates most of the energy through electrical conduction and not capacitive coupling; thus, the capacitive nature of the tissue can be neglected. In this case, it can be assumed a *quasi-static* electrical conduction model, i.e, the electric current and electric field behave, at any time, as if they were sta-

tionary [BH04, Cha03, Lab92, PH67]. Hence, the distributed heat source q in Equation (4.2), which represents the Joule loss due to the electric current flowing through the tissue, is given by:

$$q = \mathbf{E} \cdot \mathbf{J} \tag{4.3}$$

where $\mathbf{E}$ is the electric field intensity [V/m], and $\mathbf{J}$ is the current density [A/m^2]. These values can be evaluated using Laplace's equation:

$$\nabla \cdot [\sigma(T) \nabla V] = 0 \tag{4.4}$$

where ∇ is the gradient operator, expressed in Equation (2.32), $\sigma(T)$ is the temperature-dependent electrical conductivity [S/m], and V is the electric potential [V].

To determine the temperature distribution on the tissue, one must first solve Equation (4.4) in order to obtain the voltage through the domain of analysis. The distributed heat source q is next calculated by Equation (4.3), which can rewritten as:

$$q = \sigma(T) \cdot (\nabla V)^2 \tag{4.5}$$

which is Joule's Law in differential form. From this result, Equation (4.2) is next solved for the temperature distribution in the tissue.

4.3.2 Description of the Model

Numerical simulation was performed only for the stent-based electrode considered in the preliminary experimental work. The proposed model consists of a cylindrical bulk with radius of 60 mm and height of 45 mm, which represents the liver tissue. The RF ablation electrode was placed at the centre of this cylinder, at a height of 15 mm from its bottom base. Finally, a second cylinder with 12 mm of diameter was placed at the lower end of the electrode. The upper base of this cylinder is coplanar with the upper base of the outer cylinder. This minor cylinder represents the incision where the stent-based electrode is inserted into the liver and is filled with air (Figure 4.14).

Finally, the RF electrode model is a replica of the *Cook* vascular self-expandable metallic stent used in the experimental work, with a diameter of 12 mm and length of 30 mm.

4.3.3 Physical Properties and Boundary Conditions

The physical properties of the materials required for solving the proposed model were obtained from the literature [HST+01] and are summarized in Table 4.1. In this initial approach, all properties were considered temperature independent.

The values of the initial conditions were chosen so as to reproduce the verified conditions during the experimental work. The initial temperature of the liver was set to 11°C or 16°C, according to the temperature measured in the tissue samples. The outer boundaries of the model correspond to Dirichlet boundaries, and they were set to a constant temperature of 17°C, the room temperature. All these values were obtained at the time of each experiment. During the experimental work, the liver samples were placed on a high density expanded polystyrene board. Because of that, the bottom base of the outer cylinder was considered as a Neumann boundary, i.e., no heat flows through this boundary.

Regarding the boundary conditions associated to the electric part of the problem, the bottom base of the outer cylinder was considered as the grounding plane (0 V). The remainder outer boundaries of the model were considered Neumann boundaries. The model was solved observing the electrode as a Dirichlet boundary with fixed voltages of 50 and 75 V, as well as the step-like voltage expressed in Equation (4.1), in order to simulate all the situations tested experimentally.

For solving every numerical model, it was used the solver PARDISO implemented in the commercial finite element analysis software COMSOL Multiphysics 3.5a (COMSOL, Inc. Burlington, MA, USA). The stent model was created in AutoCAD (Autodesk, Mill Valley, California, USA) and exported in 3D ACIS format to COMSOL. Also, it was only modelled a quarter of the whole model, due to the symmetry of the problem to be solved (Figure 4.14). The model consisted of 133 418 tetrahedral elements, and it was solved on a PC computer with Intel Core 2 Quad CPU @2.34Ghz, 8GB of RAM, on a 64 bits platform.

Table 4.1: Material properties used in the numerical simulation of the preliminary stent-based electrode (from [HST+01]).

Element	**Material**	ρ [kg/m^3]	c [J/kg·K]	k [W/m·K]	σ [S/m]
Electrode	Nitinol	6450	840	18	$1 \cdot 10^8$
Hole	Air	1.202	1	0.025	0
Tissue	Liver	1060	3600	0.512	0.333

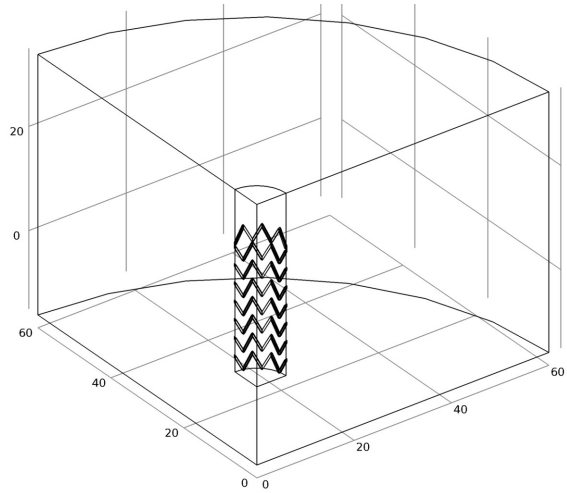

Figure 4.14: Proposed model for simulation of the preliminary experimental set-up. Taking into account the symmetry of the problem, it was considered only a quarter of the model.

The numerical models were solved for the time intervals during which the RF power generator was connected. The cooling down of the liver tissue after turning off the power generator was not considered during simulations.

4.3.4 Numerical Results

In order to compare the numerical and experimental data, the values of the temperature at 1, 2 and 3 cm from the stent-based electrode were obtained from the solved models, considering the same locations used for the temperature probes during the experimental work (Figure 4.2). Figures 4.15, 4.16 and 4.17 present the graphics of the values obtained both numerical and experimentally versus time (experimental data represented by dashed lines).

The temperatures obtained after numerical simulation agree in some extension with the experimental data although some divergence is clear in Figure 4.15, which represents the numerical simulation of the step-like applied voltage described in Equation (4.1). For the cases of applied constant voltages, numerical and experimental data are closer. Still, the values obtained deviate as temperature increase, particularly for the temperatures readings at 1 cm from the electrode. This fact turns evident the temperature dependence of the material properties, which was not taken into account in this first approach.

Albeit these differences, when comparing the induced lesion obtained experimentally with the volume delimited by a 50°C isothermal curve (the temperature value

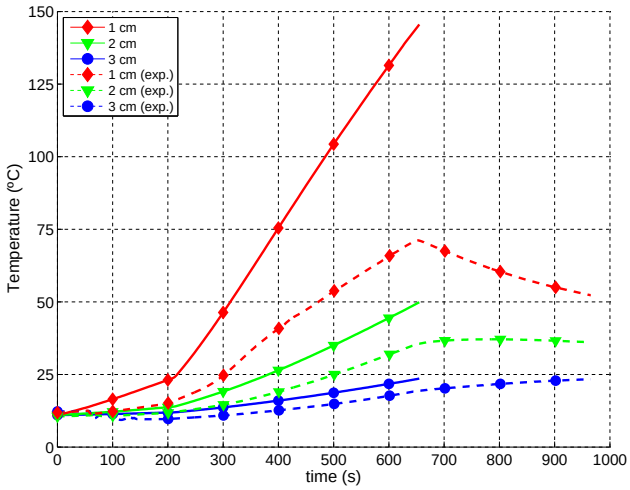

Figure 4.15: Temperatures values obtained after simulation of the step-like applied voltage described in Equation (4.1). Experimental results are also depicted, represented in dashed lines.

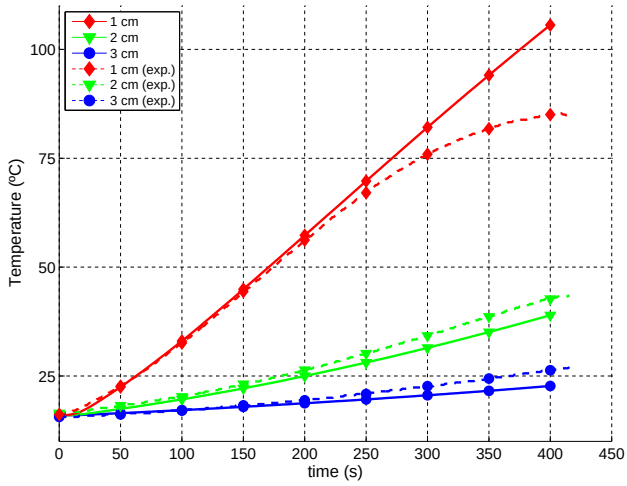

Figure 4.16: Temperatures values obtained after simulation an applied voltage of 50 V. Experimental results are also depicted, represented in dashed lines.

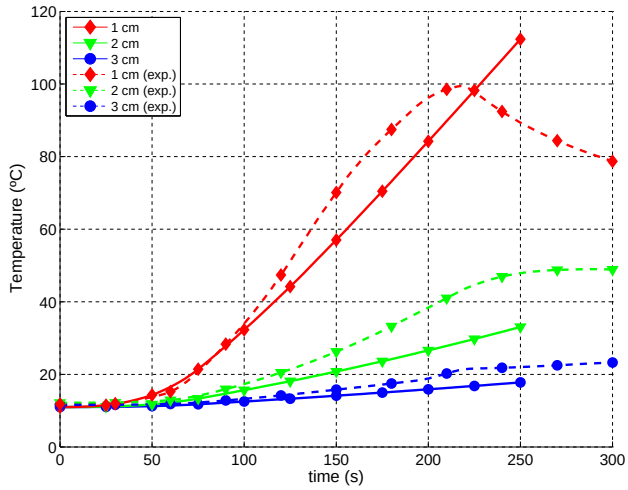

Figure 4.17: Temperatures values obtained after simulation an applied voltage of 75 V. Experimental results are also depicted, represented in dashed lines.

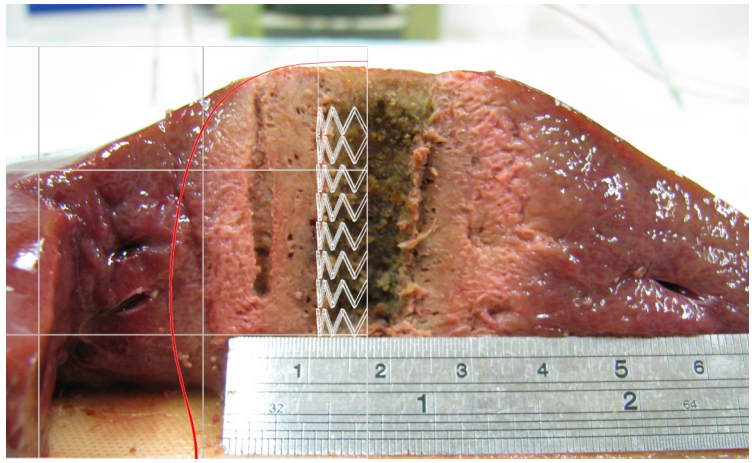

Figure 4.18: Longitudinal section of an induced thermal lesion obtained for an applied voltage of 50 V after 395 s. A 50°C isothermal curve obtained after numerical simulation is overlapped (red curve).

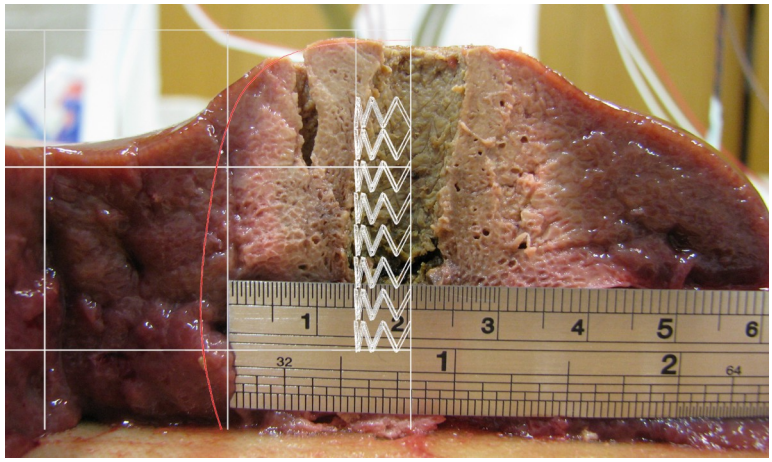

Figure 4.19: Longitudinal section of an induced thermal lesion obtained for an applied voltage of 75 V after 220 s. A 50°C isothermal curve obtained after numerical simulation is overlapped (red curve).

from which thermal necrosis occurs rapidly, as described in section 3.2.2), it can be observed that both volumes are similar. It is shown in Figure 4.18 the longitudinal section of the induced lesions obtained for an applied voltage of 50 V. The 50°C isothermal curve obtained after solving the corresponding numerical model overlaps the experimental result. It can be observed that both areas are similar, with the numerical solution somewhat wider than the experimental induced lesion. Similar result can be observed for an applied voltage of 75 V, presented in Figure 4.19.

4.4 Connecting the Electrode to the RF Generator Through a Forceps

At this point, it is clear that using a stent as a RF ablation electrode can be regarded as a feasible solution. However, in order to place and deploy the self-expandable metallic stent in the right location, it becomes necessary to provide a method or a device that allows the electrical connection of the electrode to the RF power generator.

A wire directly soldered to the stent arises some complications. Because the stent adheres to the tissue after the RF ablation procedure, the removal of it and/or the wire can be a difficult task. A straightforward solution consists of inserting the stent by a conventional procedure and connecting it to the RF generator through a third device. In this work, it is proposed to use a biopsy forceps to establish a link between the electrode and the power generator.

For the following study, it was considered a BIPAL biopsy forceps from Cordis (Bridgewater Township, New Jersey, USA), commonly used for endomyocardial biopsies. It consists of a 3-pull ring handle, stainless steel cutting jaws, and a coiled shaft (Figures 4.20 and 4.21). A spring in the handle keeps the cutting jaws closed. The movement of the forceps' jaws is commanded by moving the double rings away or toward the thumb ring (Figure 4.20a), which will open or close the jaws, respectively.

The thumb ring is attached to a metallic shaft that operates the cutting jaws when the handle rings are operated. A small modification in the handle provided an electrical connection to the RF power generator. Similarly to what was done with the initial stent-based electrode, the connecting wire of a cooled electrode commonly used with the Coviden RF power generator was soldered to the forceps' shaft, electrically connecting the jaws to the power generator (Figure 4.20b). With this modification, it turns possible to place and deploy the stent by conventional methods and connect it to the RF power generator by clamping the jaws on the proximal end of the stent (Figure 4.21).

For testing this solution, it was performed a series of RF ablation procedures with applied voltages of 50 and 100 V. The maximum applied voltage was considered so to test the worst case condition to which the set stent plus forceps can be submitted. There were two main interests from the results of these experiments: to test if the forceps, with the minor modification that was introduced, could withstand the electric current, and to verify if the electrical contact between the stent and the forceps would not be compromised during the RF ablation procedure.

The results after the tests are very similar to those presented in the previous section: regular, well-defined lesions, reaching a radius of 2 cm when applying a voltage of 100 V. The maximum current density varied from 0.3 to 1.6 A and in any case it was noticed any malfunction of the whole set, even in extreme situations. It is shown in Figure 4.22 the current and impedance measured during a RF ablation at an applied voltage of 100 V. In this test, it was decided to let the experiment run until the RF power generator shut off due to electric insulation of the electrode. This was intended in order to check the endurance of the forceps. Similar to what it was observed in Figure 4.12, the impedance decreases during the RF ablation procedure until dehydration and charring occurs, insulating the electrode. After 900 seconds, the impedance grows steeply, and the RF generator turns off automatically.

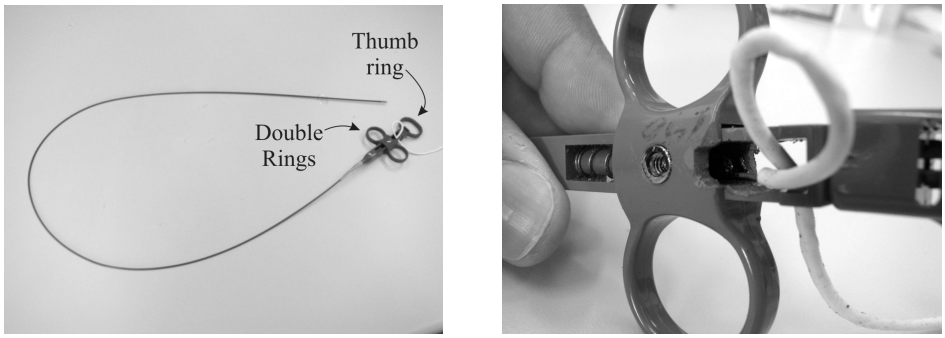

(a) (b)

Figure 4.20: (a) BI-PAL endoscopic biopsy forceps; (b) Detail of the electrical connection through the forceps's shaft.

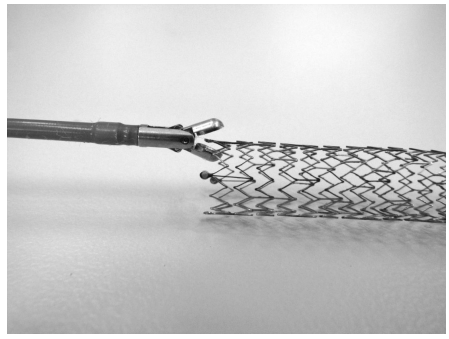

Figure 4.21: Attaching the biopsy forceps to the stent. After deploying the stent in the pretended location, the biopsy forceps are attached to the stent, clamping the forceps's jaws on the proximal end of the stent.

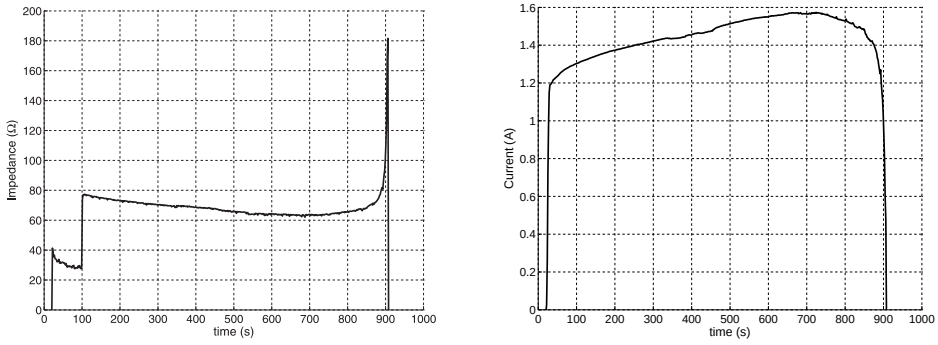

(a) (b)

Figure 4.22: (a) Impedance and (b) current values for an applied voltage of 100 V in a set-up using a biopsy forceps for electrical connection between the electrode and the RF power generator.

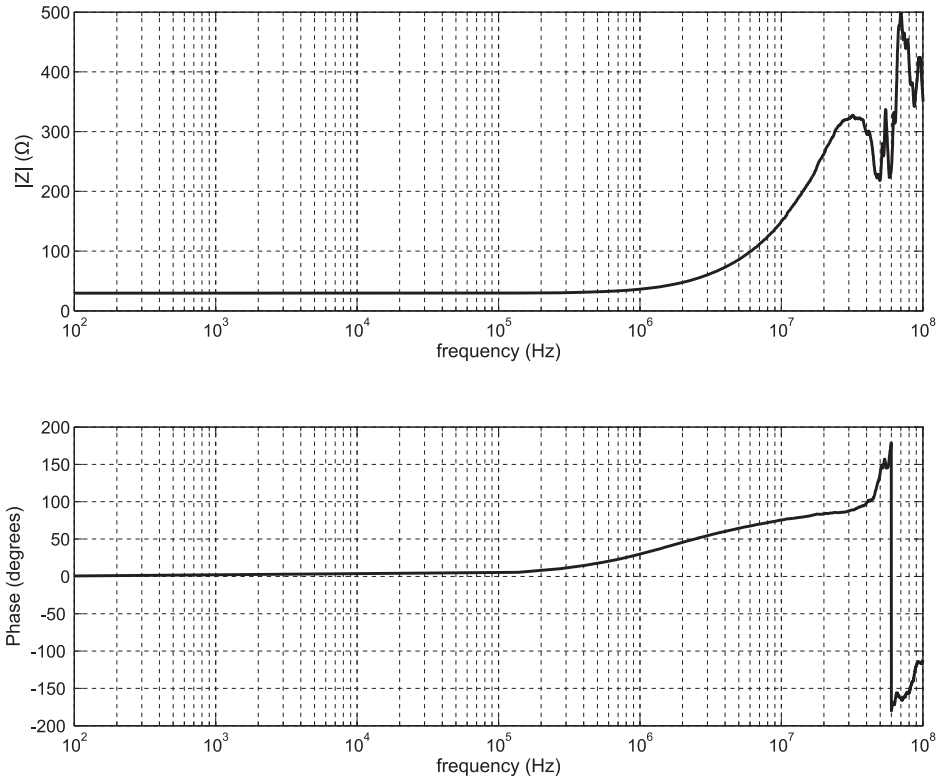

Figure 4.23: Electrical characterization of the biopsy forceps. Impedance values, magnitude and phase, obtained from 40 Hz to 110 MHz.

In any case, the biopsy forceps did not show, at the end of each performed test, any damage or deformation, temporary or permanent. Also, it did not heat excessively in any test. In the worst case-scenario tested, which results are presented in Figure 4.22, the forceps were slightly warm (evaluated by contact with hand). The forceps was used repeatedly, without any problem, although this type of equipment is commonly used once.

Finally, it was observed that attaching the forceps in series with the electric circuit did not significantly alter the impedance measured by the RF power generator. From Figures 4.12 and 4.22, it can be verified that the initial value of impedance is very similar in both cases.

For a better insight about the influence of the forceps on the overall electric circuit, an Agilent 4294A impedance analyser was used to measure the impedance of the biopsy forceps used during the experiments. In Figure 4.23, it is presented the graphic of the impedance values, both magnitude and phase, measured throughout the test-

frequency range of the equipment, from 40 Hz to 110 MHz. From the data obtained, it can be observed that the impedance of the forceps presents a steady value from low frequency values to close to 1 Mhz. From this threshold, the impedance values increase. Once the present work is concerned with applications for RF ablation, the values above 1 Mhz were disregarded.

In the frequency range of 100 kHz–1 MHz, the magnitude of the forceps impedance ranges from 18 to 28 Ω, approximately. At 470 kHz, this value is about 20 Ω (the electric reactance is about 3 Ω, inductive). It was considered that electric impedance introduced by the forceps in the circuit is not significant, and so the forceps can be regarded as a practical solution for the electrical connection of the stent-based electrode to the RF power generator. Again, this is a solution made up from a commercial available forceps that was not design for driving any electric current, and most certainly a concept design considering this possibility will bring a more electrically efficient device.

4.5 Conclusions

In this chapter it was presented the preliminary experimental and numerical work carried out to verify the practicability of using a self-expandable metallic stent as a effective electrode for RF therapeutic treatment of tumours located in tubular organs. It was intended to evaluate if this endo-prosthesis, used as palliative method for mechanically reopening organs like colon or biliary ducts, can be considered for RF ablation treatments.

Experimental and numerical results show that the volume of tissue adjacent to the stent-based electrode is preferentially heated, although the numerical simulation presents larger temperatures and slightly larger lesion volumes. These differences can be explained by:

1. In the numerical simulations considered, electrical and thermal coefficients used were obtained from scientific references instead of measuring the effective values on the tissue samples used.

2. Dependency of electrical conductivity against temperature was not considered in the numerical simulations. Electrical conductivity is temperature (and time) dependent which is very significant near 100°C [Cha03].

3. In experimental work, the tissue heating process caused liquid evaporation and that reflects energy not used, which was not considered in the proposed numerical models.

Also, it was observed that the BIPAL biopsy forceps considered so far in this work can be used as electrical connector between the stent and the RF power generator. The tissue was again heated and destroyed in a regular way. Experimental results show that, even for high power conditions, the forceps did not present any kind of damage at the end of the experiments. It could even be reused after a large number of trials.

Finally, these initial experiments revealed satisfactory and very promising results on the application of a stent-based electrode for the treatment of tumours located in tubular organs.

CHAPTER 5

Characterization of the Induced Lesion

There never are any unsuccessful experiments: they are all successful in their own definite conditions, so that negatives cannot nullify positive results.

Claude Bernard

5.1 Objectives

In the previous chapter, it was verified that the proposed stent-based electrode can be regarded as a feasible active electrode for the RF ablation of tumours located in tubular organs. However, it is necessary to characterize the volume of the lesion that it is possible to achieve using this RF ablation electrode.

Thermal lesions were induced in bovine livers samples, and the volume of the obtained lesion was measured. Also, it was created a numerical model to simulate the experimental RF ablations. These models used the value of electric conductivity that was measured during the experimental work.

This chapter describes the experimental and numerical procedures that were taken into account in this analysis. It is intended to characterize the size of the lesion ob-

tained as a function of the applied voltage and duration of the RF ablation procedure. Also, it is intended to validate the numerical modelling of the stent-based electrode which will be used in the remaining presented work.

5.2 *Ex Vivo* Experimentation

5.2.1 Experimental Set-up

Experimental work was performed on bovine livers collected at a local slaughter house, approximately two hours after abating the animals. In each liver, a vertical hole with 8-9 mm of diameter was made in the centre of it for placing the electrode.

A biliary self-expandable metallic stent from Boston Scientific, with a diameter of 10 mm and a length of 40 mm (Figure 5.1), was used as RF ablation electrode. The stent was placed in the liver, and it was connected to the RF generator through a BIPAL endoscopic biopsy forceps, with the modifications presented in section 4.4. This way the electrode can be placed properly using a conventional percutaneous or endoscopic procedure, achieving the electrical connection to the RF generator by clamping the forceps' jaws on the proximal end of the stent.

Two RTD temperature sensors were placed at 1 and 2 cm of the RF ablation electrode. A National Instruments NI USB-9219 acquisition board was used to read the temperature sensors and the data was registered with LabVIEW SignalExpress software. Also, voltage, current intensity and electrical impedance measured by the RF generator were registered.

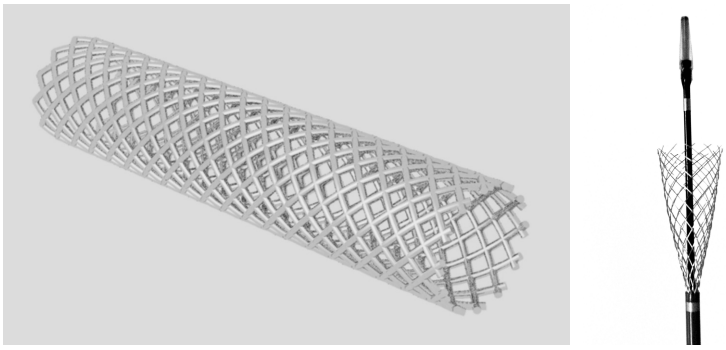

(a) (b)

Figure 5.1: (a) Wallflex biliary self-expandable metallic stent from Boston Scientific. (b) A detailed image of the stent in the endoscopic applicator.

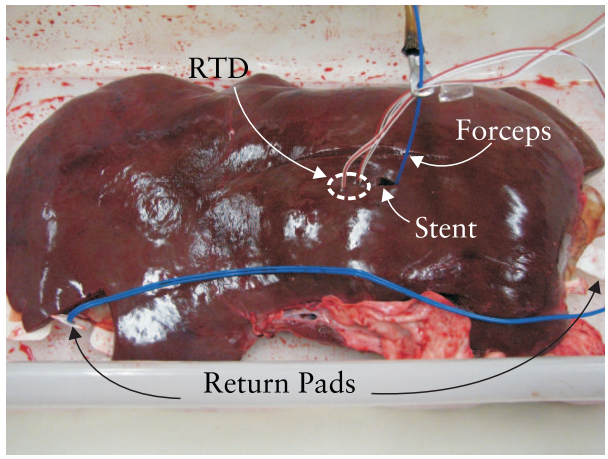

Figure 5.2: Experimental set-up used for characterize the size of the volume lesion obtained with the stent-based electrode. The electrode and temperature sensors are placed on the top of the thicker part of the liver. Grounding pads are placed at both ends of the liver to achieve a regular distribution of the electric current.

To obtain a current distribution around the electrode as symmetrical as possible, a return pad was placed at each end of the liver. The RF generator was set to impedance control mode. It is shown in Figure 5.2 one of the set-ups commonly used during the experimental tests performed in this study.

5.2.2 Measurement of the Electrical Conductivity

In order to reproduce numerically as close as possible results obtained during experimentation, it was measured the electrical conductivity in each liver sample used. The measurements were performed using the four-electrode method [TGS90], which is a method widely used to measure biological tissue impedance and resistivity [HST$^+$03, SBC$^+$04, SCM$^+$99].

Four-Electrode Method

The four-electrode method is a resistive method commonly used in the study of horizontal and vertical discontinuities and also in the detection of three-dimensional bodies of anomalous electrical conductivity [KBH02].

In resistive methods, a current is injected into the tissue through two electrodes connected to a proper power generator. The resulting potential distribution in the tissue is then mapped by means of two other electrodes, attaining this way information about the electrical resistivity.

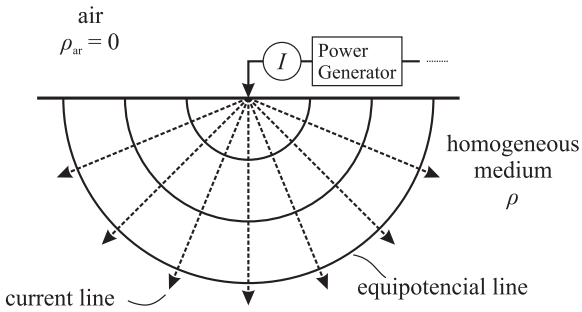

Figure 5.3: Equipotential and current lines due to an electrode placed on the surface of a homogeneous medium of electrical resistivity ρ

In Figure 5.3, it is presented a single electrode placed on the surface of a homogeneous medium. The air above the surface has zero electrical conductivity, and the electrode is connected to a power generator with a return electrode located far away, so its influence can be neglected. In this case, the electric potential at a radial distance r from the electrode can be expressed as [Rey97, TGS90]:

$$V = \frac{I\rho}{2\pi} \tag{5.1}$$

If the return electrode B is placed at a finite distance from the electrode A, the electric potential at C (Figure 5.4) is given by the sum of the contributions V_A and V_B which can be expressed as:

$$V_C = \frac{I\rho}{2\pi}\left(\frac{1}{r_1} - \frac{1}{r_2}\right) \tag{5.2}$$

where r_1 and r_2 are the distances from point C to points A and B, respectively. The

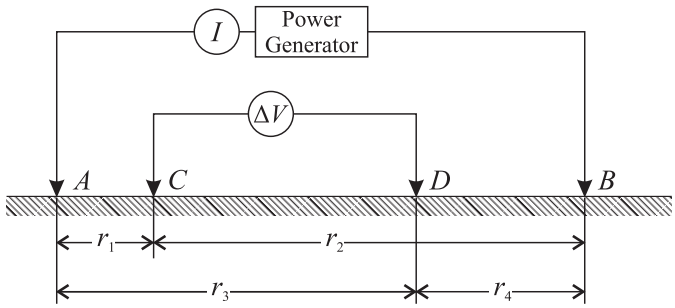

Figure 5.4: Generalized configuration of four electrodes located on the surface of a homogeneous medium of electrical resistivity ρ. Two electrodes are driving current into the medium, and the other two electrodes are used to measure the voltage between the points C and D.

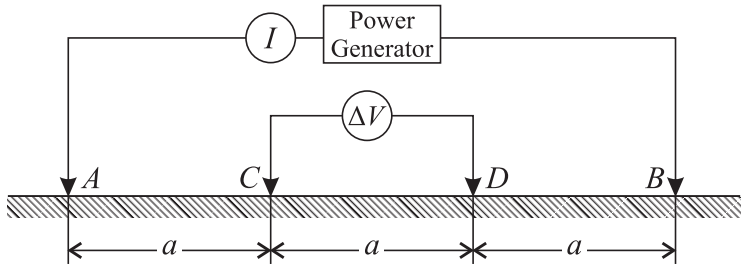

Figure 5.5: Wenner electrode configuration. All the electrodes are equidistantly placed along a line.

potential at the point D can be obtained analogously. Finally, the voltage between C and D is given by:

$$\Delta V = \frac{I\rho}{2\pi}\left[\left(\frac{1}{r_1}-\frac{1}{r_2}\right)-\left(\frac{1}{r_3}-\frac{1}{r_4}\right)\right] \tag{5.3}$$

The electrical resistivity of the medium is then obtain by:

$$\rho = \frac{2\pi\Delta V}{I\left[\left(\frac{1}{r_1}-\frac{1}{r_2}\right)-\left(\frac{1}{r_3}-\frac{1}{r_4}\right)\right]} \tag{5.4}$$

In homogeneous mediums, the electric resistivity obtained in Equation (5.4) is constant and independent from the electrode spacing. If the electrodes are equidistantly placed, Equation (5.4) can be rewritten as:

$$\rho = 2\pi a\frac{\Delta V}{I} \tag{5.5}$$

where a is the distance between electrodes (Figure 5.5). In this case, it is said that the electrodes are presented in *Wegner configuration*.

Measurement Probe

The measurement probe consisted of a four-electrode probe with silver electrodes coated with silver chloride (*silver-silver chloride electrodes*). The Ag/AgCl electrode is one of the most popular electrophysiology electrodes with a large number of applications. This kind of electrode approaches characteristics of a perfectly non-polarizable electrode that can be easily produced in laboratory [Neu98].

To prepare an Ag/AgCl electrode, a silver wire and a large silver plate (or platinum plate) are immersed into a solution of potassium chloride at the concentration of 1 M.

The silver wire is then connected to the anode of a DC power source and the plate to the other terminal, obtaining this way an electrochemical cell. The DC source is set to a voltage of 0.5V, and electrolysis process is run for a few minutes. The electric current peaks as soon as the process starts (there have to be taken measures to limit the peak current, e.g., placing a resistor in series with the circuit) but, as soon as the AgCl layer increases, the chemical reaction slows down and the current drops significantly [Bah81, Egg97].

Silver wire with a diameter of 0.4 mm were used to prepared the electrodes of the measurement probe used in this study. After coating the electrodes, they were placed in a row in an acrylic piece with electrode spacing of 1.5 mm and a depth of 6 mm. The outer electrodes were used to inject electric current into the liver, while the inner electrodes were used to measure the potential difference in the liver tissue. In Figure 5.6, it is shown the measurement probe that was made and used in this study.

Measurement System

After measuring the electric current delivered to the tissue and the voltage between the inner electrodes of the measurement probe, the electrical resistivity of the tissue samples was determined using Equation (5.4), where $a = 1.5$mm.

The electric current in controlled by a function generator which is connected to one of the outer electrodes of the measuring probe. The other outer electrode is connected to a current-to-voltage amp-op circuit with a gain value of 1 000 (amp-op U4 in Figure 5.7).

The potential difference between the inner electrodes of the probe is measured by an instrumentation amplifier circuit (amp-ops U1, U2 and U3 in Figure 5.7). Considering that $R2 = R5$, $R3 = R6$ and $R4 = R7$, and taking into account the values presented in Figure 5.7, the output voltage at the instrumentation amplifier circuit, V_{out1}, is given by:

$$V_{out1} = 50(V_2 - V_1) \tag{5.6}$$

In order to minimize the current flow through the inner voltage electrodes, two voltage follower circuits are buffering the inputs of the instrumentation amplifier circuit (amp-ops U5 and U6).

Finally, to register the values of current and voltage measured at the tissue samples, the outputs of the current-to-voltage converter and the instrumentation amplifier circuit were connected to a Tektronix TDS 1002 oscilloscope.

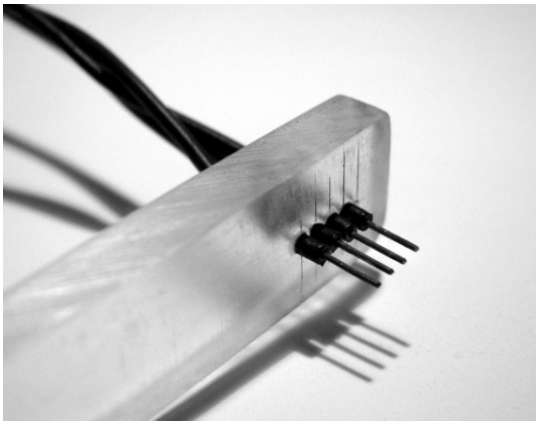

Figure 5.6: Four-electrode probe used for measurement of the electrical conductivity of liver tissue.

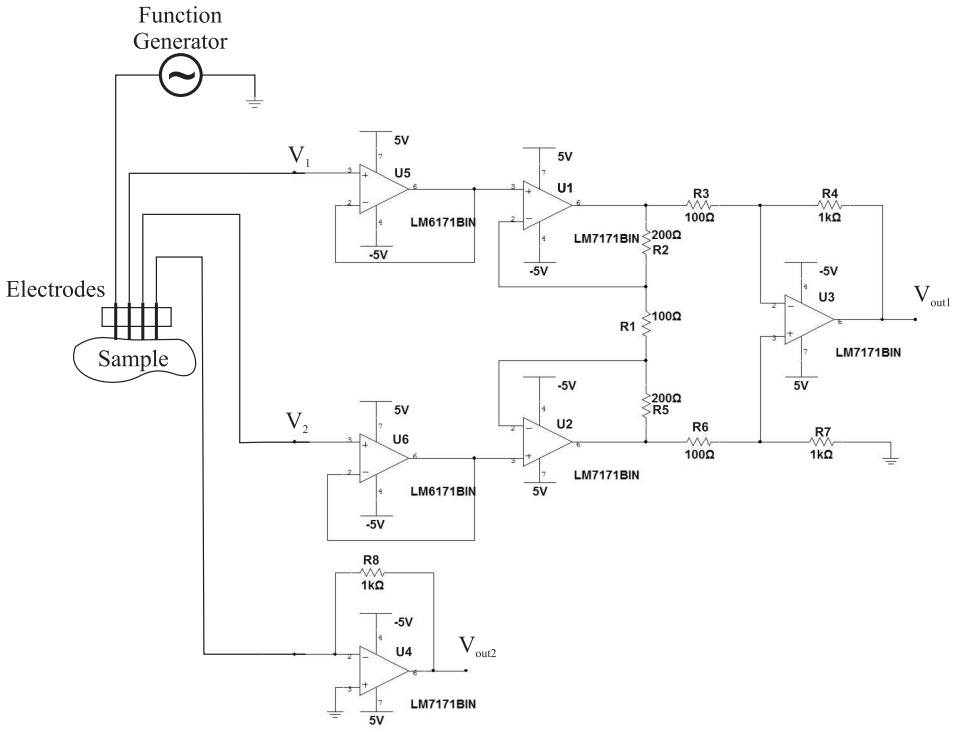

Figure 5.7: Schematic of the circuit used for conditioning the voltage and the current obtained from the measuring probe.

5.2.3 Methodology

There were performed RF ablation procedures of 5, 10 and 15 minutes long, using output voltages of 25, 50, 75 and 100 V. After each procedure, the liver was sectioned along a longitudinal plane and the lesion induced was measured. There was no histological examination involved but only visual observation.

Concerning the measurement of the electrical conductivity of the samples used during the RF ablations tests, there were performed 2 to 5 readings in 5 to 10 points in each liver. The frequency considered was 470 kHz, which corresponds to the output voltage frequency of the Covidien RF power generator used.

5.2.4 Results

Electrical Conductivity of the Tissue

There were performed about 500 measurements along this experimentation work. All the data gathered from the measurement of the electrical conductivity in all the samples of liver used was averaged, and standard deviation was calculated. It was obtained an electrical conductivity value of 0.13 ± 0.06 S/m at 470 kHz. These values were obtained for an average liver temperature of 24.6 ± 2.3°C.

Volume of the Induced Lesions

Considering all the experiments carried out, the average value of the initial impedance of the tissue was 68 ± 16.2 Ω. In each experimental RF ablation procedure, it

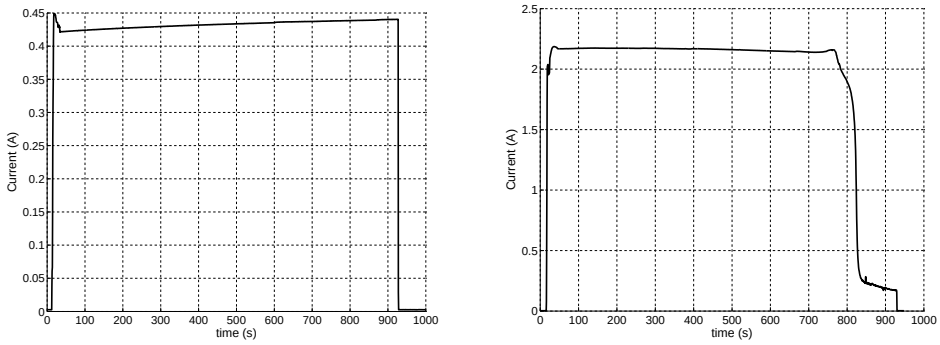

(a) (b)

Figure 5.8: Current intensity delivered by the power generator during a RF ablation procedure of 15 minutes for an applied voltage of (a) 25 V, and (b) 100 V.

was possible to observe that the electrical current supplied by the RF power source increased with time, thus increasing the power supplied. This reflects the positive temperature coefficient of the electrical conductivity of the tissue [FS96], which was later considered in the numerical simulation performed for this study. In Figure 5.8a, it is shown the graph representation of current intensity against time for an applied voltage of 25 V. In this case, the current grows almost linearly until the RF power generator is turned off.

On the other hand, the electric current intensity did not present this behaviour in all tests performed. When using an applied voltage of 100 V, it was verified that the RF power generator reached its maximum current output of 2 A. This can be observed in Figure 5.8b. After 400 s, the current intensity reaches a maximum of 2.15 A.

Gas formation and tissue charring can occur much easily at 100 V, which leads to a sudden increase of the electrical impedance of the tissue, thus reducing the electric current delivered by the RF power generator. This fact can be verified in Figure 5.8b. After 750 s, the electric current drops significantly and keeps reducing until the power generator switches off. In this case, the power source did not shut-down as it did in Figure 4.22. In the latter, the 999Ω security impedance threshold of the power generator was exceeded, and it turned off automatically.

As it would be expected, temperature in the tissue starts to rise as soon as a voltage is applied. This temperature increase will depend on the time of the procedure and the applied voltage. However, independently of the time considered, no lesion was induced in the tissue for an applied voltage of 25 V.

In Figure 5.9, there are presented the longitudinal sections of the induced lesions obtained after a RF ablation of 15 minutes for applied voltages from 25 to 100 V. It can be observed that, for an applied voltage of 25 V, the tissue does not show any sign of denaturation, even after 15 minutes. As the voltage increases (from Figure 5.9a to Figure 5.9d), the lesion around the electrode tract becomes very clear. For applied voltages of 75 and 100 V, the lesions obtained are well-defined when compared with those obtained at 50 V. The tissue adjacent to the stent presented itself totally dehydrated and, at 100 V, there were signs of carbonization. In Figure 5.9d, it is possible to observe that the inner wall of the electrode's tract is darkened, revealing signs of charring.

In Figures 5.10 to 5.12, there are shown the longitudinal sections of the induced lesions after 5, 10 and 15 minutes for applied voltages of 50, 75 and 100 V. It can be observed that, for an applied voltage of 50 V, it is possible to induce some thermal

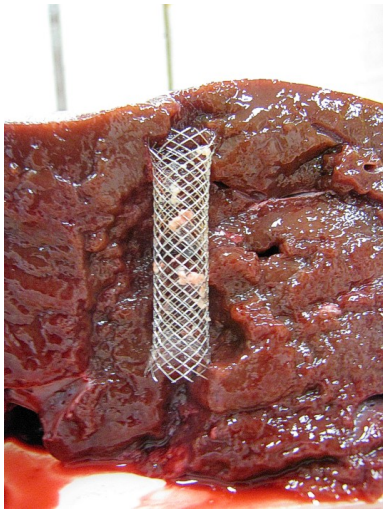

(a)

(b)

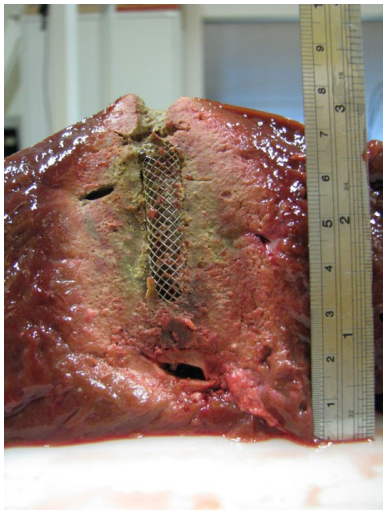

(c)

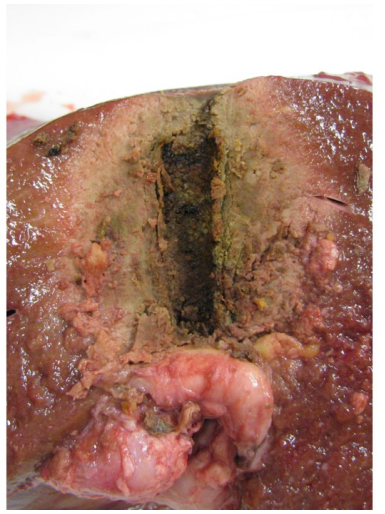

(d)

Figure 5.9: Induced thermal lesions in bovine liver after a RF ablation procedure of 15 minutes at an applied voltage of (a) 25 V, (b) 50 V, (c) 75 V, and (d) 100 V.

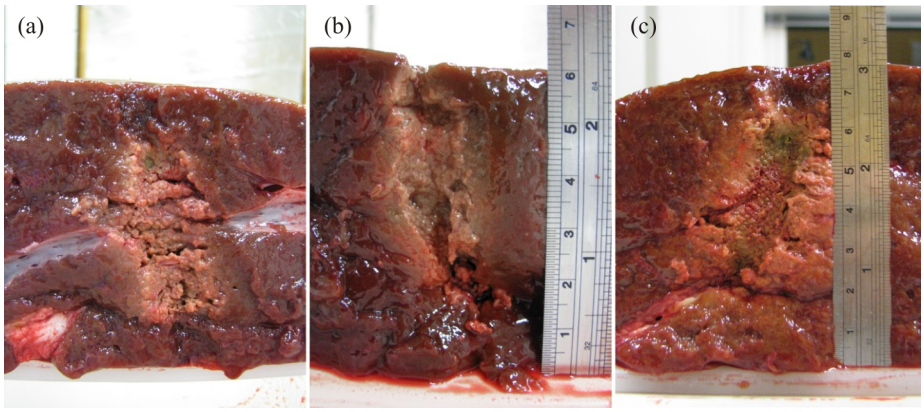

Figure 5.10: Longitudinal section of the induced lesion obtained for an applied voltage of 50 V after (a) 5 minutes; (b) 10 minutes; and (c) 15 minutes.

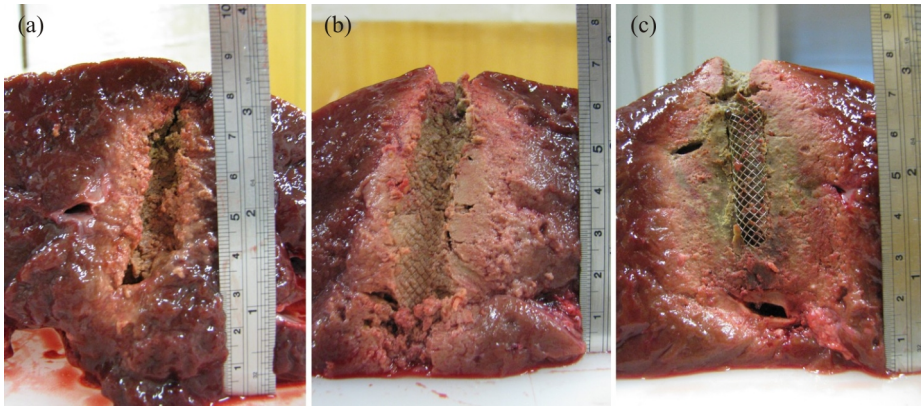

Figure 5.11: Longitudinal section of the induced lesion obtained for an applied voltage of 75 V after (a) 5 minutes; (b) 10 minutes; and (c) 15 minutes.

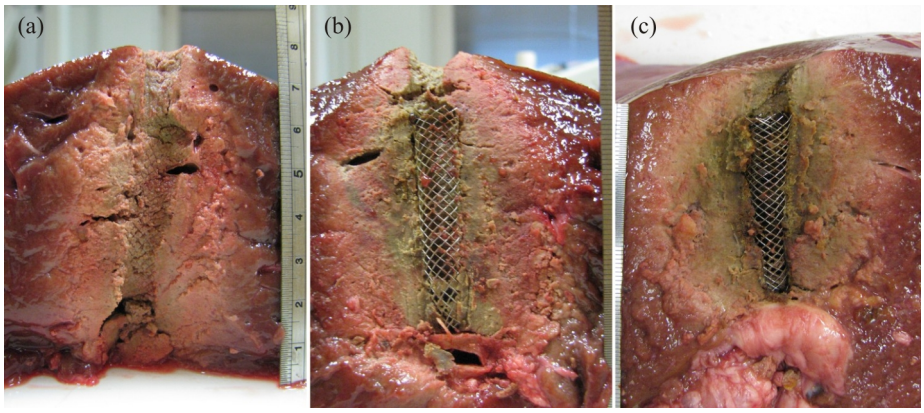

Figure 5.12: Longitudinal section of the induced lesion obtained for an applied voltage of 100 V after (a) 5 minutes; (b) 10 minutes; and (c) 15 minutes.

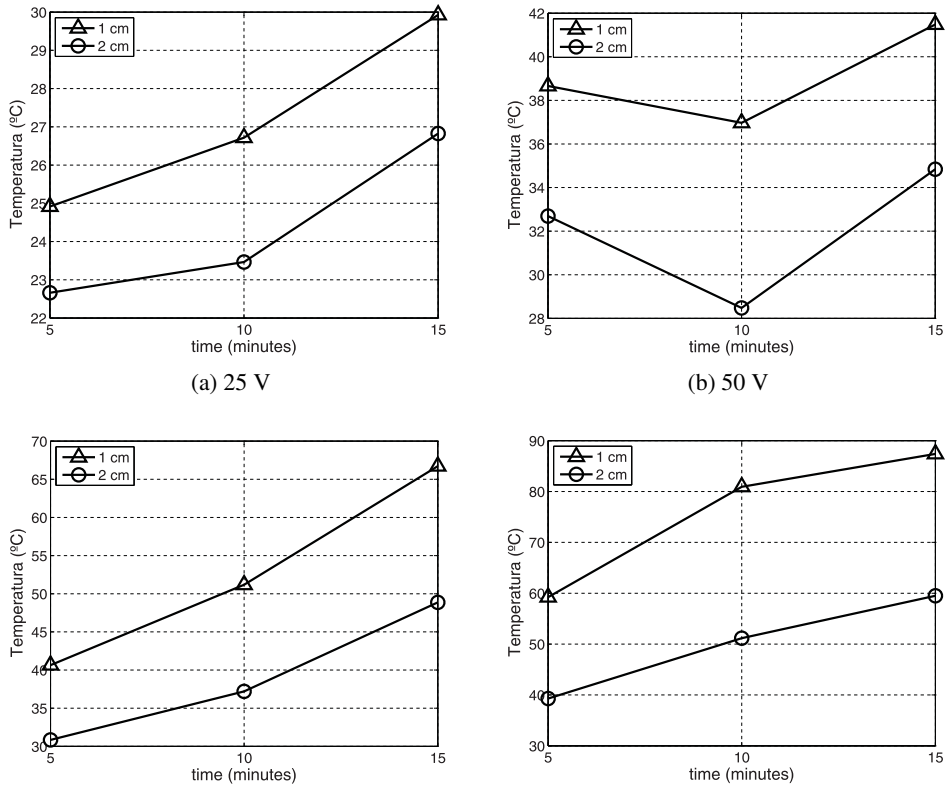

(a) 25 V (b) 50 V

(c) 75 V (d) 100 V

Figure 5.13: Average temperature readings measured at 1 and 2 cm from the electrode for an applied voltage of (a) 25 V; (b) 50 V; (c) 75 V; and (d) 100 V.

necrosis after 5 minutes (Figure 5.10a). However, it will affect only a slim rim around the electrode, and the lesion obtained presents a fuzzy boundary. As expected, the lesion becomes larger for longer RF ablation procedures, although the boundaries of the lesions are not sharply delineated (Figures 5.10b and 5.10c).

For larger applied voltages, the induced lesions become larger and well-defined. After 5 minutes, at 75 V, the induced lesion is very similar to the one obtained after 15 minutes at 50 V (Figure 5.11a). After 10 minutes, the lesion becomes well-defined (Figure 5.11b), and tissue dehydration becomes evident adjacent to the electrode after 15 minutes (Figure 5.11c).

The thermal necrosis develops much faster for an applied voltage of 100 V. In Figure 5.12a it is shown that, just after 5 minutes, the induced lesion has a considerable size already, and its contour is well-defined. Dehydration of the tissue around the electrode is visible after 10 minutes as the lesions grows larger (Figure 5.12b). Finally,

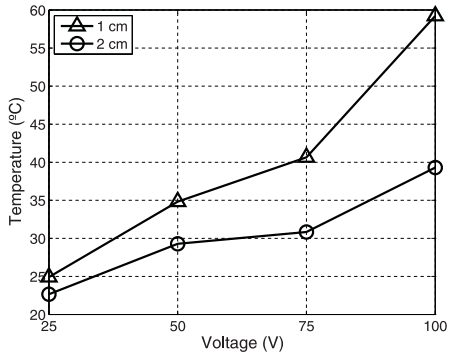

(a) 5 minutes

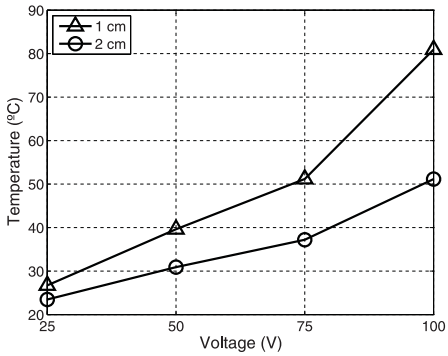

(b) 10 minutes

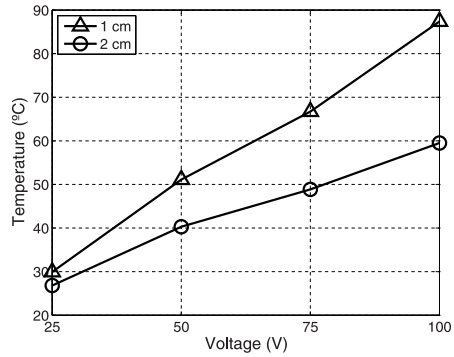

(c) 15 minutes

Figure 5.14: Average temperatures after (a) 5 minutes; (b) 10 minutes; and (c) 15 minutes.

as stated before, after 15 minutes the tissue is severely dehydrated and, in most cases, signs of carbonization is visible in the tissue adjacent to the electrode (Figure 5.12c).

The average value of the temperature readings from the RTD sensors placed at 1 and 2 cm from the electrode are presented in Figure 5.13. It can be observed that the temperatures for an applied voltage of 25 V (Figure 5.13a) are not enough for inducing a thermal lesion: none of the values recorded exceeded the temperature of 30°C.

In general, the measured temperature values increase almost linearly. However, for an applied voltage of 50 V, the graph presents a sag at 10 minutes. This can be explained by the fact that the samples used during the experiments for this case presented an initial average temperature of 22.75°C, almost 4°C lower than the initial average temperature of the liver samples used during the experiments at 50 V.

When plotting the average temperature measurements against the applied voltage (Figure 5.14), it becomes clear the fact that the 50°C threshold is far from being

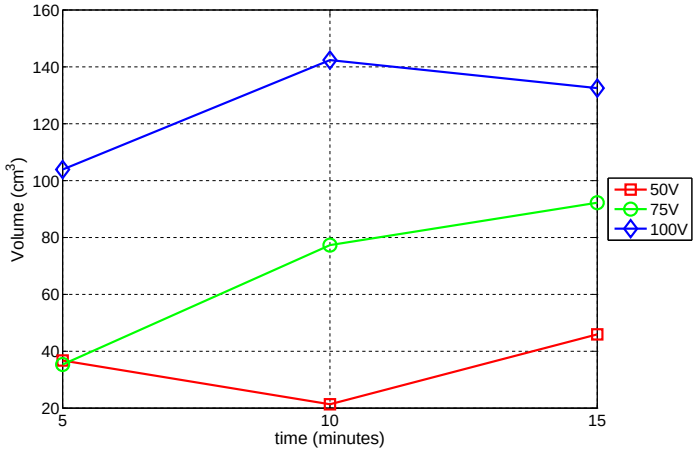

Figure 5.15: Cylindrical volume approximation of the lesions induced in the tissue by RF ablation.

exceeded at 2 cm after 5 minutes. This was verified at any of the applied voltage values (Figure 5.14a). Even at 1 cm, the temperature threshold is only exceeded for an applied voltage above 75 V. Figure 5.14 also shows that the temperature increases more rapidly for an applied voltage of 100 V. This is specially clear after 5 and 10 minutes (Figures 5.14b and 5.14c).

As it was previously mentioned, it was only performed visual analysis of the induced lesions. For this, it was considered that the inner pale zone of the tissue corresponded to the thermal lesion [CLG$^+$00]. For each lesion, it was registered the maximum height and the maximum width. The width was obtained by cross measuring the lesion, so the diameter of the stent (10 mm) is included. For obvious reasons, the results for 25 V were disregarded. For each voltage-time pair, the volume of the lesion was approximated by a cylinder with dimensions given by the average values obtained. These values are presented in Figure 5.15.

As expected, a larger lesion is obtained considering larger values of voltage and/or time. There are two remarks concerning these results. First, the volume of the induced lesion grows slower from 10 minutes. It agrees with the fact that, as time elapses, the peripheral tissue is mainly heated by conductive heat transfer, a much slower process. However, for an applied voltage of 100 V, it is possible to notice a slight decrement in the volume of the induced lesion. In fact, two of the samples presented an unnoticed fat layer below the stent that affected the current distribution significantly, producing a shorter lesion, thus a smaller volume. In Figure 5.12c, it is possible to observe the referred fat layer, and also it is possible to notice that the lesion did not grow significantly below the electrode as in the remain cases presented.

A second remark concerns again with the sag observed at the curve for an applied voltage of 50 V. As already mentioned, some of the samples were cooler than the rest of livers used during the experimental work, and this fact has a significant on the volumes obtained after a RF procedure of 10 minutes.

5.3 Numerical Simulation

The numerical simulation consists of a coupled thermal electrical analysis, which was already discussed in detail in section 4.3.1. However, some differences were considered in the numerical models used in the study presented in this chapter that will be described next.

5.3.1 Description of the Model

The model consists of a cylinder with 100 mm of radius and 80 mm of height which represents the liver tissue. At the centre, a second cylinder of radius of 5 mm and height of 55 mm represents the aperture (air) where the electrode is placed. The top bases of both cylinders are coplanar.

The stent-based electrode is made from 24 nitinol wires with 0.25 mm diameter. Each wire consists of a helix with a pitch of 25 mm and a diameter of 10 mm. Twelve of the helices are clockwise and the others are counter-clockwise. The electrode has a length of 40 mm and it is place at the bottom of the inner cylinder of the model.

Taking into account the symmetry of the problem, it was modelled only a quarter of the model. The model considered in this study is depicted in Figure 5.16.

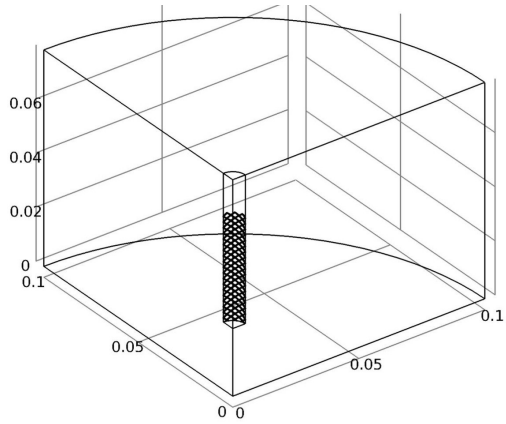

Figure 5.16: Model considered for numerical characterization of the induced lesion. Only a quarter of the model was considered taking into account the symmetry of the problem.

Table 5.1: Material properties (from [HST+01], except electrical conductivity of liver tissue).

Element	Material	ρ [kg/m^3]	c [J/kg·K]	k [W/m·K]	σ [S/m]
Electrode	Nitinol	6450	840	18	$1 \cdot 10^8$
Hole	Air	1.202	1	0.025	0
Tissue	Liver	1060	3600	0.512	$\sigma(T)$

5.3.2 Physical Properties and Boundary Conditions

The material properties considered in the simulation of this study are presented in Table 5.1. All the properties, except for the electrical conductivity of the liver tissue, were obtained from the literature [HST+01].

The conductivity of the tissue was considered temperature-dependent and the simulations were performed considering a temperature coefficient of 2%/°C [FS96]. Based on the result presented in section 5.2.4, the temperature of the liver was set to 0.13 S/m at 25°C. When the temperature reaches the value of 100°C, the electrical conductivity abruptly drops to 0.01 S/m. This allows to simulate the electrical insulation of the electrode that verifies when gas forms at this temperature value [HCW+03].

The thermal boundary conditions were chosen so that the model approximates the conditions of the laboratory at the time of the experimental tests. The outer boundaries of the model (Dirichlet boundary conditions) were set to 22°C, which corresponds to the average room temperature value. Because the livers samples used in the experimental tests were placed on a high density expanded polystyrene board, the bottom plane of the outer cylinder was considered as a thermal insulator (Neumann boundary condition). Finally, the initial temperature of the liver was set to 25°C.

The electrical potential applied to the stent is constant during each RF ablation procedure. The numerical simulations were performed considering voltage values of 25, 50, 75 and 100 V at the boundaries of the stent. The bottom and the sides of the larger cylinder are considered at zero volts. The upper surface of the model is considered an electrical insulator.

The models were solved using the solver PARDISO implemented in the finite element software COMSOL Multiphysics 3.5a (COMSOL, Inc. Burlington, MA, USA). Due to the complex structure of the electrode, this was modelled in AutoCAD (Autodesk, Mill Valley, California, USA) and exported in 3D ACIS format to COMSOL. The model proposed have a total of 192 846 tetrahedra (quarter of a model).

It took about 2.21 hours for solving the numerical model at 25 V, and 15 hours at 100 V. The time for solving the numerical model increased for larger values of applied voltage. All the models were solved on a computer with Intel Core 2 Quad CPU @2.34Ghz, 8GB of RAM, on a 64 bits platform.

5.3.3 Determination of the Lesion Volume from the Numerical Solutions

For the assessment of the volume of the induced lesion from the data obtained after solving the proposed numerical model, one of the following criteria can be considered:

1. The biological damage can be describe as a function of both temperature and time, as expressed by the Arrhenius integral (Equation (2.37)):

$$\Omega(x,t) = \int_0^t A \exp\left(\frac{\Delta E}{RT(x,\tau)}\right) d\tau \tag{2.37}$$

   As already mentioned, both A and ΔE are dependent of the type of tissue, and they are evaluated from experimental data [Ber06].

2. The boundary of the volume of the induced lesion can be determined from the temperature distribution, considering a 50°C isothermal surface. As mentioned in section 3.2.2, thermal necrosis is achieved in very short time after exposing the tissue to a temperature above this threshold. The assessment of the volume of the lesion from the 50°C isothermal surface has been used extensively in literature [BH05, HWM+03a, JW97, PWF+95, TSH+02].

Haemmerich *et al.* [HWM03b] performed a comparative study between these two criteria on cardiac and liver tissue. They concluded that the lesion determination by an isothermal surface could overestimate the lesion size for small treatment times below 30 s, common in cardiac RF ablation. On the other hand, this criterion could underestimate the lesion size for very large treatment times greater than 20 minutes in hepatic ablation. Nevertheless, the 50°C isothermal surface predicts the lesion with acceptable accuracy.

Taking into account that the simulations performed in this study are no longer than 15 minutes, it was considered the 50°C isothermal surface criterion for assessment of the lesion volume from the numerical data.

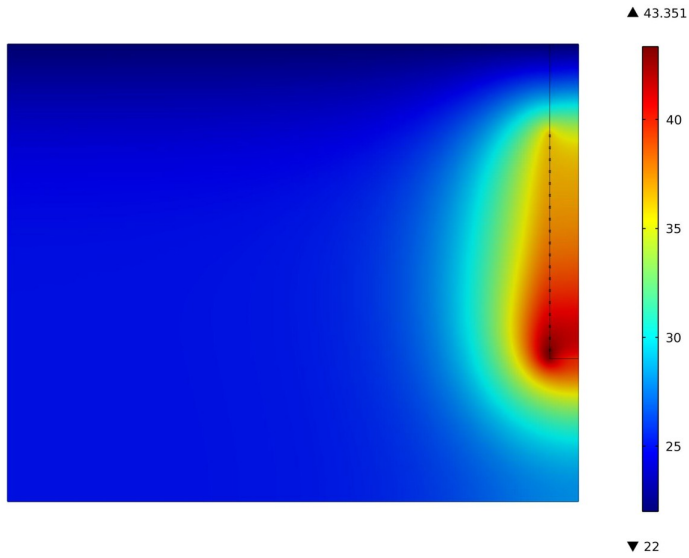

Figure 5.17: Temperature distribution on a longitudinal section of the model for an applied voltage of 25 V after 15 minutes. It can be observed the in any point of the model the temperature reaches the value of 50°C.

5.3.4 Numerical Results

From the numerical solution, it was analysed the temperature distribution considering an isothermal surface of 50°C, as referred in section 5.3.3. In Figure 5.17, it is presented the temperature profile for an applied voltage of 25 V after a RF ablation of 15 minutes. As it can be noticed, in any point of the model the temperature reaches the threshold of 50°C, which agrees with the experimental results.

In Figures 5.18 and 5.19 are presented the lesion volumes assessed from a 50°C isothermal surface for an applied voltage of 50 and 100 V, respectively. There are presented the volumes after 5 and 15 minutes. Again, the numerical results agree in some extension with the experimental data. It is possible to observe some resemblance between these images and the lesions presented in Figures 5.10 and 5.12, obtained experimentally.

Finally, the volumes were calculated in a similar manner to the one considered for the experimental data. It was considered the height and the width of the volume enclosed by the isothermal surface and it was approximated by a cylinder. The results are depicted in the graphic of Figure 5.20. Experimental data is also represented (dashed lines) for comparison.

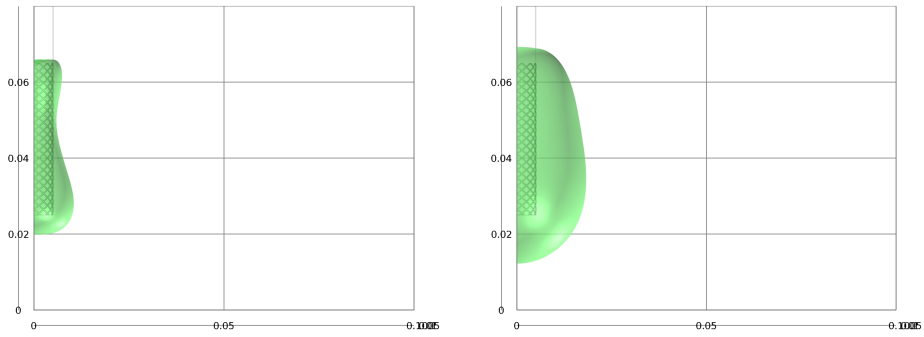

(a) 5 minutes (b) 15 minutes

Figure 5.18: Lesion volume assessed from an isothermal surface of 50°C considering an applied voltage of 50 V after (a) 5 minutes; (b) 15 minutes

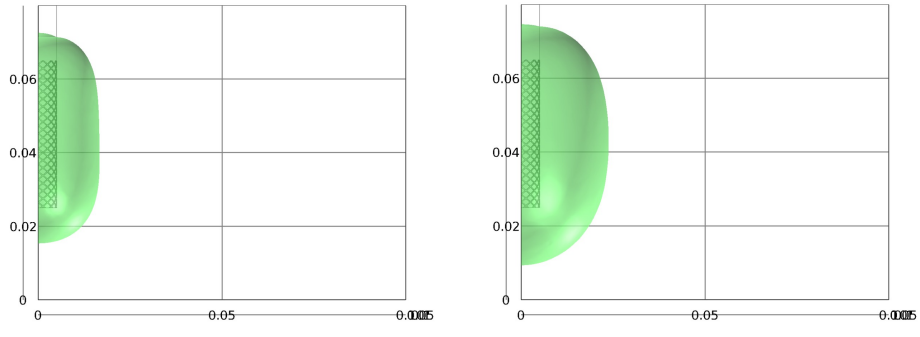

(a) 5 minutes (b) 15 minutes

Figure 5.19: Lesion volume assessed from an isothermal surface of 50°C considering an applied voltage of 100 V after (a) 5 minutes; (b) 15 minutes

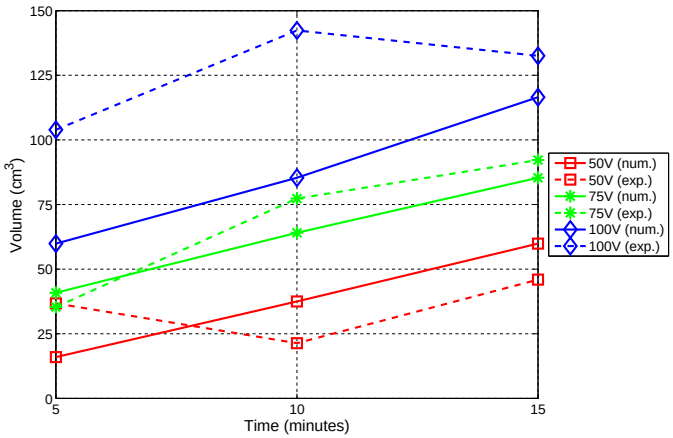

Figure 5.20: Cylindrical volume approximation of the lesions induced in the tissue by RF ablation. Numerical and experimental results.

5.4 Conclusions

In this chapter, it was characterized the volume of the thermal lesion induced in liver tissue using the proposed stent-based electrode. RF ablation experiments were performed to assess the dimensions of the induced lesions. Also, numerical data obtained after numerical simulation was compared with the experimental results in order to validate the proposed numerical model. During the experimental work, the electrical conductivity of the liver tissue was obtained with a measurement probe prepared at the laboratory. The measurements were performed at the frequency of 470 kHz, the operating frequency of the RF power generator used during the experimental work. The electrical conductivity value obtained was considered in the proposed numerical model, so the results could resemble the experimental data as much as possible.

The volume of the lesion obviously depends on the voltage applied and the time of the procedure. As the voltage and/or the time increase, the induced lesion is larger. However, no induced lesion is achieved for an applied voltage of 25 V, even after a RF ablation of 15 minutes. The same fact was observed in the numerical results obtained, regarding a volume lesion delimited by an isothermal surface of 50°C.

The size of the damaged tissue obtained can be rather large when considering large values of voltage and time. For an applied voltage of 100 V, a severe tissue dehydration is observed next to the electrode after 10 minutes and charring can occur after longer periods. In this case, the resulting lesion can exceed 50 mm of diameter. Regarding the fact that the stent-based electrode is meant to be used for the treatment of tumours located in tubular organs, this means that precautions have to be taken in order not to injure the duct involved.

The results obtained through numerical simulations show a good agreement with those obtained by experimentation, particularly for applied voltages of 50 and 75 V. However, the experimental and numerical data at 100 V diverge. One limitation of this model is the fact that the temperature dependence of the thermal properties of the liver tissue was not considered in this study due to the lack of data on this subject. This may lead to some inaccurate results, particularly for the applied voltage of 100 V. In this case, the rapidly temperature increase near the electrode may affect the thermal and even the electrical properties of the tissue, which might explain the significant divergence between numerical and experimental data. Still, considering the fragility of the hollow organs that undergo RF ablation procedure, as well as the power that is delivered at 100 V, it is very unlikely that this voltage amplitude will be considered.

CHAPTER 6

Effects of the Geometry of the Electrode on the Temperature Distribution

"Data! Data! Data!" he cried impatiently. "I can't make bricks without clay."

Sir Arthur Conan Doyle
in The Adventure of the Copper Beeches

6.1 Objective

It was shown that the proposed stent-based electrode can provide a practicable way for heating biological tissues. It is targeted for RF ablation procedures in tumours located in duct organs, like colon, oesophagus or bile duct, where needle-based electrodes, commercially available, are not suitable.

The proposed electrode is made from interlaced nitinol wires, which form a flexible tube that can be easily folded into small dimensions. Later, it can be thermally expanded, taking advantage of the shape memory effect of nitinol [DPS99, SPD04]. So far, it was considered the possibility of using commercial self-expandable metallic

stents that can be deployed by conventional methods, and then connected to the RF power generator through an electrically modified forceps which attaches to the proximal end of the stent, obtaining this way a complete electric circuit to perform a RF thermal ablation.

In the previous chapter, the stent-based electrode that was used, consisted of a set of circular helices of nitinol wire. Right-handed and left-handed helices are used in the same proportion, forming a mesh-like flexible cylinder (Figure 5.1). In this chapter, it is presented a study to evaluate the effect of the geometry of the stent-based electrode on the temperature distribution and the volume of the induced thermal lesion. Attention is given to the mesh density of the stent, particularly, to the number of helices used to form the electrode.

Results show that higher density mesh leads to a larger and more regular lesion. However, a high number of helices does not imply a significantly increment of the volume of the lesion. Most of the commercial available stents resemble the geometry studied in this work and, therefore, they can be used as a part of a RF ablation procedure proposed.

6.2 Numerical Model

6.2.1 Theoretical Model

Once again, the proposed numerical analysis consists of a coupled thermal analysis, thoroughly introduced in section 4.3.1. Only significant differences are observed at the model itself, which will outline next.

6.2.2 Description of the Model

For the present analysis, a cylindrical model with a radius of 100 mm and a height of 80 mm was created. This cylinder represents the biological tissue (liver) where energy will be deposited. A second cylinder, centred at the former one, represents the aperture where the stent-based electrode is placed, and it is considered filled with air. This cylinder has a radius of 5 mm and height of 55 mm. The top of both cylinders are coplanar.

The electrode consists of a stent of 40 mm length and 10 mm diameter, made from interlaced nitinol wires with 0.25 mm diameter. Each wire is shaped as a helix with a pitch 25 mm. Different models of the stent-based electrode were considered,

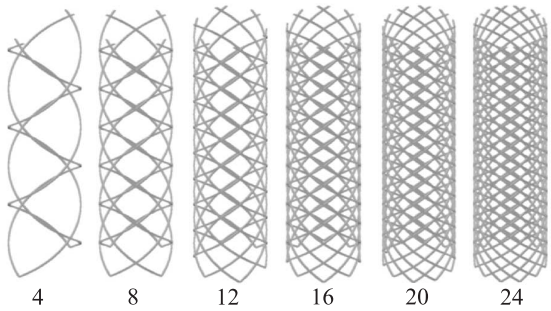

Figure 6.1: Different stent geometries obtained after varying the number of interlaced helices.

varying the number of helices. Models with a total of 4, 8, 12, 16, 20 and 24 helices were created and placed symmetrically, i.e., half of the helices is right-handed and the other half is left-handed. All stents were placed centred at the bottom of the smaller cylinder. In Figure 6.1, there are presented the different stents geometries obtained after varying the number of interlaced helices.

6.2.3 Physical Properties and Boundary Conditions

This study is based on the experimental conditions verified during the characterization of the induced thermal lesion performed in the previous chapter.

The material properties used in the proposed model are presented in Table 5.1. The electrical conductivity of the tissue was considered temperature-dependent, increasing 2%/°C, with a value of 0.13 S/m at 25°C. When temperature reaches the value of 100°C, electrical conductivity abruptly drops to 0.01 S/m to simulate the electrical insulation of the electrode verified when gas forms above this temperature value [HCW$^+$03].

Dirichlet boundary conditions for the temperature were set to 22°C for the surfaces away from the active electrode, except for the bottom plane, which was considered a thermal insulator surface. The initial temperature of the tissue was set to 25°C.

In this study, there were considered constant voltages of 25, 50, 75 and 100 V at the active electrode. The bottom base and the sides to the outer cylinder were set to zero volts, to simulate the return electrode.

As in the cases studied in the previous chapters, the 3D models of the stents were created in AutoCAD (Autodesk, Mill Valley, California, USA) and exported in 3D ACIS format, an adequate format for importing 3D models into COMSOL Mul-

tiphysics 3.5a (COMSOL, Inc. Burlington, MA, USA). Again, taking into account the symmetry of the problem, it was only modelled a quarter of the whole model. In Figure 5.16, it is presented the model with an electrode of 24 helices considered in this study. The number of elements varied from 54 050 tetrahedra, for the model with a stent of 4 helices, to 184 117 tetrahedra, for the stent with 24 helices. The number of elements grows almost linearly as the number of helices increased. All models were solved on a PC computer with Intel Core 2 Quad CPU @2.34Ghz, 8GB of RAM, on a 64 bits platform. The time for solving each model depended on the applied voltage and the number of tetrahedra, varying from nearly 30 minutes (model with electrode of 4 helices and an applied voltage of 25 V) to 15 hours and 15 minutes (model with electrode of 24 helices and an applied voltage of 100 V).

6.3 Determination of the Lesion Size

In this study, it was intended to evaluate the size of the lesion after RF ablation procedures of 15 minutes. The lesion size was defined as the volume of tissue with a temperature above a defined threshold value at the end of each simulation. As previously mentioned in section 3.2.2, if the temperature reaches a value of 50-52°C, it takes about 4 to 6 minutes to induced thermal necrosis in the tissue. However, if the temperature rises above 60°C, thermal necrosis is attained almost instantaneously. Volumes delimited by isothermal surfaces of 50 and 60°C were considered.

For each simulation, the 50 and 60°C isothermal surfaces can be obtained from COMSOL. Each surface is presented as a large set of point coordinates where the temperature is equal to 50 or 60°C, depending on the surface considered. Next, it was developed a script in Matlab (Mathworks, Natick, Massachusetts, USA) that processes this set of coordinate points to calculate the volume enclosed by each of one of these surfaces.

6.4 Results and Discussion

As expected, the numerical results show that the volume of lesion, increases with voltage and time. Larger applied voltage values, as well as longer RF ablation procedures, can induce a larger volume. However, when considering an applied voltage of 25 V, the temperature does not reach the 50°C threshold in any point of any of the models considered, even after 15 minutes.

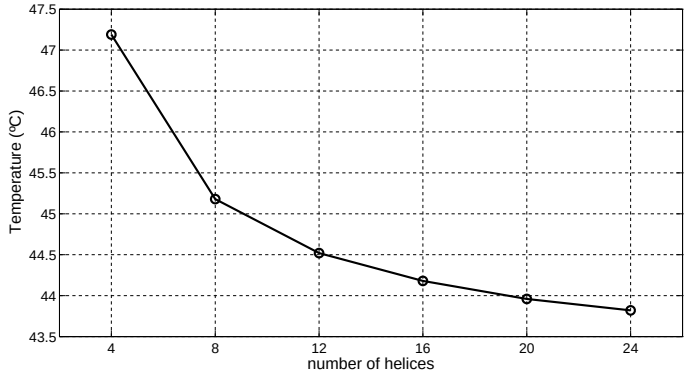

Figure 6.2: Maximum temperature obtained for an applied voltage of 25 V after 15 minutes versus the number of wires used to build the stent-based electrode. As the number of wires increases, the value of the maximum temperature decreases. However, in any model is exceeded the temperature threshold of 50°C.

In Figure 6.2, it is presented the graph of the maximum temperature achieved versus the number of helices used in each model. The presented data refer to RF ablations of 15 minutes. The maximum temperature verified is achieved in the model with an electrode of 4 helices. As the number of helices increases, the maximum temperature obtained decreases. This plot shows that it was not possible to induce thermal necrosis in any of these models under the conditions considered.

Independently of the number of helices in each electrode, the volume of the damaged tissue is irregular when considering an applied voltage of 50 V during 5 minutes. Both isothermal surfaces at 50 and 60°C are, in fact, very irregular when considering a stent with 4 nitinol wires, as presented in Figure 6.3. As the number of helices that compose the stent increases, maintaining the values of time and voltage, the volume becomes less bumpy. This can be observed in Figure 6.4, where it is presented the delimited volumes obtained with a stent-based electrode of 12 helices. Actually, there are no significant differences on the shapes of the volumes obtained when the number of wires is larger than 12. In Figure 6.5, it is presented the volumes obtained with a stent made of 24 helices. Comparing this figure with Figure 6.4, it can be seen that both shapes are almost identical.

Increasing the applied voltage and/or the duration of the RF ablation lead to more regular volumes, even when the electrode is built with only 4 nitinol wires. In Figure 6.6, there are presented the volumes obtained after 5 minutes, considering increasing values of the applied voltage. At 75 V (Figure 6.6b), the surface of the volumes seem very regular, particularly the volume delimited by the isothermal surface

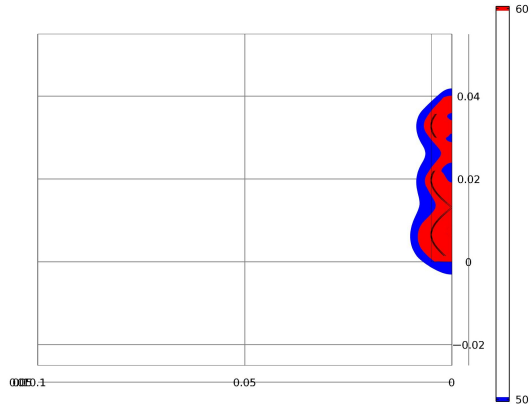

Figure 6.3: Isothermal surfaces of 50 and 60°C obtained after 5 minutes at 50 V with a stent-based electrode using 4 interlaced helices.

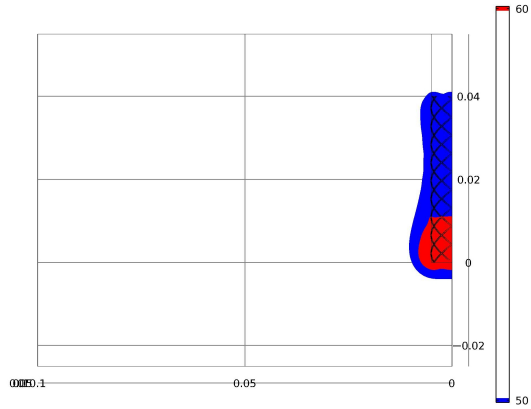

Figure 6.4: Isothermal surfaces of 50 and 60°C obtained after 5 minutes at 50 V with a stent-based electrode using 12 interlaced helices.

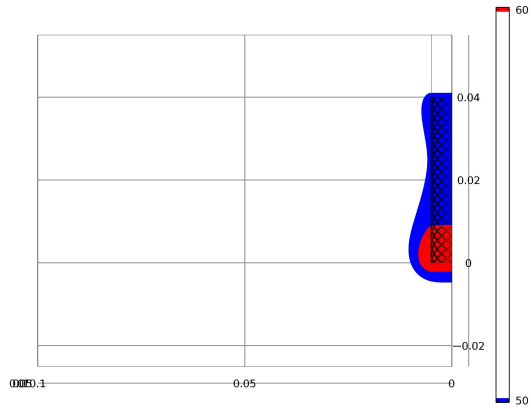

Figure 6.5: Isothermal surfaces of 50 and 60°C obtained after 5 minutes at 50 V with a stent-based electrode using 24 interlaced helices.

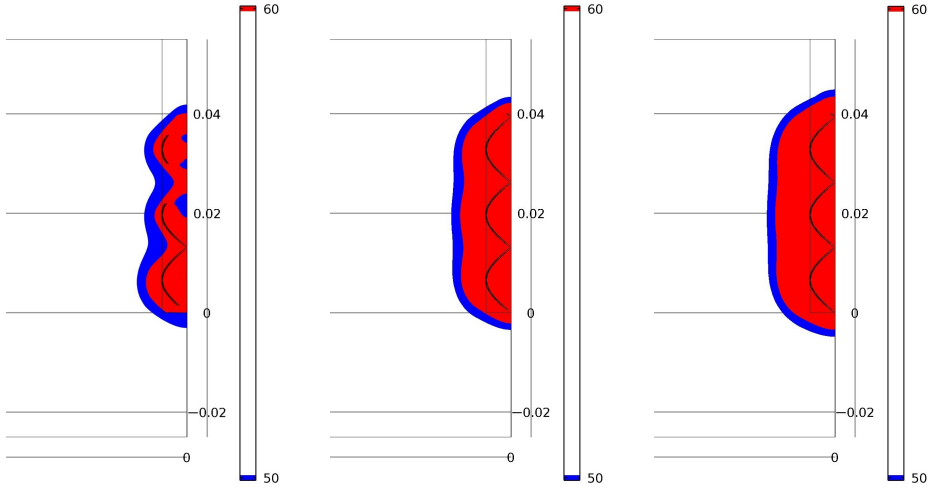

(a) 50 V (b) 75 V (c) 100 V

Figure 6.6: Isothermal surfaces of 50 and 60°C obtained after 5 minutes at (a) 50 V; (b) 75 V; and (c) 100 V. As the applied voltage increases, the surface of the volumes obtained are more regular.

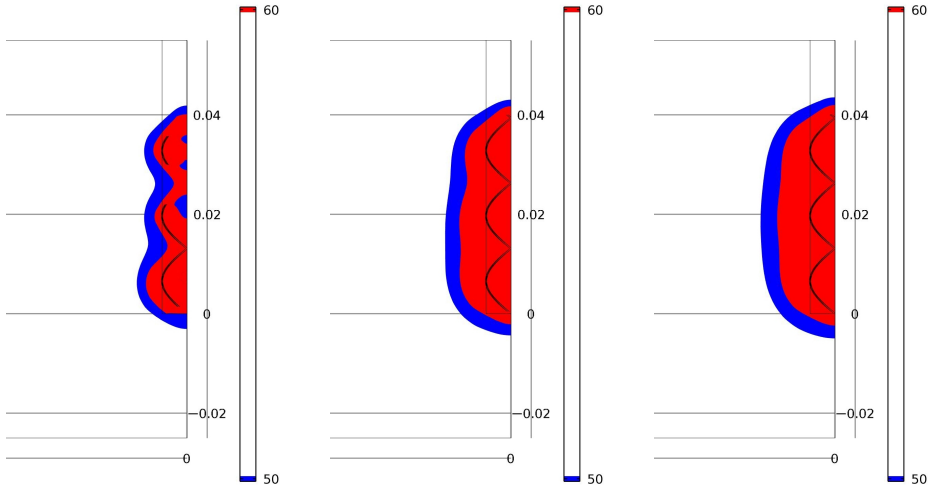

(a) 5 minutes (b) 10 minutes (c) 15 minutes

Figure 6.7: Isothermal surfaces of 50 and 60°C obtained considering an applied voltage of 50 V after (a) 5 minutes; (b) 10 minutes; and (c) 15 minutes. The obtained volumes are more regular as time elapses.

of 50°C. At 100 V (Figure 6.6c), it can be said that both volumes present a smooth surface.

In Figure 6.7, there are presented the results obtained again with an electrode made of 4 nitinol wires. In this case, the isothermal surfaces were obtained for the same applied voltage, 50 V, but with different increasing times. As time elapses, it can be observed that the surface of the obtained volumes are more regular. After 10 minutes (Figure 6.7b), the isothermal surface of 60°C is still somewhat bumpy, but the isothermal surface of 50°C is nearly smooth. After 15 minutes (Figure 6.7c), both surfaces look very regular.

The results obtained after evaluating the volume delimited by the isothermal surface of 50°C are presented in Figures 6.8 to 6.10. In general, results show that the volume obtained with the electrode of 4 helices is smaller. As the number of interlaced wires increases, the volume also increases. However, the latter is less pronounced as the number of helices grows larger. This becomes clear in Figure 6.11. In this figure, it is presented the graphic of the volume delimited by an isothermal surface of 50°C against the number of interlaced wires. This plot is obtained considering an applied voltage of 75 V, and it shows the curves for results after 5, 10 and 15 minutes. In this figure, it is shown that increasing the number of helices leads to an asymptotic increase of the lesion volume.

Still concerning these results, there are two remarks to point out. First, the volumes obtained at 50 V are very alike, except for the electrode with 4 helices. In Figure 6.8, it can be observed that the results concerning this electrode diverges from the rest of the models. Due to the reduced number of helices, the current density is much higher next to the wires of this electrode, so the temperature rises much faster in this case. The electric conductivity of the tissue drops quicker, and insulation of the electrode occurs, thus limiting the volume size in this case. This also explains the second remark: the volume with the electrode of 4 helices is higher in the first minute of the RF ablation due to the fast heating of the tissue.

For illustrating this, in Figure 6.12, it is presented the temperature distribution after 40 seconds at an applied voltage of 50 V, considering a stent with 4 helices. It can be observed that there are areas of higher temperature around the wires, and it is obtained a maximum temperature of 69.4°C. On the other hand, in Figure 6.13, it is shown the same situation but for an electrode with 24 helices. It can be noticed that the temperature spreads along the electrode more uniformly than in Figure 6.12. In this case, the maximum temperature is much lower, only 46.3°C.

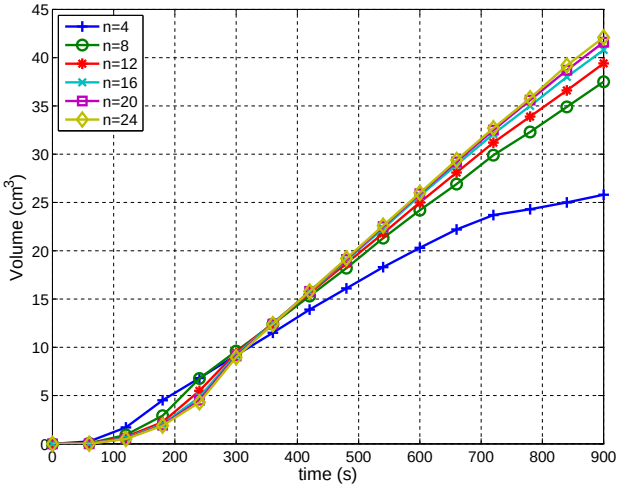

Figure 6.8: Volume delimited by the isothermal surface of 50°C considering an applied voltage of 50 V.

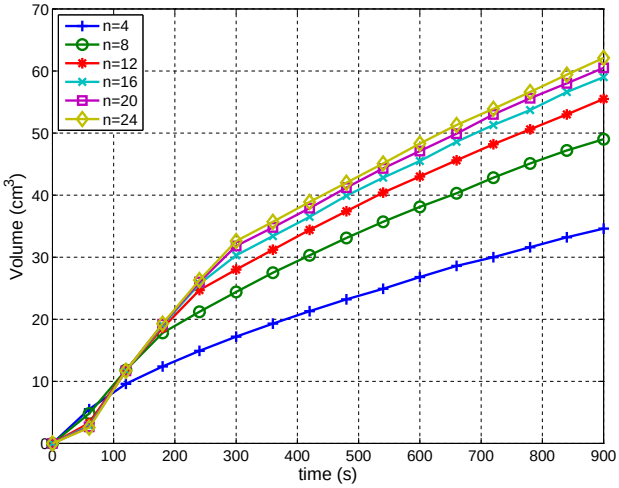

Figure 6.9: Volume delimited by the isothermal surface of 50°C considering an applied voltage of 75 V.

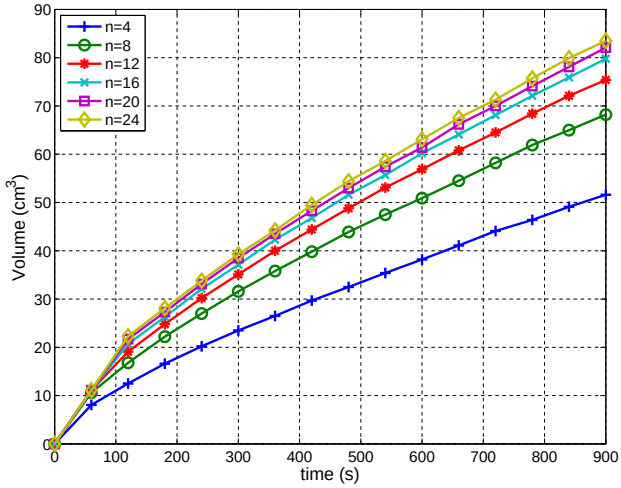

Figure 6.10: Volume delimited by the isothermal surface of 50°C considering an applied voltage of 100 V.

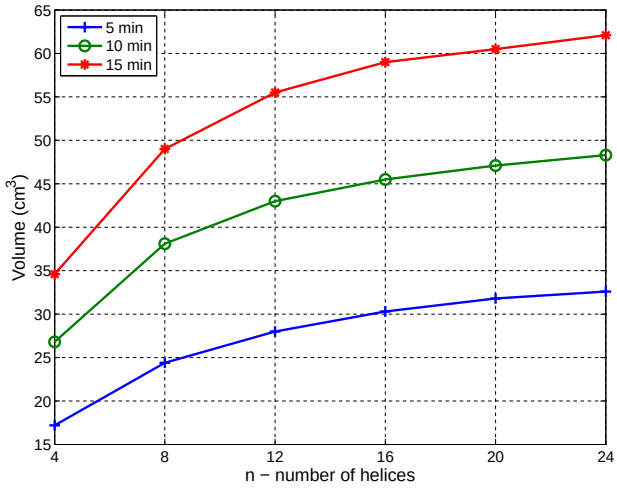

Figure 6.11: Volume delimited by an isothermal surface of 50°C versus the numbers of helices of the electrode. Results after 5, 10 and 15 minutes. The curves present an asymptotic behaviour as the number of helices of the stent-based electrode increases.

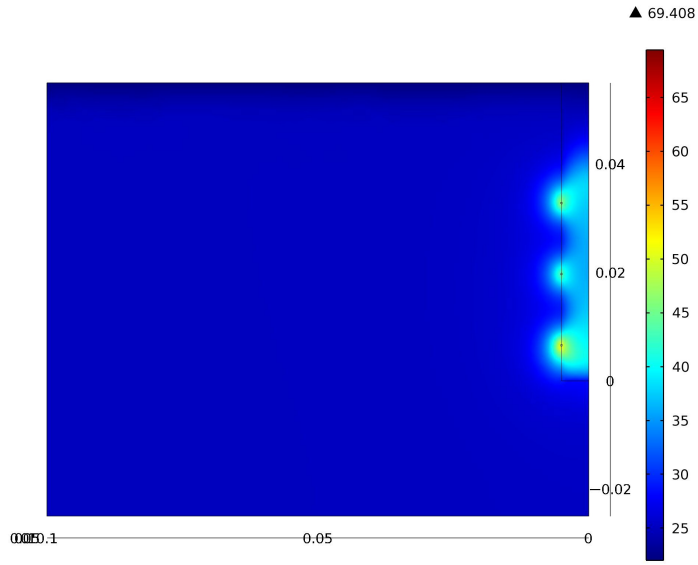

Figure 6.12: Temperature distribution obtained after using a stent-based electrode of 4 helices for an applied voltage of 50 V during 40 seconds. Maximum temperature: 69.4°C.

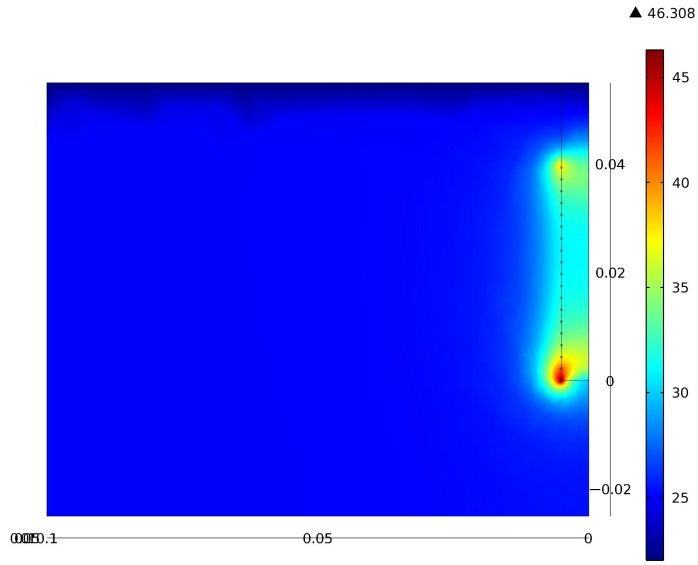

Figure 6.13: Temperature distribution obtained after using a stent-based electrode of 24 helices for an applied voltage of 50 V during 40 seconds. Maximum temperature: 46.3°C.

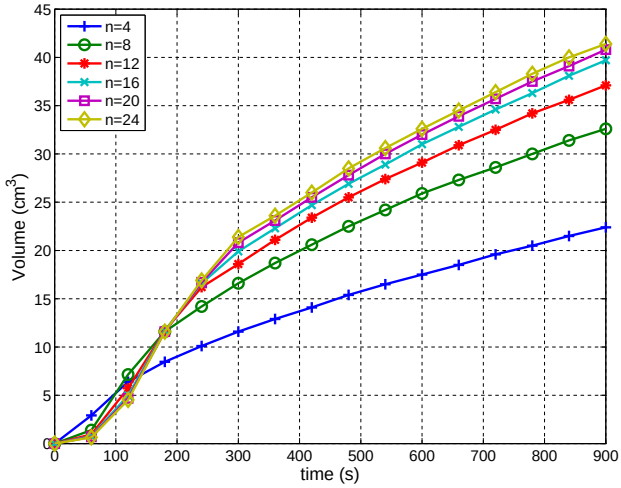

Figure 6.14: Volume delimited by the isothermal surface of 60°C considering an applied voltage of 75 V. Results are very similar to those obtained for a temperature threshold of 50°C, although the volumes obtained in this case are smaller.

The analysis of the volumes delimited by isothermal surfaces of 60°C shows similar results to the those obtained so far: larger values of time, voltage and/or number of helices correspond to larger lesion volumes. Naturally, because the temperature threshold is higher, the lesion volumes obtained are smaller than those considered for a temperature threshold of 50°C. For instance, Figure 6.14 depicts the lesion volume obtained for an applied voltage of 75 V. Besides from the fact volumes obtained are smaller, these results are very similar to those presented Figure 6.9.

6.5 Conclusions

The main goal of this study was to perform a computational analysis to evaluate the effect of the geometry of a stent-based electrode on the temperature distribution and the volume of the lesion obtained on a RF ablation procedure. This electrode is made of several helices, disposed symmetrically and with a constant pitch. Varying the number of helices has an impact on the mesh density of the electrode and, therefore, the geometry of the stent. For this study, there were considered applied voltages of 25, 50, 75 and 100 V during 15 minutes.

At 25 V, it was verified that no lesion was obtained for any of the geometries considered. The temperature of the tissue does not exceed the temperature threshold of 50°C in any cases considered. Below this temperature threshold, cellular damage might not be achieved hence no lesion can be induced.

For an applied voltage of 50 V, it is possible to exceed the temperature threshold of 50°C, and it is possible to induce thermal necrosis. After 5 minutes, at this voltage level, the lesion volume achieved is irregular, particularly for geometries with a small number of helices. As time and/or applied voltage increases, a more regular and larger lesion volume is induced. For a larger number of helices, the lesion volume is also larger, although the increasing number of helices leads to a horizontally asymptotic increase of the lesion volume.

Finally, as expected, results show a smaller lesion volume when a temperature threshold of 60°C is considered for assessing the lesion size. Despite these smaller volumes, it can be assured that the lesion was, in fact, induced because cellular death occurs almost instantaneously.

It can be concluded that the electrode geometry has a significant impact on the lesion volume created. A higher stent density mesh, which is obtained using a larger number of helices, leads to a larger and more regular lesion, which will depend also on the value of the applied voltage and the duration of the RF ablation procedure. However, as the number of helices increases, the increased volume is less significant.

Commercial stents solutions are available that follow the geometries expressed in this work and, therefore, they can be used as a part of a RF ablation procedure considering the solution presented in chapter 4.

CHAPTER 7

RF Ablation of a Cholangiocarcinoma: Numerical Simulation

...there is hidden order in Nature, to be found only by patient search.

Garrett Birkhoff

7.1 Introduction

Cholangiocarcinoma is a malignant cancer arising from the neoplastic transformation of the epithelial cells lining the intra-hepatic and extra-hepatic bile ducts. It is the second most common primary hepatic malignancy and mortality rates are increasing worldwide [GBS+10]. Because there are no early symptoms, the majority of patients are diagnosed at an advanced stage, when surgical therapies are excluded [GA10]. Biliary obstruction in patients with unresectable cholangiocarcinoma can usually be managed by percutaneous or endoscopic self-expandable mechanical stents because

of their feasibility and lower risk of cholangitis[1] [PPH+09]. As nitinol stents can be used to reduce stricture problems of the bile duct, these can be also considered as potential electrodes for hyperthermia treatments.

In this chapter, it is presented the finite element modelling and analysis of a stent-based electrode, which is located in the common bile duct, next to the portal vein and the hepatic artery (the portal triad) and evaluation of the volume of the lesion obtained with this type of electrode.

First results indicated that the tissue lesion induced using this kind of electrode is not entirely uniform due to the convective heat transfer associated to the blood flow on the portal vein and hepatic artery. Also, it was verified that the tissue next to the electrode ends are preferentially heated which also contributes to obtain a non-uniform lesion.

In order to overcome this situation, it was considered the possibility of modifying the properties of the biological tissue, particularly the in the middle section of the tumour. It has been demonstrated that it is possible to increase the tissue heating during a RF ablation procedure by injecting a saline solution, thus modifying the electrical conductivity, energy deposition and heating of the tissue [CH97, GAG+01, MNM+97]. This procedure is commonly referred as saline-enhanced RF ablation, and it was already introduced in section 3.3.5. This procedure is also considered in the study presented in this chapter.

The numerical results show that it is possible to reduce irregularity of the volume obtained, although blood perfusion has a significant impact in the final result.

7.2 RF Ablation Without Saline Solution

7.2.1 Theoretical Model

The numerical simulation of the models consists of the analysis of a coupled thermal electrical problem. As described earlier in sections 2.3.2 and 4.3.1, the temperature at each point of the tissue can be expressed by the bioheat equation:

$$\rho c_p \frac{\partial T}{\partial t} = \nabla \cdot k \nabla T - \omega_b c_b (T - T_b) + Q_m + q \tag{4.2}$$

The energy generated by the metabolic process, Q_m, can be neglected since it is very small. Also, the term $\omega_b c_b (T - T_b)$, which refers to blood perfusion in the tissue,

[1] cholangitis – infection of the biliary tract

is neglected due to the presence of the porta vein and the hepatic artery. The blood temperature in these large blood vessels is considered unaffected by the thermal field in the surrounding tissue [Cha80]. Also, the blood flow is considered as a moving heat sink which adds the following contribution to the right hand of Equation (4.2):

$$-\rho_b c_b \mathbf{u}_b \cdot \nabla T \tag{7.1}$$

where ρ_b is the blood density [kg/m^3] and $\mathbf{u}_b$ is the velocity of the blood [m/s]. Adding this contribution to the right hand of Equation (4.2), it is obtained the Chen and Holmes model [AXH94].

The rest of the theoretical model, concerning the electrical part of the problem, follows the description of section 4.3.1: the electrode energy deposition in Equation (4.2), q, is due to Joule loss, and it can be calculated considering a RF voltage is applied between the stent and the return pad. The resulting voltage through the domain obeys Laplace's equation (Equation (4.4)).

At each iteration, Equation (4.4) is evaluated in order to calculate the distributed heat source, q, to be used in Equation (4.2) plus the contribution expressed in Equation (7.1). Then, temperature distribution is calculated and the tissue's electrical conductivity, which is temperature-dependent, is recalculated.

The steps during the solution of the finite element model started at 0.01 s and they were subsequently and automatically controlled by the solver software.

7.2.2 Description of the Model

Model Geometry

In this work, it was considered a simplified 3D model of the porta hepatis. The porta hepatis is a transverse fissure of the liver where the portal vein and the hepatic artery enter the liver, and the bile duct leaves. The cholangiocarcinoma can occur anywhere along the intra-hepatic or extra-hepatic biliary tree, and approximately 60% to 80% of cholangiocarcinomas encountered are located in the perihilar region [NPS$^+$96].

The 3D model was created considering an external cylinder (liver) with a radius of 100 mm and height of 100 mm. The bile duct and the portal vein are modelled as cylinders with a radius of 5 mm, and the hepatic artery is a cylinder with radius of 2 mm [TVT$^+$06].

The portal vein and the bile duct are positioned on a circumference of 6 mm radius, and separated by an angle of 120°. The hepatic artery is located so the minimum

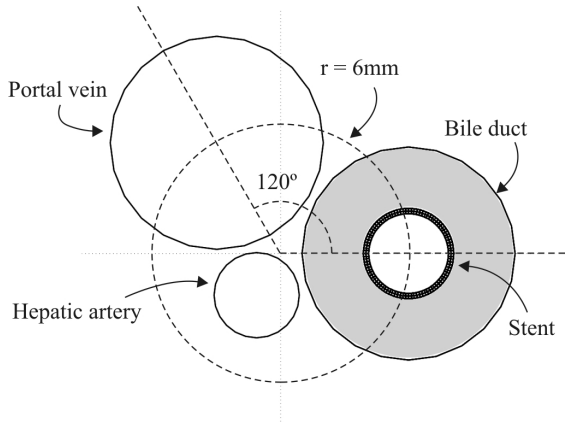

Figure 7.1: Cross sectional representation of the location of portal vein, hepatic artery, and bile duct in the considered model. The tumour is represented by the shaded area inside the bile duct. The stent-based electrode is placed inside the tumour.

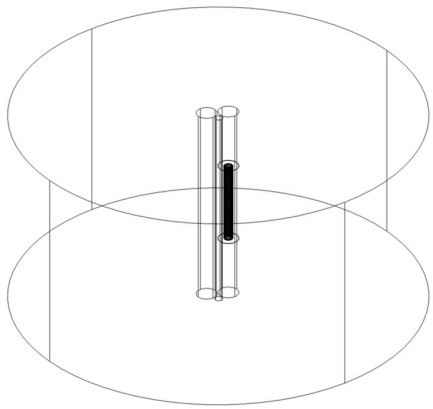

Figure 7.2: Simplified model of the portal hepatis.

distance between the three ducts is the same. The tumour is represented by a tube of 40 mm length, 5 mm radius and 3 mm thickness, placed in the middle of the bile duct. In Figure 7.1, it is shown the considered positions of the blood vessels and the bile duct. The tumour is represented by the shaded area inside the bile duct.

The electrode is made up of 24 nitinol wires with 0.25 mm diameter. Each wire is a helix of radius 2 mm with a pitch of 25 mm. The whole electrode is 40 mm long placed inside the tumour. In Figure 7.2, it is depicted the model considered in this simulation.

Table 7.1: Blood vessels properties used in the numerical simulation of the cholangiocarcinoma RF ablation.

Material	**Diameter** [**mm**]	**Blood perfusion** [**ml/min**]
Portal vein	10	327.55
Hepatic artery	4	20.5

Table 7.2: Material properties used in the numerical simulation of the cholangiocarcinoma RF ablation.

Element	**Material**	ρ [**kg/m^3**]	c [**J/kg·K**]	k [**W/m·K**]	σ [**S/m**]
Electrode	Nitinol	6450	840	18	$1 \cdot 10^8$
Hole	Air	1.202	1	0.025	0
Tissue	Liver	1060	3600	0.512	$\sigma_l(T)$
Tumorous tissue	Tumour	1060	3600	0.512	$\sigma_t(T)$
Blood vessels	Blood	1000	4180	0.543	0.667

Material Properties

The material properties required for solving the models considered in this work were obtained from the preceding work presented in chapter 5 and from literature [HST+01, HST+03, TVT+06]. These values are summarized in Table 7.1 and Table 7.2.

Both electrical conductivities for healthy and tumorous tissue were considered temperature-dependent, increasing 2% per degree Celsius. At 100°C, these values drop to 0.001 S/m, allowing this way to simulate the electrical insulation verified when gas forms next to the electrode above this temperature value. The electrical conductivity of the liver was set to 0.13 S/m at 25°C, and, for the tumorous tissue, it was considered equal to 0.269 S/m, also at 25°C.

Boundary Conditions

Regarding the electrical problem, numerical simulations were performed considering constant source voltages of 20, 22, 24, 26, 28, 30 and 35 V, applied to the stent-based electrode boundaries. The external boundary of the model was considered at ground potential, simulating this way a return path located away from the active electrode.

The temperature at the external surfaces of the model, the initial temperature of the tissues and the temperature of blood were set to the temperature value of 37°C.

The stent structure was created in AutoCAD (Autodesk, Mill Valley, California, USA) and exported in 3D ACIS format to COMSOL Multiphysics 4.1 (COMSOL, Inc. Burlington, MA, USA). The remaining parts of the model were modelled within COMSOL Multiphysics, which was also used for 3D finite element analysis.

All models were solved with PARDISO solver considering a RF ablation procedure of 10 minutes (600 seconds). Each model took an average time of 2.5 hours to solve, except for the model in which the applied voltage was set to 35 V. In this case, the model took over 17 hours of computing to be solved. All models were solved in a PC with an Intel Core 2 Quad CPU @2.34Ghz, with 8GB of RAM, on a 64 bits platform (Windows Vista).

7.2.3 Determination of the Volume Size

As in previous simulations, the assessment of the volume size of the induced lesion is considering a temperature threshold criterion. For the sole purpose of comparison, there were considered two temperature thresholds: 50 and 60°C. The volume of tissue within the isothermal surface defined by one of these values is considered as destroyed.

The volumes were calculated using COMSOL Multiphysics. For this, it was integrated the volume where the temperature was equal or greater than the value of temperature threshold. The same procedure was followed in the remaining of the present study.

7.2.4 Results

In Figures 7.3 and 7.4, there are presented the volumes obtained considering isothermal surfaces of 50 and 60°C, respectively. It can be observed that these volumes increase almost linearly with time, except for an applied voltage of 35 V. In this case, the volume stops growing after approximately 380 seconds. At this point, the temperature of the tissue adjacent to the electrode reaches the value of 100°C, and its impedance rises significantly, insulating the electrode. This can be observed in Figure 7.5, where it is presented the graphic of the current versus time. After 380 seconds, the electric current starts to decrease, and it drops significantly near to 400 seconds. As it can be noticed, the insulation of the electrode only occurs at 35 V. The lower values considered for simulation did not heat the tissue excessively.

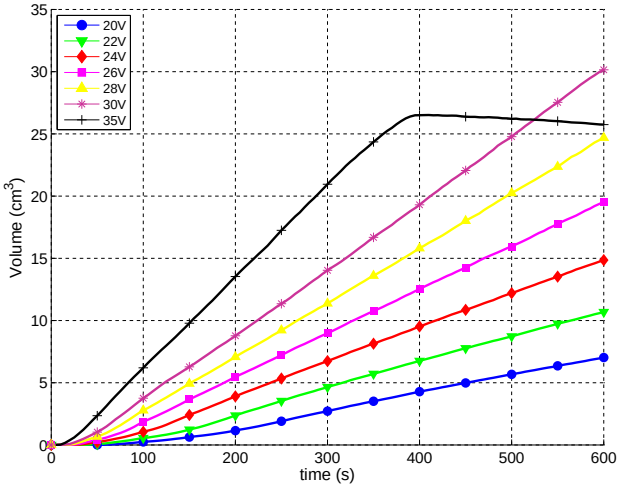

Figure 7.3: Volumes obtained considering an isothermal surface of 50°C for applied voltages from 20 to 35 V.

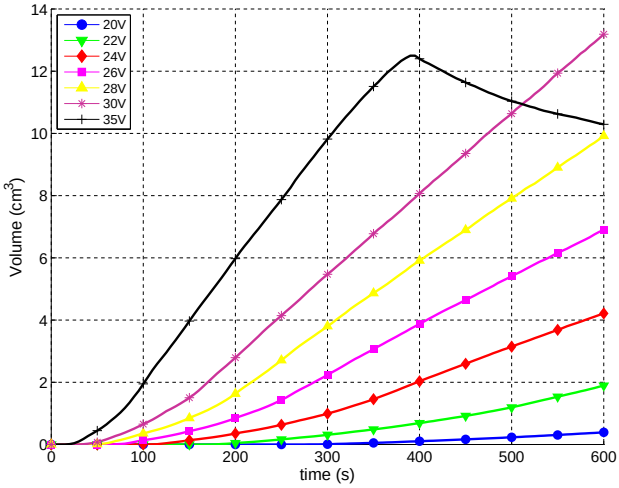

Figure 7.4: Volumes obtained considering an isothermal surface of 60°C for applied voltages from 20 to 35 V.

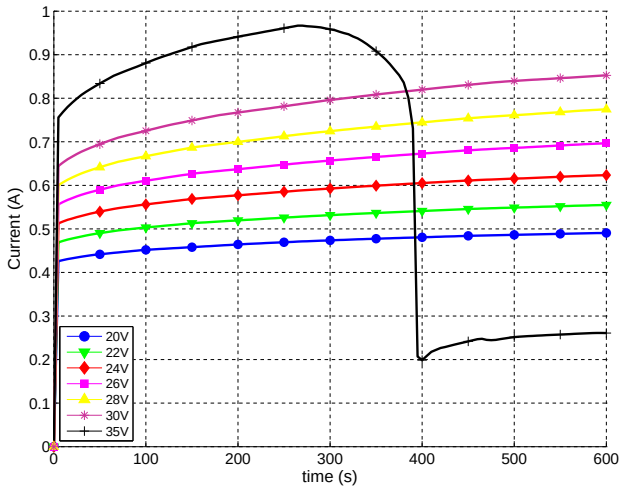

Figure 7.5: Electrical current delivered by the electrode for applied voltages from 20 to 35 V.

In both Figures 7.3 and 7.4, it can also be noticed an unexpected tendency: after 380 seconds, the volume does just not stop growing, but it starts to decrease. Naturally, the tissue does not recover after being thermally destroyed, particularly when considering a volume enclosed by an isothermal surface of 60°C, where thermal necrosis is achieved almost instantaneously. Actually, as soon as the electric current decreases, energy deposition by Joule effect is less significant. At this point, the convective heat transfer due to the presence of the blood vessels starts to cool down the surrounding tissue, thus the isothermal surface decreases, which explains this volume reduction. In fact, it is the temperature of the tissue that reduces, not the volume of damaged tissue.

Besides the size of the volume of induced lesion, the shape of the volume is of extreme importance because it is intended to damage only the tumour and to reduce any risk of harming the bile duct severely.

In Figure 7.6 and Figure 7.7 are presented the volumes delimited by an isothermal surface of 50°C at 20 and 35 V, respectively. It can be observed in Figure 7.6 that, at first, the temperature exceeds the 50°C threshold in the tissue adjacent to the ends of the electrode. The whole rest of the tumour is finally heated as time elapses. The same fact is observed in Figure 7.7, although, in this case, the tissue is heated up much rapidly. It becomes clear that the convective heat transfer due to the blood flow has a significant effect on the way the volume grows. At 20 V, the tissue on the side of

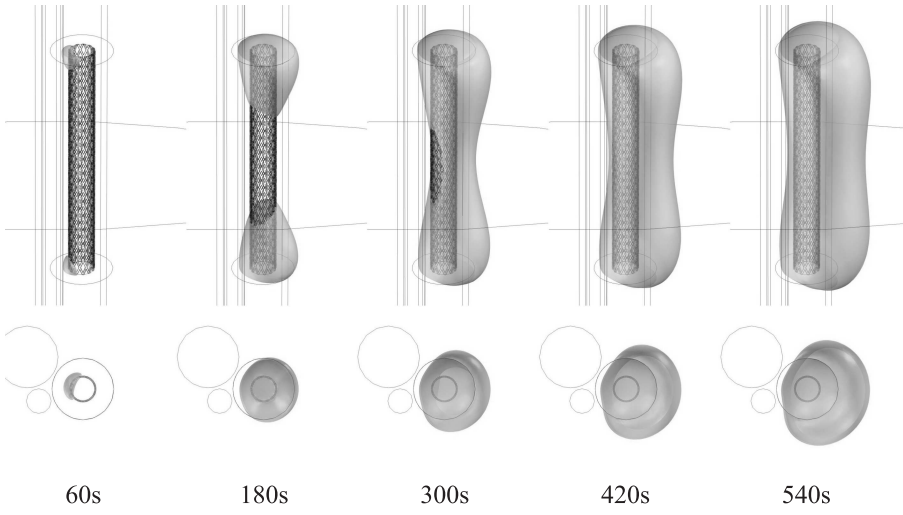

Figure 7.6: Volume obtained considering an isothermal surface of 50°C for an applied voltage of 20 V.

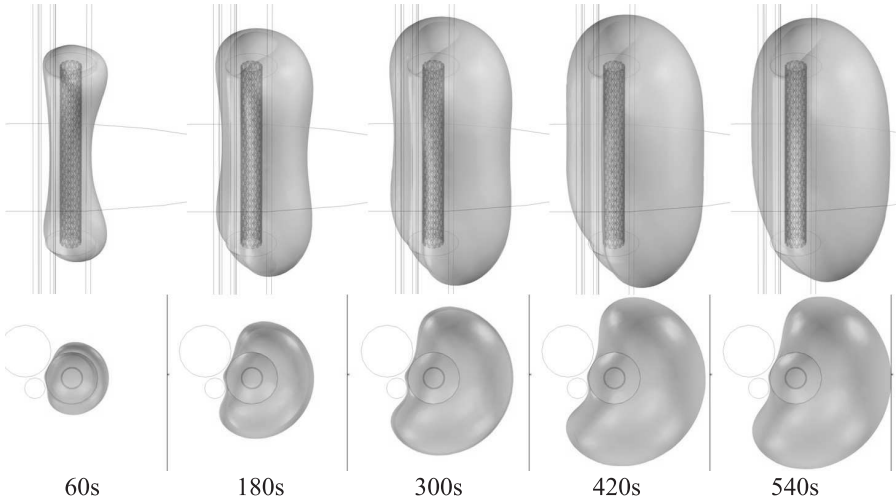

Figure 7.7: Volume obtained considering an isothermal surface of 50°C for an applied voltage of 35 V.

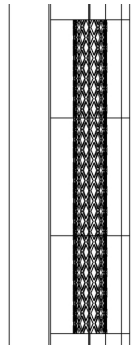

Figure 7.8: Detail of the porta hepatis model showing the tumour divided in three sections. The presence of the saline solution in the middle portion of the tumour is simulated increasing the electrical conductivity of the middle section of the tumour model.

the blood vessels is hardly heated. On the other hand, at 35 V, the energy deposition overcomes the cooling effect due to convective heat transfer.

7.3 Saline-Enhanced RF Ablation: First Approach

It was verified in the previous section that the tissue lesion induced using the stent-based electrode is not uniform due to the convective heat transfer associated to the blood perfusion of the portal vein and hepatic artery. Also, it was verified that the tissue next to the electrode ends is preferentially heated, which also contributes to obtain a non-uniform lesion. To minimize this difficulty, it is intended to change the electrical conductivity of the tumorous tissue in order to increase the energy deposition in the middle section of the tumour. In this section, it is presented one to the approaches that was considered to study this procedure.

7.3.1 Modelling the Saline Solution in the Tissue

As expected, the numerical modelling follows the detail description presented in section 7.2.2. The difference is in how the tumorous tissue is handled in the model.

The model of the tumour consists of a tube with length of 40 mm, radius of 5 mm, and thickness of 3 mm. This tube was then cross-sectioned into three parts for simulating the volume regions with different electrical conductivities (Figure 7.8). The middle section of the tumour has a height of 15 mm, and each end section has a height of 12.5 mm. The presence of the saline solution in the tumorous tissue is simulated by varying the electrical conductivity in the middle section of the tumour.

The properties of the materials considered in the model are those presented in Table 7.1 and Table 7.2. However, the electrical conductivity of the tumour is handled differently. For the electrical conductivity of the outer sections of the tumour, it was considered a value of 0.269 S/m at 25°C, varying 2%/°C. The middle section corresponds to the tumour volume with a saline solution. In this volume, it is considered that the electrical conductivity is increased by a multiple of the electrical conductivity of the outer sections, i. e.,

$$\sigma_{tc} = ks \cdot \sigma_{te} \tag{7.2}$$

where σ_{tc} is the electrical conductivity of the middle section of the tumour, σ_{te} is the electrical conductivity of the tumour ends, and ks is a proportional factor. There were considered enhanced-saline RF ablation models for ks varying from 2 to 5. It was also considered that σ_{tc} declines abruptly to 0.001 S/m above 100°C. The case for $ks = 1$ corresponds to a RF ablation without saline solution, presented in the previous section.

Finally, the boundary conditions of the proposed model are the same to those described in section 7.2.2.

7.3.2 Results and Discussion

From Figure 7.9 to Figure 7.14, there are depicted the graphs of the curves of the volume of damaged tissue versus time, considering volumes delimited by isothermal surfaces of 50 and 60°C, and for applied voltages of 20, 28 and 35 V. As expected, increasing the applied voltage increases the volume of induced damaged tissue. However, it can be noticed that for an applied voltage of 20 V (Figure 7.9 and Figure 7.10), the higher the electrical conductivity of the middle section of the tumour tissue, the lower the volume obtained. This situation is completely inverted as the applied voltage increases. In Figure 7.11 and Figure 7.12, it is possible to observe that, after 10 minutes, it is obtained a larger volume of damaged tissue as the electrical conductivity of the middle section of the tumour tissue increases. In fact, considering a volume delimited by an isothermal surface of 50°C, this situation is already verified for an applied voltage of 22 V. On the other hand, for a volume enclosed by an isothermal surface of 60°C, this is only verified when applied voltage is above 26 V.

Major differences on the value of the volumes are verified as the temperature of the tissue reaches 100°C. Similarly to what was observed at the numerical solution obtained considering no saline solution for an applied voltage of 35 V, it is possible

to observe in Figure 7.13 and Figure 7.14 that, at some instant, the volume of injured tissue does not longer increase significantly with time: the lower the value of *ks* the sooner the volume stops growing. Again, this can be explained with the sudden decrease of the electrical conductivity of the tissue as soon as the temperature reaches 100°C next to the electrode. From this point, the electrical current decreases and so the tissue is no longer significantly heated, which leads to a steady volume lesion. For lower values of *ks*, the tissue surrounding the electrode heats up more quickly. This leads to a sooner electrical isolation of the electrode, and so a smaller volume of damaged tissue is obtained. This was verified for both volumes delimited either by an isothermal surface of 50 or 60°C.

In Figure 7.15, it is depicted the representation of the norm of the current density close to the electrode for an applied voltage of 35 V, considering $ks = 2$ from 240 s to 540 s. This interval corresponds to the time frame at which the temperature of the tissue reaches 100°C. As soon as the voltage is applied, a large current density is attained, especially at both ends of the electrode which causes the high heating of the ends of the tumour tissue. The ends of the tumour model confront the air volume located above and below it. This leads to a larger energy deposition at these points than in the middle portion of the tumour. As the tissue is heated up over a temperature value of 100°C, the electric conductivity decreases as well as the electric current. The electric current density becomes very low at the ends of the tumour at first, and it finally drops significantly all over the tissue surrounding the electrode, leading to a slow damaged tissue growth with time, as verified in Figures 7.13 and 7.14.

In Figure 7.16 and Figure 7.17, there are depicted the different values of volume delimited by an isothermal surface of 50°C obtained for a constant value of *ks* at the different applied voltages considered. These graphs show that the amount of damaged tissue is larger for increasing values of voltage. Also, as *ks* increases, the volume of damaged tissue also increases, as it was stated before. This is particularly clear for an applied voltage of 35 V. For larger values of *ks*, the tissue takes longer to heat above 100°C, so the electrical conductivity of the tissue adjacent to the electrode does not drop, and the electric current continues to flow into the tissue. For voltage values up to 30 V, there is no electrode insulation, and the volume increase slightly as *ks* increases. Comparing the curves of Figure 7.3, which corresponds to the numerical solution without saline solution, with Figures 7.16 and 7.17, it can be observed that the values of volume after 10 minutes are slightly larger for increasing values of *ks*. Also, it can be noticed that, at 35 V, the electrode insulation occurs later. Without

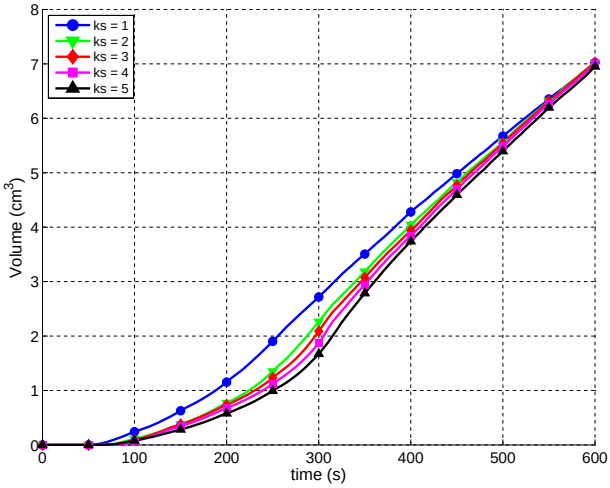

Figure 7.9: Volume of lesion obtained for an applied voltage of 20 V considering an isothermal surface of 50°C.

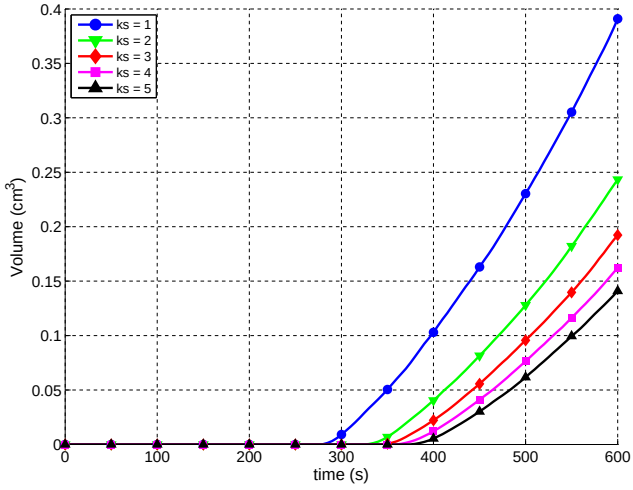

Figure 7.10: Volume of lesion obtained for an applied voltage of 20 V considering an isothermal surface of 60°C.

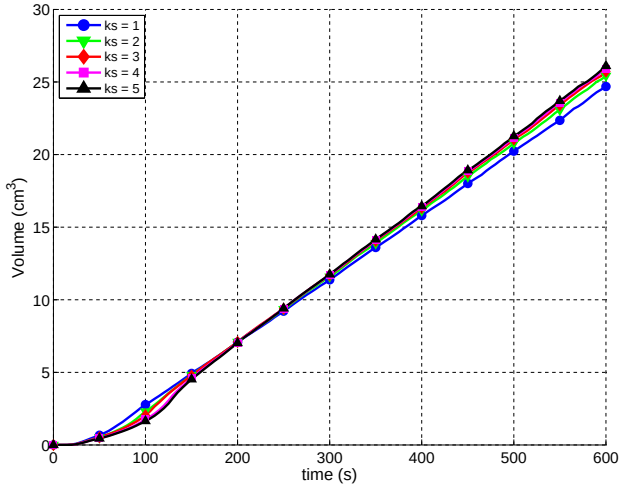

Figure 7.11: Volume of lesion obtained for an applied voltage of 28 V considering an isothermal surface of 50°C.

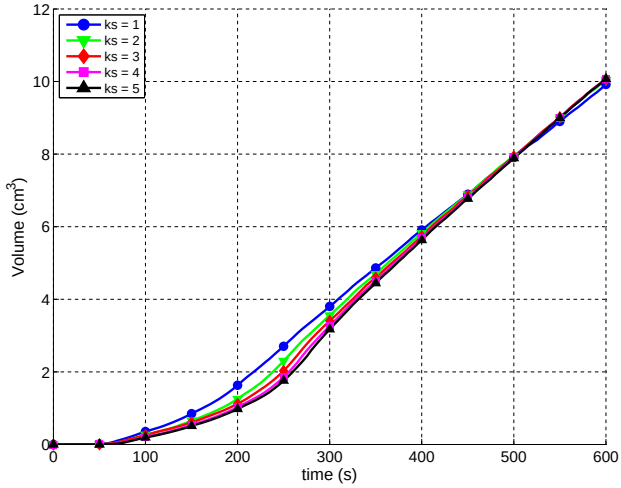

Figure 7.12: Volume of lesion obtained for an applied voltage of 28 V considering an isothermal surface of 60°C.

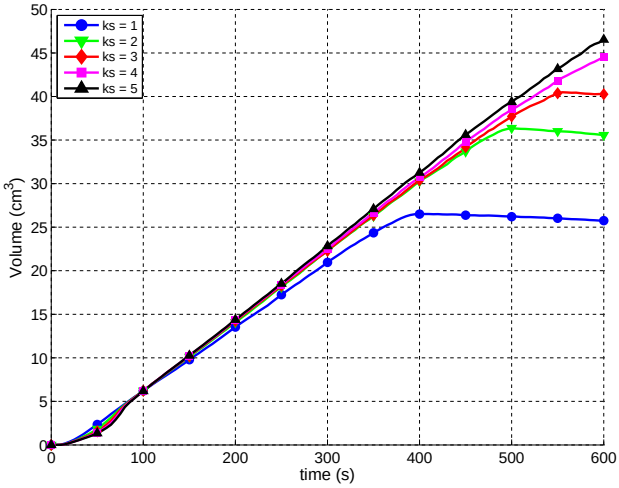

Figure 7.13: Volume of lesion obtained for an applied voltage of 35 V considering an isothermal surface of 50°C.

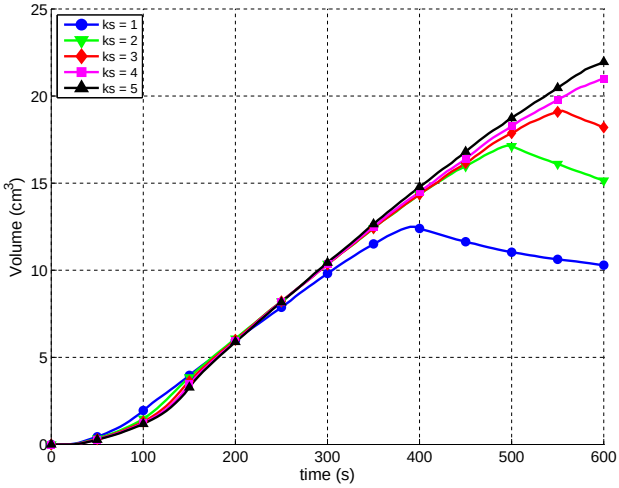

Figure 7.14: Volume of lesion obtained for an applied voltage of 35 V considering an isothermal surface of 60°C.

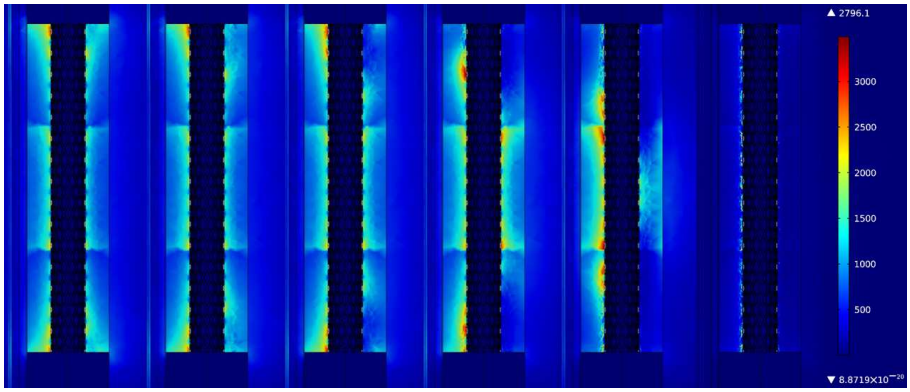

Figure 7.15: Current density (norm) obtained for an applied voltage of 35 V with $ks = 2$.

saline solution, the obtained volume stops growing after 380 seconds. This value is about 500 seconds for $ks = 2$, and there is no electric insulation for $ks = 5$.

At this point, it is necessary to set a compromise between the applied voltage and the enhanced electrical conductivity of the tissue. For that, not only the size of the volume obtained is important but also its shape is clearly an relevant factor to take into account. It is necessary to achieve a regular volume so the tumour tissue is preferably damaged.

As already mentioned, apart from the cases where the tissue temperature reaches the value of 100°C, it is possible to observe that, for the same applied voltage, the values obtained are approximated. Although these values are very alike, the shape of the volumes obtained differs. From Figure 7.18 to Figure 7.20, there are depicted the volumes obtained considering an isothermal surface of 50°C at 22 V. The volumes depicted in Figure 7.18 were obtained previously, when no saline solution was considered ($ks = 1$). Figure 7.19 and Figure 7.20 were obtained for $ks = 2$ and $ks = 5$, respectively.

After 180 seconds, it is possible to observe significant differences in the shapes of the volume obtained. The main difference is in the middle portion of the volume. As ks increases, the middle section of the tumour takes longer to heat up, particularly on the side next to the blood vessels due to convective heat transfer. On the other hand, as time elapses, the volume keeps growing on the opposite side of the blood vessels, becoming bigger for larger values of ks.

Another interesting observation is related to the voltage applied and the shape of the volume obtained. As it was already mentioned, the volume of damaged tissue

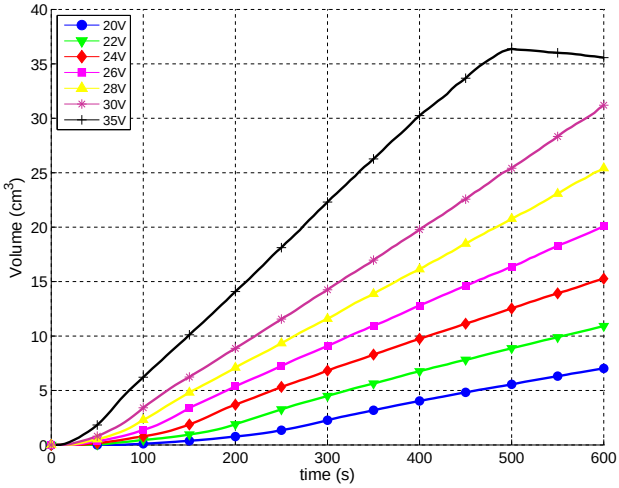

Figure 7.16: Volume of lesion obtained for several voltage values considering isothermal surfaces of 50°C, with $ks = 2$

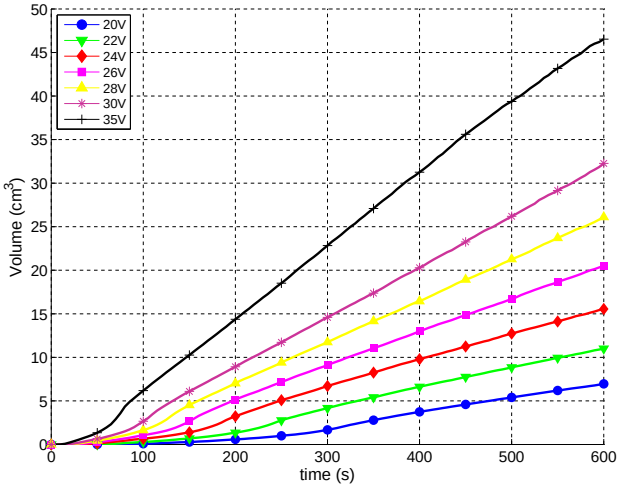

Figure 7.17: Volume of lesion obtained for several voltage values considering isothermal surfaces of 50°C, with $ks = 5$

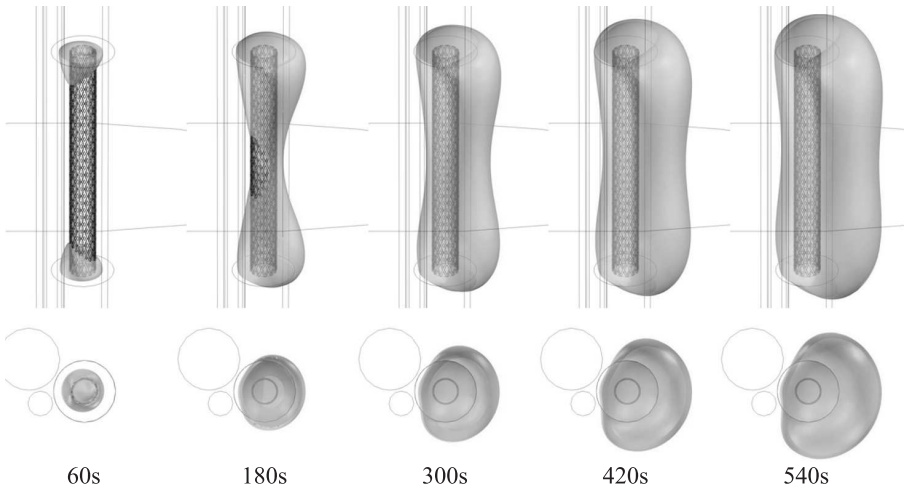

Figure 7.18: Volume of lesion considering an isothermal surface of 50°C at 22 V without saline solution ($ks = 1$)

.

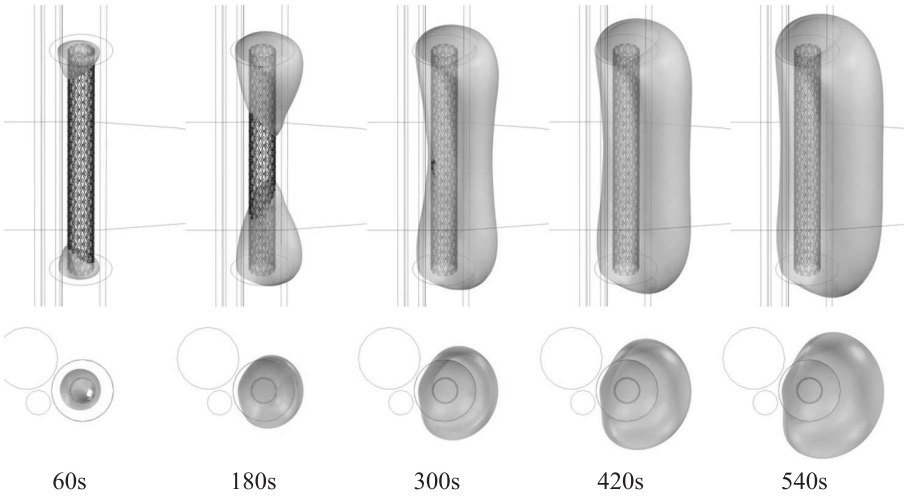

Figure 7.19: Volume of lesion considering an isothermal surface of 50°C at 22 V for $ks = 2$

.

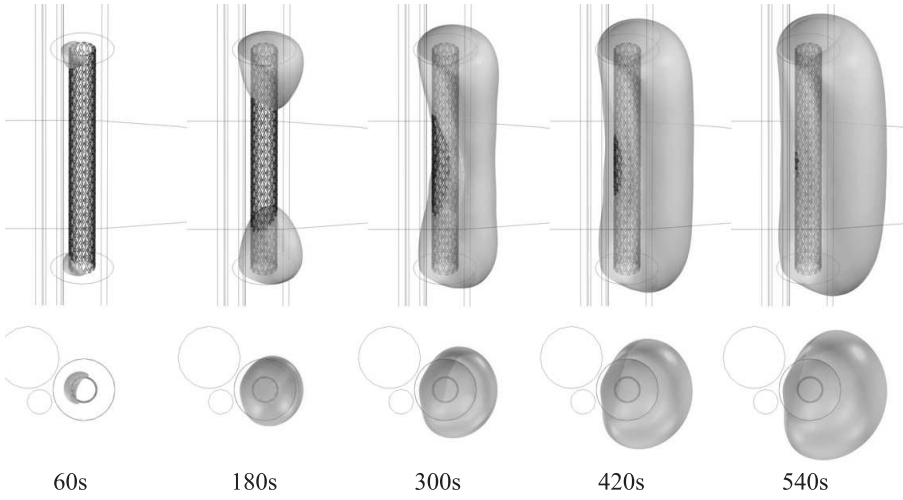

Figure 7.20: Volume of lesion considering an isothermal surface of 50°C at 22 V for $ks = 5$

.

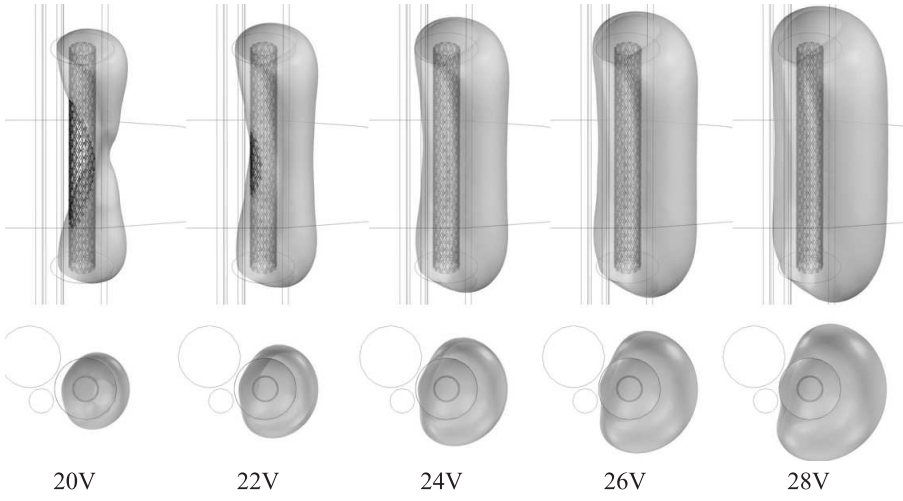

Figure 7.21: Volume of lesion obtained for different applied voltages considering an isothermal surface of 50°C and $ks = 3$

.

increases as the applied voltage increases. However, the volumes obtained for higher voltages are more regular. As the applied voltage rises, the tissue is heated more rapidly, this way overcoming the convective heat transfer due to the blood vessels. In Figure 7.21, it is represented the volumes obtained for different applied voltages, considering an isothermal surface of 50°C and $ks = 3$. Again, volumes are larger as the applied voltage increases, also the volumes are more regular as stated before.

7.4 Saline-Enhanced RF Ablation: Second Approach

So far, diffusion of the saline solution across the tumorous tissue was not taken into account and so the shape of the lesion induced in the tissue might not be totally accurate. Considering the small dimension of the bile duct, and considering that it is important not to injure this organ, it is very necessary to obtain a more accurate volume of damaged tissue in order to prevent the destruction of the bile duct.

To overcome the limitations of the previous model, in the following study, it is intended to perform a numerical analysis of a radiofrequency ablation procedure using the proposed stent-based electrode and considering a Gaussian function to represent the diffusion of the saline solution across the tumorous tissue. This analysis is performed taking into account different values of concentration for the saline solution, as well as different patterns for the saline solution spread across the tumour, from a narrow distribution to a wide one.

7.4.1 Conductivity of the Tumorous Tissue

The theoretical ground, as well as the model geometry considered, is the one presented in section 7.2. The main difference is related to the electrical conductivity of the tumour. This is considered temperature-dependent and position-dependent. It was considered that a saline solution was injected in the middle portion of the tumour and it diffused symmetrically to both sides of it considering a Gaussian function. The geometric model created was obtained considering the axis of the tumour parallel to the z-axis and centred at $z = 5$, so the electrical conductivity will depend on the value of z.

Taking into account the injected saline solution, the electrical conductivity in the middle of the tumour is considered a multiple of the electrical conductivity and it decreases as one moves from the middle to the ends of the tumour. Thus, the electrical

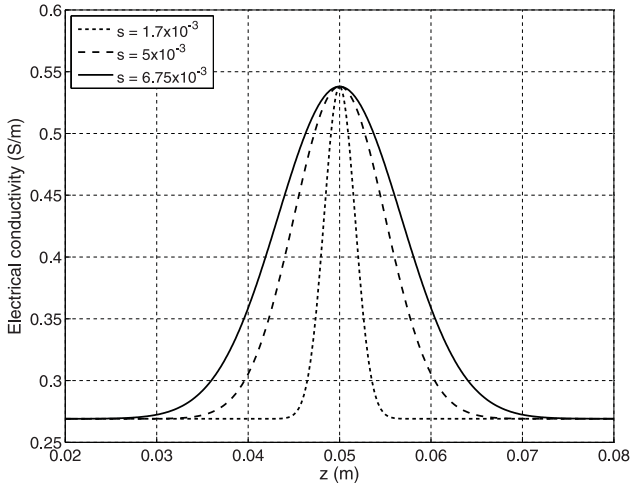

Figure 7.22: Representation of the electrical conductivity of the tumour enhanced with saline solution. The curves are obtained considering $ks = 2$, at 25°C. There are represented the three spread profiles considered in this study.

conductivity can be approximated to:

$$\sigma_t(T,z) = [1 + 0.02(T - T_{25^\circ\mathrm{C}})] \left[\sigma_{\text{tumour}} + \sigma_{\text{saline}} \exp \frac{(z-0.05)^2}{2s^2} \right] \tag{7.3}$$

where T is the temperature, z is the position on the z-axis (parallel to the axis of the tumour) and s is a measure of how the saline solution is spread along the axis of the tumour. σ_{tumour} corresponds to the electrical conductivity of the tumorous tissue at 25°C with a value of 0.269 S/m, σ_{saline} is the electrical conductivity of the saline solution, dependent of its concentration. The electrical conductivity of the saline is considered as a multiple of σ_{tumour}, i. e., $\sigma_{\text{saline}} = (ks-1)\sigma_{\text{tumour}}$, where $ks \geqslant 1$ (for $ks = 1$ there is no saline solution and the conductivity of the tumour is just temperature dependent).

The parameter s is a measure of how the saline solution spread along the tumour. A higher value of s corresponds to a wider bell-shaped function, as depicted in Figure 7.22. In the present analysis, it was considered three different values of s: $1.7 \cdot 10^{-3}$, $5 \cdot 10^{-3}$ and $6.75 \cdot 10^{-3}$. For these values, the electrical conductivity decreases to 66.6% of its peak value, which is verified at the middle of the tumour, at 0.25, 0.75 and 1 cm away from the middle of the tumour, respectively. In the presented analysis, it was considered ks varying from 1 (no saline solution) to 5. For example, in Figure 7.22, there are presented the curves of the electrical conductivity of the tumour for ks = 2 at 25°C.

Finally, as mentioned before, the electrical conductivity of the tumorous tissue, as well as the electrical conductivity of the liver tissue, were considered temperature dependent, increasing 2% per degree Celsius, and dropping to 0.001 S/m above 100°C, allowing this way to simulate the electrical insulation verified when gas forms at this temperature value.

All models were solved with PARDISO solver considering a RF ablation procedure of 10 minutes (600 seconds). The model had 808 262 tetrahedra, and each numerical problem took an average time of 2.5 hours to solve using a computer with an Intel Core 2 Quad CPU @2.34Ghz, with 8GB of RAM, on a 64 bits platform (Windows Vista).

7.4.2 Results and Discussion

The results presented in this section follow the volume assessment previously described, i.e, it is considered that the tissue undergoes through thermal necrosis if its temperature is above 50 or 60°C.

From Figure 7.23 to Figure 7.26, there are presented the volumes of damage tissue obtained for $s = 5 \cdot 10^{-3}$ and ks varying from 1 to 5, considering isothermal surfaces of 50 and 60°C. Results obtained at 20 V and 30 V are depicted. It can be observed that, as expected, increasing the applied voltage also increases the volume of induced damaged tissue.

It is shown in Figures 7.23 that, for an applied voltage of 20 V, the volumes obtained are slightly different as ks varies. As the electrical conductivity increases, the volume of damaged tissue obtained is somewhat smaller. However, these values tend to converge as time elapses and they are very similar after 10 minutes. This behaviour can be observed at every value of applied voltage considered. Nonetheless, the values of volume converge sooner as voltage increases. At 30 V (Figure 7.24), it can be noticed that the values converge close to 170 seconds. From this point, the values of volume slightly start to diverge and the volume obtained is larger for greater values of ks. It is possible to observe a similar behavior when considering a volume enclosed by an isothermal surface of 60°C (Figures 7.25 and 7.26). In this case, as expected, the volumes obtained are smaller and the values take longer to converge. For example, at 30 V (Figure 7.26) the values converge after approximately 400 seconds, but, at 20 V (Figure 7.26), they do not converge even after 10 minutes.

From Figure 7.27 to Figure 7.30, there are presented the values of the volume obtained varying the value of s. As ks and the applied voltage increase, it can be

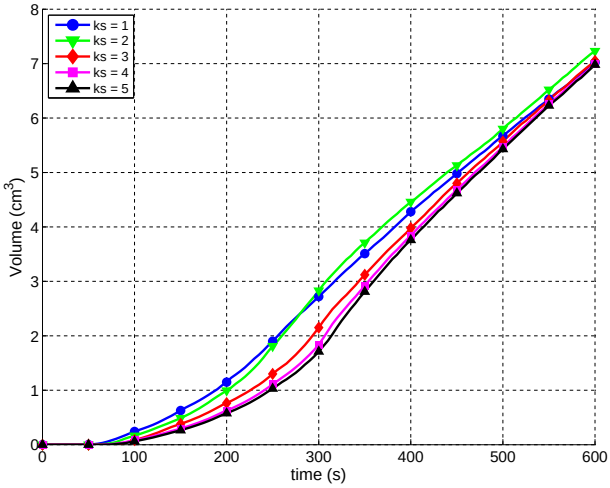

Figure 7.23: Volumes obtained for $s = 5 \cdot 10^{-3}$ considering an isothermal surface of 50°C for an applied voltage of 20 V

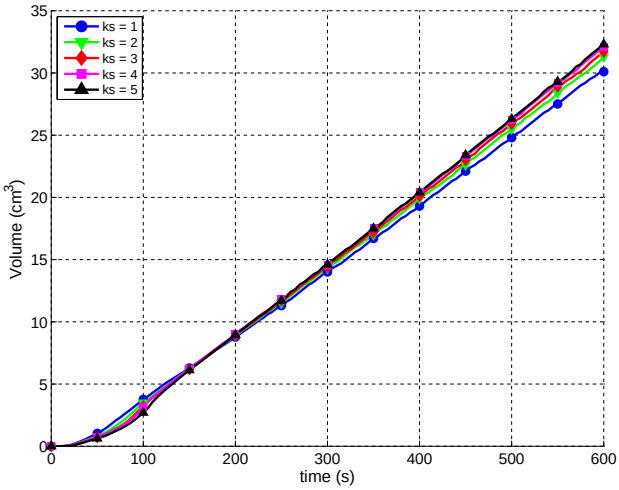

Figure 7.24: Volumes obtained for $s = 5 \cdot 10^{-3}$ considering an isothermal surface of 50°C for an applied voltage of 30 V

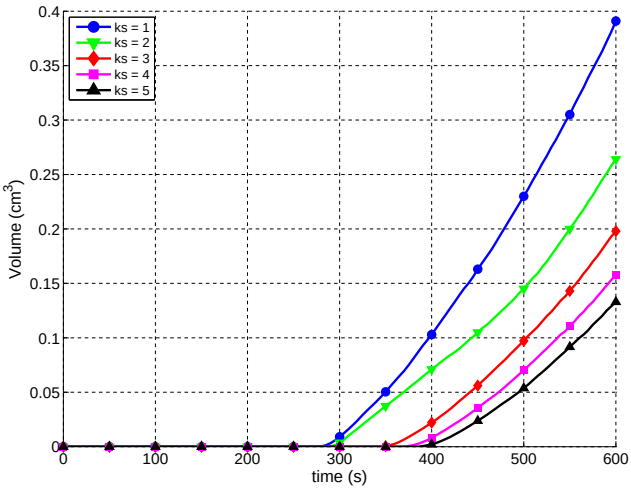

Figure 7.25: Volumes obtained for $s = 5 \cdot 10^{-3}$ considering an isothermal surface of 60°C for an applied voltage of 20 V

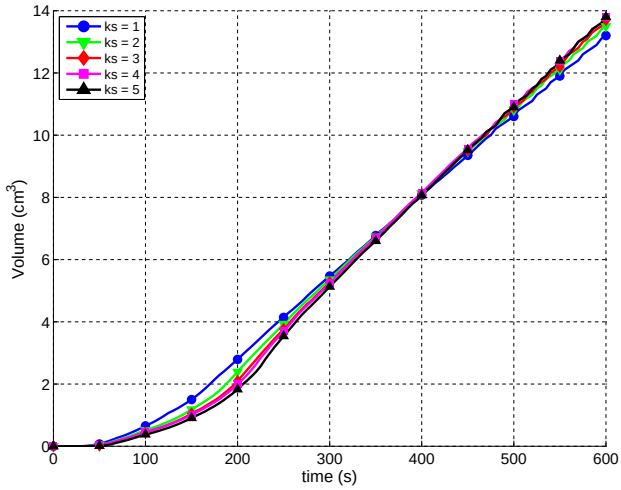

Figure 7.26: Volumes obtained for $s = 5 \cdot 10^{-3}$ considering an isothermal surface of 60°C for an applied voltage of 30 V

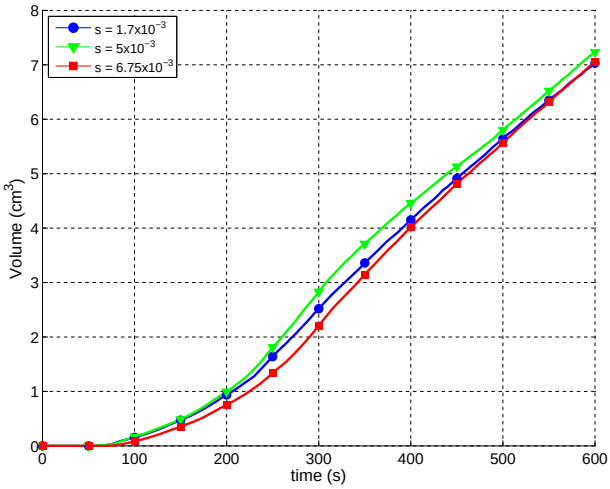

Figure 7.27: Volumes obtained considering an isothermal surface of 50°C at 20 V for $ks = 2$

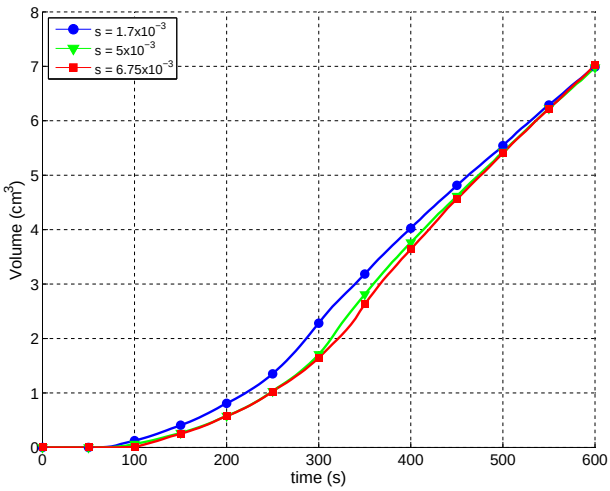

Figure 7.28: Volumes obtained considering an isothermal surface of 50°C at 20 V for $ks = 5$

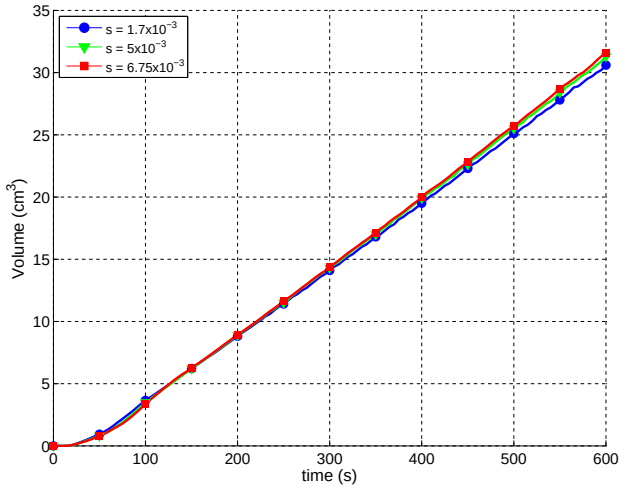

Figure 7.29: Volumes obtained considering an isothermal surface of 50°C at 30 V for $ks = 2$

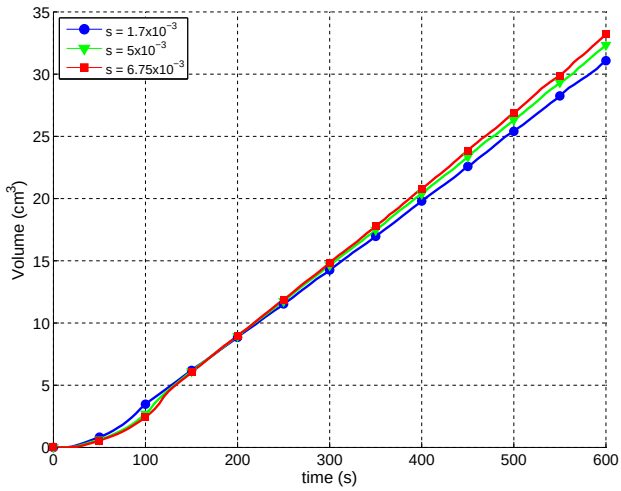

Figure 7.30: Volumes obtained considering an isothermal surface of 50°C at 30 V for $ks = 5$

observed that the values of volume obtained for different values of s do not differ significantly. Except for the situation depicted in Figure 7.27, the values obtained with $s = 1.7 \cdot 10^{-3}$ are, initially, somewhat larger. As time elapses, the volumes for $s = 6.75 \cdot 10^{-3}$ become bigger, exceeding the values obtained for other values of s.

As it was considered in the previous section, besides the size of the volume of damaged tissue obtained, it is clearly important to understand how the shape of the volume is influenced. It is necessary to achieve a regular volume so the tumorous tissue is preferably damaged saving the bile duct from any harm.

Recalling the Figure 7.6, in which no saline solution was considered, it can be observed that the ends of the tumour are preferentially heated first and the rest of the tumour is heated later. Also, it can be observed that the volume grows significantly on the opposite side to the blood vessels. Convective heat due to the presence of these major vessels has a significant impact on the shape of the volume obtained.

In Figure 7.31, it is presented the volume obtained for voltages from 20V to 28V considering $ks = 3$ and $s = 1.7 \cdot 10^{-3}$ after 5 minutes. Same results are depicted in Figure 7.32 but for $s = 6.75 \cdot 10^{-3}$. Again, the ends of the tumour are at first preferentially heated. However, the volume is more regular when considering a narrow diffusion of the saline solution in the middle portion of the tumour. This becomes more evident as ks and s increase. In Figure 7.33 and Figure 7.34, there are presented the volumes obtained at an applied voltage of 20 V for all the values of s considered in this study, with ks = 2 and ks = 5, respectively. Again, it can be observed that, as ks and s increase, the middle portion of the tumour takes longer to heat up. In a long term, this will lead to a large volume of damaged tissue, still, it will grow too large damaging not only the tumour but also the bile duct.

7.5 Conclusions

It this chapter, it was presented the numerical simulation for a RF ablation procedure of a cholangiocarcinoma using the proposed stent-based electrode. For this study, it was proposed the simulation of a conventional RF ablation and an enhanced-saline radiofrequency ablation. In this last case, it was intended to modify the electrical conductivity of the tissue in order to induce a more regular lesion, aiming the tumour.

The results obtained without enhancing the electrical conductivity show that it is possible to heat the tumorous tissue adjacent to the electrode, although the voltage applied and duration are important variables to take into account in order to achieve

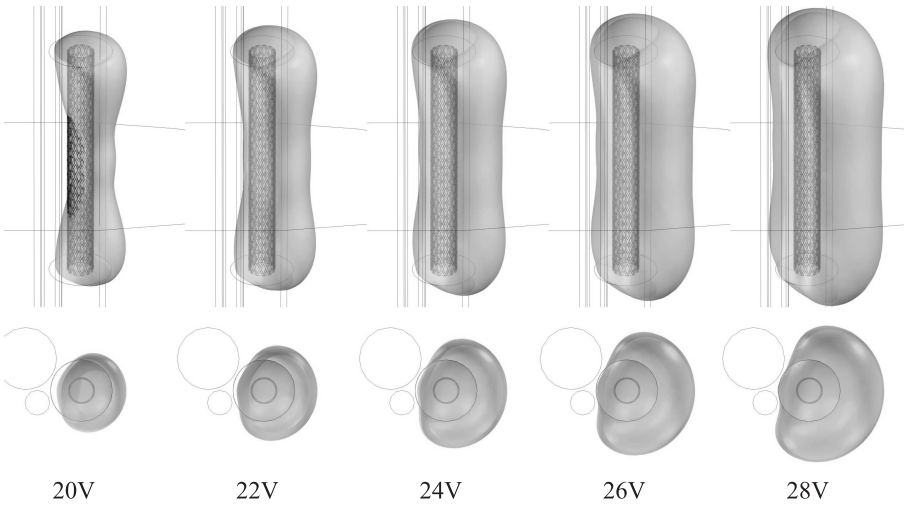

Figure 7.31: Volumes obtained considering an isothermal surface of 50°C with $ks = 3$ and $s = 1.7 \cdot 10^{-3}$ after 300 seconds

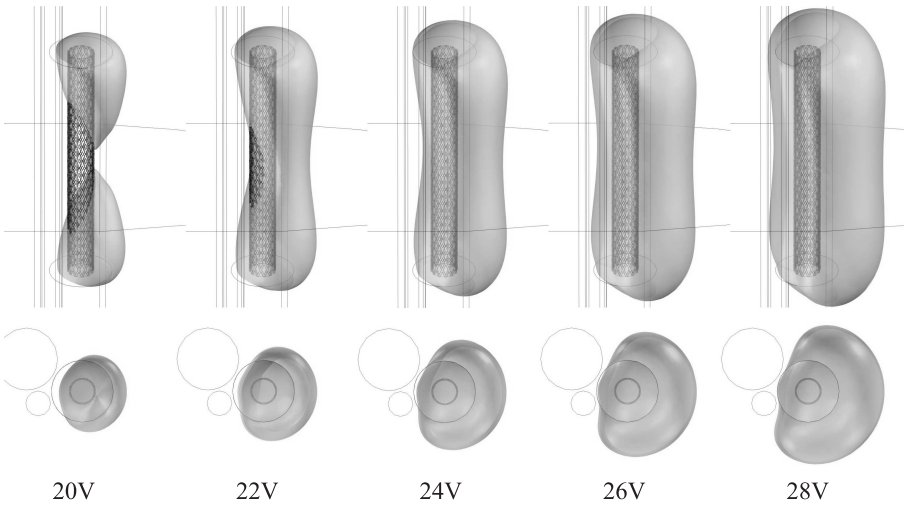

Figure 7.32: Volumes obtained considering an isothermal surface of 50°C with $ks = 3$ and $s = 6.75 \cdot 10^{-3}$ after 300 seconds

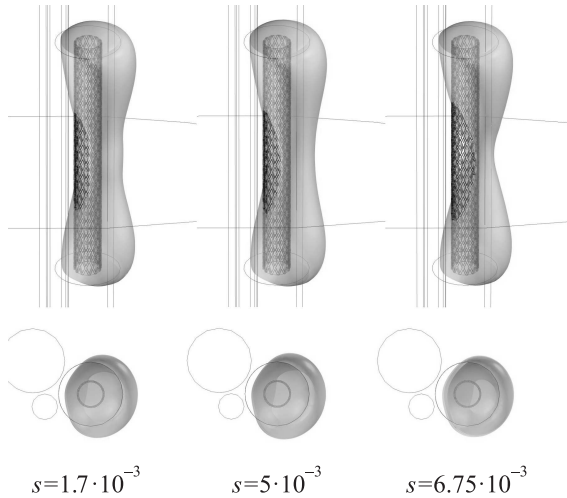

Figure 7.33: Volumes enclosed by an isothermal surface of 50°C at 20 V after 300 seconds with $ks = 2$

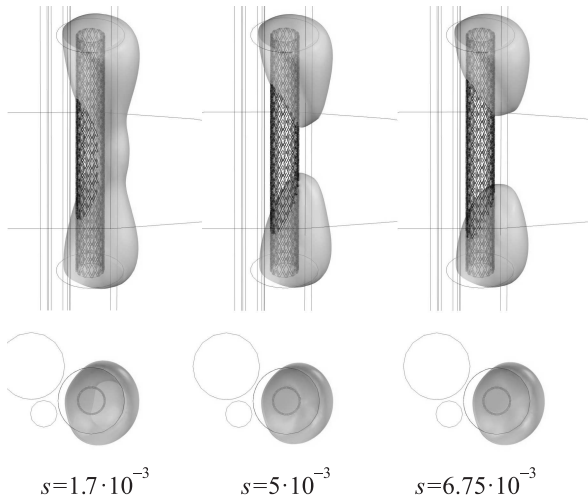

Figure 7.34: Volumes enclosed by an isothermal surface of 50°C at 20 V after 300 seconds with $ks = 5$

a preferred heating of the tumour. Large applied voltages lead to an induced lesion that grows too fast, in a non uniform manner, easily exceeding the dimension of the tumour and potentially harming the bile duct, as well as tissue around it. For lower voltages, it is possible to obtain a volume of induced lesion that grows slower, however, this volume still is not as uniform as at it would be ideal. Blood perfusion has also a meaningful effect on the temperature distribution around the bile duct, with a significant impact on the final size of the induced lesion.

As expected, altering the electric conductivity in the middle section of tumour tissue led to different shapes of volumes of damaged tissue. Two important facts should be highlighted:

1. As the electric conductivity of the middle section of the tumour increases the size of the volume of induced damage also increases;

2. As the applied voltage increases the volume obtained increases.

Comparing the size of the volumes with and without the infusion of saline solution, it can be noticed that the differences are not very pronounced. Increasing the conductivity leads to a slight increment of the size of the volume. However, the difference can be significant if the applied voltage is high enough. In this case, the volume size can be limited by the electrical insulation of the electrode when the temperature of the tissue adjacent to it exceeds the value of 100°C. When this occurs, there are gas formation and tissue charring that increase the electrical impedance of the tissue, which limits the power deposition.

Concerning the shape of the volume, increasing the electrical conductivity produced a more regular shape of the volume, particularly on the opposite side to the blood vessels: the convective heat transfer due to the blood flow in the porta vein and the hepatic artery has a strong influence on the shape of the volume between the blood vessels and the bile duct.

Also, it was verified that increasing the electrical conductivity excessively might lead, in a first stage, to an irregular shape. On the other hand, higher values of voltage produce more regular shapes.

Because it is more important to heat the tumour, the main concern is not to achieve a large volume of damaged tissue. Instead, it is necessary to induce a well-located lesion so the bile duct is not harmed as well during the radio frequency ablation procedure. Combining a relative high voltage while increasing slightly the electrical conductivity of the tumour might have this effect.

When considering a spread pattern of the saline solution on the tumour, which is represented by a position-dependence of the electrical conductivity, it was verified also a significant effect on the shape of the volume. A higher saline solution concentration, ks, associated to a wider diffusion along the tumour, s, lead to a steep heating of the ends of the tumour, thus obtaining an irregular induced lesion. A more regular shape could be achieved considering a relatively low saline solution concentration with a narrow diffusion width. Still, the blood flow in the porta vein and the hepatic artery have, again, significant impact on the final value of volume obtained.

Finally, the volume obtained is not perfectly regular as expected, and the simulations performed point out that the induced lesion may still exceed the tumour itself, which might damage the bile duct.

It should be noticed that, unlike the simplified model considered for the present numerical simulation, the porta hepatis is a more complex structure, with different pulsating blood flows and connective tissue which were not considered in the present work.

CHAPTER 8

Conclusion

"Would you tell me, please, which way I ought to go from here?"
"That depends a good deal on where you want to get to," said the Cat.
"I don't much care where " said Alice.
"Then it doesn't matter which way you go," said the Cat.

Lewis Carroll
in Alice's Adventures in Wonderland

8.1 Summary of the Research

In this work, it is proposed a stent-based electrode to be used in the hyperthermia treatment of tumours located in tubular organs, like the oesophagus, colon or bile duct. The types of cancer that are associated with this kind of organs – oesophageal cancer, colorectal cancer and cholangiocarcinoma – are, in most of the cases, incurable. Palliative cares of these pathologies involve reducing stricture problems caused by the occlusion of the lumen of these organs.

Due to its good mechanical and biocompatibility characteristics, nitinol self expandable metallic stents are a popular endo-prosthesis used for relieving these stricture problems. The experimental work performed show that, besides its mechanical applications, stents can be regarded as well as a potential electrode for performing RF ablation therapy on tumours located in these tubular organs. Further experimental work allowed to assess and characterize the size and shape of the volume of damaged tissue that can be induced with this type of electrode. The obtained results demonstrated that it is possible to achieve a regular volume of damaged tissue, that depends on the applied voltage and the duration of the procedure.

Also, during the experimental work, it was measured the electrical conductivity of the liver samples that were used. The obtained average value was considered in a numerical model, based on finite element method, in order to approximate it to the experimental set-up used in this study. The numerical results for temperature distribution and volume of induced lesion were in good agreement with those obtained experimentally.

From the validated numerical model, it was studied the effect of the geometry of the stent-based electrode on the size and shape of the volume of induced lesion. The stent can be considered as a set of nitinol wires shaped as helices, which resembles a mesh tube. When the number of helices varies, the mesh density of the stent changes, which naturally reflects on the temperature distribution during a RF ablation procedure. It was shown that, as the number of helices of the stent increases, the volume of induced lesion becomes larger and more regular. It could be proposed a stent-based electrode with the number of helices as large as possible to produce a large, regular lesion. However, when considering the application for the RF ablation of a cholangiocarcinoma, the catheter for percutaneously apply the stent should have a large diameter, which might hamper the insertion of the electrode. On the other hand, it was verified that increasing the number of helices leads to a minor volume increase, i.e., a denser mesh will not produce a significant increase of the volume of induced lesion. Numerical results showed that from 20 to 24 helices the volume does not increase significantly. Furthermore, it can be obtained a regular lesion for a lower number of helices. Considering that most of the commercial stents resemble the configuration of the proposed numerical model, those can be regarded as potential electrodes for RF ablation.

It was studied the application of the proposed stent-based electrode on the RF ablation treatment of a cholangiocarcinoma. The cholangiocarcinoma is a cancerous tumour of the bile duct, which is located next to two large blood vessels: the hepatic

artery and the porta vein. It was considered a simplified model of the porta hepatis, and it was simulated the RF thermal ablation of the tumour. The results showed that, as expected, the convective heat transfer associated to the blood flow in these vessels has a significant impact on the temperature distribution during a RF ablation. It was observed that there are some difficulties on heating up properly the tumorous tissue between the bile duct and the blood vessels. Also, it was verified that the tissue adjacent to the ends of the stent-based electrode is heated preferentially. This is likely caused by the proximity of the ends of the electrode to the ground plane.

Finally, a saline-enhanced RF ablation of the cholangiocarcinoma was also simulated. Regarding the RF ablation of tumours in soft-tissue organs, it has been shown that it is possible to increase the tissue heating by modifying its electrical conductivity. This is achieved by injecting a saline solution into the tissue before the RF ablation procedure. In the numerical model considered, the electrical conductivity of the tumorous tissue was increased to simulate the change of the electrical conductivity due to the presence of the saline solution. The results evince that it is possible to obtain a more regular volume, where a compromise between applied voltage and saline solution injected into the tissue should be regarded. Still, the effect of the convective heat transfer is significant on the temperature distribution.

In conclusion, from the experimental and numerical results, this work added some contributions to the area of radio frequency ablation, proposing a therapeutic procedure for the treatment of tumours located in tubular organs. It has been shown that commercial stents can be regarded as potential RF active electrodes that can be connected percutaneously to the RF power generator through a modified forceps, presented in this work. Also, it has been shown that numerical modelling represents an valuable tool for predicting the temperature distribution, regarding the application of the proposed electrode.

8.2 Future Work

It is the author believe that there is much to be done on this subject in order to provide a better solution on the palliative treatment of tumorous cancers located in tubular organs. Radio frequency thermal ablation has proved to be an excellent therapy for the treatment of tumours in sof-tissue organs, and certainly its application can be expanded to the treatment of, for example, oesophagus, colon or bile duct cancers. However, there is still a road to travel.

At this point, it becomes clear that *in vivo* experimentation is required for a better assessment of the potential of the proposed electrode. Unlike the RF ablation on soft-tissue organs, in which the tumour plus a surgical safety margin of healthy tissue have to be destroyed for eradicating the tumour, there is no space for safety margins when it comes to tubular organs: an extensive induced lesion may represent a severe risk to the organ. Further experimental studies could provide a better characterization of the lesions that can be induced in the tumours.

Also, further investigations can be directed in order to consider alternative solutions that avoid a physical connection to a power generator. Hyperthermia therapies involving the application of an external ac magnetic field can provide an interesting solution to this problem. In this case, the external field could be used to heat the stent significantly and induce thermal necrosis in the adjacent tissue [BLP84]. However, in order to heat properly the device, as well as to produce a regular, well-defined lesion, new stent geometries and materials should be considered in this case. A step further can be the application of a nanoparticle magnetic fluid combined with the stent. The magnetic fluid hyperthermia, based in magnetic nanoparticles, has gained a large attention in biomedical applications [MSK11, PCJD03], and it can provide a new set of alternatives for additional investigations.

Other therapies can be also considered for applying the proposed electrode. Electroporation, for example, is a procedure that has been studied for the last couple of decades in the treatment of cancer. Basically, it is a phenomenon that increases the permeability of the cell membrane by exposing the cell to electric pulses [WC96]. Electroporation can either be reversible or irreversible. In reversible electroporation, the cell membrane reversibly opens, after which cells can survive. In irreversible electroporation, the cell membrane irreversibly opens, after which the cells die [DMR05]. The latter has been recently considered in literature as a promising technique for the treatment of cancer [GZK$^+$10, PJW$^+$11]. This may be an interesting issue for further research.

Bibliography

[AAR+10a] C. F. L. Antunes, T. R. O. Almeida, N. Raposeiro, B. Gonçalves, and P. Almeida, "A tubular electrode for radiofrequency ablation therapy," in *ICBET 2010 - International Conference on Biomedical Engineering and Technology*, Paris, France, 2010.

[AAR+10b] ——, "Effects of the geometry of a tubular electrode on the temperature distribution in biological tissue," in *14th Biennial IEEE Conference on Electromagnetic Field Computation*, Chicago, USA, 2010.

[AAR+10c] ——, "Thermal ablation in biological tissue using tubular electrode," in *14th Biennial IEEE Conference on Electromagnetic Field Computation*, Chicago, USA, 2010.

[AAR+10d] C. F. R. L. Antunes, T. R. Almeida, N. Raposeiro, B. Gonçalves, P. Almeida, and A. Antunes, "A tubular electrode for radiofrequency ablation therapy," *World Academy of Science, Engineering and Technology*, no. 70, pp. 517–523, 2010.

[AAR11a] C. F. L. Antunes, T. R. Almeida, and N. Raposeiro, "Inducing thermal lesion on a cholangiocarcinoma considering a saline-enhanced radiofrequency ablation," in *EHE2011 - 4th International Conference on Electromagnetic Fields, Health and Environment*, Coimbra, Portugal, 2011.

[AAR+11b] C. F. L. Antunes, T. R. Almeida, N. Raposeiro, B. Gonçalves, and P. Almeida, "Determination of lesion volume induced in biological tissue using a tubular electrode for radiofrequency ablation - numerical and experimental analysis," in *EHE2011 - 4th International Conference on Electromagnetic Fields, Health and Environment*, Coimbra, Portugal, 2011.

[AAR11c] C. F. L. Antunes, T. R. Almeida, and N. Raposeiro, "Finite element modeling of cholangiocarcinoma radiofrequency ablation," in *10th International Conference of the European Bioelectromagnetic Association*, Rome, Italy, 2011.

[AAR11d] ——, "Producing a regular volume for thermal lesion on a cholangiocarcinoma considering a saline-enhanced radiofrequency ablation," in *XV International Symposium on Electromagnetic Fields in Mechatronics, Electrical and Electronic Engineering. ISEF 2011.*, Funchal, Madeira Island (Portugal), 2011.

[AAR12a] C. F. R. L. Antunes, T. R. Almeida, and N. Raposeiro, "Saline-enhanced RF ablation on a cholangiocarcinoma: a numerical simulation," *COMPEL – The International Journal for Computation and Mathematics in Electrical and Electronic Engineering*, vol. 31, no. 4, pp. 1055–1066, 2012.

[AAR+12b] C. F. R. L. Antunes, T. R. O. Almeida, N. Raposeiro, B. Gonçalves, and P. Almeida, "Intraductal RF/stent ablation," in *CIRSE 2012 – Cardiovascular and Interventional Radiological Society of Europe*, Lisbon, Portugal, 2012.

[AAR12c] C. F. R. L. Antunes, T. R. O. Almeida, and N. Raposeiro, "Producing a regular volume for thermal lesion on a cholangiocarcinoma considering a saline-enhanced radiofrequency ablation (accepted for publication)," *Electrical Review*, 2012.

[AAR12d] ——, "Using a tubular electrode for radiofrequency ablation: numerical and experimental analysis (accepted for publication)," *COMPEL - The International Journal for Computation and Mathematics in Electrical and Electronic Engineering*, 2012.

[ABLG11] M. Ahmed, C. L. Brace, F. T. Lee, and S. N. Goldberg, "Principles of and advances in percutaneous ablation," *Radiology*, vol. 258, no. 2, pp. 351–369, 2011.

[AHLM07] P. Abitabile, U. Hartl, J. Lange, and C. A. Maurer, "Radiofrequency ablation permits an effective treatment for colorectal liver metastasis," *European Journal of Surgical Oncology*, vol. 33, no. 1, pp. 67–71, 2007.

[ALW+02] M. Ahmed, S. M. Lobo, J. Weinstein, J. B. Kruskal, G. S. Gazelle, E. F. Halpern, S. K. Afzal, R. E. Lenkinski, and S. N. Goldberg, "Improved coagulation with saline solution pretreatment during radiofrequency tumor ablation in a canine model," *Journal of Vascular and Interventional Radiology*, vol. 13, no. 7, pp. 717–24, 2002.

[AMM+10] H. Y. Akyildiz, J. Mitchell, M. Milas, A. Siperstein, and E. Berber, "Laparoscopic radiofrequency thermal ablation of neuroendocrine hepatic metastases: Long-term follow-up," *Surgery*, vol. 148, no. 6, pp. 1288–1293, 2010.

[Ang] AngioDynamics, "RITA© 1500X – User's guide and service manual (for software version 8.60 and above)." [Online]. Available: http://www.angiodynamics.com/uploads/pdf/042210-040340_RITA%201500X%20IFU.pdf

[Ang10a] ——, "StarBurst Talon/Talon Semi-Flex RFA Devices. Product information," 2010. [Online]. Available: http://www.angiodynamics.com/uploads/pdf/03-25-10-02-20-53-MLC%20340%20US.pdf

[Ang10b] ——, "StarBurst© MRI & SDE RFA Devices. Product information," 2010. [Online]. Available: http://www.angiodynamics.com/uploads/pdf/03-25-10-02-16-05-MLC%20342%20US.PDF

[Ang10c] ——, "StarBurst© XL & Semi-Flex RFA devices. Product information," 2010. [Online]. Available: http://www.angiodynamics.com/uploads/pdf/03-25-10-02-12-10-MLC%20341%20US.pdf

[Ang10d] ——, "StarBurst© Xli-e/Xli-e Semi-Flex RFA devices. Product information," 2010. [Online]. Available: http://www.angiodynamics.com/uploads/pdf/03-25-10-02-14-15-MLC%20343%20US.pdf

[Ang10e] ——, "UniBlate RFA Electrode. Product information," 2010. [Online]. Available: http://www.angiodynamics.com/uploads/pdf/03-25-10-02-24-12-MLC%20357%20US.pdf

[Ang12] ——, "StarBurst© radiofrequency ablation system," 2012. [Online]. Available: http://www.angiodynamics.com/products/what-is-rfa

[ASC+05] H. Axel, V. Stefan, W. Christel, G. Rainer, A. Peter, K. Thomas, and M. Maurice Stephan, "Minimally invasive treatment of renal cell carcinoma: Comparison of 4 different monopolar radiofrequency devices," *European Urology*, vol. 48, no. 4, pp. 584–592, 2005.

[Ass10] A. Assis, *The Experimental and Historical Foundations of Electricity*. C. Roy Keys Incorporated, 2010.

[AXH94] H. Arkin, L. X. Xu, and K. R. Holmes, "Recent developments in modeling heat transfer in blood perfused tissues," *IEEE Transactions on Biomedical Engineering*, vol. 41, no. 2, pp. 97–107, 1994.

[Bah81] A. T. Bahill, "Bioinstrumentation," in *Bioengineering: Biomedical, Medical and Clinical Engineering*. Prentice-Hall, 1981, pp. 45–54.

[BAS05] E. J. Berjano, J. L. Alió, and J. Saiz, "Modeling for radio-frequency conductive keratoplasty: implications for the maximum temperature reached in the cornea," *Physiological Measurement*, vol. 26, no. 3, pp. 157–172, 2005.

[BB78] C. J. F. Böttcher and P. Bordewijk, *Theory of Electric Polarization*, 2nd ed. Elsevier, 1978, vol. 2.

[BCW75] H. F. Bowman, E. G. Cravalho, and M. Woods, "Theory, measurement, and application of thermal properties of biomaterials," *Annual Review of Biophysics and Bioengineering*, vol. 4, no. 1, pp. 43–80, 1975.

[Ben98] P. Benjamin, *A history of electricity: (The intellectual rise in electricity) from antiquity to the days of Benjamin Franklin*. J. Wiley & Sons, 1898.

[Ber06] E. J. Berjano, "Theoretical modeling for radiofrequency ablation: State-of-the-art and challenges for the future," *Biomedical Engineering OnLine*, vol. 5, no. 1, p. 24, 2006.

[Ber07] P. Bertucci, "Therapeutic attractions: Early applications of electricity to the art of healing brain, mind and medicine: Essays in eighteenth-century neuroscience," H. Whitaker, C. U. M. Smith, and S. Finger, Eds. Springer US, 2007, pp. 271–283.

[BGB+99] F. Burdío, A. Güemes, J. M. Burdío, T. Castiella, M. A. De Gregorio, R. Lozano, and T. Livraghi, "Hepatic lesion ablation with bipolar saline-enhanced radiofrequency in the audible spectrum," *Academic Radiology*, vol. 6, no. 11, pp. 680–686, 1999.

[BGB+03] F. Burdío, A. Güemes, J. M. Burdío, A. Navarro, R. Sousa, T. Castiella, I. Cruz, O. Burzaco, and R. Lozano, "Bipolar saline-enhanced electrode for radiofrequency ablation: Results of experimental study of in vivo porcine liver," *Radiology*, vol. 229, no. 2, pp. 447–456, 2003.

[BGB07] R. Barauskas, A. Gulbinas, and G. Barauskas, "Investigation of radio-frequency ablation process in liver tissue by finite element modeling and experiment," *Medicina*, vol. 43, no. 4, pp. 310–325, 2007.

[BH04] E. J. Berjano and F. Hornero, "Thermal-electrical modeling for epicardial atrial radiofrequency ablation," *IEEE Transactions on Biomedical Engineering*, vol. 51, no. 8, pp. 1348–1357, 2004.

[BH05] ——, "A cooled intraesophageal balloon to prevent thermal injury during endocardial surgical radiofrequency ablation of the left atrium: a finite element study," *Physics in Medicine and Biology*, vol. 50, no. 20, pp. N269–N279, 2005.

[BK07] S. M. Becker and A. V. Kuznetsov, "Thermal damage reduction associated with *in vivo* skin electroporation: A numerical investigation justifying aggressive pre-cooling," *International Journal of Heat and Mass Transfer*, vol. 50, no. 1-2, pp. 105–116, 2007.

[BKP+09] M. Burstow, T. Kelly, S. Panchani, I. M. Khan, D. Meek, B. Memon, and M. A. Memon, "Outcome of palliative esophageal stenting for malignant dysphagia: a retrospective analysis," *Diseases of the Esophagus*, vol. 22, no. 6, pp. 519–525, 2009.

[BLP84] N. F. Borrelli, A. A. Luderer, and J. N. Panzarino, "Hysteresis heating for the treatment of tumours," *Physics in Medicine and Biology*, vol. 29, no. 5, pp. 487–494, 1984.

[BM03] A. Bhattacharya and R. L. Mahajan, "Temperature dependence of thermal conductivity of biological tissues," *Physiological Measurement*, vol. 24, no. 3, pp. 769–783, 2003.

[Bos] Boston Scientific, *RF 3000^{TM} Operation and Service Manual*.

[Bos06a] ——, "LeVeen CoAccess Electrode System. Product information," 2006. [Online]. Available: http://www.bostonscientific.com/templatedata/imports/collateral/Radiology/broc_leveencoacc_01_us.pdf

[Bos06b] ——, "LeVeen Needle Electrode. Product information," 2006. [Online]. Available: http://www.bostonscientific.com/templatedata/imports/collateral/Radiology/broc_levneedelec_01_us.pdf

[Bos12] ——, "Liver and soft tissue ablation," 2012. [Online]. Available: http://www.bostonscientific.com/procedure/ProcedureLanding.bsci/,,/navRelId/1000.1002/method/PRODUCTS/id/10000971/seo.serve

[BPB01] S. Baldwin, A. Pelman, and J. Bert, "A heat transfer model of thermal balloon endometrial ablation," *Annals of Biomedical Engineering*, vol. 29, no. 11, pp. 1009–1018, 2001.

[Bri80] D. Brian, "To make a vain man humble," *Physics Education*, vol. 15, no. 4, p. 248, 1980.

[Cav06] E. Cavicchi, "Nineteenth-century developments in coiled instruments and experiences with electromagnetic induction," *Annals of Science*, vol. 63, no. 3, pp. 319–361, 2006.

[CDF+97] S. A. Curley, B. S. Davidson, R. Y. Fleming, F. Izzo, L. C. Stephens, P. Tinkey, and D. Cromeens, "Laparoscopically guided bipolar radiofrequency ablation of areas of porcine liver," *Surgical Endoscopy*, vol. 11, no. 7, pp. 729–733, 1997.

[Cel] Celon AG medical instruments, "CelonLab POWER – Instructions for use."

[Cel05a] ——, “CelonProSurge,” 2005. [Online]. Available: http://www.celon.com/eng/index.php?level=3_1&abschnitt=3_1_

[Cel05b] ——, “CelonProSurge plus,” 2005. [Online]. Available: http://www.celon.com/eng/navi_haupt.php?level=3_3_3&abschnitt=3_3_3_

[CG11] J. E. R. Cosman and C. D. Gonzalez, “Bipolar radiofrequency lesion geometry: Implications for palisade treatment of sacroiliac joint pain,” *Pain Practice*, vol. 11, no. 1, pp. 3–22, 2011.

[CH97] M. G. Curley and P. S. Hamilton, “Creation of large thermal lesions in liver using saline-enhanced RF ablation,” in *19th Annual International Conference of the IEEE Engineering in Medicine and Biology Society*, vol. 6, Chicago, USA, 1997, pp. 2516–2519.

[Cha80] J. C. Chato, “Heat transfer to blood vessels,” *Journal of Biomechanical Engineering*, vol. 102, no. 2, pp. 110–119, 1980.

[Cha87] ——, “Thermal properties of tissues,” in *Handbook of bioengineering*, R. Skalak and S. Chien, Eds. McGraw-Hill, 1987, pp. 9.1–9.13.

[Cha03] I. A. Chang, “Finite element analysis of hepatic radiofrequency ablation probes using temperature-dependent electrical conductivity,” *Biomedical Engineering OnLine*, vol. 2, no. 12, 2003.

[CJS+98] B. Cady, R. L. Jenkins, G. D. Steele, W. D. Lewis, M. D. Stone, W. V. McDermott, J. M. Jessup, A. Bothe, P. Lalor, E. J. Lovett, P. Lavin, and D. C. Linehan, “Surgical margin in hepatic resection for colorectal metastasis: a critical and improvable determinant of outcome,” *Annals of Surgery*, vol. 227, no. 4, pp. 566–571, 1998.

[CL10] L. Crocetti and R. Lencioni, “Radiofrequency ablation of pulmonary tumors,” *European Journal of Radiology*, vol. 75, no. 1, pp. 23–27, 2010.

[CLG+00] C. H. Cha, F. T. Lee, J. M. Gurney, B. K. Markhardt, T. F. Warner, F. Kelcz, and D. M. Mahvi, “CT versus sonography for monitoring radiofrequency ablation in a porcine liver,” *American Journal of Roentgenology*, vol. 175, no. 3, pp. 705–711, 2000.

[CLK+01] S. B. Chinn, F. T. Lee, G. D. Kennedy, C. Chinn, C. D. Johnson, T. C. Winter, T. F. Warner, and D. M. Mahvi, "Effect of vascular occlusion on radiofrequency ablation of the liver," *American Journal of Roentgenology*, vol. 176, no. 3, pp. 789–795, 2001.

[CMB+04] S. A. Curley, P. Marra, K. Beaty, L. M. Ellis, J. N. Vauthey, E. K. Abdalla, C. Scaife, C. Raut, R. Wolff, H. Choi, E. Loyer, P. Vallone, F. Fiore, F. Scordino, V. De Rosa, R. Orlando, S. Pignata, B. Daniele, and F. Izzo, "Early and late complications after radiofrequency ablation of malignant liver tumors in 608 patients," *Annals of Surgery*, vol. 239, no. 4, pp. 450–8, 2004.

[CN04] I. A. Chang and U. D. Nguyen, "Thermal modeling of lesion growth with radiofrequency ablation devices," *Biomedical Engineering On-Line*, vol. 3, no. 27, p. 19, 2004.

[Col04] "Health Sciences, #152," Columbia University Libraries, 2004. [Online]. Available: http://www.columbia.edu/cu/lweb/eresources/exhibitions/treasures/html/152.html

[Com08] "Hauksbee, Francis," Complete Dictionary of Scientific Biography, 2008. [Online]. Available: http://www.encyclopedia.com/doc/1G2-2830901893.html

[Cov] Covidien, "Cool-tip™ RF ablation system." [Online]. Available: http://www.cool-tiprf.com/product.html

[Cov09] ——, "Cool-tip™ RF ablation system," 2009. [Online]. Available: http://www.cool-tiprf.com/images/R0006588_Cool-tip_SellSheet.pdf

[Cov12] ——, "Product information – hardware," 2012. [Online]. Available: http://www.cool-tiprf.com/hardware.html

[Cum22] E. P. Cumberbatch, "Discussion on diathermy in surgical practice," *Proceedings of the Royal Society of Medicine*, vol. 15, no. Surgery Section, pp. 87–88, 1922.

[CYY+04] M.-H. Chen, W. Yang, K. Yan, M.-W. Zou, L. Solbiati, J.-B. Liu, and Y. Dai, "Large liver tumors: Protocol for radiofrequency ablation and its clinical application in 110 patients – mathematic model, overlapping

mode, and electrode placement process," *Radiology*, vol. 232, no. 1, pp. 260–271, 2004.

[DFA+01] G. D. Dodd, M. S. Frank, M. Aribandi, S. Chopra, and K. N. Chintapalli, "Radiofrequency thermal ablation: Computer analysis of the size of the thermal injury created by overlapping ablations," *American Journal of Roentgenology*, vol. 177, no. 4, pp. 777–782, 2001.

[DG96] J. Dobson and P. Grassi, "Magnetic properties of human hippocampal tissue – evaluation of artefact and contamination sources," *Brain Research Bulletin*, vol. 39, no. 4, pp. 255–259, 1996.

[DMl86] C. H. Durney, H. Massoudi, and M. F. lskander, "Radiofrequency radiation dosimetry handbook," 1986. [Online]. Available: http://niremf.ifac.cnr.it/docs/HANDBOOK/home.htm

[DMR05] R. V. Davalos, L. M. Mir, and B. Rubinsky, "Tissue ablation with irreversible electroporation," *Annals of Biomedical Engineering*, vol. 33, no. 2, pp. 223–231, 2005.

[Dob07] J. Dobson, "Magnetic properties of biological material," in *Bioengineering and Biophysical Aspects of Electromagnetic Fields (Handbook of Biological Effects of Electromagnetic Fields)*, 3rd ed., F. S. Barnes and B. Greenebaum, Eds. CRC Press - Taylor & Francis, 2007, pp. 101–113.

[DPS99] T. Duerig, A. Pelton, and D. Stöckel, "An overview of nitinol medical applications," *Materials Science and Engineering: A*, vol. 273-275, pp. 149–160, 1999.

[DSK+00] I. Dodd, Gerald D., M. C. Soulen, R. A. Kane, T. Livraghi, W. R. Lees, Y. Yamashita, A. R. Gillams, O. I. Karahan, and H. Rhim, "Minimally invasive treatment of malignant hepatic tumors: At the threshold of a major breakthrough," *Radiographics*, vol. 20, no. 1, pp. 9–27, 2000.

[Duc90] F. A. Duck, *Physical Properties of Tissue: A Comprehensive Reference Book*. Academic Press, 1990.

[dVH50] N. H. de V. Heathcote, "Guericke's sulphur globe," *Annals of Science*, vol. 6, no. 3, pp. 293–305, 1950.

[DVP00] K. R. Diller, J. W. Valvano, and J. A. Pearce, "Bioheat transfer," in *The CRC Handbook of Thermal Engineering*, F. Kreith, Ed. CRC Press, 2000, pp. 4.114–4.187.

[Egg97] B. R. Eggins, *Biosensors –An Introduction*. John Wiley & Sons, 1997.

[EHD+06] J. F. Edd, L. Horowitz, R. V. Davalos, L. M. Mir, and B. Rubinsky, "*In vivo* results of a new focal tissue ablation technique: irreversible electroporation," *IEEE Transactions on Biomedical Engineering*, vol. 53, no. 7, pp. 1409–1415, 2006.

[End11] J. D. Enderle, "Biolectric phenomena," in *Introduction to Biomedical Engineering*, 3rd ed., J. D. Enderle and J. D. Bronzino, Eds. Academic Press, 2011, pp. 747–815.

[FF09] S. Finger and I. Ferguson, "The role of the gentleman's magazine in the dissemination of knowledge about electric fish in the eighteenth century," *Journal of the History of the Neurosciences*, vol. 18, no. 4, pp. 347–365, 2009.

[FNH+08] B. J. Fahey, R. C. Nelson, S. J. Hsu, D. P. Bradway, D. M. Dumont, and G. E. Trahey, "In vivo guidance and assessment of liver radiofrequency ablation with acoustic radiation force elastography," *Ultrasound in Medicine & Biology*, vol. 34, no. 10, pp. 1590–1603, 2008.

[Fos02] K. R. Foster, "Herman P. Schwan: A scientist and pioneer in biomedical engineering," *Annual Review of Biomedical Engineering*, vol. 4, pp. 1–27, 2002.

[Fra] R. B. Frankel, "Magnetotactic bacteria photo gallery." [Online]. Available: http://www.calpoly.edu/~rfrankel/mtbphoto.html

[FS89] K. R. Foster and H. P. Schwan, "Dielectric properties of tissues and biological materials: A critical review," *Critical Reviews in Biomedical Engineering*, vol. 17, no. 1, pp. 25–104, 1989.

[FS96] ——, "Dielectric properties of tissues," in *Handbook of Biological Effects of Electromagnetic Fields*, 2nd ed., C. Polk and E. Postow, Eds. CRC Press, 1996, pp. 25–102.

[GA10] M. Gatto and D. Alvaro, "New insights on cholangiocarcinoma," *World Journal of Gastrointestinal Oncology*, vol. 2, no. 3, 2010.

[Gab07] C. Gabriel, "Dielectric properties of biological materials," in *Bioengineering and Biophysical Aspects of Electromagnetic Fields (Handbook of Biological Effects of Electromagnetic Fields)*, 3rd ed., F. S. Barnes and B. Greenebaum, Eds. CRC - Taylor & Francis, 2007, pp. 88–137.

[GAG+01] S. N. Goldberg, M. Ahmed, G. S. Gazelle, J. B. Kruskal, J. C. Huertas, E. F. Halpern, B. S. Oliver, and R. E. Lenkinski, "Radio-frequency thermal ablation with NaCl solution injection: Effect of electrical conductivity on tissue heating and coagulation - phantom and porcine liver study," *Radiology*, vol. 219, no. 1, pp. 157–165, 2001.

[GB67] L. Geddes and L. Baker, "The specific resistance of biological material – a compendium of data for the biomedical engineer and physiologist," *Medical and Biological Engineering and Computing*, vol. 5, no. 3, pp. 271–293, 1967.

[GBS+10] M. Gatto, M. C. Bragazzi, R. Semeraro, C. Napoli, R. Gentile, A. Torrice, E. Gaudio, and D. Alvaro, "Cholangiocarcinoma: Update and future perspectives," *Digestive and Liver Disease*, vol. 42, no. 4, pp. 253–260, 2010.

[GD01] S. N. Goldberg and D. E. Dupuy, "Image-guided radiofrequency tumor ablation: Challenges and opportunities – part I," *Journal of Vascular and Interventional Radiology*, vol. 12, no. 9, pp. 1021–1032, 2001.

[Ged99] L. A. Geddes, "d'Arsonval, physician and inventor," *IEEE Engineering in Medicine and Biology Magazine*, vol. 18, no. 4, pp. 118–122, 1999.

[GG96] C. Gabriel and S. Gabriel, "Compilation of the dielectric properties of body tissues at RF and microwave frequencies," 1996. [Online]. Available: http://niremf.ifac.cnr.it/docs/DIELECTRIC/home.html

[GGB+09] D. A. Gervais, S. N. Goldberg, D. B. Brown, M. C. Soulen, S. F. Millward, and D. K. Rajan, "Society of Interventional Radiology position statement on percutaneous radiofrequency ablation for the treatment of liver tumors," *Journal of Vascular and Interventional Radiology*, vol. 20, no. 1, pp. 3–8, 2009.

[GGC96] C. Gabriel, S. Gabriel, and E. Corthout, "The dielectric properties of biological tissues: I. Literature survey," *Physics in Medicine and Biology*, vol. 41, no. 11, pp. 2231–2249, 1996.

[GGD+95] S. N. Goldberg, G. S. Gazelle, S. L. Dawson, W. J. Rittman, P. R. Mueller, and D. I. Rosenthal, "Tissue ablation with radiofrequency: Effect of probe size, gauge, duration, and temperature on lesion volume," *Academic Radiology*, vol. 2, no. 5, pp. 399–404, 1995.

[GGH+96] S. N. Goldberg, G. S. Gazelle, E. F. Halpern, W. J. Rittman, P. R. Mueller, and D. I. Rosenthal, "Radiofrequency tissue ablation: Importance of local temperature along the electrode tip exposure in determining lesion shape and size," *Academic Radiology*, vol. 3, no. 2, pp. 212–218, 1996.

[GGS+96] S. N. Goldberg, G. S. Gazelle, L. Solbiati, W. J. Rittman, and P. R. Mueller, "Radiofrequency tissue ablation: Increased lesion diameter with a perfusion electrode," *Academic Radiology*, vol. 3, no. 8, pp. 636–644, 1996.

[GHF+00] I. S. Gill, T. H. S. Hsu, R. L. Fox, A. Matamoros, C. D. Miller, R. F. Leveen, M. T. Grune, G. T. Sung, and M. E. Fidler, "Laparoscopic and percutaneous radiofrequency ablation of the kidney: acute and chronic porcine study," *Urology*, vol. 56, no. 2, pp. 197–200, 2000.

[GHS+08] S. Garrean, J. Hering, A. Saied, W. S. Helton, and N. J. Espat, "Radiofrequency ablation of primary and metastatic liver tumors: a critical review of the literature," *The American Journal of Surgery*, vol. 195, no. 4, pp. 508–520, 2008.

[GL05] A. R. Gillams and W. R. Lees, "CT mapping of the distribution of saline during radiofrequency ablation with perfusion electrodes," *CardioVascular and Interventional Radiology*, vol. 28, no. 4, pp. 476–480, 2005.

[GLG96a] S. Gabriel, R. W. Lau, and C. Gabriel, "The dielectric properties of biological tissues: II. Measurements in the frequency range 10 Hz to 20 GHz," *Physics in Medicine and Biology*, vol. 41, no. 11, pp. 2251–2269, 1996.

[GLG96b] ——, "The dielectric properties of biological tissues: III. Parametric models for the dielectric spectrum of tissues," *Physics in Medicine and Biology*, vol. 41, no. 11, pp. 2271–2293, 1996.

[GM00] S. Grimnes and O. G. Martinsen, *Bioimpedance & Bioelectricity Basics*. Academic Press, 2000.

[GM10] ——, "Alpha-dispersion in human tissue," *Journal of Physics: Conference Series*, vol. 224, no. 1, p. 012073, 2010.

[Gol01] S. N. Goldberg, "Radiofrequency tumor ablation: principles and techniques," *European Journal of Ultrasound*, vol. 13, no. 2, pp. 129–147, 2001.

[GSG+99] S. N. Goldberg, M. C. Stein, G. S. Gazelle, R. G. Sheiman, J. B. Kruskal, and M. E. Clouse, "Percutaneous radiofrequency tissue ablation: Optimization of pulsed-radiofrequency technique to increase coagulation necrosis," *Journal of Vascular and Interventional Radiology*, vol. 10, no. 7, pp. 907–916, 1999.

[GSHG00] S. N. Goldberg, L. Solbiati, E. F. Halpern, and G. S. Gazelle, "Variables affecting proper system grounding for radiofrequency ablation in an animal model," *Journal of Vascular and Interventional Radiology*, vol. 11, no. 8, pp. 1069–1075, 2000.

[GSS78] E. H. Grant, R. J. Sheppard, and G. P. South, *Dielectric Behaviour of Biological Molecules in Solution*, ser. Monographs on Physical Biochemistry. Oxford University Press, 1978.

[Guy84] A. W. Guy, "History of biological effects and medical applications of microwave energy," *IEEE Transactions on Microwave Theory and Techniques*, vol. 32, no. 9, pp. 1182–1200, 1984.

[GZK+10] Y. Guo, Y. Zhang, R. Klein, G. M. Nijm, A. V. Sahakian, R. A. Omary, G.-Y. Yang, and A. C. Larson, "Irreversible electroporation therapy in the liver: Longitudinal efficacy studies in a rat model of hepatocellular carcinoma," *Cancer Research*, vol. 70, no. 4, pp. 1555–1563, 2010.

[Hab08] R. W. Y. Habash, *Bioeffects and Therapeutic Applications of Electromagnetic Energy*. CRC Press - Taylor & Francis, 2008.

[Hae01] D. Haemmerich, "Finite element modeling of hepatic radio frequency ablation," Ph.D. dissertation, University of Wisconsin-Madison. USA, 2001.

[Ham69] B. J. Hammond, "2000 years of therapeutic electricity," *Electronics and Power*, vol. 15, no. 6, pp. 190–194, 1969.

[HCW+03] D. Haemmerich, L. Chachati, A. S. Wright, D. M. Mahvi, J. Lee, F. T., and J. G. Webster, "Hepatic radiofrequency ablation with internally cooled probes: effect of coolant temperature on lesion size," *IEEE Transactions on Biomedical Engineering*, vol. 50, no. 4, pp. 493–500, 2003.

[Hen47] F. C. Henriques, "Studies of thermal injury V: The predictability and the significance of thermally induced rate processes leading to irreversible epidermal injury." *Archives of Pathology*, vol. 43, no. 5, pp. 489–502, 1947.

[HJK+10] R.-T. Hoffmann, T. F. Jakobs, C. H. Kubisch, C. Trumm, C. Weber, M. Siebels, T. K. Helmberger, and M. F. Reiser, "Renal cell carcinoma in patients with a solitary kidney after nephrectomy treated with radiofrequency ablation: Mid term results," *European Journal of Radiology*, vol. 73, no. 3, pp. 652–656, 2010.

[HM47] F. C. Henriques and A. R. Moritz, "Studies of thermal injury I: The conduction of heat to and through skin and the temperatures attained therein. a theoretical and an experimental investigation," *The American Journal of Pathology*, vol. 23, no. 4, pp. 530–549, 1947.

[HMS95] M. F. Hoey, P. M. Mulier, and J. G. Shake, "Intramural ablation using radiofrequency energy via screw-tip catheter and saline electrode," *Pacing and Clinical Electrophysiology*, vol. 18, Part II, p. 917, 1995.

[HNW+04] J. Hänsler, D. Neureiter, M. Wasserburger, R. Janka, T. Bernatik, T. Schneider, W. Müller, M. Frieser, S. Schaber, D. Becker, E. G. Hahn, and D. Strobel, "Percutaneous US-guided radiofrequency ablation with perfused needle applicators: Improved survival with the VX2 tumor model in rabbits," *Radiology*, vol. 230, no. 1, pp. 169–174, 2004.

[Hom67] R. W. Home, "Francis Hauksbee's theory of electricity," *Archive for History of Exact Sciences*, vol. 4, no. 3, pp. 203–217, 1967.

[HOT+02] D. Haemmerich, O. Ozkan, J. Tsai, S. Staelin, S. Tungjitkusolmun, D. Mahvi, and J. Webster, "Changes in electrical resistivity of swine liver after occlusion and postmortem," *Medical and Biological Engineering and Computing*, vol. 40, no. 1, pp. 29–33, 2002.

[How85] G. J. Howes, "The phylogenetic relationships of the electric catfish family Malapteruridae (Teleostei: Siluroidei)," *Journal of Natural History*, vol. 19, no. 1, pp. 37–67, 1985.

[HRT84] E. J. Hall and L. Roizin-Towle, "Biological effects of heat," *Cancer Research*, vol. 44, no. 10 Supplement, pp. 4708s–4713s, 1984.

[HSH+09a] R. J. Halter, A. Schned, J. Heaney, A. Hartov, and K. D. Paulsen, "Electrical properties of prostatic tissues: I. Single frequency admittivity properties," *The Journal of Urology*, vol. 182, no. 4, pp. 1600–1607, 2009.

[HSH+09b] ——, "Electrical properties of prostatic tissues: II. Spectral admittivity properties," *The Journal of Urology*, vol. 182, no. 4, pp. 1608–1613, 2009.

[HST+01] D. Haemmerich, T. Staelin, S. Tungjitkusolmun, J. Lee, F. T., D. M. Mahvi, and J. G. Webster, "Hepatic bipolar radio-frequency ablation between separated multiprong electrodes," *IEEE Transactions on Biomedical Engineering*, vol. 48, no. 10, pp. 1145–1152, 2001.

[HST+03] D. Haemmerich, S. T. Staelin, J. Z. Tsai, S. Tungjitkusolmun, D. M. Mahvi, and J. G. Webster, "*In vivo* electrical conductivity of hepatic tumours," *Physiological Measurement*, vol. 24, no. 2, pp. 251–260, 2003.

[HTS+02] D. Haemmerich, S. Tungjitkusolmun, S. T. Staelin, J. Lee, F. T., D. M. Mahvi, and J. G. Webster, "Finite-element analysis of hepatic multiple probe radio-frequency ablation," *IEEE Transactions on Biomedical Engineering*, vol. 49, no. 8, pp. 836–842, 2002.

[Hur85] W. D. Hurt, "Multiterm debye dispersion relations for permittivity of muscle," *IEEE Transactions on Biomedical Engineering*, vol. BME-32, no. 1, pp. 60–64, 1985.

[HVW+06a] A. Häcker, S. Vallo, C. Weiss, R. Grobholz, T. Stein, T. Knoll, and M. S. Michel, "Bipolar and multipolar radio frequency ablation with resistance controlled power output: Standardized ex vivo kidney tissue evaluation," *The Journal of Urology*, vol. 175, no. 3, pp. 1122–1126, 2006.

[HVW+06b] A. Häcker, S. Vallo, C. Weiss, T. Stein, P. Alken, T. Knoll, and M. S. Michel, "Technical characterization of a new bipolar and multipolar radiofrequency device for minimally invasive treatment of renal tumours," *British Journal of Urology International*, vol. 97, no. 4, pp. 822–828, 2006.

[HWM+03a] D. Haemmerich, A. Wright, D. Mahvi, F. Lee, and J. Webster, "Hepatic bipolar radiofrequency ablation creates coagulation zones close to blood vessels: A finite element study," *Medical and Biological Engineering and Computing*, vol. 41, no. 3, pp. 317–323, 2003.

[HWM03b] D. Haemmerich, J. G. Webster, and D. M. Mahvi, "Thermal dose versus isotherm as lesion boundary estimator for cardiac and hepatic radiofrequency ablation," in *Proceedings of the 25th Annual International Conference of the IEEE Engineering in Medicine and Biology Society*, vol. 1, 2003, pp. 134–137.

[Iss08] R. D. Issels, "Hyperthermia adds to chemotherapy," *European Journal of Cancer*, vol. 44, no. 17, pp. 2546–2554, 2008.

[IWJR+08] A. D. Izzo, J. T. Walsh Jr, H. Ralph, J. Webb, M. Bendett, J. Wells, and C.-P. Richter, "Laser stimulation of auditory neurons: Effect of shorter pulse duration and penetration depth," *Biophysical Journal*, vol. 94, no. 8, pp. 3159–3166, 2008.

[JOT12] S. Jones, P. O'Donovan, and D. Toub, "Radiofrequency ablation for treatment of symptomatic uterine fibroids," *Obstetrics and Gynecology International*, 2012. [Online]. Available: http://www.ncbi.nlm.nih.gov/pmc/articles/PMC3180825/

[JW97] M. K. Jain and P. D. Wolf, “Finite element analysis predicts dose-response relationship for constant power and temperature controlled radiofrequencg ablation,” in *Proceedings of the 19th Annual International Conference of the IEEE Engineering in Medicine and Biology Society*, vol. 1, Chicago, USA, 1997, pp. 165–168 vol.1.

[KBH02] P. Kearey, M. Brooks, and I. Hill, “Electrical surveying,” in *An Introduction to Geophysical Exploration*, 3rd ed. Blackwell Science, 2002, pp. 183–207.

[KITS11] T. Kinoshita, E. Iwamoto, H. Tsuda, and K. Seki, “Radiofrequency ablation as local therapy for early breast carcinomas,” *Breast Cancer*, vol. 18, no. 1, pp. 10–17, 2011.

[KLK06] T. Kim, H. Lim, and H. Kim, “Excessive hyperthermic necrosis of a pulmonary lobe after hypertonic saline-enhanced monopolar radiofrequency ablation,” *CardioVascular and Interventional Radiology*, vol. 29, no. 1, pp. 160–163, 2006.

[KMU+94] S. Kimura, T. Morimoto, T. Uyama, Y. Monden, Y. Kinouchi, and T. Iritani, “Application of electrical impedance analysis for diagnosis of a pulmonary mass,” *Chest*, vol. 105, no. 6, pp. 1679–1682, 1994.

[KO02] B. W. Kuvshinoff and D. M. Ota, “Radiofrequency ablation of liver tumors: Influence of technique and tumor size,” *Surgery*, vol. 132, no. 4, pp. 605–612, 2002.

[Kom05] K. Koman, “The science of hurt,” Havard Magazine, Nov/Dec 2005 2005. [Online]. Available: http://harvardmagazine.com/2005/11/the-science-of-hurt.html

[Kuh95a] A. W. Kuhfeld, “Medical electricity I: Electrostatics,” *IEEE Engineering in Medicine and Biology Magazine*, vol. 14, no. 1, pp. 101–102, 1995.

[Kuh95b] ——, “Medical electricity II: Galvanism,” *IEEE Engineering in Medicine and Biology Magazine*, vol. 14, no. 3, pp. 344–346, 1995.

[Lab92] S. Labonte, “A theoretical study of radio-frequency ablation of the myocardium,” Ph.D. dissertation, 1992.

[Lab94a] ——, "A computer simulation of radio-frequency ablation of the endocardium," *IEEE Transactions on Biomedical Engineering*, vol. 41, no. 9, pp. 883–890, 1994.

[Lab94b] ——, "Numerical model for radio-frequency ablation of the endocardium and its experimental validation," *IEEE Transactions on Biomedical Engineering*, vol. 41, no. 2, pp. 108–115, 1994.

[LAU+10] C.-H. Liu, R. Arellano, R. Uppot, A. Samir, D. Gervais, and P. Mueller, "Radiofrequency ablation of hepatic tumours: effect of post-ablation margin on local tumour progression," *European Radiology*, vol. 20, no. 4, pp. 877–885, 2010.

[LAW+06] Z. Liu, M. Ahmed, Y. Weinstein, M. Yi, R. L. Mahajan, and S. N. Goldberg, "Characterization of the RF ablation-induced 'oven effect': The importance of background tissue thermal conductivity on tissue heating," *International Journal of Hyperthermia*, vol. 22, no. 4, pp. 327–342, 2006.

[LBC96] T. R. Larson, D. G. Bostwick, and A. Corica, "Temperature-correlated histo pathologic changes following microwave thermoablation of obstructive tissue in patients with benign prostatic hyperplasia," *Urology*, vol. 47, no. 4, pp. 463–469, 1996.

[LDH+02] J. R. Leyendecker, G. D. Dodd, G. A. Halff, V. A. McCoy, D. H. Napier, L. G. Hubbard, K. N. Chintapalli, S. Chopra, W. K. Washburn, R. M. Esterl, F. G. Cigarroa, R. E. Kohlmeier, and F. E. Sharkey, "Sonographically observed echogenic response during intraoperative radiofrequency ablation of cirrhotic livers," *American Journal of Roentgenology*, vol. 178, no. 5, pp. 1147–1151, 2002.

[LF07] H. S. Locke and S. Finger, "Gentleman's Magazine, the advent of medical electricity, and disorders of the nervous system brain, mind and medicine: Essays in eighteenth-century neuroscience," H. Whitaker, C. U. M. Smith, and S. Finger, Eds. Springer US, 2007, pp. 257–270.

[LGM+97] T. Livraghi, S. N. Goldberg, F. Monti, A. Bizzini, S. Lazzaroni, F. Meloni, S. Pellicanò, L. Solbiati, and G. S. Gazelle, "Saline-enhanced

radio-frequency tissue ablation in the treatment of liver metastases (abstract)," *Radiology*, vol. 202, no. 1, pp. 205–210, 1997.

[LHK+04] J. M. Lee, J. K. Han, S. H. Kim, K. S. Shin, J. Y. Lee, H. S. Park, H. Hur, and B. I. Choi, "Comparison of wet radiofrequency ablation with dry radiofrequency ablation and radiofrequency ablation using hypertonic saline preinjection: Ex vivo bovine liver," *Korean Journal of Radiology*, vol. 5, no. 4, pp. 258–265, 2004.

[LIR+10] S. Laufer, A. Ivorra, V. E. Reuter, B. Rubinsky, and S. B. Solomon, "Electrical impedance characterization of normal and cancerous human hepatic tissue," *Physiological Measurement*, vol. 31, no. 7, pp. 995–1009, 2010.

[LKC+10] C.-Y. Lai, D. E. Kruse, C. F. Caskey, D. N. Stephens, P. L. Sutcliffe, and K. W. Ferrara, "Noninvasive thermometry assisted by a dual-function ultrasound transducer for mild hyperthermia," *IEEE Transactions on Ultrasonics, Ferroelectrics and Frequency Control*, vol. 57, no. 12, pp. 2671 – 2684, 2010.

[LKL+03] J. M. Lee, Y. K. Kim, Y. H. Lee, S. W. Kim, C. A. Li, and C. S. Kim, "Percutaneous radiofrequency thermal ablation with hypertonic saline injection: In vivo study in a rabbit liver model," *Korean Journal of Radiology*, vol. 4, no. 1, pp. 27–34, 2003.

[Lor96] T. Lorentzen, "A cooled needle electrode for radiofrequency tissue ablation: Thermodynamic aspects of improved performance compared with conventional needle design," *Academic Radiology*, vol. 3, no. 7, pp. 556–563, 1996.

[Mac93] A. Macdonald, "A brief review of the history of electrotherapy and its union with acupuncture," *Acupuncture in Medicine*, vol. 11, no. 2, pp. 66–75, 1993.

[MBBT90] J. P. McGahan, P. D. Browning, J. M. Brock, and H. Tesluk, "Hepatic ablation using radiofrequency electrocautery," *Investigative Radiology*, vol. 25, no. 3, pp. 267–270, 1990.

[MD01] J. P. McGahan and I. Dodd, Gerald D., “Radiofrequency ablation of the liver: Current status,” *Americal Journal of Roentgenology*, vol. 176, no. 1, pp. 3–16, 2001.

[MDP+05] P. Mulier, B. Dupas, P. Pereira, T. de Baere, R. Lencioni, R. Leveillee, G. Marchal, L. Michel, and Y. Ni, “Electrodes and multiple electrode systems for radiofrequency ablation: a proposal for updated terminology,” *European Radiology*, vol. 15, no. 4, pp. 798–808, 2005.

[MGB+96] J. P. McGahan, W.-Z. Gu, J. M. Brock, H. Tesluk, and C. Darryl Jones, “Hepatic ablation using bipolar radiofrequency electrocautery,” *Academic Radiology*, vol. 3, no. 5, pp. 418–422, 1996.

[MH47] A. R. Moritz and F. C. Henriques, “Studies of thermal injury II: The relative importance of time and surface temperature in the causation of cutaneous burns,” *The American Journal of Pathology*, vol. 23, no. 5, pp. 695–720, 1947.

[MMN+02] S. Mulier, P. Mulier, Y. Ni, Y. Miao, B. Dupas, G. Marchal, I. De Wever, and L. Michel, “Complications of radiofrequency coagulation of liver tumours,” *British Journal of Surgery*, vol. 89, no. 10, pp. 1206–1222, 2002.

[MNB+01] Y. Miao, Y. Ni, H. Bosmans, J. Yu, J. Vaninbroukx, S. Dymarkowski, H. Zhang, and G. Marchal, “Radiofrequency ablation for eradication of pulmonary tumor in rabbits,” *Journal of Surgical Research*, vol. 99, no. 2, pp. 265–271, 2001.

[MNE+10] A. Motoyoshi, M. Noguchi, M. Earashi, Y. Zen, and H. Fujii, “Histopathological and immunohistochemical evaluations of breast cancer treated with radiofrequency ablation,” *Journal of Surgical Oncology*, vol. 102, no. 5, pp. 385–391, 2010.

[MNL10] E. M. Merkle, R. C. Nelson, and J. S. Lewin, “Renal cell carcinoma: Follow-up with magnetic resonance imaging after percutaneous radiofrequency ablation,” in *Methods of Cancer Diagnosis, Therapy, and Prognosis*, ser. Methods of Cancer Diagnosis, Therapy, and Prognosis, M. A. Hayat, Ed. Springer Netherlands, 2010, vol. 6, pp. 108–113.

[MNM+97] Y. Miao, Y. Ni, S. Mulier, K. Wang, M. F. Hoey, P. Mulier, F. Penninckx, J. Yu, I. De Scheerder, A. L. Baert, and G. Marchal, "Ex vivo experiment on radiofrequency liver ablation with saline infusion through a screw-tip cannulated electrode," *Journal of Surgical Research*, vol. 71, no. 1, pp. 19–24, 1997.

[MNM+00] Y. Miao, Y. Ni, S. Mulier, J. Yu, I. De Wever, F. Penninckx, A. L. Baert, and G. Marchal, "Treatment of VX2 liver tumor in rabbits with "wet" electrode mediated radio-frequency ablation," *European Radiology*, vol. 10, no. 1, pp. 188–194, 2000.

[MNM+03] S. Mulier, Y. Ni, Y. Miao, A. Rosière, A. Khoury, G. Marchal, and L. Michel, "Size and geometry of hepatic radiofrequency lesions," *European Journal of Surgical Oncology*, vol. 29, no. 10, pp. 867–878, 2003.

[MNY+02] Y. Miao, Y. Ni, J. Yu, H. Zhang, and G. Marchal, "Evaluation of radiofrequency ablation as an alternative for the treatment of brain tumor in rabbits," *Journal of Neuro-Oncology*, vol. 56, no. 2, pp. 119–126, 2002.

[Mor47] A. R. Moritz, "Studies of thermal injury III: The pathology and pathogenesis of cutaneous burns. an experimental study," *The American Journal of Pathology*, vol. 23, no. 6, pp. 915–941, 1947.

[Mou91] M. R. Mourino, "From Thales to Lauterbur, or from the lodestone to MR imaging: magnetism and medicine," *Radiology*, vol. 180, no. 3, pp. 593–612, 1991.

[MSK11] A. Miaskowski, B. Sawicki, and A. Kraszewski, "The use of magnetic nanoparticles in low frequency inductive hyperthermia," in *EHE2011 – 4th International Conference on Electromagnetic Fields, Health and Environment*, Coimbra, Portugal, 2011.

[MTD+02] R. Munver, C. B. Threatt, F. C. Delvecchio, G. M. Preminger, and T. J. Polascik, "Hypertonic saline-augmented radiofrequency ablation of the VX-2 tumor implanted in the rabbit kidney: a short-term survival pilot study," *Urology*, vol. 60, no. 1, pp. 170–175, 2002.

[MTWG06] A. H. Mahnken, J. A. Tacke, J. E. Wildberger, and R. W. Günther, "Radiofrequency ablation of osteoid osteoma: Initial results with a bipolar ablation device," *Journal of Vascular and Interventional Radiology*, vol. 17, no. 9, pp. 1465–1470, 2006.

[Nat] "Electrostatic generator," National High Magnetic Field Laboratory - University of Florida. [Online]. Available: http://www.magnet.fsu.edu/education/tutorials/museum/electrostaticgenerator.html

[NE06] G. Ndrepepa and H. Estner, "Ablation of cardiac arrhytmias – energy sources and mechanisms of lesion formation," in *Catheter Ablation of Cardiac Arrythmias – A practical approach*, C. Schmitt, I. Deisenhofer, and B. Zrenner, Eds. Springer, 2006, pp. 35–53.

[Neu98] M. R. Neuman, "Biopotential electrodes," in *Medical Instrumentation – Application and Design*, 3rd ed., J. G. Webster, Ed. John Wiley & Sons, 1998, pp. 183–232.

[Ng00] H. H. Ng, "Malapterurus electricus," Animal Diversity Web, 2000. [Online]. Available: http://animaldiversity.ummz.umich.edu/site/accounts/information/Malapterurus_electricus.html

[NH95] S. Nath and D. E. Haines, "Biophysics and pathology of catheter energy delivery systems," *Progress in Cardiovascular Diseases*, vol. 37, no. 4, pp. 185–204, 1995.

[Nic11] T. A. Nickloes, "Pringle maneuver," Medscape reference, 2011. [Online]. Available: http://emedicine.medscape.com/article/1895599-overview

[NMM+05] Y. Ni, S. Mulier, Y. Miao, L. Michel, and G. Marchal, "A review of the general aspects of radiofrequency ablation," *Abdominal Imaging*, vol. 30, no. 4, pp. 381–400, 2005.

[NPS+96] A. Nakeeb, H. A. Pitt, T. A. Sohn, J. Coleman, R. A. Abrams, S. Piantadosi, R. H. Hruban, K. D. Lillemoe, C. J. Yeo, and J. L. Cameron, "Cholangiocarcinoma. A spectrum of intrahepatic, perihilar, and distal tumors," *Annals of Surgery*, vol. 224, no. 4, pp. 463–475, 1996.

[NYP+95] H. Nakagawa, W. S. Yamanashi, J. V. Pitha, M. Arruda, X. Wang, K. Ohtomo, K. J. Beckman, J. H. McClelland, R. Lazzara, and W. M. Jackman, "Comparison of in vivo tissue temperature profile and lesion geometry for radiofrequency ablation with a saline-irrigated electrode versus temperature control in a canine thigh muscle preparation," *Circulation*, vol. 91, no. 8, pp. 2264–2273, 1995.

[OB96] J. L. O'Connor and D. A. Bloom, "William T. Bovie and electrosurgery," *Surgery*, vol. 119, no. 4, pp. 390–396, 1996.

[OHC08] S. Ozen, S. Helhel, and O. Cerezci, "Heat analysis of biological tissue exposed to microwave by using thermal wave model of bio-heat transfer (TWMBT)," *Burns*, vol. 34, no. 1, pp. 45–49, 2008.

[PBFP05] D. M. Parkin, F. Bray, J. Ferlay, and P. Pisani, "Global cancer statistics, 2002," *CA Cancer Journal for Clinicians*, vol. 55, no. 2, pp. 74–108, 2005.

[PCJD03] Q. A. Pankhurst, J. Connolly, S. K. Jones, and J. Dobson, "Applications of magnetic nanoparticles in biomedicine," *Journal of Physics D: Applied Physics*, vol. 36, no. 13, pp. R167–R181, 2003.

[Pen48] H. H. Pennes, "Analysis of tissue and arterial blood temperatures in the resting human forearm," *Journal of Applied Physiololy*, vol. 85, no. 1, pp. 5–34, 1998 (originally published 1948).

[Pet84] R. Pethig, "Dielectric properties of biological materials: Biophysical and medical applications," *IEEE Transactions on Electrical Insulation*, vol. EI-19, no. 5, pp. 453–474, 1984.

[PH67] R. Plonsey and D. Heppner, "Considerations of quasi-stationarity in electrophysiological systems," *Bulletin of Mathematical Biology*, vol. 29, no. 4, pp. 657–664, 1967.

[PHG05] A. Peyman, S. Holden, and C. Gabriel, "Dielectric properties of biological tissues at microwave frequencies," Mobile Telecommunications and Health Research Program (MTHR) - Department of Health, U.K., Tech. Rep., 2005. [Online]. Available: http://www.mthr.org.uk/research_projects/documents/Rum3FinalReport.pdf

[PHL+99] T. J. Polascik, U. Hamper, B. R. Lee, Y. Dai, J. Hilton, C. A. Magee, J. K. Crone, M. J. Shue, M. Ferrell, V. Trapanotto, M. Adiletta, and A. W. Partin, "Ablation of renal tumors in a rabbit model with interstitial saline-augmented radiofrequency energy: preliminary report of a new technology," *Urology*, vol. 53, no. 3, pp. 465–470, 1999.

[Pic03] M. Piccolino, *The taming of the ray: electric fish research in the enlightenment from John Walsh to Alessandro Volta*. L.S. Olschki, 2003.

[Pic07] ——, "The taming of the electric ray: From a wonderful and dreadful "art" to "animal electricity" and "electric battery"," in *Brain, Mind and Medicine: Essays in Eighteenth-Century Neuroscience*, H. Whitaker, C. U. M. Smith, and S. Finger, Eds. Springer US, 2007, pp. 125–143.

[PJW+11] M. Pech, A. Janitzky, J. Wendler, C. Strang, S. Blaschke, O. Dudeck, J. Ricke, and U.-B. Liehr, "Irreversible electroporation of renal cell carcinoma: A first-in-man phase I clinical study," *CardioVascular and Interventional Radiology*, vol. 34, no. 1, pp. 132–138, 2011.

[PK87] R. Pethig and D. B. Kell, "The passive electrical properties of biological systems: their significance in physiology, biophysics and biotechnology," *Physics in Medicine and Biology*, vol. 32, no. 8, pp. 933–970, 1987.

[PPH+09] W. H. Paik, Y. S. Park, J.-H. Hwang, S. H. Lee, C. J. Yoon, S.-G. Kang, J. K. Lee, J. K. Ryu, Y.-T. Kim, and Y. B. Yoon, "Palliative treatment with self-expandable metallic stents in patients with advanced type III or IV hilar cholangiocarcinoma: a percutaneous versus endoscopic approach," *Gastrointestinal Endoscopy*, vol. 69, no. 1, pp. 55–62, 2009.

[PSO+98] E. J. Patterson, C. H. Scudamore, D. A. Owen, A. G. Nagy, and A. K. Buczkowski, "Radiofrequency ablation of porcine liver in vivo: effects of blood flow and treatment time on lesion size," *Annals of Surgery*, vol. 227, no. 4, pp. 559–565, 1998.

[PTS+04] P. L. Pereira, J. Trubenbach, M. Schenk, J. Subke, S. Kroeber, I. Schaefer, C. T. Remy, D. Schmidt, J. Brieger, and C. D. Claussen, "Radiofrequency ablation: In vivo comparison of four commercially available devices in pig livers," *Radiology*, vol. 232, no. 2, pp. 482–490, 2004.

[PWF+95] D. Panescu, J. G. Whayne, S. D. Fleischman, M. S. Mirotznik, D. K. Swanson, and J. G. Webster, "Three-dimensional finite element analysis of current density and temperature distributions during radiofrequency ablation," *IEEE Transactions on Biomedical Engineering*, vol. 42, no. 9, pp. 879–890, 1995.

[Rey97] J. M. Reynolds, "Electrical resistivity methods," in *An Introduction to Applied and Environmental Geophysics*. John Wiley & Sons, 1997, pp. 418–440.

[RFPB90] S. Rossi, F. Fornari, C. Pathies, and L. Buscarini, "Thermal lesions induced by 480 kHz localized current field in guinea pig and pig liver," *Tumori*, vol. 76, no. 1, pp. 54–7, 1990.

[RLV+00] S. S. Raman, D. S. K. Lu, D. J. Vodopich, J. Sayre, and C. Lassman, "Creation of radiofrequency lesions in a porcine model," *American Journal of Roentgenology*, vol. 175, no. 5, pp. 1253–1258, 2000.

[SBC+04] Y. Salazar, R. Bragos, O. Casas, J. Cinca, and J. Rosell, "Transmural versus nontransmural in situ electrical impedance spectrum for healthy, ischemic, and healed myocardium," *IEEE Transactions on Biomedical Engineering*, vol. 51, no. 8, pp. 1421–1427, 2004.

[Sch57] H. P. Schwan, "Electrical properties of tissue and cell suspensions," in *Advances in Biological and Medical Physics*. New York: Academic Press, 1957, vol. 5, pp. 147–209.

[Sch94] ——, "Electrical properties of tissues and cell suspensions: mechanisms and models," *Proceedings of the 16th Annual International Conference of the IEEE Engineering in Medicine and Biology Society, 1994. Engineering Advances: New Opportunities for Biomedical Engineers.*, pp. A70–A71 vol.1, 1994.

[SCM+99] D. Schwartzman, I. Chang, J. J. Michele, M. S. Mirotznik, and K. R. Foster, "Electrical impedance properties of normal and chronically infarcted left ventricular myocardium," *Journal of Interventional Cardiac Electrophysiology*, vol. 3, no. 3, pp. 213–224, 1999.

[SDD+07] C. J. Simon, D. E. Dupuy, T. A. DiPetrillo, H. P. Safran, C. A. Grieco, T. Ng, and W. W. Mayo-Smith, "Pulmonary radiofrequency ablation:

Long-term safety and efficacy in 153 patients," *Radiology*, vol. 243, no. 1, pp. 268–275, 2007.

[SF80a] J. L. Schepps and K. R. Foster, "The UHF and microwave dielectric properties of normal and tumour tissues: variation in dielectric properties with tissue water content," *Physics in Medicine and Biology*, vol. 25, no. 6, pp. 1149–1159, 1980.

[SF80b] H. P. Schwan and K. R. Foster, "RF-field interactions with biological systems: Electrical properties and biophysical mechanisms," *Proceedings of the IEEE*, vol. 68, no. 1, pp. 104–113, 1980.

[SFS82] R. D. Stoy, K. R. Foster, and H. P. Schwan, "Dielectric properties of mammalian tissues from 0.1 to 100 Mhz; a summary of recent data," *Physics in Medicine and Biology*, vol. 27, no. 4, pp. 501–513, 1982.

[SFT+09] A. Stang, R. Fischbach, W. Teichmann, C. Bokemeyer, and D. Braumann, "A systematic review on the clinical benefit and role of radiofrequency ablation as treatment of colorectal liver metastases," *European Journal of Cancer*, vol. 45, no. 10, pp. 1748–1756, 2009.

[SFW86] S. R. Smith, K. R. Foster, and G. L. Wolf, "Dielectric properties of VX-2 carcinoma versus normal liver tissue," *IEEE Transactions on Biomedical Engineering*, vol. BME-33, no. 5, pp. 522–524, 1986.

[SGE+00] A. Siperstein, A. Garland, K. Engle, S. Rogers, E. Berber, A. Foroutani, A. String, T. Ryan, and P. Ituarte, "Local recurrence after laparoscopic radiofrequency thermal ablation of hepatic tumors," *Annals of Surgical Oncology*, vol. 7, no. 2, pp. 106–113, 2000.

[SJV+10] J. Súarez, J. Jiménez, R. Vera, A. Tarifa, E. Balén, V. Arrazubi, J. Vila, and J. Lera, "Stent or surgery for incurable obstructive colorectal cancer: an individualized decision," *International Journal of Colorectal Disease*, vol. 25, no. 1, pp. 91–96, 2010.

[SK56] H. P. Schwan and C. F. Kay, "Specific resistance of body tissues," *Circulation Research*, vol. 4, no. 6, pp. 664–70, 1956.

[SK58] H. Semat and R. Katz, *Physics*. New York: Rinehart & Company, Inc., 1958.

[SPD04] D. Stoeckel, A. Pelton, and T. Duerig, "Self-expanding nitinol stents: material and design considerations," *European Radiology*, vol. 14, no. 2, pp. 292–301, 2004.

[Spe60] K. E. Spells, "The thermal conductivities of some biological fluids," *Physics in Medicine and Biology*, vol. 5, no. 2, pp. 139–153, 1960.

[SRDL10] N. Salas, R. Ramanathan, S. Dummett, and R. Leveillee, "Results of radiofrequency kidney tumor ablation: renal function preservation and oncologic efficacy," *World Journal of Urology*, vol. 28, no. 5, pp. 583–591, 2010.

[SRHG97] A. E. Siperstein, S. J. Rogers, P. D. Hansen, and A. Gitomirsky, "Laparoscopic thermal ablation of hepatic neuroendocrine tumor metastases," *Surgery*, vol. 122, no. 6, pp. 1147–1155, 1997.

[SS80] M. A. Stuchly and S. S. Stuchly, "Dielectric properties of biological substances – tabulated," *Journal of Microwave Power*, vol. 15, no. 1, pp. 19–25, 1980.

[SS90] ——, "Electrical properties of biological substances," in *Biological Effects and Medical Applications of Electromagnetic Energy*, O. P. Ghandi, Ed. Prentice-Hall, 1990.

[SS94] A. V. Shahidi and P. Savard, "A finite element model for radiofrequency ablation of the myocardium," *IEEE Transactions on Biomedical Engineering*, vol. 41, no. 10, pp. 963–968, 1994.

[SSA+04] S. Sabeti, M. Schillinger, J. Amighi, C. Sherif, W. Mlekusch, R. Ahmadi, and E. Minar, "Primary patency of femoropopliteal arteries treated with nitinol versus stainless steel self-expanding stents: Propensity score–adjusted analysis," *Radiology*, vol. 232, no. 2, pp. 516–521, 2004.

[SSH+07] D. J. Schutt, M. M. Swindle, K. L. Helke, G. Bastarrika, F. Schwarz, and D. Haemmerich, "Sequential activation of ground pads reduces skin heating during radiofrequency tumor ablation: *In Vivo* porcine results," *IEEE Transactions on Biomedical Engineering*, vol. 57, no. 3, pp. 746–753, 2007.

[Süs79] C. Süsskind, "The "story" of nonionizing radiation research," *Bulletin of the New York Academy of Medicine*, vol. 55, no. 11, pp. 1152–1163, 1979.

[SWS02] L. Sha, E. R. Ward, and B. Stroy, "A review of dielectric properties of normal and malignant breast tissue," in *Proceedings IEEE Southeast-Con, 2002*, Columbia, SC , USA, 2002, pp. 457–462.

[TCG82] E. Tyler, C. Caldwell, and J. N. Ghia, "Transcutaneous electrical nerve stimulation: An alternative approach to the management of postoperative pain," *Anesthesia and Analgesia*, vol. 61, no. 5, pp. 449–456, 1982.

[TGS90] W. M. Telford, L. P. Geldart, and R. E. Sheriff, "Resistivity methods," in *Applied Geophysics*, 2nd ed. Cambridge University Press, 1990, pp. 522–539.

[TK11] K. Thomson and S. T. Kee, "Clinical research on irreversible electroporation of the liver," in *Clinical Aspects of Electroporation*, S. T. Kee, J. Gehl, and E. W. Lee, Eds. Springer, 2011, pp. 237–246.

[TMB+02] B. Thierry, Y. Merhi, L. Bilodeau, C. Trépanier, and M. Tabrizian, "Nitinol versus stainless steel stents: acute thrombogenicity study in an ex vivo porcine model," *Biomaterials*, vol. 23, no. 14, pp. 2997–3005, 2002.

[TPM+10] L. Thanos, L. Poulou, L. Mailli, M. Pomoni, and D. Kelekis, "Image-guided radiofrequency ablation of a pancreatic tumor with a new triple spiral-shaped electrode," *CardioVascular and Interventional Radiology*, vol. 33, no. 1, pp. 215–218, 2010.

[TSH+02] S. Tungjitkusolmun, S. T. Staelin, D. Haemmerich, T. Jang-Zern, C. Hong, J. G. Webster, J. Lee, F. T., D. M. Mahvi, and V. R. Vorperian, "Three-dimensional finite-element analyses for radio-frequency hepatic tumor ablation," *IEEE Transactions on Biomedical Engineering*, vol. 49, no. 1, pp. 3–9, 2002.

[TSN+09] L. Tarantino, I. Sordelli, V. Nocera, A. Piscopo, C. Ripa, D. Parmeggiani, and P. Sperlongano, "Ablation of large HCCs using a new saline-enhanced expandable radiofrequency device," *Journal of Ultrasound*, vol. 12, no. 2, pp. 69–74, 2009.

[TVT+06] C. Tziafalia, M. Vlychou, K. Tepetes, N. Kelekis, and I. V.Fezoulidis, "Echo-doppler measurements of portal vein and hepatic artery in asymptomatic patients with hepatitis B virus and healthy adults," *Journal of Gastrointestinal and Liver Diseases*, vol. 15, no. 4, pp. 343–346, 2006.

[Val04] Valleylab, "Cool-tip™ system technical specifications," 2004.

[Val11] J. W. Valvano, "Tissue thermal properties and perfusion," in *Optical-thermal response of laser-irradiated tissue*, 2nd ed., A. J. Welch and M. J. C. van Gemert, Eds. Springer, 2011, pp. 455–485.

[VCD85] J. W. Valvano, J. R. Cochran, and K. R. Diller, "Thermal conductivity and diffusivity of biomaterials measured with self-heated thermistors," *International Journal of Thermophysics*, vol. 6, no. 3, pp. 301–311, 1985.

[VHC09] J. M. Villagrán, A. B. Horcajadas, and E. O. Cruz, "Tratamiento mediante radiofrecuencia percutánea de los tumores óseos benignos: osteoma osteoide, osteoblastoma y condroblastoma," *Radiología*, vol. 51, no. 6, pp. 549–558, 2009.

[VSR09] D. Volkmer, M. Sichlau, and T. B. Rapp, "The use of radiofrequency ablation in the treatment of musculoskeletal tumors (*abstract*)," *Journal of the American Academy of Orthopaedic Surgeons*, vol. 17, no. 12, pp. 737–743, 2009.

[Wat48] W. Watson, "The electric boy," 1748. [Online]. Available: http://www.princeton.edu/~his291/Electric_Boy.html

[WC96] J. C. Weaver and Y. A. Chizmadzhev, "Theory of electroporation: A review," *Bioelectrochemistry and Bioenergetics*, vol. 41, no. 2, pp. 135–160, 1996.

[Whi10] E. T. Whittaker, *A History of the Theories of Aether and Electricity*, ser. Dublin University Press Series. London: Longmans, Green, and Co., 1910.

[Wor08] World Health Organization, “World cancer report 2008,” International Agency of Research on Cancer, 2008. [Online]. Available: http://www.iarc.fr/en/publications/pdfs-online/wcr/2008/wcr_2008.pdf

[WRC+00] T. Wood, D. Rose, M. Chung, D. Allegra, L. Foshag, and A. Bilchik, “Radiofrequency ablation of 231 unresectable hepatic tumors: Indications, limitations, and complications,” *Annals of Surgical Oncology*, vol. 7, no. 8, pp. 593–600, 2000.

[ZDM+98] A. R. Zlotta, B. Djavan, C. Matos, J.-C. Noel, M.-O. Peny, and D. E. Silverman, “Percutaneous transperineal radiofrequency ablation of prostate tumour: safety, feasibility and pathological effects on human prostate cancer,” *British Journal of Urology*, vol. 81, no. 2, pp. 165–175, 1998.

Errata

The following identified errors were already corrected in the presented version of the text (long solidus overlay represents erased text and underlines represents added text):

pag. xi:
The entry of Figure 2.6 is wrong. It should be read: "2.6 Debye dispersion considering a multi-term dispersion model. Change of the relative permittivity for the *n*-term."

pag. xii:
The entry of Figure 3.8 is missing: "3.8 Representation of a hepatic RF ablation set-up...44"

pag. xiv:
The entry of Figure 4.23 is wrong. It should be read: "4.23 Electrical characterization of the biopsy forceps. Impedance values, magnitude and phase, obtained from 40 Hz to 110 MHz."

pag. xx:
line 19 – "...conclusões deste trabalho evidenciam que é o procedimento ..."
line 22 – "Sugere-se ainda que os *stents* atualmente disponíveis no mercado possam ser vistos..."

pag. 2:
line 13 – "...and a much larger proportion in women."

pag. 5:
line 2 – "It is concerned with the mesh density..."

pag. 6:
line 11 – "RF ~~ablations~~ ablation and enhanced-saline RF ablation were considered."

pag. 11:
line 4 – "...although other mechanisms can be also presented, particularly..."

pag. 15:
line 15 – "Comparing Equations ~~(2.2)~~ (2.7) and (2.18)..."

pag. 18:
line 13 – "The β *dispersion* is verified at frequencies ~~of~~ from..."

pag. 21:
line 16 – Expression $\Delta\varepsilon_n = \varepsilon_s - \varepsilon_\infty$ should be written as $\Delta\varepsilon_n = \varepsilon_{sn} - \varepsilon_{\infty n}$

pag. 21:
The caption of Figure 2.6 is wrong. It should be read: "Debye dispersion considering a multi-term dispersion model. Change of the relative permittivity for the *n*-term."

pag. 25:
line 20 – "...also accounts for variations in the electrical conductivity because..."

pag. 29:
Thermal conductivity, k, is missing in Equation (2.31):
$\rho c_p \frac{\partial T}{\partial t} = \nabla \cdot k\nabla T - \omega_b c_b (T - T_b) + Q_m$

pag. 36:
line 7 – "...because of its ability to produce an electric shock up to 220 V..."

pag. 38:
line 14 – "...so he could stay insulated from the ground..."

pag. 50:
line 8 – "One should ~~be~~ add that tissue conductivity..."

pag. 59:
line 12 – "...saline solution perfusion ~~into~~ into the tissue."

pag. 82:
Thermal conductivity, k, is missing in Equation (4.2):
$\rho c_p \frac{\partial T}{\partial t} = \nabla \cdot k\nabla T - \omega_b c_b (T - T_b) + Q_m + q$

pag. 91:
The caption of Figure 4.23 is wrong. It should be read: "Electrical characterization of

the biopsy forceps. Impedance values, magnitude and phase, obtained from 40 Hz to 110 MHz."

pag. 93:
line 1 – "...the tissue heating process caused liquid evaporation..."

pag. 97:
line 17 – "...tissue is then mapped..."

pag. 112:
line 14 – "...for the experimental data."
line 16 – "The results are depicted in the graphic...".

pag. 119:
line 18 – "...the RF ablation lead to more..."

pag. 122:
line 3 – "In Figure 6.7, there are presented..."
line 13 – "...wires increases,..."

pag. 126:
line 5 – "...a temperature threshold of 60°C 50°C."

pag. 130:
line 26 – "...electrical problem."

pag. 131:
last line – "...so the distance between the axis of the three ducts is the same." was corrected to "... so the minimum distance between the three ducts is the same".

pag. 136:
line 17 – "The whole rest of the tumour is finally heated..."

pag. 138:
line 14 – "...the tumorous tissue is handled in the model."

pag. 139:
line 12 – "It was also considered that k_s σ_{tc} declines abruptly..."

pag. 140:
line 4 – "...of the electrical conductivity of the tissue..."

pag. 148:
line 9 – "...the tissue might not be totally accurate."